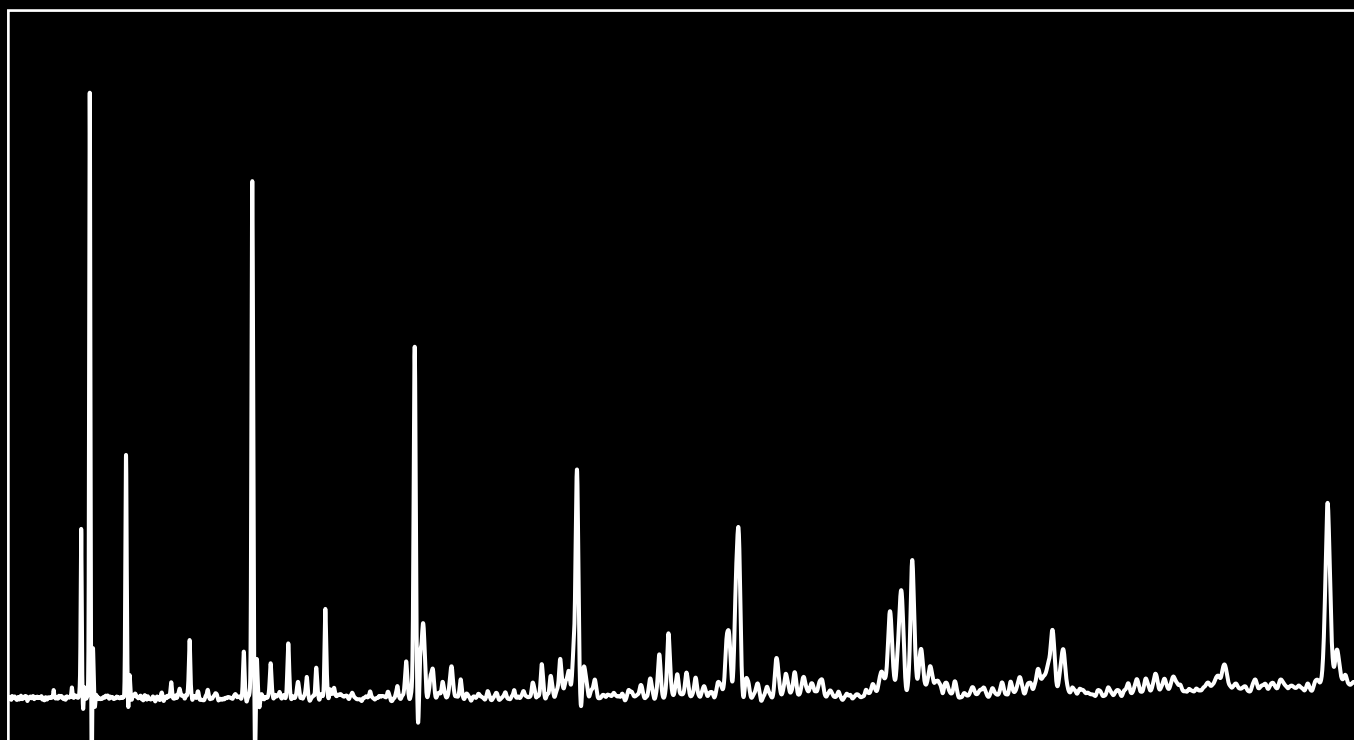


# On the Genesis and Measurement of Complex Organics and Isotopic Ratios in Hypervelocity Impact Ice Spectra

---



A thesis by  
Zach Ulibarri  
Advisor: Tobin Munsat

UNIVERSITY OF COLORADO

---

**On the Genesis and  
Measurement of Complex  
Organics and Isotopic Ratios in  
Hypervelocity Impact Ice  
Spectra**

---

**Zach Ulibarri**

**Advisor: Tobin Munsat**

December 10, 2021





IMPACT



Dedicated to my parents, especially my mother, for making the sacrifices  
you have made to get me to where I am today.

## Acknowledgements

I would like to thank the entirety of the IMPACT lab, both past and present. I feel incredibly lucky to have worked with such an interesting, helpful, and friendly cast of characters, especially when I compare my own experiences to those of my fellow grad students elsewhere. No matter where I end up next, I have no doubt that it will be quite difficult to find an environment that I so enjoy working in as IMPACT.

In particular I would like to thank David James and John Fontanese. DJ, it is hard for me to imagine what trajectory my research would have taken without you, as much of what I know about experimental physics was taught to me by you. DJ and John, both of you have been instrumental in helping the following research come to life, whether it was by offering up your own brilliant solutions to laboratory problems I was facing or by giving me an intelligent mind for me to ping ideas off of. You have also both helped me keep my sanity by providing entertaining banter in between the trials and tribulations of experimental physics.

I must likewise thank Keith Drake, for you have also taught me much of what I know, both during my time as an REU student in the lab and whilst you were dragging me up mountains and teaching me how to rock climb. The mountaineering has also been a necessity for the maintenance of my sanity.

I'd also like to thank my comrades-in-arms, Peter Siegfried, Lihsia Yeo, Joseph Samaniego, Lewis Patterson, and Chealsye Bowley. In the immortal words of Vonnegut, 'We are here to help each other get through this thing, whatever it is.' The happiest years of my life thus far have been those I've spent in grad school, and I thank you for sharing them with me.

And of course I must thank Tobin Munsat, my advisor. Tobin, if I were given the gift of being able to start life over knowing what I know now, I'd probably do a number of things differently, but there's no way in hell I'd choose a different advisor.

-Cheers,  
Zach



The author atop Uncompahgre Peak on August 28th, 2017, photographed by Keith Drake.

# Contents

List of Figures	ix
<b>1 Introduction</b>	<b>2</b>
1.1 Dust and Ice . . . . .	2
1.2 Dust begets dust . . . . .	3
1.3 Icy Ocean Worlds . . . . .	4
1.4 Active dust sources . . . . .	7
1.5 Impact Ionization Time of Flight . . . . .	8
1.6 Roadmap . . . . .	9
<b>2 Experimental Setup</b>	<b>11</b>
2.1 The IMPACT Dust Accelerator . . . . .	11
2.2 The Ice Target . . . . .	15
2.2.1 Diagram and description . . . . .	15
2.2.2 Interferometry . . . . .	18
2.3 The TOF System . . . . .	19
2.4 Alignment . . . . .	21
2.4.1 Target Alignment . . . . .	21
2.4.2 Beam Wandering . . . . .	23
2.4.3 System Alignment . . . . .	24
2.5 Surface Temperature . . . . .	26
2.5.1 <i>In-situ</i> Thermistors . . . . .	28

<b>3</b>	<b>Ice Preparation Methods</b>	<b>30</b>
3.1	Vapor Deposition . . . . .	30
3.2	Flash Freezing . . . . .	34
3.2.1	Methods . . . . .	37
3.2.2	Clathrate Capture . . . . .	38
3.3	Airbrushing . . . . .	39
3.3.1	Initial Attempts . . . . .	39
3.3.2	The Airbrush Chamber . . . . .	40
3.3.3	Methods . . . . .	41
3.4	Freeze Dried Surfaces . . . . .	42
3.5	Comparison of Airbrushed and Freeze-Dried Surfaces . . . . .	44
<b>4</b>	<b>Detection of Amino Acids and Fragmentation Products</b>	<b>46</b>
4.1	Importance . . . . .	46
4.1.1	Targets of Study . . . . .	46
4.1.2	Amino Acids as Biosignatures . . . . .	48
4.2	Impact Ionization TOF Instruments . . . . .	50
4.3	Experimental Setup . . . . .	52
4.4	Results . . . . .	54
4.4.1	Discussion . . . . .	64
<b>5</b>	<b>Measurement of D-H Ratios</b>	<b>72</b>
5.1	Importance . . . . .	72
5.1.1	Impact Ionization Time of Flight Measurements . . . . .	76

5.2	Experimental Setup . . . . .	77
5.3	Results . . . . .	86
<b>6</b>	<b>Suggestions for Future Work</b>	<b>94</b>
6.1	Experiments . . . . .	94
6.2	System Improvements . . . . .	100
<b>A</b>	<b>Supplementary Images</b>	<b>106</b>
<b>B</b>	<b>The Colorado Solar Wind Experiment</b>	<b>139</b>
B.1	Introduction . . . . .	139
B.2	Ion Source and Vacuum Systems . . . . .	141
B.3	Diagnostics . . . . .	144
B.4	Performance . . . . .	145
B.5	Planned Experiments . . . . .	148
B.6	Summary and Conclusion . . . . .	152
<b>C</b>	<b>References</b>	<b>153</b>

## List of Figures

1	Mass yield as a function of impact velocity for a number of impact masses into water ice (where silicate content $G = 0\%$ ) and into a pure basalt sample (where $G = 100\%$ ). The mass yield increases with both impactor mass and velocity, and it is over an order of magnitude higher for water ice than for basalt. In particular, the yield reaches a factor of 1000 for IDP-relevant impactors into water ice. Reprinted with permission from [28]. . . . .	5
2	A model of the potential Europa subsurface from NASA JPL [47]. . . . .	6
3	Active plumes on Enceladus as seen by the Cassini spacecraft. Image from NASA JPL [47]. . . . .	7
4	A density map of the distribution of dust particles for the IMPACT dust accelerator. . . . .	12
5	A schematic diagram of the IMPACT dust accelerator at the University of Colorado. . . . .	13
6	A photograph of the ice target chamber, which is shown on the left. The large cylindrical chamber on the right is the large accelerator chamber, denoted ‘Target Chamber’ on Fig. 5. In this photo, the chamber has not been connected to the chamber yet, and the vacuum gate valve connector is covered in foil for cleanliness. . . . .	14
7	A system diagram of the cryogenic ice target. A copper target is actively cooled by flowing liquid nitrogen. Mixtures of $H_2O$ and HDO are leaked into the system, growing ice over time, and their relative vapor pressures are measured by a residual gas analyzer to determine ice composition. Ice thickness is measured with Fabry-Perot interferometry. The ice is bombarded by hypervelocity dust coming from the accelerator, and an electric field provided by a metallic grid accelerates ions within the resulting ejecta plume towards a micro-channel plate detector TOF system. . . . .	16
8	A picture of the vapor deposition modular target installed on the copper block. . . . .	17

9	A diagram of the interferometry system. A visible red laser is split into two beams, with one being sent to a photodetector. The other beam is sent to a mirror target with an ice layer grown on top. Reflected light off of the front and back surfaces of the ice are sent to another photodetector. The slight delay from the beam reflected off of the back creates an interference pattern that can be used to measure ice thickness as it grows.	18
10	(A) A photograph of the modified lens stack. (B) A diagram of the modified TOF lens stack. Metal washers have been added underneath the precision ground ceramic spacers to extend the length of the inner insulating sleeve. This allows the acceleration grid to be moved out to the extremity of the lens stack.	20
11	A photograph of the target as seen from looking down the TOF tube from where the MCP assembly is normally mounted. The circular target mirror is just left of center of the acceleration grid ring, indicating that the system is not properly aligned. Fixing this would be straightforward, but may result in breaking the brazed joint between the stainless steel tubes and the copper block. Such a breakage could entail a serious expenditure of time in the shop to be fixed.	25
12	Plots of the temperature calibration experiments. It was found that without N-grease applied to both sides of the Kapton sheet, poor thermal contact was made, with the actual target surface only getting down to 131 K despite a temperature of 77.8 K on the copper block, as shown in (A). After N-grease was applied, the target surface reached 84 K, as shown in (B)	27
13	A diagram of the etched gold thermistors for <i>in-situ</i> temperature measurement (A), and a photograph of a microscope view of the etched thermistor pad after soldering and sparking, showing that it is not continuous and is therefore broken (B).	28
14	A photograph of a vapor deposition target with a gold-coated mirror. This model uses indium rather than N-grease as a thermal conductant.	31

15	A water spectrum produced by a 16 km/s iron dust particle impacting a water ice surface prepared by vapor deposition. Red triangles show observed mass lines, and the top axis provides species identification where applicable. WN H is shorthand for $(\text{H}_2\text{O})_n\text{H}$ . . . . .	33
16	A schematic view of the flash freezing system. A target recess is used to hold small volumes of aqueous solution. A Vespel door or cover is fitted into the canted slots on the copper target, isolating this solution from atmosphere. The ‘drip step’ is used to isolate the solution from the Vespel cover, as without it the door often freezes shut. . . . .	35
17	Three photos of the flash freezing target, showing the target after immersion in the LN <sub>2</sub> , the cold target with an amino acid solution and with the cover partially removed, and finally in the ice target chamber during an actual experimental run. . .	36
18	A photograph of the glovebox used in the airbrushing experiments. The antechamber is on the left. Note that it features its own venting, nitrogen, and vacuum lines as well as its own vacuum gauge. The floor of the main chamber is padded with aluminum foil-wrapped foam to prevent cracking of the plastic in the even of LN <sub>2</sub> leaks. . . . .	41
19	A photograph of the aluminum flatplate modular target. . . .	43
20	A diagram of the freeze-drying process. (A) An airbrushed surface with a homogenous mixture of water (aqua) and amino acids (blue) is slowly raised to room temperature while a vacuum pump removes evaporating water, yielding (B), a surface composed entirely of the amino acid in solid form. This surface is then installed into the ice target chamber at room temperature. If desired, the system can be cooled down and vapor deposition can be used to produce (C), a surface of the amino acid coated by a thin layer of water ice. This can be used to more carefully control the relative ion content of the water clusters and the amino acid lines in TOF data. . . . .	44
21	Summed spectra for impacts of velocities between 3 and 4 km/s in Experiment 1, which featured a bare histidine surface exposed to the dust beam. Pink and green lines denote mass groups of breakup products. Blue lines show water lines. Yellow lines denote contaminants or other mass aliases. . . .	55

22	Summed spectra for impacts of velocities between 7 and 8 km/s in Experiment 1, which featured a bare histidine surface exposed to the dust beam. A detail without the dominating histidine line is shown in the supplemental Fig. 58. . . . .	56
23	Summed spectra for impacts of velocities between 14 and 15 km/s in Experiment 1, which featured a bare histidine surface exposed to the dust beam. A detail without the histidine region is shown in the supplemental Fig. 65. . . . .	57
24	Summed spectra for impacts of velocities between 3 and 4 km/s in Experiment 2, which featured a 60 nm water ice layer covering the histidine surface. Pink and green lines denote mass groups of breakup products. Blue lines show water lines. Yellow lines denote contaminants or other mass aliases. The histidine molecule dominates the spectrum, and a detail without this dominating line is shown in the supplemental Fig. 66. . . . .	58
25	Summed spectra for impacts of velocities between 7 and 8 km/s in Experiment 2, which featured a 60 nm water ice layer covering the histidine surface. A detail without the dominating histidine line is shown in the supplemental Fig. 70. . . . .	59
26	Summed spectra for impacts of velocities between 14 and 15 km/s in Experiment 2, which featured a 60 nm water ice layer covering the histidine surface. A detail without the histidine region is shown in the supplemental Fig. 77. . . . .	60
27	Electron ionization mass spectrum of histidine, modified from the NIST Webbook [143]. . . . .	61
28	Ion content of mass groups 110 and 83 relative to the histidine parent molecule as functions of impact velocity. The dashed lines are fits to the first three velocity bins, and the solid lines are fits to the 6-7 km/s and higher velocity bins. . . . .	65
29	Ion content of mass groups 27, 42, 52, and 69 relative to the histidine parent molecule as functions of impact velocity. The dashed lines are fits to the first three velocity bins, and the solid lines are fits to the 6-7 km/s and higher velocity bins. . . . .	66
30	Ion content of mass groups 93, 122, and 137 relative to the histidine parent molecule as functions of impact velocity. The dashed lines are fits to the first three velocity bins, and the solid lines are fits to the 6-7 km/s and higher velocity bins. . . . .	67

31	Ion content of all mass groups combined relative to the histidine parent molecule as functions of impact velocity. The dashed lines are fits to the first three velocity bins, and the solid lines are fits to the 6-7 km/s and higher velocity bins. . .	68
32	Plot of the modelled D/H ratio of water in the early planetary disc. Reprinted with permission from [146]. . . . .	74
33	Measured D/H ratios of the solar system. Saturnian system objects are shown in Green, while Jovian system objects are shown in in cyan. Note that Phoebe is nearly an order of magnitude higher in D/H than the rest of Saturn’s satellites. Reprinted with permission from [159]. . . . .	75
34	RGA partial pressure vs time plot for the D <sub>2</sub> O-dominated solution with D/H = 4.2. The leak valve supplying the D <sub>2</sub> O/H <sub>2</sub> O mixture is opened at t ≈ 1500s and closed at t ≈ 7500s. Masses are described in Table 3. . . . .	79
35	The D and H ion regions of individual class 1 spectra exemplars, which exhibit easy to identify hydrogen and deuterium mass lines without excessive noise around them. These spectra are all taken from the high concentration dataset, where the D/H ratio was measured by the RGA to be 4.2. The hydrogen ion region is bracketed by pink lines, and the deuterium region is bracketed by green lines. . . . .	82
36	An expanded view of an individual class 1 exemplar spectrum.	83
37	The D-H ion regions of individual class 2 spectra exemplars, which sometimes have significant noise around the D and H lines. Ions may also be spread out in discretized peaks rather than continuous curves. The hydrogen ion region is bracketed by pink lines, and the deuterium region is bracketed by green lines. . . . .	84
38	The D-H ion regions of class 3 spectra exemplars. The hydrogen ion region is bracketed by pink lines, and the deuterium region is bracketed by green lines. . . . .	85
39	RGA partial pressure vs time plot for the mid level solution with D/H measured as 0.17. Masses are described in Table 3.	87
40	RGA partial pressure vs time plot for the third and final low level solution with D/H measured to be 0.035. Masses are described in Table 3. . . . .	88

41	D and H regions of the summed spectra of the high concentration experiment with $D/H = 4.2$ , separated by spectra class. . . . .	89
42	D and H regions of the summed spectra for the mid concentration experiment with $D/H = 0.17$ , separated by spectra class. . . . .	90
43	D and H regions of the summed spectra for the low concentration experiment with $D/H = 0.033-0.035$ , separated by spectra class. . . . .	91
44	An example spectrum showing a strong mass 32 detection in water ice doped with $CO_2$ . While mass 32 may simply be molecular oxygen, it may also be methanol, $CH_3OH$ . Other features of the spectrum are protonated $CO_2$ , $COH$ , $CO$ , and $C$ and $CH$ species. Note that elemental oxygen is also a strong feature of the spectrum. Even so, molecular $O_2$ is expected to charge negatively, and thus should not typically be present in this positive ion spectrum. . . . .	99
45	A plot of the spectrum collection efficiency for the month of October 2021. Experiments performed with the true airbrush method are colored in red, experiments performed with freeze-dried targets at room temperature are colored in blue, and experiments performed with freeze-dried targets with water layers grown on top are colored cyan. The red horizontal line denotes the average true airbrush collection efficiency. . . . .	102
46	Three photographs showing the assembly process of the vapor deposition target. . . . .	106
47	A photograph of the flash freezing target before the door has been removed in an actual experimental run. . . . .	107
48	RGA partial pressure vs time plot for the first level solution with $D/H$ measured as 0.033. Masses are described in Table 3. . . . .	108
49	RGA partial pressure vs time plot for the second low level solution with $D/H$ measured as 0.033. Masses are described in Table 3. . . . .	109
50	Examples of discarded spectra in the D-H experiments. Some of these spectra, e.g. Shot 249 in the upper right, very likely contain valid D and H ions, but the spectra are of such low quality that they were rejected. The expected hydrogen ion region is bracketed by pink lines, and the deuterium region is bracketed by green lines. . . . .	110

51	Plots of the D and H regions of the co-added spectra from the first low concentration experiment, where the RGA measured a D/H ratio of the water ice at 0.033. . . . .	111
52	Plots of the D and H regions of the co-added spectra from the second low concentration experiment, where the RGA measured a D/H ratio of the water ice at 0.033. . . . .	112
53	Plots of the D and H regions of the co-added spectra from the second low concentration experiment, where the RGA measured a D/H ratio of the water ice at 0.035. . . . .	113
54	Detail of the summed spectra for impacts of velocities between 3 and 4 km/s in Experiment 1, which had no ice layer covering the histidine surface. . . . .	114
55	Detail of the summed spectra for impacts of velocities between 4 and 5 km/s in Experiment 1, which had no ice layer covering the histidine surface. . . . .	115
56	Detail of the summed spectra for impacts of velocities between 5 and 6 km/s in Experiment 1, which had no ice layer covering the histidine surface. . . . .	116
57	Detail of the summed spectra for impacts of velocities between 6 and 7 km/s in Experiment 1, which had no ice layer covering the histidine surface. . . . .	117
58	Detail of the summed spectra for impacts of velocities between 7 and 8 km/s in Experiment 1, which had no ice layer covering the histidine surface. . . . .	118
59	Detail of the summed spectra for impacts of velocities between 8 and 9 km/s in Experiment 1, which had no ice layer covering the histidine surface. . . . .	119
60	Detail of the summed spectra for impacts of velocities between 9 and 10 km/s in Experiment 1, which had no ice layer covering the histidine surface. . . . .	120
61	Detail of the summed spectra for impacts of velocities between 10 and 11 km/s in Experiment 1, which had no ice layer covering the histidine surface. . . . .	121
62	Detail of the summed spectra for impacts of velocities between 11 and 12 km/s in Experiment 1, which had no ice layer covering the histidine surface. . . . .	122

63	Detail of the summed spectra for impacts of velocities between 12 and 13 km/s in Experiment 1, which had no ice layer covering the histidine surface. . . . .	123
64	Detail of the summed spectra for impacts of velocities between 13 and 14 km/s in Experiment 1, which had no ice layer covering the histidine surface. . . . .	124
65	Detail of the summed spectra for impacts of velocities between 14 and 15 km/s in Experiment 1, which had no ice layer covering the histidine surface. . . . .	125
66	Detail of the summed spectra for impacts of velocities between 3 and 4 km/s in Experiment 2, which had a 60 nm water ice layer covering the histidine surface. . . . .	126
67	Detail of the summed spectra for impacts of velocities between 4 and 5 km/s in Experiment 2, which had a 60 nm water ice layer covering the histidine surface. . . . .	127
68	Detail of the summed spectra for impacts of velocities between 5 and 6 km/s in Experiment 2, which had a 60 nm water ice layer covering the histidine surface. . . . .	128
69	Detail of the summed spectra for impacts of velocities between 6 and 7 km/s in Experiment 2, which had a 60 nm water ice layer covering the histidine surface. . . . .	129
70	Detail of the summed spectra for impacts of velocities between 7 and 8 km/s in Experiment 2, which had a 60 nm water ice layer covering the histidine surface. . . . .	130
71	Detail of the summed spectra for impacts of velocities between 8 and 9 km/s in Experiment 2, which had a 60 nm water ice layer covering the histidine surface. . . . .	131
72	Detail of the summed spectra for impacts of velocities between 9 and 10 km/s in Experiment 2, which had a 60 nm water ice layer covering the histidine surface. . . . .	132
73	Detail of the summed spectra for impacts of velocities between 10 and 11 km/s in Experiment 2, which had a 60 nm water ice layer covering the histidine surface. . . . .	133
74	Detail of the summed spectra for impacts of velocities between 11 and 12 km/s in Experiment 2, which had a 60 nm water ice layer covering the histidine surface. . . . .	134

75	Detail of the summed spectra for impacts of velocities between 12 and 13 km/s in Experiment 2, which had a 60 nm water ice layer covering the histidine surface. . . . .	135
76	Detail of the summed spectra for impacts of velocities between 13 and 14 km/s in Experiment 2, which had a 60 nm water ice layer covering the histidine surface. . . . .	136
77	Detail of the summed spectra for impacts of velocities between 14 and 15 km/s in Experiment 2, which had a 60 nm water ice layer covering the histidine surface. . . . .	137
78	A beautiful photograph of the ice target from behind, looking upstream into the dust source. . . . .	138
79	A photo of the CSWE chamber. Ionized gas is created in the ion source, and an accelerating potential pulls the ions into the experimental chamber. A differential pressure chamber prevents excess gas build up in the experimental chamber. . .	142
80	A diagram of the CSWE ion source. Nitrogen gas is ionized by energetic electrons emitted from a hot cathode. Ions are extracted through a screen grid by a negatively biased accelerating grid. Curvature of these grids diverges the beam to increase its cross-section and uniformity. A hot filament neutralizer supplies electrons to maintain quasi-neutrality of the flowing plasma. . . . .	143
81	Sample traces from the Ion Energy Analyzer (IEA) showing measured ion current as a function of retarding potential for three different ion energies. Solid lines denote the measured current, while dotted lines denote the derivative. There is a sharp drop at each specified energy, indicating that the flow is highly uniform in its velocity distribution. . . . .	144
82	A top-down diagram of the coordinates used in the CSWE. The X-axis measures horizontal displacement from the beam's center axis, while the Z-axis measures the distance from the source itself. . . . .	145
83	Plots of the particle flux for each position on the x and z axes. These values were calculated from the IEA measurements. The green shaded region denotes the designated experimental region. Note that the flux at 80 mA and 200 V is lower than the flux at 40 mA. . . . .	147

84	Plots of the electron density for each position on the x and z axes. These values were analyzed from the Langmuir probe measurements. The green shaded region denotes the designated experimental space. . . . .	149
85	Plots of the ratio of beam to thermal ion density for each position on the x and z axes. These values were calculated from the IEA measurements. . . . .	150
86	A diagram of the planned experiments. 1. Solar wind interaction with magnetic anomalies. 2. Dust charging and dynamics. 3. Plasma wakes. 4. topographical wakes. . . . .	151

## Abstract

Impact ionization time of flight mass spectrometers (TOF-MS) are a class of spaceflight instrument designed to study the molecular composition of dust grains ejected from airless solar system objects by impacting them at speeds of several km/s. The kinetic energy of the impact ionizes molecules from the dust grain, allowing them to be studied using TOF-MS. Such instruments have been used in the past to study a number of different solar system objects, most notably when the Cassini Cosmic Dust Analyzer (CDA) measured the chemistry of icy dust grains from the subsurface ocean of Enceladus. While some laboratory work has been performed to match CDA flight spectra, previous studies have not used actual hypervelocity dust impacts into ice. Here we describe a series of experiments based on a cryogenic target system at the University of Colorado dust accelerator at the Institute for Modeling Plasma, Atmospheres, and Cosmic Dust (IMPACT), which enables impact experiments into ice under highly realistic conditions.

Using a novel airbrush ice system, surfaces of histidine both with and without a water ice cover were bombarded by hypervelocity dust grains. TOF chemical analysis of the impact plume suggests that the amino acid fragmentation rate is largely constant below 6 km/s, but begins to rise significantly beyond 7 km/s. It also suggests that the presence of a water ice matrix mitigates impact stress and reduces the fragmentation rates at all velocities by a factor of about two. Further, the spectra show that fragmentation products are fundamentally related to those found in the NIST database of electron impact ionization mass spectra of histidine. This indicates that even in the event of breakup during detection, it may be possible to use the breakup products as a means to identify the parent molecule with impact ionization TOF instruments, thus enabling this type of instrument to detect and characterize complex organics.

Similar experiments were performed with ice created with a known D-H ratio. Co-added TOF spectra from the impact plume indicates that the D-H ratio can be accurately recovered with this method. This means that impact ionization mass spectrometers on a variety of future spacecraft may be able to measure the D-H ratio of icy ocean worlds, comets, and other airless icy bodies.

# 1 Introduction

## 1.1 Dust and Ice

Water ice is prevalent throughout the solar system, found on planets, moons, and comets, among other bodies. While terrestrial ice is shielded from the vacuum of space by the Earth's atmosphere, in permanently shadowed lunar regions and throughout the outer solar system there exist great volumes of water ice that are exposed directly to space and all the rich astrophysical phenomena that come with it. Water ice is found on the Jovian satellites Io, Europa, Ganymede, and Callisto, as well as moons of Saturn, Uranus, and Pluto (as well as Pluto itself for that matter), along with a host of other objects [1, 2, 3, 4, 5, 6]. These ices, lacking atmospheric cover or merely having tenuous atmospheric cover, experience bombardment from charged particles, from ultraviolet and x-ray light, and from micrometeoroids, or interplanetary dust particles (IDPs).

These bombardment processes supply energy and sometimes new chemical species to the water ice, enabling surface chemistry evolution over long time periods. While there exists a great body of literature probing the effects of charged particle and radiation bombardment of water ices, there has been a comparative dearth of laboratory studies of micrometeoritic bombardment. This is despite the fact that studies have suggested that IDPs are at minimum as important as these other sources of bombardment in terms of the long-term chemical evolution of the surface ice [7, 8, 9, 10, 11, 12, 13].

The importance of dust is due in part to its ubiquity in the solar system. Estimates of the total flux of IDPs into the Earth upper atmosphere, for example, vary, but it is believed to be in the tens or hundreds of tons per day, all in the form of sub-gram particles [14]. But IDPs can be found throughout the solar system, originating from a number of different sources and carrying a great deal of information about those sources in their composition and characteristics [15]. This enables the emerging concept of Dust Astronomy, wherein spacecraft instruments are used to measure the composition of dust particles while also measuring their velocity and trajectory, thus constraining their origin [16, 17]. Such instruments would be able to, for example, differentiate between dust particles from Jupiter Family Comets (JFCs), Halley and Oort Cloud Comets (OCCs), asteroids, and Interstellar Dust (ISD), among other sources, while also cataloging their compositional data. A side-by-side comparison of dust emanating from JFCs and from asteroids would deter-

mine if they formed in the same early-solar system reservoirs or if they are compositionally distinct [17]. It has long been argued that cometary nuclei, being frozen since the formation of the planets, are pristine sources of ice and organics from that time [18, 19]. Dust Astronomy instruments that study large quantities of JFC IDPs could determine to what extent this family preserves unprocessed pre-solar material [17].

## 1.2 Dust begets dust

Perhaps one of the most intriguing processes that IDPs drive is the creation of yet more dust. As particles strike the surfaces of airless bodies at high velocity, they kick up ejecta particles in the form of dust grains. This process has been described for a number of solar system objects, including moons, asteroids, Kuiper Belt Objects (KBOs), as well as for Mercury and Pluto and its moons [20, 21, 22, 23, 24, 25, 26]. For larger parent bodies, most of these particles cannot achieve escape velocity and either populate ring systems or fall back to the parent surface, turning over regolith in a gardening process [20, 27]. While smaller moons have less surface area to collect dust impacts, the smaller escape velocities for these smaller objects means that a greater fraction of the ejecta are not gravitationally bound. In particular, Poppe and Horányi showed that Hydra and Nix each contribute similar amounts of ejecta to the Pluto system as do Charon and Pluto itself [26].

This ejecta effect is amplified by the focusing of IDPs by planetary gravity wells, as gravitational lensing increases the flux and velocities of IDPs at the surfaces of orbiting moons. For example, IDPs that are pulled in by Jupiter or Saturn to strike their respective moons Ganymede and Enceladus do so with a velocity that is typically twice its value when it enters the gravity well [20, 27]. The flux of particles at Ganymede is estimated to be 5.8 times greater than it is in the near-Jupiter environment, and the flux at Enceladus is estimated to be 6.8 times higher than the near-Saturn environment [20].

While any airless body may produce dust ejecta as a result of IDP bombardment, the amount of ejecta is particularly high for surface ices. Koschny and Grün studied the mass yields of impacts into ice with various levels of silicate content and pure silicates [28]. Defining mass yield,  $Y$ , as

$$Y = \frac{m_c}{m_p}, \tag{1}$$

where  $m_p$  is the mass of the impacting particle and  $m_c$  is the mass of the crater excavated by that impact, they found that this yield increased with velocity and impactor mass, but also with the purity of the water. Specifically, the mass yield was found to be

$$Y = 2.85 \cdot 10^{-8} (0.0149)^{G/100} \cdot \left( \frac{1 - G/100}{\rho_{ice}} + \frac{G/100}{\rho_{sil}} \right) \cdot m_p^{b-1} v_p^{2b} \quad (2)$$

where  $G$  is the percentage of silicate content of the target material,  $b$  is dimensionless constant of 1.23,  $m_p$  is the mass of the impacting particle, and  $v_p$  is the impactor velocity. Figure 1, printed with permission from [28], shows the yield as a function of impact velocity for a number of impactor masses into both pure water and pure basalt. For IDP-relevant masses and velocities, the yield reaches over 1000, meaning that an impacting IDP of mass  $m$  may produce several thousand  $m$  worth of ejecta.

Thus, while IDPs can produce ejecta dust clouds by impacting the surface of any airless body, the effect is particularly pronounced for impacts into ice surfaces, such as may be found on icy ocean worlds.

### 1.3 Icy Ocean Worlds

There exist in the outer solar system a special class of planetary objects called ocean worlds that are known or believed to harbor liquid water oceans, either globally or locally [29]. This has tremendous implications for the search for extraterrestrial life because our own terrestrial biology is so fundamentally based on exploiting the special properties of liquid water [30, 31]. This has made icy ocean worlds high priority targets for exploration missions.

There are a great number of known or suspected ocean worlds even in our own solar system. Ganymede, the largest moon in the solar system (larger even than the planet Mercury), is nonetheless somewhat typical of ocean worlds, with deep interior, high pressure oceans sandwiched between ice layers [32]. The outer ice shell is thought to be  $\sim 100$  km thick [32, 33, 34], but the centers of Ganymede's largest craters have interesting domes and flattened surfaces, often thought to be the result of refreezing melted ice [35, 36]. Other features appear to be the result of cryovolcanism [37], whereby volatiles, in this case water, are ejected much like magma on terrestrial volcanoes. Nonetheless, the thickness of Ganymede's ice shell makes it difficult

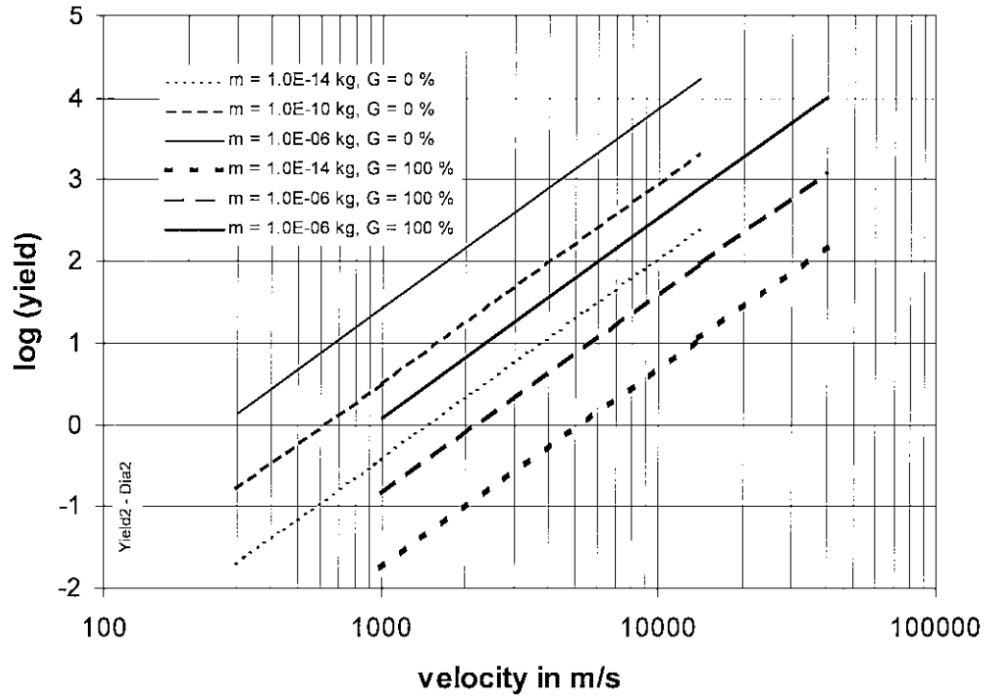


Figure 1: Mass yield as a function of impact velocity for a number of impact masses into water ice (where silicate content  $G = 0\%$ ) and into a pure basalt sample (where  $G = 100\%$ ). The mass yield increases with both impactor mass and velocity, and it is over an order of magnitude higher for water ice than for basalt. In particular, the yield reaches a factor of 1000 for IDP-relevant impactors into water ice. Reprinted with permission from [28].

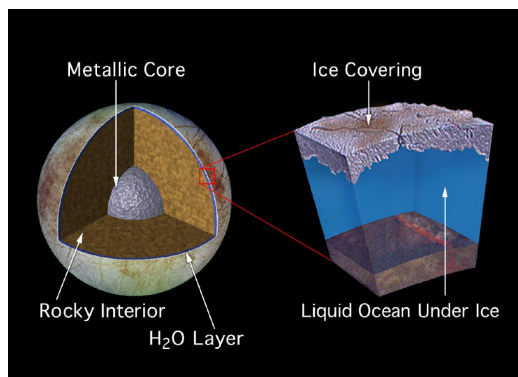


Figure 2: A model of the potential Europa subsurface from NASA JPL [47].

to transport oxidants, created on the surface by solar irradiation, down into the ocean. This would fundamentally limit the biotic potential of any life that might possibly exist in Ganymede’s oceans [32].

Europa and Enceladus, moons of Jupiter and Saturn respectively, are then particularly attractive ocean worlds due to the relative thinness of their ice shells [32, 38], which would make flow of oxidants from the surface to the subsurface much more tenable. Enceladus is known to have a global liquid water ocean under an ice crust approximately 20 km thick, but that shell may taper down to as little as 5 km at the south pole [39, 40, 41, 42]. There are several lines of evidence that Europa has a subsurface liquid water ocean, most notably from the combination of gravitational data and the Galileo spacecraft’s magnetometer data that suggests a conductive layer near the surface [33, 43]. The thickness of Europa’s ice shell is not well constrained, and is generally thought to be between a few km and a few tens of km thick [32, 44, 45, 46].

Moreover, both Europa and Enceladus’s oceans are thought to be in contact with a rocky seafloor [32, 42], as shown in Fig 2, which is from NASA JPL [47]. This enables a wide range of water-rock chemical reactions that are known to drive terrestrial biology in Earth’s own ocean floors [48, 49, 50].

Thus, the oceans of Europa and Enceladus could potentially support life via oxidants created by radiation at the surface and chemical inventories and interactions provided by hydrothermal vents at the ocean floor, making both ocean worlds prime candidates for extraterrestrial life searches [48, 50]. This has made them the focus of a number of planned and proposed missions due to the liquid water oceans that are known or believed to be beneath their ice

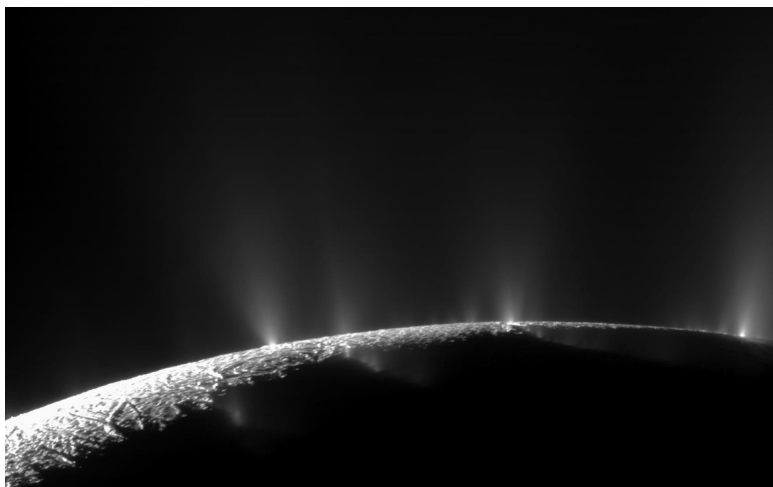


Figure 3: Active plumes on Enceladus as seen by the Cassini spacecraft. Image from NASA JPL [47].

crust surfaces [51, 52, 53, 54, 55].

#### 1.4 Active dust sources

One of the most intriguing aspects of the Enceladus system is the active plumes of water vapor that are known to be erupting from its south polar region [41, 56, 57]. A photo taken by the Cassini spacecraft of such plumes is shown in Fig. 3. The plumes are continuous streams of micron-sized dust grains, gas, and ionized particles emanating directly from the subsurface ocean [42, 57]. Indeed, it was chemical analysis of these plumes that first suggested that the ocean water was in contact with the rocky core of the moon [42]. The large majority of dust grains released from plumes are lofted on ballistic trajectories that eventually re-impact the surface [58]. So powerful and steady are these plumes that they have been modelled to deposit as much as 0.5 mm of new surface material in the immediate vicinity of the plumes and up to tens of microns at the equator each year [59]. The plumes are also known to contain organics [60], some with molecular masses in excess of 200 u [61].

There have been tentative detections of similar plume activity on Europa, first from the Hubble Space Telescope and then by indirect detections from Galileo spacecraft instruments [62, 63, 64, 65]. If such plumes exist, they are

likely to be transient rather than the steady streams observed at Enceladus.

It should also be noted that plumes have also been observed on Triton, although their composition and origin remain a mystery [66, 67]. This moon of Neptune is another fascinating potential ocean world. Like Europa and Enceladus, it features a young surface relatively unmarred by craters, suggesting active geology [68, 69], but the dark coloration of the plumes suggests a source other than water vapor [66, 67].

Thus, in addition to the dust production sources described in Section 1.2, active plumes present yet another way in which icy dust grains can be lofted into the environments surrounding icy ocean worlds, and they provide particularly enticing targets for study because they come from the subsurface. The combination of these two processes — ejection of surface material via IDP bombardment and plume emission of subsurface material — creates rich populations of icy dust that can be studied even without landing on the parent body. This allows for flexible and comparatively inexpensive missions that do not require landing, with all of its complexity and planetary protection requirements [70], but which can still directly sample surface material, provided of course that they have instruments capable of studying icy dust grains collected during a fast fly-by.

## 1.5 Impact Ionization Time of Flight

Impact ionization time of flight (TOF) mass spectrometers are a class of dust analysis instruments that have been flown on a number of missions, most famously with the Cassini spacecraft’s Cosmic Dust Analyzer (CDA) [71, 72, 73, 74]. These instruments use a metal target plate, typically composed of rhodium or gold, that impacts dust grains as the spacecraft flies through them at high velocity, typically  $> 3$  km/s. At such speeds, referred to as hypervelocities, the kinetic energy of the impacting dust particle results in its vaporization and ionization. This process is exploited by using tailored electric fields to accelerate generated ions towards a high-speed detector. Because doubly ionized particles are rarely, if ever, seen in this impact process (even at very high velocity [73]), each ion species is imparted with the same amount of kinetic energy, meaning that they are accelerated to different velocities by the electric fields. They thus spread out in time according to their mass, with the highest mass particles taking the longest to reach the detector. This forms a TOF system which can be used to analyze the chemical composition of the dust grains. Such instruments are prime candidates for

studying the dust populations throughout the solar system, be they from icy ocean worlds, comets, or any other source.

The CDA provided highly valuable data to the Cassini spacecraft’s mission studying the Saturnian system. Most notably, it identified water ice, salts, and organics in the plumes of Enceladus [41, 42, 61, 75]. It also confirmed previous observations that suggested the plumes were being emitted from a liquid water source [41], and it further showed that the carbonaceous and silicate content of the plumes strongly suggested that such a liquid reservoir was in contact with the moon’s rocky core [42, 75]. The instrument also showed that many of the icy dust grains from the plumes contained not merely organic content but high mass organics in excess of 200 u, an important observation for habitability studies [42, 57, 61, 76, 77].

Because of this versatility, there are several planned or proposed missions that include impact ionization TOF instruments. The SURface Dust Analyzer (SUDA) will fly on the Europa Clipper [52, 78]. It combines an impact ionization TOF with simple velocity measurements that allow it trace ellipses of probability for the launch point of each measured particle. This will allow it to not only measure the bulk composition of Europa on its flybys, but also to determine if and how surface features differ from one another compositionally [79].

The Interstellar Mapping and Acceleration Probe (IMAP) [80] mission will carry the (IDEX) [81]. This will provide unique measurements of the interstellar dust (ISD) particle composition.

The proposed Enceladus Life Finder (ELF) [54, 82] and the proposed Explorer of Enceladus and Titan (E<sup>2</sup>T) [83] missions both would make use of the Enceladus Icy Jet Analyzer (ENIJA) [84], an impact ionization TOF with significantly higher mass resolution than the CDA. This would enable it to study the composition of the high mass organics found in the Enceladus plumes, something the CDA was never designed to do. The proposed Fragments from the Origins of the Solar System and our Interstellar Locale (FOSSIL) mission would use several impact ionization instruments in tandem to produce a Dust Astronomy ‘telescope’ that may study bulk composition of JFCs, OCCs, and ISD particles [16, 17].

## 1.6 Roadmap

In order to make sense of past and future data taken by these instruments, there must be well-characterized laboratory experiments that study what

types of signals may be expected from impact ionization of a variety of materials. There must additionally be studies of how dust grains ejected from the surfaces of airless icy bodies by IDP impact may or may not be changed by the impact process. This thesis describes a suite of experiments based on a cryogenic ice target system at the Institute for Modelling Plasma, Atmospheres, and Cosmic Dust (IMPACT) dust accelerator facility at the University of Colorado. It enables study of hypervelocity impacts into ice surfaces with a variety of compositions under highly realistic and controlled conditions.

Chapter 2 describes the IMPACT dust accelerator and the ice target system itself. Chapter 3 explains the various methods of ice creation, covering vapor deposition, flash freezing, and a novel airbrush method. Chapter 4 describes a set of experiments probing the ability of impact ionization instruments to detect and characterize amino acids, an important class of organic molecules necessary for Earth-based life and a prime target for habitability studies. Chapter 5 details the use of impact ionization TOF mass spectrometry to determine the deuterium-hydrogen ratio of water ice. This ratio is an important metric for solar system formation models and may be used to constrain when and where certain planetary objects were formed. Chapter 6 describes several suggestions for future work, including experiments and hardware upgrades. Appendix A provides a number of supplemental figures, plots, and photographs. Appendix B is a copy of a paper I published early in my graduate career about the Colorado Solar Wind Project, a large-cross-section high-current steady state ion source that is being used to study the solar wind. It does not fit into the context of the rest of this thesis, which of course concerns itself with ice and hypervelocity impacts, and it is thus presented as an appendix.

## 2 Experimental Setup

### 2.1 The IMPACT Dust Accelerator

The IMPACT dust accelerator facility at the University of Colorado has been operational since 2011, and it provides a well-characterized beam of dust particles with a variety of compositions [85]. The accelerator uses a 3 MV Pelletron, typically operated at 2.2 MV for reliability, to produce a potential through which dust particles of various compositions are accelerated. Iron and aluminum are the two primary sources of dust, but a number of other particles have been flown as well, including polypyrrole, indium-tin oxide, olivine, and latex. In general, the accelerator launches particles with diameters between 20 nm and 5  $\mu\text{m}$  at velocities between 0.5 and 100 km/s. Particles smaller and/or faster than this are most likely also launched, but cannot be accurately measured and characterized. Fig. 4 gives the characteristic dust distribution of the IMPACT accelerator. A diagram of the accelerator is shown in Fig. 5.

A set of three beamline detectors measure the induced charge on cylindrical tubes as dust particles pass through them. By measuring the magnitude of the induced charge,  $Q$ , the charge of the dust particle itself is obtained. By measuring the time delay between induced charges on the first and last detectors, a velocity,  $v$ , measurement is made. Because the potential through which the particle has been accelerated is determined by the accelerator,  $\Phi = 2.2\text{MV}$ , the relevant conservation of energy equation

$$Q\Phi = \frac{1}{2}mv^2, \quad (3)$$

can be used to solve for  $m$ , the mass of the dust particle. Because the dust material is known for each run, so too is the dust density. This density and mass can then be used to calculate an effective radius of the dust particle. While few dust particles are truly spherical, this approximation is a useful metric in a variety of experiments. Thus, each accelerated particle is non-destructively measured to obtain its mass, effective radius, velocity, and charge. This data is stored in a database and can be recalled as needed to assign velocities or other metadata to individual dust events.

The DCS detectors, or Dust Coordinate Sensors, each have a grid of wires connected to charge sensitive amplifiers (CSAs). As dust particles pass through the detectors, they induce image charges on these wires, with

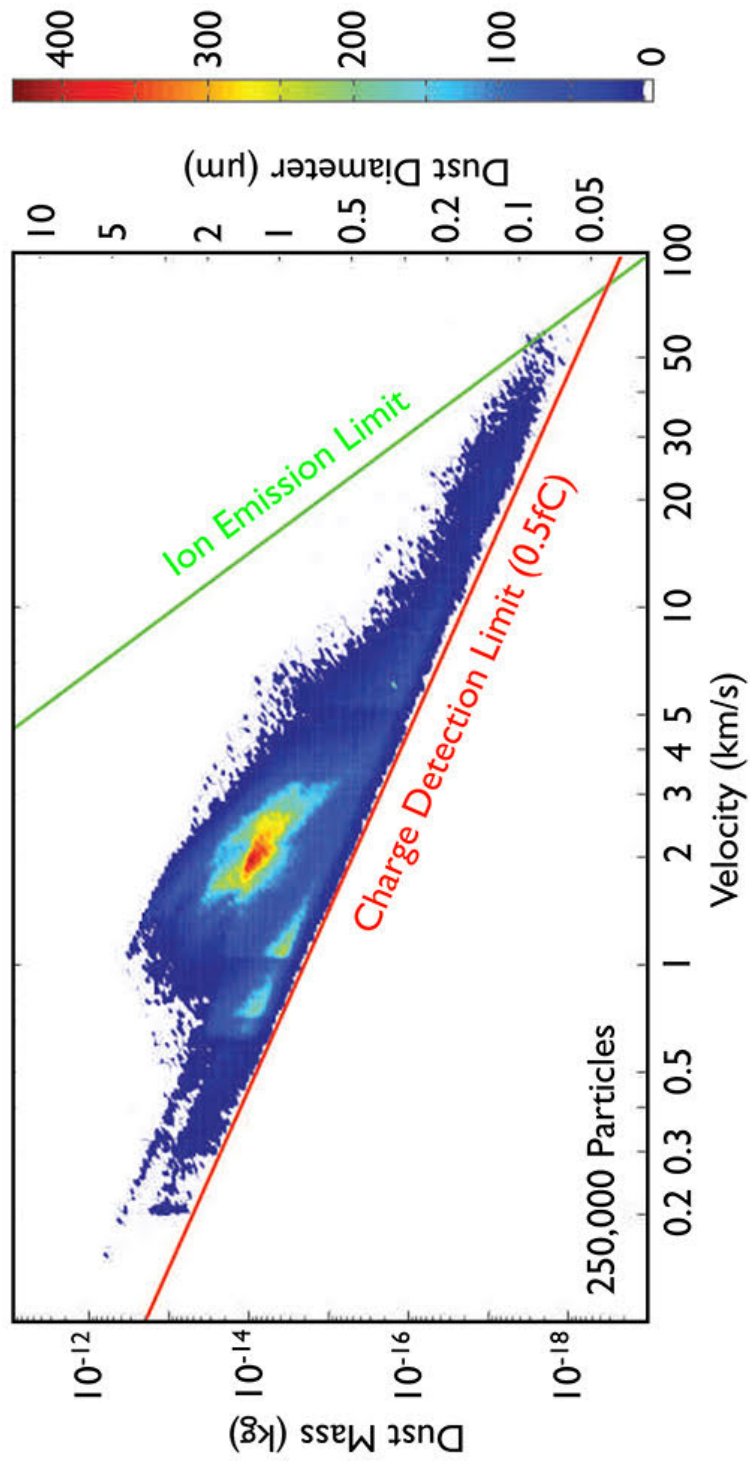


Figure 4: A density map of the distribution of dust particles for the IMPACT dust accelerator.

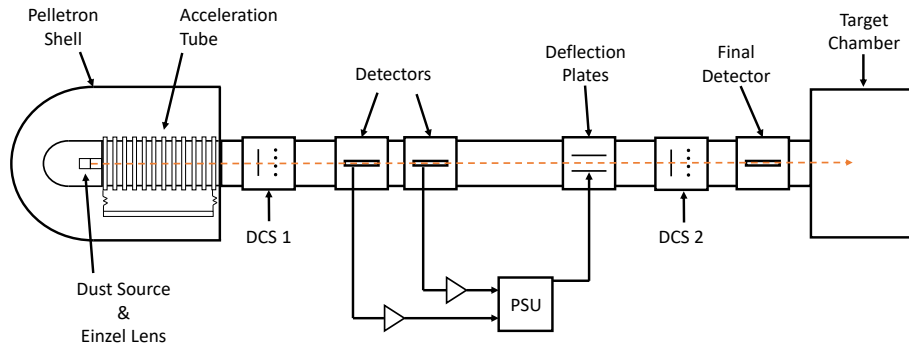


Figure 5: A schematic diagram of the IMPACT dust accelerator at the University of Colorado.

stronger charges induced on closer wires. By comparing the strength of the induced charge on each wire, the position of the particle can be deduced, giving DCS the ability to provide real-time position measurements of the dust beam. One DCS is located upstream near the source, and a second is located downstream near the end of the accelerator. By measuring X and Y data at two points, the particle trajectory can be determined, and the position of impact can be estimated for a target at arbitrary distance from the source. I populated and characterized all 24 circuits for the second DCS detector as part of a summer research program in 2013.

The Particle Selection Unit (PSU), which is a Field-Programmable Gate Array (FPGA) rapidly collects and analyzes all these dust parameters. A LabVIEW program is used to set user-specified parameter ranges for each experiment, and the PSU determines if each dust particle is within these acceptable ranges. Beyond the detectors is a set of deflection plates with a 6 kV potential across them. This potential is sufficient to knock any particle out of the beamline to impact into the chamber side walls. However, if the PSU determines that a dust particle matches all user-defined criteria, it sends a timed pulse that deactivates the deflection plate potential, allowing

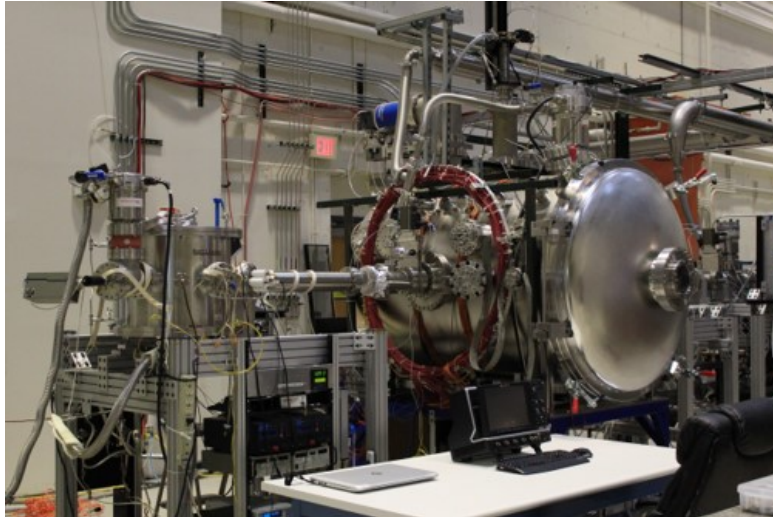


Figure 6: A photograph of the ice target chamber, which is shown on the left. The large cylindrical chamber on the right is the large accelerator chamber, denoted ‘Target Chamber’ on Fig. 5. In this photo, the chamber has not been connected to the chamber yet, and the vacuum gate valve connector is covered in foil for cleanliness.

the particle through. In this way, the PSU actively down-selects particles so that only those within the user-defined parameter space may continue through the accelerator, while the down-selected particles are eliminated. Thus, carefully controlled experiments can be performed with well-specified parameter ranges. As an example, experiments where only dust particles with radii above 100 nm and with velocities between 3 and 4 km/s can be performed.

For most experiments at IMPACT, a large experimental target chamber is used (‘target chamber’ on Fig. 5), but this chamber can also be used as a simple pass-through by attaching other chambers to its downstream side with a vacuum gate valve. IMPACT has a number of such chambers, from a gas target to simulate atmospheric ablation to a dedicated chamber for the SUDA instrument, but the focus of this thesis will be experiments performed in the cryogenic ice target system, shown just downstream of the accelerator’s primary target chamber in Fig. 6

## 2.2 The Ice Target

### 2.2.1 Diagram and description

The ice target is composed of a copper block mounted to a removable flange on the bottom of an ultra-high vacuum chamber. The design has gone through several iterations, and the actual target piece has been modularized to accept different target assemblies for different ice growth methods or different target materials. A schematic diagram of the ice target chamber is shown in Fig. 7, and a picture of the target components is shown in Fig. 8.

The target flange has a pair of stainless steel tubes that are welded through it. These tubes are both brazed to the target's solid copper block, and an internal routing in the copper block connects them, allowing liquid or gas to flow from outside the vacuum chamber through the copper block itself. Liquid nitrogen (LN<sub>2</sub>) is pumped through this route to actively cool the target down to temperatures below 85 K. The copper block also has a variety of threaded helicoils mounted on its sides to facilitate extra hardware, most notably a diode thermometer.

The top of the copper block is a smooth, flat surface upon which vacuum-safe Apiezon thermal N-grease is applied [86]. A sheet of Kapton polyimide film sits on top of this, and an additional layer of N-grease is applied on its surface [87]. Modular targets in the rough shape of the letter 'L' are then mounted on this top layer of grease and bolted to the copper block with PEEK thermoplastic screws [88]. The PEEK screws are nonconducting and pass outside the electrically insulating Kapton sheet, allowing the modular target to be tightly pressed to the copper block while keeping it electrically isolated. The tight press combined with the two layers of N-grease provide thermal conductivity. In addition to Fig. 6, supplemental images can be found in Section A, most notably with Fig. 46.

Once a modular target has been installed and an ice surface has been prepared, the target is exposed to particles coming from the dust accelerator. Because the dust is travelling at speeds in the km/s range or higher, upon impact a plasma ejecta plume is created on a microscopic scale. Ions within that ejecta plume, whether they had existed as ions in the surface before ejection or whether they were ionized by the kinetic energy of the violent impact process, are accelerated by an electric field applied between the target, typically charged to  $\pm 2.5 - 4.5$  kV, and a grounded acceleration grid  $\sim 1$  cm in front of the target. Ions are accelerated down a flight tube towards a

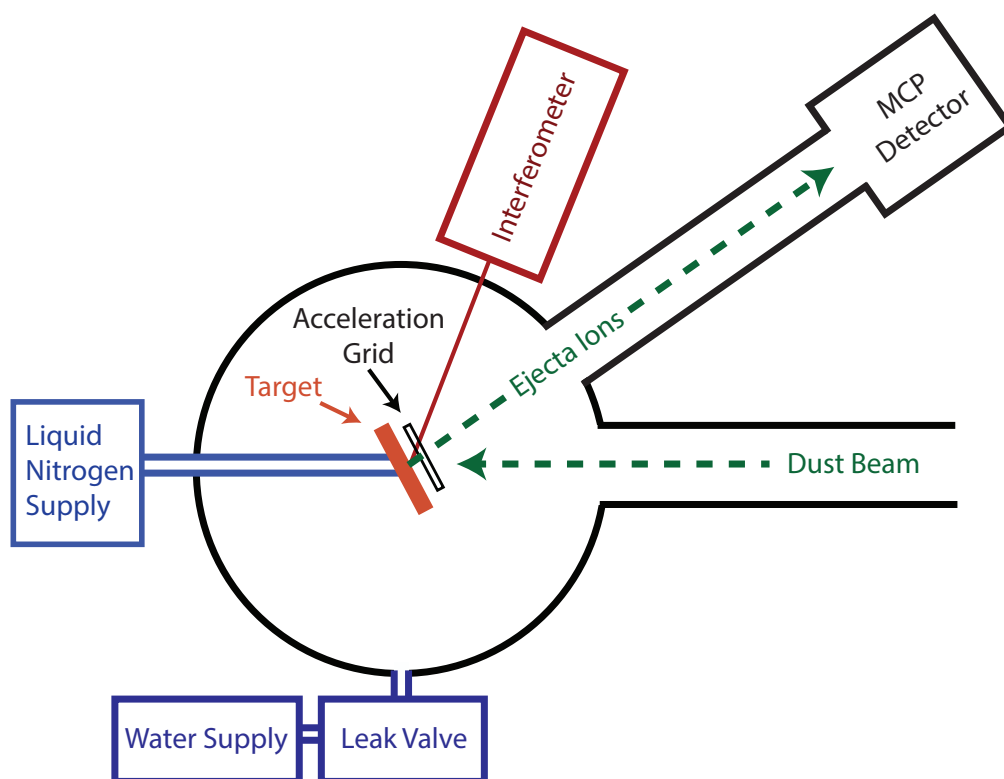


Figure 7: A system diagram of the cryogenic ice target. A copper target is actively cooled by flowing liquid nitrogen. Mixtures of  $\text{H}_2\text{O}$  and  $\text{HDO}$  are leaked into the system, growing ice over time, and their relative vapor pressures are measured by a residual gas analyzer to determine ice composition. Ice thickness is measured with Fabry-Perot interferometry. The ice is bombarded by hypervelocity dust coming from the accelerator, and an electric field provided by a metallic grid accelerates ions within the resulting ejecta plume towards a micro-channel plate detector TOF system.

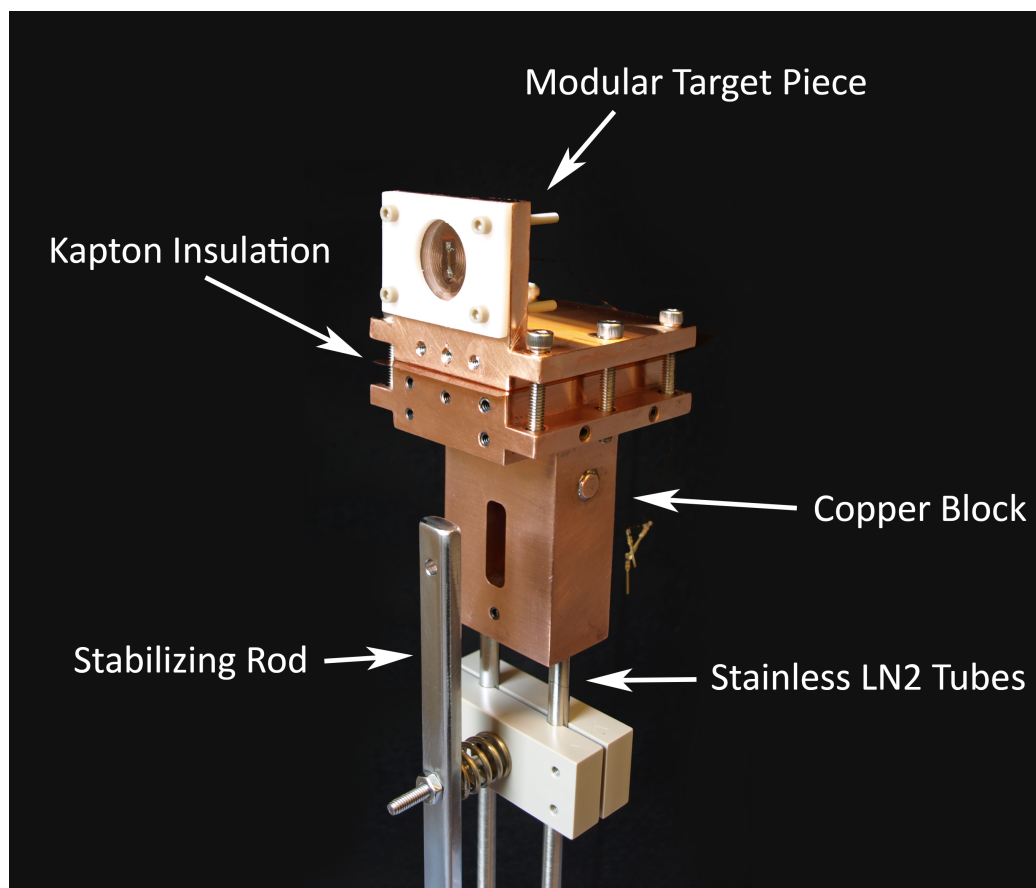


Figure 8: A picture of the vapor deposition modular target installed on the copper block.

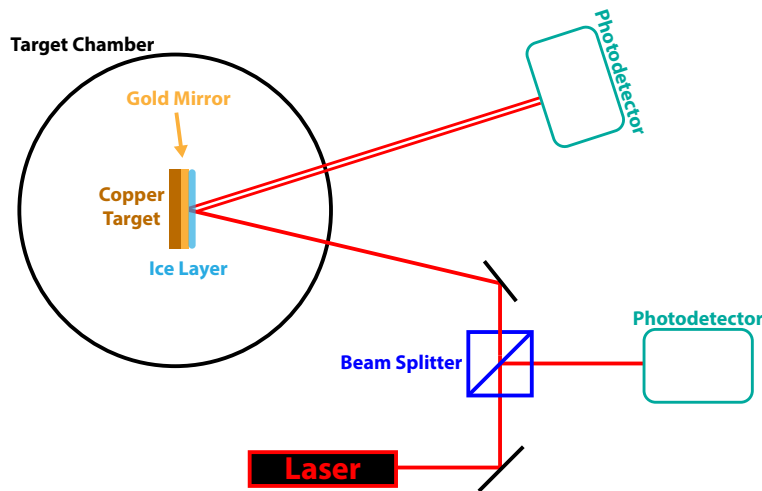


Figure 9: A diagram of the interferometry system. A visible red laser is split into two beams, with one being sent to a photodetector. The other beam is sent to a mirror target with an ice layer grown on top. Reflected light off of the front and back surfaces of the ice are sent to another photodetector. The slight delay from the beam reflected off of the back creates an interference pattern that can be used to measure ice thickness as it grows.

microchannel plate detector (MCP), thus creating a TOF mass spectrometry system. The TOF system was purchased from Jordan TOF Products, Inc., but several modifications have been made, most notably in the lens stack assembly, as described in section 2.3.

A system of precision leak valves are used to introduce various vapors into the system. Reservoirs of water or other liquids or gasses are kept in isolated vessels attached to the system through these leak valves. When the copper block has been cooled by the LN<sub>2</sub>, these leak valves allow for controlled release of vapor or gas from these reservoirs, and thus vapor deposition to be used to grow ice, as described in Section 3.1.

### 2.2.2 Interferometry

A 632.8 nm (visible red) laser mounted on a small optical table outside the chamber is split into two beams to create an interferometry system, as shown in Fig. 9. One beam is sent to a photodetector on the optical table. The

other beam is passed through an optical window near the top of the chamber and sent towards a mirror surface on the target itself. If an ice layer is present on this mirror, the light will reflect off of both the front and rear surfaces of the ice, creating a Fabry-Perot interferometry signal. Reflected light exits another optical window where it is collected by a second photodetector. The amplitude of this signal relative to the original beam passed to the first photodetector can be measured to assess the interference pattern.

### 2.3 The TOF System

The TOF system is a modified version of the off-the-shelf Jordan Time of Flight Products C-677 TOF lens stack and flight tube system [89]. This linear TOF system was originally designed for laser ionization systems, and thus it has been modified to work with the ice target. While the original design used a solid repeller plate biased at high positive potential relative to an extraction grid and a grounded acceleration grid, the ice target TOF uses only an acceleration grid. This is because the target itself is biased to high potential, in effect forming its own repeller plate. The original design, therefore, had the acceleration grid much further downstream than is necessary or even desired for the ice target. To maximize signal collection, the acceleration grid was thus moved to the end of the TOF lens stack, as shown in the photograph Fig. 10 (A) and the diagram Fig. 10 (B).

In order to maintain the ability to bias the acceleration grid relative to the ground metal rod that forms the backbone of the TOF lens stack, #0 metal washers were added underneath the precision ground ceramic spacers. This allows the insulating ceramic inner sleeve to be pushed out to the end of the lens stack as shown in Fig. 10 (B), where they were not designed to extend to, preventing the grid from being in electrical contact with the metal rods. PEEK washers are then used as insulating buffers for the metal nuts that hold the system in tension. This allows the acceleration grid to be biased as desired, though in practice it is typically held at ground.

In addition to these lens stack customizations, the flight tube was eventually modified to reduce its length. This was done in order to increase the ion collection, at the expense of mass resolution. The total flight length was reduced from 100 cm to 67.5 cm. However, an extension nipple was also fabricated such that the original length can be easily restored if desired.

The lens stack also features two pairs of steering plates in perpendicular planes to one another. These plates allow a voltage to be applied across the

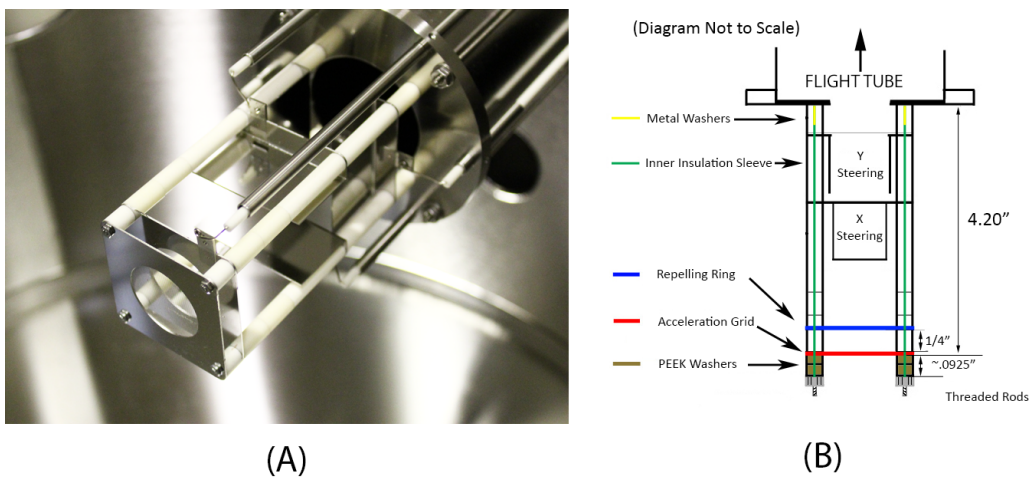


Figure 10: (A) A photograph of the modified lens stack. (B) A diagram of the modified TOF lens stack. Metal washers have been added underneath the precision ground ceramic spacers to extend the length of the inner insulating sleeve. This allows the acceleration grid to be moved out to the extremity of the lens stack.

flight path of the ions to steer them to increase signal collection. A ‘repeller ring’ single-element Einzel lens is also sometimes used in the stack, and a voltage applied to this can be used to focus the ion stream. However, in practice, these elements have not been used, and the repeller ring is most often removed from the system. The stochastic nature of the dust impact process means that highly variable total ion counts emerge from shot-to-shot. This means that it is often difficult to compare even collections of spectra to determine if the ion collection has improved or degraded when steering or repelling potentials are applied. Thus, while experiments were performed to try to determine what the optimum steering potentials and repeller ring potentials were, none were conclusive. It was found that steering potentials of  $>500$  volts steered the ion beam off the MCP detector completely, but no significant difference in ion collection was observed while varying the potentials. A further experiment was performed in which the positive and negative potentials that steered the ions off the MCP were recorded, and then a mid-point potential was selected, but even with this no meaningful increase in ion content was observed. It could very well be that optimizing steering and

repelling potentials will significantly increase the system signal-to-noise ratio (SNR), and I therefore propose an experiment for future work in Section 6.2.

To complete the TOF system, a Jordan Time of Flight Products C-726 40 mm Dual MCP Detector Assembly is mounted on the downstream side of the flight tube. This MCP is connected to an oscilloscope for data collection during experiments. It is typically operated at -3800 V, near the top end of its rated range, to optimize for what is often small observed total ion content in many experiments. While this increases the signal amplitude, it also increases the noise, meaning that it does not change the observed SNR. Nonetheless, the increased signal voltages result in greater volumes of spectra being collected.

## 2.4 Alignment

Two types of alignment are necessary for optimum system performance. *Target alignment* ensures that the target itself is properly aligned with the acceleration grid, flight tube, and MCP detector. This alignment makes use of Thorlabs HNL008L HeNe 632.8 nm laser, which is also used for interferometry as described in Sec. 3.1. *System alignment* ensures that the dust beam from the accelerator impacts the target surface in the desired location. This form of alignment uses a visible red laser mounted directly to the accelerator for the explicit purpose of aligning instruments placed in the dust beam path.

### 2.4.1 Target Alignment

Target alignment is critical to ensure that the maximum ion content of each dust impact is received by the MCP detector (thus maximizing SNR). This is done by ensuring that the target surface is parallel with the acceleration grid and MCP detector and normal to the flight tube axis. Because the electric field created by the potential between the target surface and the acceleration grid is responsible for directing the ejecta ions down the flight tube, a misalignment between these two components would result in the ions not being accelerated directly towards the MCP detector. If the misalignment is large enough, the ions, or some significant fraction of them, may miss the MCP altogether.

The grid itself is mounted to the TOF system directly, and precision ground ceramic spacers are used to ensure that it is held parallel to the MCP detector as part of the TOF stack assembly, as shown in Fig. 10 (A). Target

alignment, then, depends on getting the target surface itself parallel to the TOF system.

Two pass-through optical windows on the chamber are mounted in front of and above and below the target at  $25^\circ$ , both pointing directly to the target. The laser is aimed such that the beam passes directly through the center of the top (entry) window onto the target surface. When a mirror target is installed, the beam will pass down to the bottom (exit) window, and when the system is perfectly aligned, the reflected beam will pass through the direct center of this window as well.

A Thorlabs Det-100A photodetector is installed outside the exit window, enabling computer monitoring of the amplitude of the reflected beam. In order to ensure proper alignment, the return beam must pass through the center of the exit window. However, a significant problem with using this detector for target alignment is that the surface area of the photodetector is roughly a cm in diameter, far larger than the laser beam itself. This means that a beam that passes off-center may still present maximum signal amplitude to the photodetector because the laser dot is still entirely collected by the detector.

To solve this, a delrin cap was custom-machined and installed onto the bottom exit port. The cap is centered on the exit window itself, and a small circular hole was drilled out approximately 1 mm in diameter, roughly the size of the laser beam at the exit port, at the exact center of the cap. This ensures that even a slight misalignment will result in a significantly smaller photodetector signal as some of the light will be blocked. The cap was made out of white delrin because the laser dot still partially penetrates its thin surface. This enables rough alignment to be done visually with the cap still installed, and once the return beam is near the center of the cap, fine alignment can be performed by maximizing the photodetector signal amplitudes with minute adjustments.

The target alignment is adjusted by controlling both yaw and pitch. The flange that the ice target is built upon is mounted to a rotating assembly that allows it to be turned even under vacuum. This controls the target yaw.

In the original iterations of the ice target assembly, only yaw could be adjusted while the system was in vacuum. Pitch was controlled by a spring acting between a stainless steel stabilizing rod and a pair of PEEK attachment plates on the stainless steel tubes (both of which are shown in the foreground of Fig. 8). Screws that went through the center of the spring could be adjusted to fight against this tension and produce the desired pitch.

However, this could only be adjusted by hand when the target chamber was open to atmosphere. Improved designs now allow for pitch to be controlled even during experiments. The design for this seemingly simple task is surprisingly nontrivial due to the requirements of having to maintain thermal isolation, produce no or minimal stress on the copper-stainless brazed joints, provide enough force to actually move the target, and to be long enough to cover the required distance while still being small enough to be installed without removing the ice target assembly.

This is accomplished with a long rod attached to a linear translation stage that allows the user to move the rod forward and backwards from outside the chamber. The rod itself is actually composed of two separate aluminum bars, each in an ‘L’ shape that mate together. This allows them to be installed separately, such that the ice target doesn’t need to be removed. If the bars had been straight rather than ‘L’ shaped, they would press against the copper rather than the stainless tubes, producing stress likely strong enough to break the brazed joints. The ‘L’ shape then allows them to drop below the plane of the installation flange and act on the PEEK attachment plates instead.

### 2.4.2 Beam Wandering

The pitch control system as described in Section 2.4.1 is in constant tension to prevent the target from moving. However, thermal expansion and contraction still significantly alter target alignment, meaning that alignment must be done while the system has reached experimental temperatures. This is what necessitated the creation of the pitch control system that allows target alignment even in vacuum conditions.

Further, it has been observed that in some experiments where the system is kept cold for several hours, the alignment may wander in a seemingly random direction. The wandering is significant enough to walk the reflected interferometry return beam out of the hole on the delrin cap, resulting in an instantaneous signal drop.

This wandering process is poorly understood. It does not always occur, and it often appears to happen rapidly rather than as a slow travel. Furthermore, the seeming randomness of it means that it cannot be predicted, and the only measurements of it are therefore from the interferometry system after the fact. Perhaps most perplexing is that there is no evidence of this sort of wandering occurring for the earliest iterations of the ice target, when the stabilizing rod was in fact much weaker than it is now. That is,

having a much stronger stabilizing rod may in fact be a contributing factor to beam wandering. Understanding and resolving this process should be an important priority in future work.

### 2.4.3 System Alignment

System alignment ensures that the dust beam impacts the ice target at the desired location. The accelerator features a visible red laser that can be moved into position to show the dust beam's flight path for just this purpose. To align vertically, the system is mounted to the accelerator and the adjustable feet of the ice target system are raised or lowered as needed to align this laser to the target. In the past, this was done painstakingly by using a rubber strap wrench to raise and lower these feet when the system was still resting its weight on them. However, in modern practice, the entire system is lifted up one side at a time on a hydraulic automobile floor jack to the desired location. The feet are then lowered to the floor, and the jack can then be removed. This tactic has reduced alignment time from a day-long activity to one that can be done in an afternoon.

To align horizontally, the floor jack can also be used to lift the system just off the ground and then gently push or pull it to the desired location. Care must be taken to ensure that the jack wheels are properly oriented, and of course this should never be done when the system is at high vacuum.

There is a manufacturing defect in the ice target that has never been corrected and makes perfect system alignment impossible. The stainless steel tubes that connect the copper block to the target flange cannot be simply welded to the copper. Instead, two attempts were made to braze the tubes to the copper using Indium Alloy #5. In one attempt, the brazed joint would not hold vacuum, and in the other it held vacuum until minor alignment adjustments were made, at which point the brazed seal failed and the system again could not maintain vacuum.

After these failed attempts, the system was sealed with Apollo GB brazing alloy. To facilitate this, the solid stainless steel tubes were cut and VCR connectors were used to attach the upper target assembly to the flange-welded stainless steel tubes. In this process, the tubes were bent at the machine shop, and the target thus does not sit directly in the center line of the TOF acceleration grid ring as intended. This can be seen in Fig. 11, which shows a photograph of the target looking down the TOF tube from where the MCP would normally be. The circular target mirror is just left of center

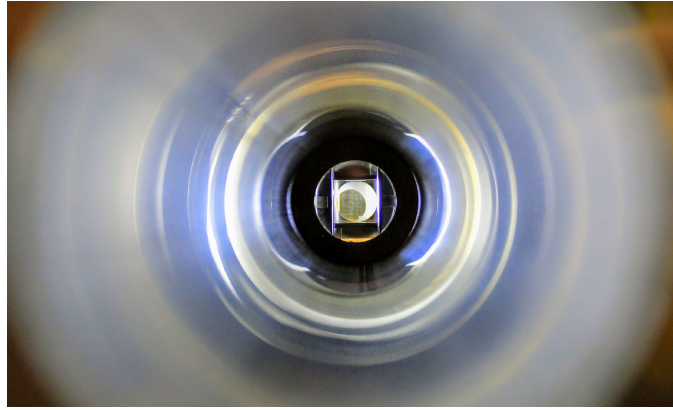


Figure 11: A photograph of the target as seen from looking down the TOF tube from where the MCP assembly is normally mounted. The circular target mirror is just left of center of the acceleration grid ring, indicating that the system is not properly aligned. Fixing this would be straightforward, but may result in breaking the brazed joint between the stainless steel tubes and the copper block. Such a breakage could entail a serious expenditure of time in the shop to be fixed.

of the acceleration grid ring, meaning that the target is not directly centered in the TOF assembly. This makes perfect system alignment impossible.

Unfortunately, fixing this seemingly simple problem risks taking the ice target offline for potentially months. The stainless steel tubes could be simply bent back into the proper position, but this would necessarily put stress on the brazed joints between them and the copper block. If the seal on these joints were to break, the system would have to be disassembled for the target assembly to be heated up to temperatures sufficient for the brazing alloy such that the joints could be resealed. This would melt the brazed joint holding the copper plug in place, which means that the plug itself would also have to be re-brazed. Care must also be taken to prevent the hidden brazing compounds in the internal copper routes from shifting and filling the routes or the stainless tubes, preventing flow. In other words, fixing a broken seal is no simple task and would require highly specialized equipment and the expertise of professional machinists. When similar leaks had been present in the indium alloy braze, it took months to rectify, due in no small part to the difficulty in reserving time from the specialized machine shops that are capable of doing so.

While the system alignment is thus persistently imperfect, it does not present a major challenge to data collection. The size of the dust beam is roughly a cm in diameter at the ice target. Since the various targets in use are generally 2.5-5 cm in diameter, the target being shifted to one side is an acceptable defect in most experiments, as the electric field is maintained over the entire surface area of most of the modular targets. Importantly, it doesn't affect target alignment as described in section 2.4.1, meaning that the surface is still parallel to the acceleration grid.

Therefore, given the risk of stopping experiments for months on end and the fact that the defect does not significantly alter results in most experiments, the decision was made to leave the system as it is. When this decision was made, it was thought that the risk could be taken when there was a comparative downtime between experiments. However, the fast tempo of experiments over the past few years has meant that no such time has ever presented itself.

## 2.5 Surface Temperature

The temperature of the target surface is a critical parameter for experiments, but it is very difficult to measure under experimental conditions because it must be kept at high potential to facilitate the TOF, and of course it must be kept in thermal isolation to keep it cold. For this reason, a diode is mounted to the copper block, which is kept at ground, and the temperature of the target itself is inferred from this measurement based on calibration data.

A modular target very similar to the one shown in Fig. 8 was used, and a gold-coated sapphire target mirror was sacrificed by soldering two wires to opposite ends of its circular face, forming a thermistor between them. This thermistor was calibrated by slowly lowering (in stages) it and a diode thermometer into LN2. They were held in each stage long enough for their temperatures to equilibrate, and the thermistor resistance for each temperature was recorded. Over the relevant range of  $T > 76$  K, the calibration was found to be linear with the fit

$$T = \left( 109.6 \frac{r}{\text{Ohm}} - 133.9 \right) K, \quad (4)$$

where  $r$  is the measured resistance of the thermometer in ohms. Because this thermistor was formed by the thin gold surface coating of the sapphire, it is a measurement of the exact surface that ice is grown on for the vapor

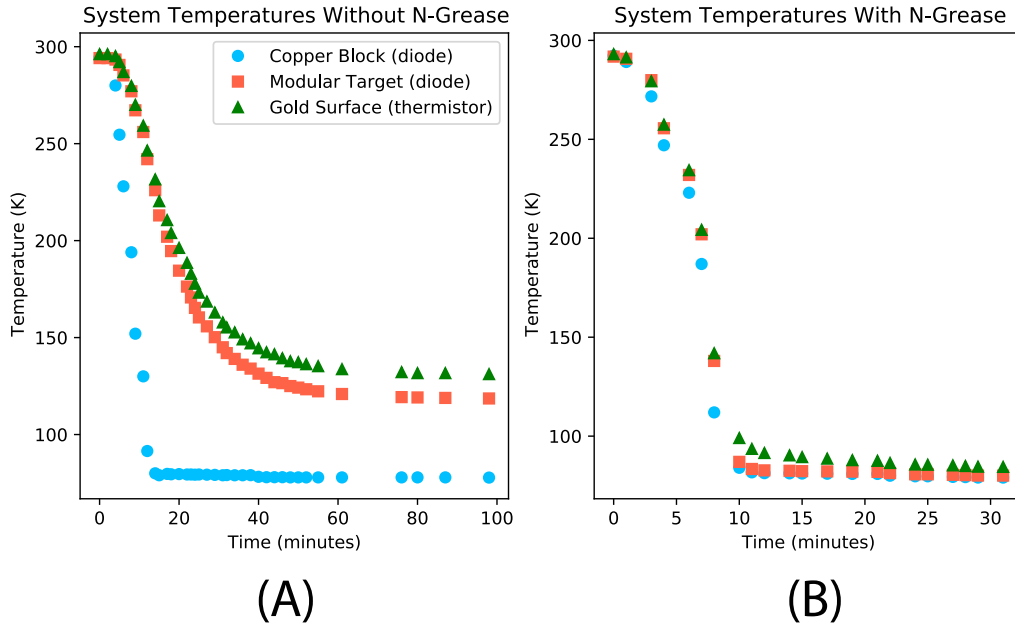
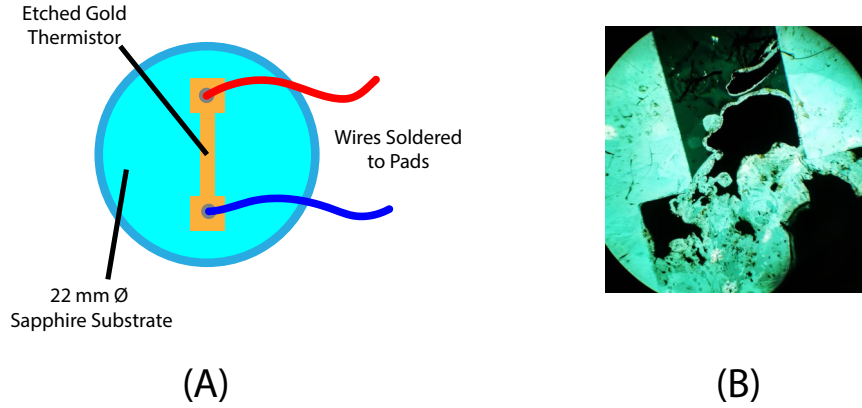


Figure 12: Plots of the temperature calibration experiments. It was found that without N-grease applied to both sides of the Kapton sheet, poor thermal contact was made, with the actual target surface only getting down to 131 K despite a temperature of 77.8 K on the copper block, as shown in (A). After N-grease was applied, the target surface reached 84 K, as shown in (B)

deposition process, as described in Section 3.1.

Once the thermistor calibration was complete, an additional diode thermometer was placed on the modular target piece, allowing the temperatures of the copper block and the copper modular target to be known precisely. The thermistor sapphire was then installed into the modular target and the system was cooled down. This was performed before the use of N-grease was standard practice, and it was found that without this thermal conductant, there was poor thermal contact between the copper block and the modular target, as shown in Fig. 12 (A). The copper block was cooled down to 77.8 K, but the modular target only cooled to 118 K, and the gold surface cooled only to 131 K.

To solve this, N-grease was applied to both sides of the Kapton insulating sheet, increasing thermal conductivity between the copper block and the modular target. Additionally, grease was applied to the back of the sapphire



[ht]

Figure 13: A diagram of the etched gold thermistors for *in-situ* temperature measurement (A), and a photograph of a microscope view of the etched thermistor pad after soldering and sparking, showing that it is not continuous and is therefore broken (B).

mirror, increasing conductivity between it and the copper modular target. With this greased system, when the copper block was cooled to 79.0 K, the copper modular target temperature was lowered to 80.0 K, while the gold surface thermistor was cooled to 84.5 K, as shown in the Fig. 12 (B). In addition, without N-grease the system has a roughly 45 minute delay between the copper block reaching minimum temperature and the target reaching minimum temperature, and this delay was reduced to 15 minutes with N-grease applied.

### 2.5.1 *In-situ* Thermistors

Several attempts were made to use the gold surface measurements during actual experimental runs, but the solder blobs attaching the wires to the gold surface would invariably spark due to high point potentials between sharp peaks on the blob and the acceleration grid. This not only hampered experiments, but over time the high transient currents shattered the gold surfaces, rendering known calibrations incorrect and eventually breaking the circuit altogether.

To get around this, several sapphire mirrors were modified to have an

etched gold thermistor on the back surface. This was accomplished by vapor depositing a 5-10 nm titanium adhesion layer onto the sapphire followed by a 20-40 nm layer of gold before photo-etching removed unwanted gold material. A modular mirror target was then made with a slot cut into the back to keep this thermistor isolated from the rest of the copper target piece. Fig. 8 shows a photograph of such a thermistor on a transparent sapphire window mounted on the ice target, although in actual experiments the front surface would be coated in gold to produce a mirror. A diagram of the etched thermistor is shown in Fig. 13 (A). While this thermistor was able to successfully measure the sapphire target mirror temperature *in-situ* in a number of experiments, it too would occasionally spark, this time between the solder blobs and the copper target piece. Fig. 13 (B) shows a photo taken through a microscope of one of the solder pads on the thermistor after use. The soldering process itself stripped some material off of the pads, and fracturing from sparking further degraded the connection until it was unusable.

Due to these issues, the *in-situ* thermistor temperature measurements were suspended, but future work may make use of the general design. These experiments were all performed with the older sapphire mirror system rather than the newer generation of larger, thicker mirrors with copper substrates. It may be possible to design a simple thermistor that works with these new substrates without sparking, perhaps even using the copper itself as a thermistor.

## 3 Ice Preparation Methods

There are three primary methods of creating ice, each with a number of variations. **Vapor deposition** is a simple, reliable, and measurable method to create uncomplicated ices *in situ* in the target chamber. **Flash freezing** is a method to rapidly freeze an aqueous solution to create a homogeneous ice surface of evenly spaced, potentially complex dopants. Finally, **airbrushing** is a method that sprays aqueous solution across a cold substrate, also to create a uniform, homogeneous surface of complex composition.

### 3.1 Vapor Deposition

Vapor deposition is the simplest method of ice creation, and it has been in use since the ice target's construction [90]. There are four similar modular target pieces used, with one shown in Fig. 8, and another shown in Fig. 14. The target piece in Fig. 8 uses clear sapphire windows 22 mm in diameter and 1 mm in thickness that have been coated with a bilayer of titanium (5-10 nm) and gold (20-40 nm), turning them into gold mirrors. These targets use thermal N-grease between the sapphire and the copper target to provide strong thermal contact. The first generations of these mirrors were supplied by colleagues, but later mirrors were coated at the Colorado Nanofabrication Lab in CU Boulder's Engineering building.

The target shown in Fig. 14 is a newer target which uses an off-the-shelf 1/4 inch thick 25 mm diameter gold-coated copper substrate mirror from Edmund optics. Using off-the-shelf components has greatly reduced turn around time between experiments, as the fragile gold mirror surfaces cannot be cleaned except by blowing them off with dry nitrogen or other gases. This is particularly relevant given that over time, the N-grease used with the sapphire mirrors has been observed to slowly 'creep' around the edges, eventually forming a very thin layer on the mirror surface. To solve this, newer mirrors replace the N-grease with indium foil sandwiched between the copper target and the copper mirror substrate. Strong clamping pressure and the soft indium foil allow good thermal interfacing between these two components. This eliminates N-grease from being anywhere near the mirror surface, making it significantly easier to assemble the target piece or replace the mirror while also increasing the longevity of each mirror. However, there have not as of yet been any calibrations of the surface temperature of these new target systems with indium foil.

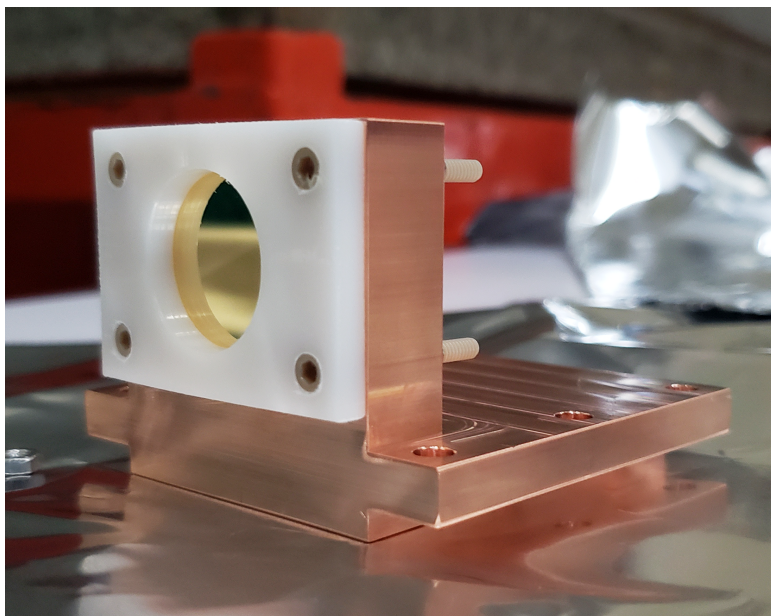


Figure 14: A photograph of a vapor deposition target with a gold-coated mirror. This model uses indium rather than N-grease as a thermal conductant.

The ice target chamber uses a turbo-molecular pump to achieve vacuum pressures in the low  $10^{-8}$  Torr range. When LN2 flows through the copper block to cool it down, it effectively forms a small-scale cryo-pump, with the entire surface area of the stainless steel tubing and copper target and block immediately freezing out particles that reach them. This has the effect of bringing system pressure down at least into the E-9 range, below the vacuum gauge minimum detectable pressure.

There are two reservoirs that can be filled with liquid or gas that connect through leak valves to the chamber. The leak valves allow precisely controlled partial pressures from each reservoir to be released into the target chamber. One valve is capable of precise control in the E-6 range, while the second precision leak valve is capable of fine control in the E-8 range.

When a gas is released from one of the leak valves, its molecules move thermally around the chamber until they are either adsorbed onto the surface of the chamber walls, pumped out by the turbo-molecular pump, or are frozen onto the target assembly, assuming it is cold enough to capture the molecules. Over time, frozen particles accumulate onto the target surface

to form ever thicker layers of frozen material, allowing for vapor deposition of ices. The tandem leak valves and reservoirs allow mixtures of gas to be released simultaneously into the system in known relative partial pressures, and thus ice mixtures can be made, say of water and methanol in known relative concentration, with one potentially orders of magnitude lower than the other.

The primary product data product resulting from the combination of dust accelerator, ice target, and TOF system is mass spectra of ice surfaces. An exemplar spectrum produced by a 16 km/s iron dust particle impact into vapor-deposited water ice is shown in Fig. 15. Red triangles show the centers of identified mass lines, and the top axis shows the characteristic water cluster sequence. As is typical in water ice spectra, the protonated water, that is  $(\text{H}_2\text{O} + \text{H})^+$ , is the dominant ion mass line rather than  $\text{H}_2\text{O}^+$ . Also as is typical, these water molecules form clusters, generally protonated, such that there is a water backbone with molecules of  $(n\text{H}_2\text{O} + \text{H})^+$  and masses of  $n \cdot 18 + 1$  amu. In this exemplar spectrum, mass lines out to 33 water molecules are observed.

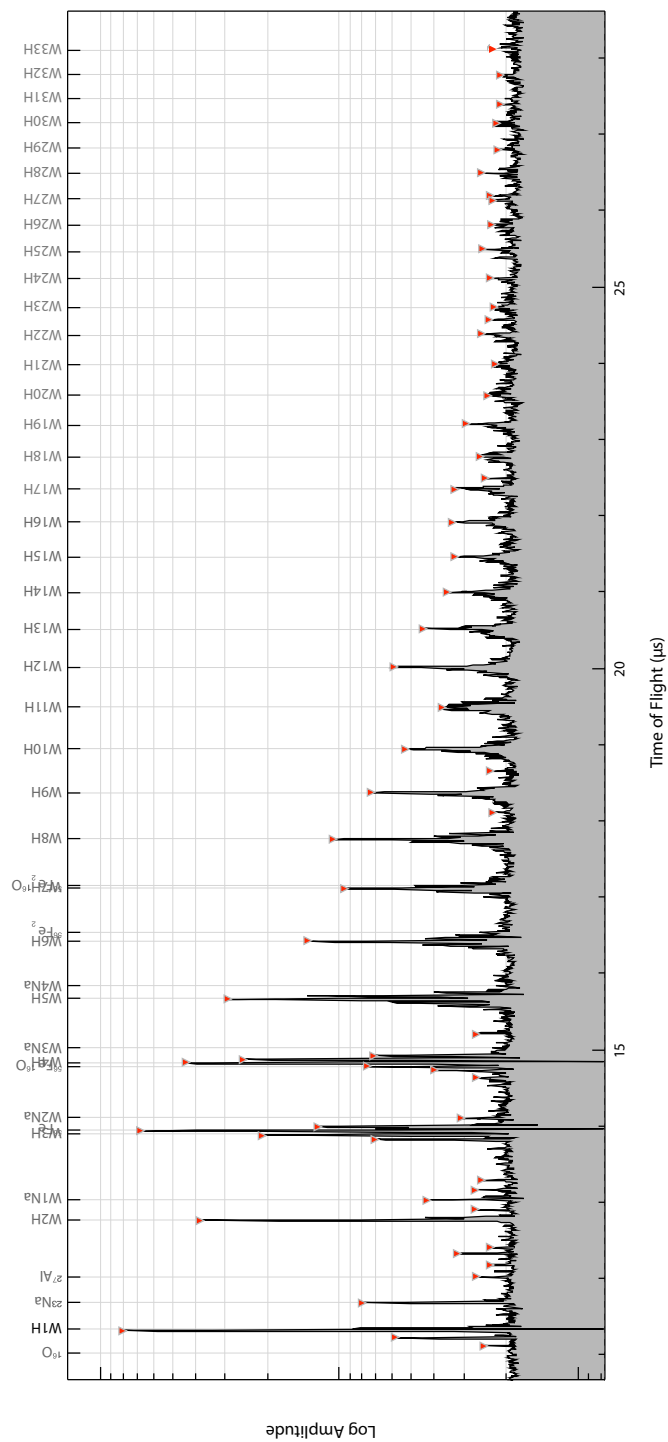


Figure 15: A water spectrum produced by a 16 km/s iron dust particle impacting a water ice surface prepared by vapor deposition. Red triangles show observed mass lines, and the top axis provides species identification where applicable. WN H is shorthand for (H<sub>2</sub>O)nH

## 3.2 Flash Freezing

The vapor deposition system is a simple, reliable, and measurable method for ice surface creation, but it can only be used to deposit simple ices composed of easily volatilized species, such as pure water or methanol. Aqueous solutions of complex organics, however, could not be deposited in this manner. If one were to attempt to vapor deposit such a solution, the water solvent would sublime and begin vapor deposition while the organic analyte would solidify and fall out of solution. Some groups have heated up organic molecules, such as amino acids, to volatilize them for deposition [91]. However, the process of heating an amino acid up will always carry a risk of fragmenting it along its weakest bonds [92]. For studies that wish to have very well-characterized concentrations of organics or that will attempt to study fragmentation processes themselves such as will be found in Sec. 4, this is unacceptable.

One might then be tempted to freeze aqueous solutions slowly, but such a slow process will excrete many analytes during the process. An obvious example is salt in water. Slowly freezing solutions of salt water will push the salt out of solution as the water freezes, eventually resulting in an ice of nearly pure water and solid salt debris on its crust. That is, the surface of such a slowly frozen aqueous solution will be anything but homogeneous.

To study mixtures of complex organics in water ice, then, alternative methods of producing homogeneous ice surfaces have been pursued. The first attempt was to use flash freezing, whereby aqueous solutions are frozen as rapidly as possible such that analytes in the water would not have time to be excreted, but would instead immediately freeze in place. Such a task is very difficult to accomplish in vacuum, where by its very nature the user has only limited contact with the targets.

A design was therefore made to perform the freezing in atmosphere, or at least outside of the vacuum chamber, but this of course creates its own host of problems relating to atmospheric contamination. Having a target piece at cryogenic temperatures in atmosphere would immediately begin accumulating frozen water vapor from the air.

To solve these problems, the flash freezing modular target was designed. It is composed of a copper piece with a circular target recess cut out of it and canted slots that accept a Vespel door or cover [93], as shown in Fig. 16. Solutions can be deposited into the recessed circle and then sealed from atmosphere by the Vespel cover. The whole assembly can then be dunked

into LN2 to rapidly freeze it, ideally so fast that any analytes cannot be excreted. The target can then be installed onto the already-cold copper block while a connection is made between a tapped hole on the Vespel door and a linear translation stage. The translation stage allows a user outside the vacuum chamber to manually pull the Vespel cover off the target after the system has been pumped down to UHV. This will expose the pristine surface, uncontaminated by atmospherics.

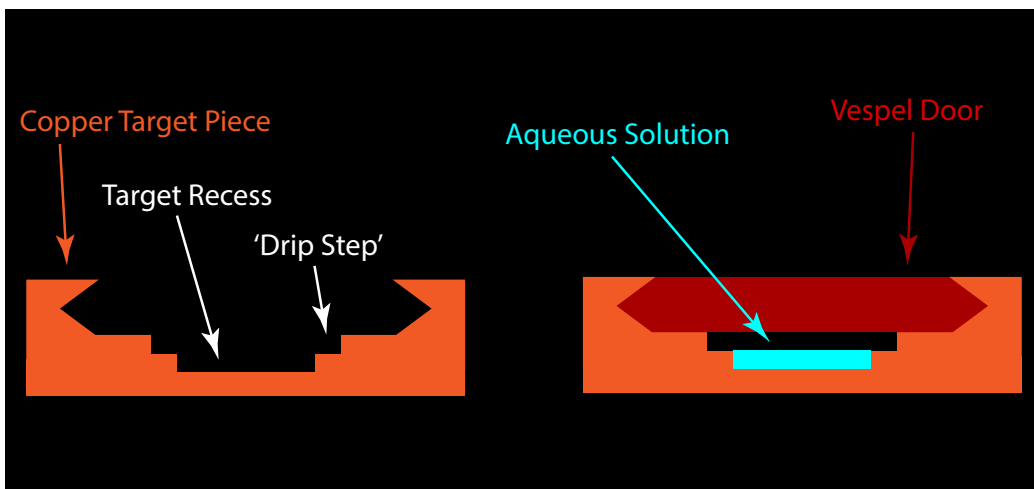


Figure 16: A schematic view of the flash freezing system. A target recess is used to hold small volumes of aqueous solution. A Vespel door or cover is fitted into the canted slots on the copper target, isolating this solution from atmosphere. The 'drip step' is used to isolate the solution from the Vespel cover, as without it the door often freezes shut.

Fig. 17 shows three photos of the flash freezing target. The first photo shows the target after a solution has been frozen in the target but with the Vespel door still in place. Note the atmospheric frost that has already begun accumulating. The second photo shows the ice surface after the door has been partially removed during a test run in atmosphere. The white ice surface is visible in the center of the target.

The wire coming out from under the white plastic clamps is used to supply acceleration potential to the target after installation. This was a design flaw of the first iterations of the flash freezing target, as it meant the user had to manually connect voltage lines during the installation process. However, installation must be performed as rapidly as possible to minimize

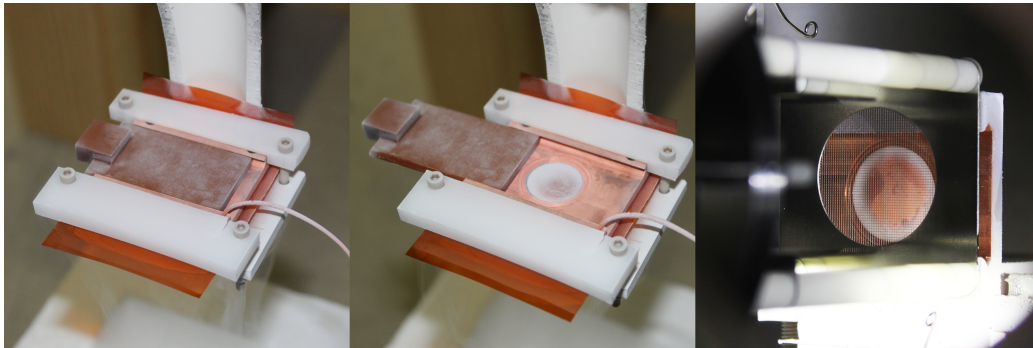


Figure 17: Three photos of the flash freezing target, showing the target after immersion in the LN<sub>2</sub>, the cold target with an amino acid solution and with the cover partially removed, and finally in the ice target chamber during an actual experimental run.

atmospheric frost accumulation and to prevent the surface from warming up before the active cooling from the LN<sub>2</sub> takes over. The user also had to align the ice target with the mounting screw holes, which seems trivial but requires wearing bulky cryogenic gloves while handling a small target mere centimeters away from the very fragile acceleration grid, and again all under time constraint.

Subsequent design changes made use of a copper adapter plate that is attached to the copper block at room temperature. Wires connected to the acceleration potential power supply can then be mounted to this plate with ease, freeing the user from having to make the electrical connection during an experiment. The adapter plate also features alignment pins with corresponding holes drilled into the target piece. This allows the user to simply drop the target onto the copper block and then screw it down to ensure thermal contact. These and other methods have reduced install time from several minutes in the first iterations to about 20 seconds.

The third photo in Fig 17 shows a pristine ice surface in vacuum during an actual experiment. Note that the ice surface itself and the copper surface that was under the Vespel cover are not covered in frost, unlike the outer surfaces of the target which were exposed to atmosphere.

### 3.2.1 Methods

There are a number of learned processes that are necessary for successful ice surface creation. A major problem with the flash freezing system is that the Vespel door can become stuck over the target ice during the freezing process, ruining the experiment. Vespel was specifically chosen because its coefficient of thermal contraction is comparable to but greater than that of copper [93]. Thus, the door would contract slightly more than its recess during freezing, preventing it from jamming itself shut. In fact, the slightly greater contraction means the door moves freely at the slightest force, and this is an effective way to test the ice surface before installation. If the door takes effort to move, then it almost certainly is a poor ice surface that needs to be remade.

This is because the water solutions themselves have been proven to be particularly adept at jamming the Vespel door during freezing. The ‘drip step’ shown in Fig. 16 is a necessary change to the original design, which simply had the target recess flush to the copper surface. The drip step allows a small pocket of air to remain in the headspace above the target recess. Without it, the solution would, through adhesion, creep up the recess walls and contact the Vespel cover. When the water was frozen, it would then jam the door shut. Attempts were made to simply reduce the amount of solution used, but this invariably led to ice surfaces with only partial coverage of the target area.

With the drip step machined into place, another source of jamming is minute angles between the target surface and the force of gravity. If the target is held even slightly off parallel to the ground, even small amounts of solution will still manage to contact the Vespel and freeze it in place. This was solved by manually using a level on the back face of the target (underneath it) before the sample is submersed in LN<sub>2</sub>.

Even with a properly aligned target, care must be taken to insert precisely the correct amount of solution into the target recess, as too much will result in jamming of the door, and too little will yield only a partially covered target surface. A difference of a few  $\mu\text{L}$  is sufficient to ruin an experiment in one of these two ways. For this reason, micropipettes must be used to carefully measure the amount of liquid used in each experiment. The precise numbers change of course with each iteration of the modular target, as the target recess has slightly different volumes. More importantly, slight differences in viscosity or solution composition will change these ‘magic numbers’. Thus,

for each new species being studied, or if significantly different concentrations of a previously studied solution are used, new magic numbers may have to be empirically determined before reliable ice surfaces can be made.

One final method that has proven to be extremely helpful is to use the surface tension of the aqueous solution to spread it out across the target recess, in particular to the outer walls. Failure to do so may result in a convex surface that bulges out in the center of the target. This is highly likely to result in jamming of the Vespel door. Using the disposable plastic tips of the micropipettor as sticks, the solution should be pressed around the outer edges of the target recess such that it adheres to the walls. When done properly with a correct magic number, this will yield a concave rather than convex surface. This is, by wide margin, the most successful type of liquid surface for flash freezing.

### 3.2.2 Clathrate Capture

The flash freezing target has proven to not be effective at creating homogeneous surface of complex organics. Experiments have been performed with a number of different amino acids, but only some of them yield any TOF detections of these species. Those that do will only feature perhaps a dozen spectra with positively identifiable organic lines out of a thousand or several hundred triggers.

The system, however, has proven to be useful nonetheless. Experiments were performed with the flash freezing target using water that had been saturated at room temperature with  $\text{CO}_2$ . This solution, effectively soda water, was flash frozen and then studied with Fe impactors. The  $\text{CO}_2$  was observed in small but easily identifiable amounts across all velocity ranges, with higher velocity impacts also dissociating CO.

Importantly, after these experiments had been performed, another attempt was made using the vapor deposition system's precision leak valve to create carefully calibrated  $\text{CO}_2$ -water ices. However, with these subsequent experiments,  $\text{CO}_2$  was never observed at any velocity or at any concentration. It is believed that during these secondary experiments, the  $\text{CO}_2$  was not captured by the ice during deposition, perhaps because the actual target surface was not sufficiently cold.

The flash freezing system, however, may have been able to trap its  $\text{CO}_2$  in clathrates such that even as the system was exposed to vacuum,  $\text{CO}_2$  remained in the ice. Follow up experiments are needed to assess exactly what

occurred during these experiments, but it can be simply said that the only observations of CO<sub>2</sub> with the ice target were made with the flash freezing target. Thus, while it has not been successful at its intended purpose of creating homogeneous complex surfaces, it still serves a unique role in the ice target experiments.

### 3.3 Airbrushing

Due to concerns about the ability of the flash freezing system to truly create a homogeneous surface, new methods of ice creation were pursued. Specifically, a method of droplet-scale deposition and freezing was designed to prevent the migration of impurities by more than the droplet scale size before freezing. The idea was to create ices in a nitrogen or vacuum environment by spraying a cold surface with droplets of an aqueous solution of amino acids. Ices prepared in nitrogen could use the flash freezing modular target so that the Vespel door could protect the ice from atmospheric contamination while it is transported into the vacuum system, just as it is in flash freezing experiments. The spray's droplets would have to be small enough that they would effectively freeze instantaneously, but they could not be so small that any excretion effects might occur during droplet formation. Ideally, such droplets would be in the tens or few hundreds of microns. Additionally, the spray would have to contain only a small volume of solution applied at a time so that the applied thermal mass is small enough to instantly freeze.

#### 3.3.1 Initial Attempts

The airbrush system was thus conceived of using a commercial artistic paint airbrush, specifically a Paasche Airbrush Talon TG-3AS [94]. Aqueous solutions of amino acids at high concentration (typically  $\sim 1$  Molar) were loaded into the airbrush at room temperature. While airbrushes typically use compressed air to drive them, such a source would certainly introduce contaminants (including atmospheric water), so a high purity, high pressure bottle of dry nitrogen was used as a propellant instead. Initial experiments were performed in Sigma Aldrich Z530212 plastic atmosphere bags [95]. Holes in the bag were cut to allow the nitrogen line to be connected and to create a relief port where excess gas could flow out. The flash freezing target and a styrofoam container filled with liquid nitrogen were placed into the bag and sealed. The target was then inserted into the LN<sub>2</sub>, and the rapid cooling

produced high volumes of gaseous nitrogen that filled the bag. The bag was then manually ‘pumped’ by depressing it, forcing excess gas out of it and, over time, purifying the atmosphere into increasing concentration of nitrogen. After several cycles of allowing the bag to inflate from evaporating nitrogen and then deflating it, the target would be removed from LN2 and sprayed with the airbrush. It would then be reinserted into the LN2, and the bag could then be opened and the target transferred to the vacuum chamber.

In practice, however, this process proved to be awkward and very difficult to reliably replicate. The bag would frequently burst despite the relief holes, and the non-rigidity of the bag made it difficult to control most of the pieces. This was problematic as the process must be performed quickly due to warming of the target, etc.

### 3.3.2 The Airbrush Chamber

To solve these issues, a glovebox dedicated to the airbrushing system was purchased. The glovebox, shown in Fig. 18, is capable of being pumped down to rough vacuum to eliminate atmospheric content before being back-filled with dry nitrogen. It additionally features an antechamber which can be independently pumped down and back-filled to rough vacuum, making it possible to introduce new components to the nitrogen environment without contaminating the primary chamber with atmospherics.

Ports allow high purity nitrogen to be brought into the chamber for driving the airbrush and back-filling, as well as to allow gas to be pumped out using a vacuum pump. Other ports were added to install six pressure relief valves that open when there is a  $\sim 1/4$  PSI positive pressure differential between the chamber and the atmosphere. These relief valves are essential to keeping the chamber from bursting when room temperature pieces are inserted into the LN2, which results in rapid evaporation. Plastic foam padding covered with aluminum foil is used to completely cover the bottom of the chamber internals. This padding is used to prevent drops of LN2 from cooling small areas and inducing cracks in the acrylic chamber floor. A pair of SHT35 relative humidity (RH) sensors measure residual moisture in the main chamber and antechamber [96]. Finally, the rough vacuum pump is connected to the system with an electric valve controlled by a foot pedal. This allows the user to easily control vacuum pumping even when both arms are inserted into the gloves.

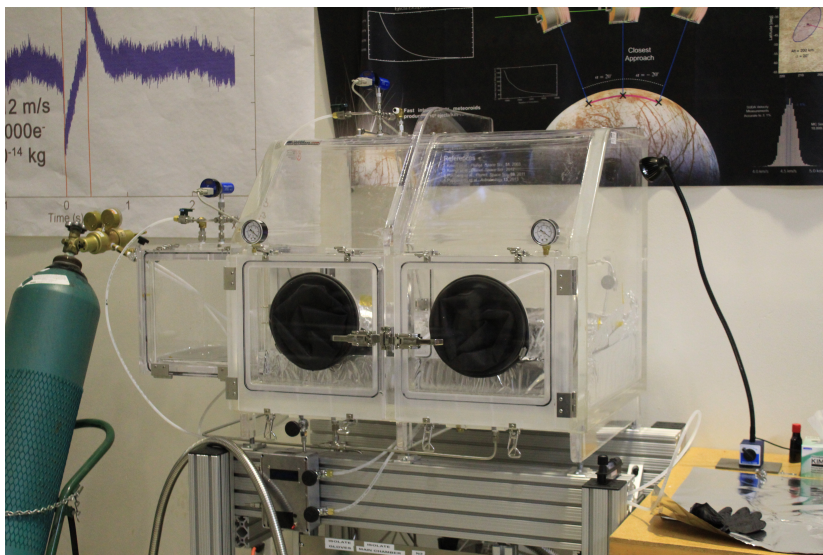


Figure 18: A photograph of the glovebox used in the airbrushing experiments. The antechamber is on the left. Note that it features its own venting, nitrogen, and vacuum lines as well as its own vacuum gauge. The floor of the main chamber is padded with aluminum foil-wrapped foam to prevent cracking of the plastic in the even of LN2 leaks.

### 3.3.3 Methods

The glovebox is pumped down to rough vacuum to eliminate atmosphere, and then it is back-filled with high purity nitrogen to produce an environment that is well below  $< 0.5\% \pm 1.5\%$  RH (the minimum detectable threshold of the current RH sensors). In atmosphere, the target is submerged in LN2 until rapid boiling ceases, and then the LN2 is topped off. It is then placed in the antechamber along with the airbrush, which is loaded with an aqueous solution, and pumped on for 5 minutes or until the antechamber pressure reaches 250 Torr. Continuous boiling of the LN2 prevents pressure from reaching far below this limit. The antechamber is then back-filled until it also measures  $< 0.5\% \pm 1.5\%$  RH. The door to the antechamber is then opened and the target is moved to the main chamber.

The airbrush is connected to the nitrogen line, and the target is pulled out of the LN2 and the Vespel door is removed. The target can now be sprayed with the aqueous solution, but care must be taken to ensure that

the solution freezes on contact. If the nozzle is held too close to the target, the thermal mass of the droplets will be sufficient to create a transient liquid water surface. While this transient liquid quickly freezes out (typically in less than a second), it has been observed that any liquid phase is sufficient to result in excretion effects with the dissolved amino acids. Such effects produce a surface layer of highly pure solid amino acid over a subsurface of water ice rather than a pure homogeneous surface of amino acids evenly mixed in water ice. Such solid surfaces are desirable for some experiments, but a simpler, more reliable method of creating them can be performed to obtain the same result, as described in Section 3.4. Thus, to create an ice with the complex organics evenly distributed in the ice matrix, the airbrush must be held sufficiently far enough away to only lightly mist the target module.

With a layer of water and amino acid ice now airbrushed onto the surface, the Vespel door is reinserted, isolating the surface from contamination. The assembly is then re-submerged into the LN2 (to keep it cold) and transferred to the antechamber which is promptly sealed and re-opened to atmosphere. From here, the process is the same as described in the flash freezing methods section, where the target is installed into the ice target chamber and quickly pumped down to vacuum before the door is removed and the pristine, homogeneous surface is exposed to the dust beam and the TOF mass spectrometer.

### 3.4 Freeze Dried Surfaces

Another method of creating surfaces is to freeze-dry an airbrushed surface under nitrogen. This involves following the airbrush method as described above, but instead of the flash freezing modular target, a simpler aluminum flatplate target is used, as shown in Fig. 19. This target has no mechanism for covering the ice after it has been created. Instead of immediately transferring the cold target to the chamber, it is isolated in the glovebox's antechamber and removed from the LN2, causing it to warm up slowly. As it warms, water in the ice surface evaporates, and the LN2 in the styrofoam container also evaporates, keeping the antechamber under positive pressure which releases through a relief valve. The vacuum pump is occasionally used to clear out gas to keep moisture content down.

In this way, as the surface water evaporates and is pumped out, the ice is effectively freeze-dried, and any amino acids from the ice are left on the

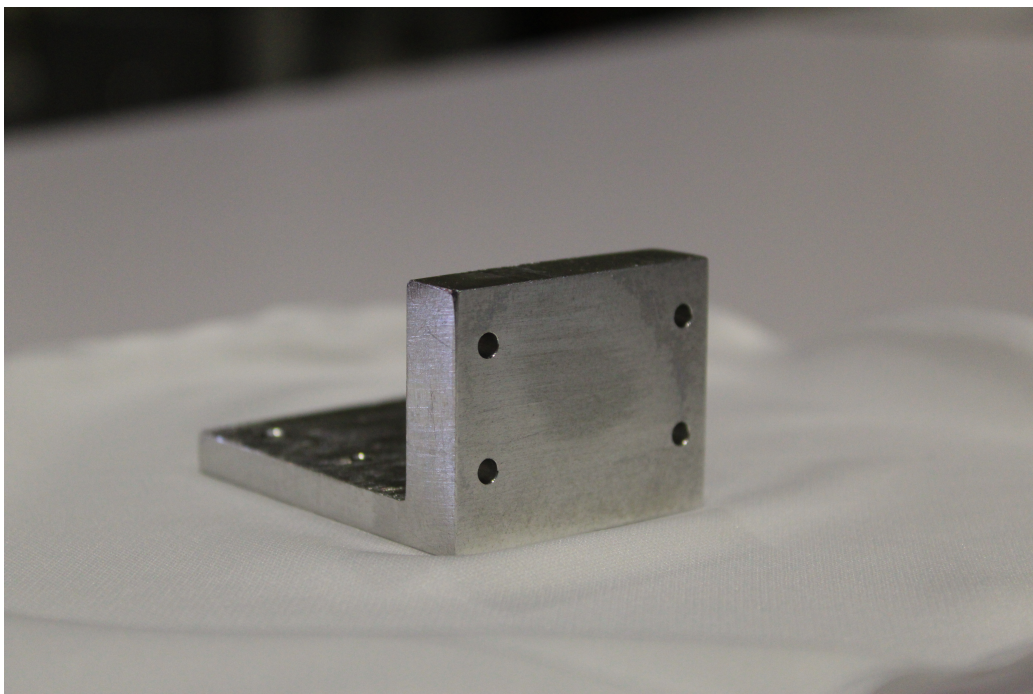


Figure 19: A photograph of the aluminum flatplate modular target.

surface, as shown schematically in Fig 20 (A) and (B). Such a surface was found to adhere strongly to the metal target pieces, and, being at least several hundred microns thick, was easily visible and thick enough to prevent impactors from reaching the aluminum substrate. It can also be transferred to the vacuum system at room temperature, which makes for a dramatically easier installation process. Thus, it was found that this was an easily repeatable method of gently creating a surface of solid amino acids over the metal substrate. Because of its simplicity and the fact that it can reproduce the results of creating a transient liquid phase as described in Section 3.3.3, this is the preferred method of creating such a surface.

Once in vacuum, the aluminum flatplate target upon which the freeze-dried surface sits can be cooled just as the copper targets are, and vapor deposition can then be performed to create a layer of water ice on top, if desired, as shown in Fig. 20 (C). In particular, this can be an effective way to control the relative strength of mass lines in the TOF spectra, as described in Section 3.5.

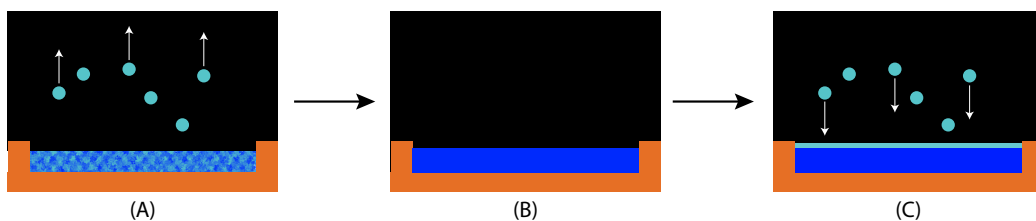


Figure 20: A diagram of the freeze-drying process. (A) An airbrushed surface with a homogenous mixture of water (aqua) and amino acids (blue) is slowly raised to room temperature while a vacuum pump removes evaporating water, yielding (B), a surface composed entirely of the amino acid in solid form. This surface is then installed into the ice target chamber at room temperature. If desired, the system can be cooled down and vapor deposition can be used to produce (C), a surface of the amino acid coated by a thin layer of water ice. This can be used to more carefully control the relative ion content of the water clusters and the amino acid lines in TOF data.

### 3.5 Comparison of Airbrushed and Freeze-Dried Surfaces

The airbrushing method is designed to produce homogeneous surfaces of water ice doped with complex organics, namely amino acids, and it appears to operate as expected. However, it has been observed that ices produced in this manner result in relatively small ion yields compared to the freeze-dried surface, regardless of whether the freeze-dried surfaces are at room temperature or have ice layers grown on top of them. This may be a result of ice surface morphology, as explained in Section 6.2, but in general this result is not understood. Whatever the physics behind this observation, the lower ion yield results in lower SNR, making it harder to analyze some of the spectra, especially at lower velocities.

Moreover, even high concentrations of amino acids in the airbrush system ( $\sim 0.5$ -1 Molar) result in TOF spectra where the amino acid, while detectable, often has much lower signal amplitude relative to water lines as compared to freeze-dried surfaces. In many spectra, the amino acids are not visible at all. In particular, many of the lower amplitude lines, such as amino acid breakup products, are not visible or not as visible in the airbrushed TOF data. This certainly is due in part to the water ice matrix diverting some of the impact energy, thus shielding the organics and resulting in less breakup products,

as described in Section 4, but this does not explain why the primary amino acid amplitudes are also lower in magnitude relative to water peaks. There may yet be more physics in this process which is not understood.

In any case, for studies which seek to investigate specifically which breakup products are produced and measured in hypervelocity impacts into water ice with amino acids, such as those in Section 4, freeze-dried surfaces, both with and without water ice on top, are highly desirable. This is because they produce surfaces with high ion yield, both across the entire spectra and individually in the breakup products, making detection of these products much easier. Additionally, freeze-dried surfaces without vapor-deposited ice layers can be compared to those with vapor-deposited ice layers, and thus the shielding effects of water ice can be directly studied.

However, airbrushed surfaces produce homogeneous ices that are more appropriate analogs of the icy ocean worlds and icy dust grains that are the primary targets that are ultimately being studied with this research. The freeze-dried surfaces, even those covered with ice, are primarily useful for calibration and exploration experiments. A precise understanding of the physics of impact ionization TOF analysis of amino acids in water ice depends on understanding the results from both ice production methods and how they relate and how they differ.

## 4 Detection of Amino Acids and Fragmentation Products

### 4.1 Importance

Assessing the inventory and stability of organic compounds is a critical step in studying the habitability of planetary objects such as icy ocean worlds [29]. The existence, abundance, and stability of complex organics directly limit the scale and productivity of potential biological systems on such objects [29], and certain types of organics may themselves be used as biosignatures, defined as detections or measurements that may provide signs of extant or past life [38].

Amino acids are of particular interest due to their fundamental role in terrestrial biology, being the constituent molecules of DNA. Thus, even in the absence of life, ascertaining celestial inventories of amino acids is critical to understanding the evolution of organics across the solar system and its role in the origin of the terrestrial genetic code [29, 77, 97].

It would therefore be a significant capability for impact ionization TOF instruments to be able to reliably detect amino acids in dust grains, whatever their source. To ascertain this possibility, there must then be a battery of laboratory experiments that use impact ionization TOF mass spectrometry to study the detectability of amino acids under hypervelocity impact and what their characteristic mass spectra signals are.

#### 4.1.1 Targets of Study

**Asteroids and Comets** It has long been hypothesized that significant fractions of prebiotic amino acids were delivered to earth via impact of cometary and meteoroidal material during the heavy bombardment period [98, 99, 100, 101]. A number of meteorites have large and diverse inventories of amino acids, most famously the Murchison meteorite with its 86 identified amino acids [102, 103], but significant quantities of amino acids have also been observed in the Yamato and Murray meteorites [97, 104, 105]. The Stardust mission brought samples of the comet Wild 2 to earth, and tentative detections of glycine were made. However, there have been persistent concerns about terrestrial contamination in this study [106, 107]. Other amino acids were also detected, but these were ruled as most likely being the result of such contamination [106, 107]. A dust analyzer on the spacecraft, the Cometary

and Interstellar Dust Analyzer (CIDA), did not detect any amino acids during its flyby of Wild 2, although it confirmed significant organic content, and it also measured quinone derivatives in ISD particles [74, 108]. The ROSINA mass spectrometer on the Rosetta spacecraft measured glycine as well as its precursors methylamine and ethylamine and the biotically necessary element phosphorus on the comet 67P/Churyumov-Gerasimenko [107].

Potential impact ionization dust analyzers on spacecraft that sample cometary coma or tails or dust from asteroids could therefore possibly encounter and study amino acids from these small bodies. Similarly, the IDEX instrument on the upcoming IMAP mission will be able to study the organic content of ISD particles [80], and the proposed FOSSIL mission could provide bulk measurements of OCC and JFC dust particles as well as measurements of asteroidal dust [17]. Detections and characterizations of amino acids from any of these targets would be highly valuable to understanding the distributions of organics throughout the solar system.

**Icy Ocean Worlds** In the case of Europa, it is expected that any organics within the top few hundred microns of the surface ice will be destroyed in a roughly 10 year timescale by the intense radiation environment [91, 109, 110, 110, 111], but there are potential mechanisms for renewal from beneath the surface. There have been tentative detections of plume activity on Europa that could actively deposit subsurface material across the surface [62, 63, 64]. Impact-generated gardening can create active mixing of both fresh and well-processed surface material [7, 112]. Finally, while the lack of surface craters visible on Europa relative to other solar system objects indicate a young surface of 40-90 Myr [113], the presence of widespread chaos terrain suggests that active resurfacing processes have occurred in the recent past, or are potentially ongoing, and observed spectroscopic differences between them and the surrounding ice suggest an interior source [114, 115, 116]. Thus, there may be organic content on the surface of Europa that is being actively exposed and irradiated. Active dust production processes such as those discussed in Section 1.2 can therefore loft potentially organic-bearing icy dust grains into ballistic trajectories around icy ocean worlds where they can be measured by impact ionization TOF instruments such as SUDA [78].

Plumes of ice grains on Enceladus have been shown to originate from the subsurface ocean, and each year they may deposit up to 0.5 mm of new surface material in the immediate vicinity of the plumes and up to tens of

microns at the equator [59, 75]. The plumes are also known to contain organics [60], some with molecular masses in excess of 200 u [61]. Thus, Enceladus provides a particularly enticing target for study with impact ionization TOF instruments, which would be able to sample plumes directly from the subsurface ocean in addition to surface material ejected via IDP bombardment. Several missions have been proposed that would carry such an impact ionization mass spectrometer [54, 82, 83].

#### 4.1.2 Amino Acids as Biosignatures

Amino acids are produced abiotically, but they can nonetheless be excellent biosignatures in certain conditions [38, 77, 117]. In particular, abiotic and biotic amino acids can be distinguished from one another using either the relative abundance of complex amino acids relative to glycine, the simplest amino acid, or enantiometric excess measurements [38].

**Relative Abundance Measurements** While terrestrial life uses 20 amino acids, this is only a small fraction of the plethora of chemically possible (and abiotically produced) amino acids [97, 99]. Higgs and Pudritz, 2009 gives an overview of the studies of abiotic supplies of amino acids [97]. This study's focus is on ascertaining the origin of the genetic code, in particular considering the relative abundances of each of the 20 biological amino acids in the prebiotic earth. Across several observed inventories and experimental production mechanisms, it finds a 'remarkably consistent' ranking of abundances between the 10 simplest biotic amino acids, a result which can be explained by the relative complexity of these organics in what are fundamentally thermodynamic production processes. As the simplest amino acid, glycine is the thermodynamically-preferred amino acid in abiotic production, most famously in the Miller-Urey experiments and similar shock synthesis studies [118, 119, 120, 121, 122, 123]. It therefore is the most abundant amino acid in observed abiotic inventories such as meteorites [97].

Higgs and Pudritz provide a table, reprinted here with permission as Table 1 [97], which shows the relative concentrations of amino acids observed in abiological contexts. Columns *M1*, *M2*, and *M3* show the inventories of the Murchison, Murray, and Yamato meteorites respectively. [102, 103, 104, 105]. Column *I1* shows abundances from Muñoz Caro et al. 2002, which studied amino acid production in a protosolar ice mixture analog composed of  $\text{H}_2\text{O}:\text{CH}_3\text{OH}:\text{NH}_3:\text{CO}:\text{CO}_2$  in a 2:1:1:1:1 molar ratio under ultraviolet ir-

RELATIVE CONCENTRATIONS OF AMINO ACIDS OBSERVED IN NONBIOLOGICAL CONTEXTS

	<i>M1</i>	<i>M2</i>	<i>M3</i>	<i>I1</i>	<i>A1</i>	<i>A2</i>	<i>A3</i>	<i>H1</i>	<i>H2</i>	<i>S1</i>	<i>S2</i>	<i>S3</i>	$R_{obs}$
G - Gly	1.00	1.0	1.000	1.000	1.000	1.000	1.000	18	12	1.000	1.000	40	1.1
A - Ala	0.34	0.4	0.380	0.293	0.540	1.795	0.155	15	8	0.473	0.097	20	2.8
D - Asp	0.19	0.5	0.035	0.022	0.006	0.077	0.059	10	10	0.000	0.581	30	4.3
E - Glu	0.40	0.5	0.110	0.000	0.010	0.018	0.000	6	11	0.000	0.000	20	6.8
V - Val	0.19	0.3	0.100	0.012	0.000	0.044	0.000	1	0	0.006	0.000	2	8.5
S - Ser	0.00	0.0	0.003	0.072	0.000	0.011	0.018	8	11	0.000	0.154	0	8.6
I - Ile	0.13	0.0	0.060	0.000	0.000	0.011	0.000	8	9	0.000	0.002	4	9.1
L - Leu	0.04	0.0	0.035	0.000	0.000	0.026	0.000	3	0	0.001	0.002	7	9.4
P - Pro	0.29	0.1	0.000	0.001	0.000	0.003	0.000	9	0	0.000	0.000	2	10.0
T - Thr	0.00	0.0	0.003	0.000	0.000	0.002	0.000	2	0	0.000	0.002	1	11.7
K - Lys	0.00	0.0	0.000	0.000	0.000	0.000	0.000	7	0	0.000	0.000	14	12.6
F - Phe	0.00	0.0	0.000	0.000	0.000	0.000	0.000	4	0	0.000	0.000	1	13.2
R - Arg	0.00	0.0	0.000	0.000	0.000	0.000	0.000	0	0	0.000	0.000	15	13.3
H - His	0.00	0.0	0.000	0.000	0.000	0.000	0.000	0	0	0.000	0.000	15	13.3
NQCYMW	0.00	0.0	0.000	0.000	0.000	0.000	0.000	0	0	0.000	0.000	0	14.2

Table 1: A table showing the abundances of the 20 biological amino acids relative to glycine from a variety of observational and experimental data. Columns *M1* – *M3* denote meteorite observations, *I1* denotes interstellar icy grains, *A1* – *A3* denote atmospheric synthesis experiments, and *S1*-*S2* denote other miscellaneous chemical synthesis experiments. Columns *H1*, *H2*, and *S3* are detection counts for the specified observations or experiments, while all other columns are abundance measurements relative to glycine. The final column,  $R_{obs}$ , is the mean of separate ranking calculations for each amino acid. Reprinted with permission from Ref. [97].

radiation [124]. Columns *A1* and *A2* show results from atmospheric shock synthesis experiments [122, 125]. Columns *H1* and *H2* show detection counts of each species from experiments simulating hydrothermal vents [126, 127]. Columns *S1* – *S3* show additional synthesis experiments with various chemical precursors [128, 129, 130]. Columns *H1*, *H2*, and *S3* are detection counts for the specified observations or experiments, while all other columns are abundance measurements relative to glycine. The final column,  $R_{obs}$ , is the mean of separate ranking calculations for each amino acid..

One of the most striking features of Table 1 is that there are a number of amino acids that are either not present at all, (NQCYMW), or only in a handful of the observations and experiments, (TKFRH). These amino acids are sufficiently complex that they are disfavored in abiotic production, and thus are exceptionally rare compared to glycine except in biotic systems.

Histidine is observed only in a single experiment, Yoshini et al., 1971 [130], but there has never been a detection of natural histidine except for biogenic sources [97, 117]. Thus, while detection of one or several of these amino acids would not be a biosignature detection in and of itself, it would be a striking result. Detection of high concentrations of several of these amino acids relative to glycine, however, would be considered a biosignature detection [38, 117].

**Enantiometric Excesses** Amino acids, excepting glycine, are chiral molecules, each having both levorotatory (L) and dextrorotatory (D) forms called enantiomers that are mirror images of each other [131]. Life on earth is observed to only use L amino acids, creating significant excesses of homochiral distributions in biotic systems, and extraterrestrial life would also very likely use only one enantiomer [117]. Abiotic systems, on the other hand, are observed to have largely heterochiral distributions. While some abiotic processes are known to create enantiometric imbalances, none can create them on the scale of biological systems, meaning that large enantiometric excesses (of either L or D) would be strong signs of past or present life [38, 117, 124, 131, 132, 133, 134]. While TOF mass spectrometry systems cannot distinguish between enantiomers, as each form has the same elemental constituents and thus the same mass, the potential for homochiral distributions as biosignatures detectable by other instruments serves to further highlight the importance of understanding the distribution of amino acids across the solar system.

## 4.2 Impact Ionization TOF Instruments

Because impact ionization TOF instruments sample dust grains at hypervelocity, the kinetic energy may be sufficient to dissociate the chemical bonds of complex organic molecules [135, 136]. Such impact events would shatter the parent molecule before it could be studied, meaning that rather than studying the composition of the dust grain, only its fragments could be studied. This may not be a problem in and of itself, as organic molecules often break up at predictable cleavage sites due to certain bonds within the molecule being weaker than others [92, 137]. This means that combinations of fragmentation products may themselves be used to identify a parent molecule, while presence of both the parent molecule and its known breakup products would provide yet stronger evidence for detection of a given molecule.

To accurately interpret detections from space-borne instruments, it is therefore critical to understand how dust grain velocity relative to the spacecraft instrument affects the signals produced by TOF analysis [136, 138].

Jamillo-Botero et al., 2021 [139] used high fidelity simulations to study the fragmentation rates for ten amino acids (not including histidine) and a number of other organics. This study found that fragmentation depended on complex relationships between ‘velocity, impact angle, molecular structure, impact surface material, and the presence of surrounding ice shells.’ The simulation results indicated that ideal spacecraft velocities that minimize fragmentation would be between 3-5 km/s for bare amino acids and between 4-6 km/s when encased in ice [139].

Laser induced liquid beam desorption and ionization (LILBID) [140] is a laboratory method that uses a pulsed laser to ablate a stream of liquid 10  $\mu\text{m}$  in diameter in vacuum that and been used to replicate CDA compositional data [75]. In these studies, the laser pulse heats up the liquid molecules and explosively disperses them into atomic, molecular, and macroscopic fragments [141]. Klenner et al., 2019 [141] used this method to replicate observed differences between CDA Type 1 spectra, composed of highly pure water ice with sub-ppm levels of sodium and potassium [75]. This study used a gated mass spectrometer with a varying delay to select different fractions of the velocity distribution created in the ablation process [141]. The fastest ions could be pulled out of the plume by quickly switching on the acceleration fields after ablation, while slower ions could be collected by pulsing with a ‘fast’ ion window followed by two slower windows. By tuning the laser pulse energy and the length of the delay, the CDA Type 1 data was successfully replicated [141].

The authors have used this as a calibration benchmark to use similar pulses and delays to study water beams carrying amino acids and fatty acids, another potential biosignature [38, 142]. They found that signal collection for complex organics was maximized when the laser pulse and delay times were set to mimic CDA spectra in the 3-6 km/s range [142]. However, while these studies are highly valuable, it is not clear how accurately the LILBID process can truly replicate the physical conditions inside impact ionization ejecta plumes. The physical mechanism, being light-based rather than impact-based, is fundamentally different. While these studies have had great success replicating velocity data for Type 1 water clusters, it is not clear to what extent tuned laser pulse energies and delay times selecting velocity distributions can be carried over into the study of fragmentation of complex

organic molecules. The selection of velocity distributions in an ablated plume provides useful data, but it remains to be seen how well this selection accurately replicates the spectroscopic characteristics and trends across different physical impact velocities for ices of arbitrary composition, or even how well liquid water may be substituted for ice in reducing impact stress on the entrained organics. Laboratory experiments must be performed with physical impacts at known velocities to investigate these effects and complement the existing data.

Here we present results from submicron iron dust particle hypervelocity bombardment of the amino acid histidine as a bare solid surface as well as a solid surface with a  $\sim 60$  nm cover of water ice. We find that histidine itself is detectable even at 15 km/s, but fragmentation increases with velocity, particularly above 7 km/s. We also find that fragmentation rates are reduced with the presence of a water ice cover by a factor of about two, but masses 110, 83, 82, and 81 are characteristic fragmentation products of histidine at every velocity for both surfaces. We also find good agreement between the observed breakup products in the measured spectra and the electron ionization spectra available from NIST [143], although the relative ion content distributions within each is significantly different.

### 4.3 Experimental Setup

Two different experiments to study the bombardment of histidine and histidine-bearing ices are described here, both using different techniques with the airbrushing system described in Section 3.3. Histidine monohydrochloride was sourced from Sigma Aldrich [144] and dissolved in various concentrations at room temperature into JT Baker 6906-02 18 M $\Omega$  water sourced from Capitol Scientific [145]. Each solution was mixed immediately before being loaded into the airbrush so as to minimize reactions and reduce parent molecule decay.

**Experiment 1** was performed with a solid surface of histidine created through the freeze-drying process as described in Sec. 3.4. A solution of  $0.750 \pm 0.003$  molar histidine monohydrochloride was mixed and then airbrushed onto the cold aluminum flatplate target (Fig. 19). While this is an extremely high concentration compared to what might be expected from planetary ices, the freeze-drying process eliminates water from the surface anyway, creating a surface of pure solid histidine monohydrochloride. Thus a high concentration was used to rapidly create thick surfaces on the target substrate. The target

was slowly warmed to room temperature and the surface ice freeze-dried. The target was then installed into the ice target chamber and pumped down to ultra high vacuum ( $\sim 10^{-8}$  Torr). A few calibration shots were typically taken at  $10^{-6}$  Torr at room temperature. Because subsequent experiments were performed with the target at  $\sim 85$  K to facilitate water ice, the target was then cooled with LN2 to this temperature, but no ice layer was deposited. Remnant water vapor in the chamber would have frozen out onto the target surface during this time, creating an ice layer far thinner than could be measured with the Fabry-Perot interferometer.

**Experiment 2** followed the same procedure with a  $0.749 \pm .003$  molar solution, except that after the target was cooled to  $\sim 85$  K, water ice was vapor deposited on the surface at a chamber pressure of  $1.0$  to  $1.3 \text{ E}^{-6}$  Torr for a period of 7 minutes. This created a water ice surface approximately 60 nm thick on top of the freeze-dried histidine layer.

Particles between 3 and 99 km/s were allowed to impact the prepared surfaces, but this study only contained impacts between 3 and 15 km/s. Spectra were collected for each dataset, and a number of false triggers and noise-dominated spectra were eliminated from each. For the impact ionization TOF system, there is no well-defined time zero as may be found in laser ablation TOF systems [e.g., 141, 146]. The data was therefore pre-processed using the Spectrum software suite to align the spectra with one another. Because these datasets feature high concentrations of histidine, the parent histidine line itself is a strong feature in most spectra. It was therefore used in addition to the water cluster backbone sequence to assign a timestretch parameter to each spectrum to convert the x-axis from the time domain to the mass domain.

Spectra were then grouped into bins of 1 km/s width, such as 3-4 km/s, 4-5 km/s, etc. Binned spectra were co-added and normalized in the mass domain using the Spectrum software. The resulting summed spectra were then smoothed with the SciPy 1D Gaussian filter of width 10 [147] to reduce noise and make it easier to fit lines to the data. The width was qualitatively chosen to reduce substructure of mass lines while preserving overall shapes and integral areas.

Exponentially modified Gaussians (EMGs) of the form

$$a_0 \frac{\lambda}{2} e^{\frac{\lambda}{2}(2\mu + \lambda\sigma^2 - 2t)} \cdot \text{erfc} \left( \frac{\mu + \lambda\sigma^2 - t}{\sqrt{2}\sigma} \right) \quad (5)$$

were fitted to the mass lines in the summed spectra. In this expression  $a_0$  is the amplitude,  $\lambda$  is an exponential decay term,  $\sigma^2$  is the variance,  $\mu$  is the mean, and  $\text{erfc}$  is the complementary error function. The integrals of these fitted lines can then be used to measure the relative ion content for each mass species. The mean value  $\mu$ , rounded to an integer, was taken as the mass of the species for data analysis.

## 4.4 Results

Denoised summed spectra for the 3-4 km/s, 7-8 km/s, and 14-15 km/s bins for Experiments 1 and 2 are shown in Figs. 21 through 26. These plots show the entire mass range, including the histidine parent molecule at mass 156. Details of the summed spectra, rescaled without the dominating histidine lines, are shown for each velocity bin in the supplemental Figs. 54 through 77. The breakup product mass lines increase dramatically across these three velocity bins, and a qualitative difference between the relative peak heights in Experiment 1 and 2 can be visually identified, particularly in the highest velocity bins. At the highest velocity studied, 14-15 km/s, maximum fragmentation occurs, presenting the strongest observed signal lines for each breakup product. The NIST electron ionization spectrum for histidine is shown in Fig. 27, reprinted from the NIST Webbook [143], where the molecule is intentionally shattered under electron bombardment and ionization to determine its breakup products. A comparison with the NIST data shows overall agreement between fragment ion species, but with a significantly different distribution of relative ion content.

In order to characterize the breakup trends across the experiments, breakup products are clustered into different observed groups, color coded on the top axis of Figs. 21 through 26. Water cluster lines are shown in two shades of blue to denote protonated and unprotonated lines. Contaminants or other obfuscating masses are colored shades of orange. Finally, observed histidine mass groups, detailed below, are colored in alternating pink and green.

While the minimal water content of Experiment 2 allows for direct reading of most the ions, the water ice cover in Experiment 1 produces mass aliases to several breakup product mass lines due to water clusters, protonated water clusters, and sodiated water clusters (from trace levels of sodium contamination). Additionally, the impacting iron dust particles alias to other mass lines in both Experiments. For example, the TOF data shows significant ion content at the mass lines 50-60. However, mass 54 aliases to  $^{54}\text{Fe}$

Experiment 1  
 Histidine Without Ice Cover  
 3-4 km/s Summed Spectra

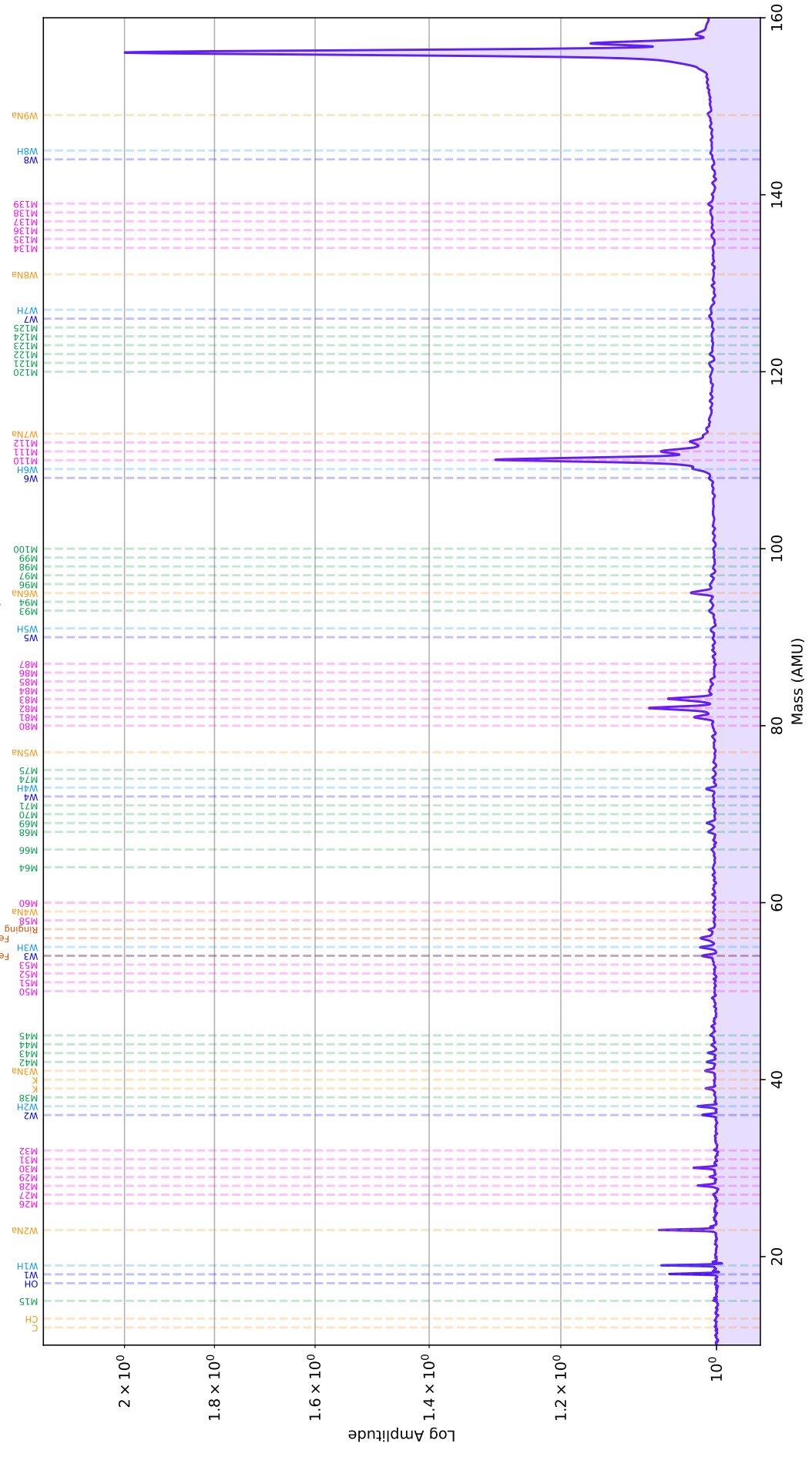


Figure 21: Summed spectra for impacts of velocities between 3 and 4 km/s in Experiment 1, which featured a bare histidine surface exposed to the dust beam. Pink and green lines denote mass groups of breakup products. Blue lines show water lines. Yellow lines denote contaminants or other mass aliases.

Experiment 1  
 Histidine Without Ice Cover  
 7-8 km/s Summed Spectra

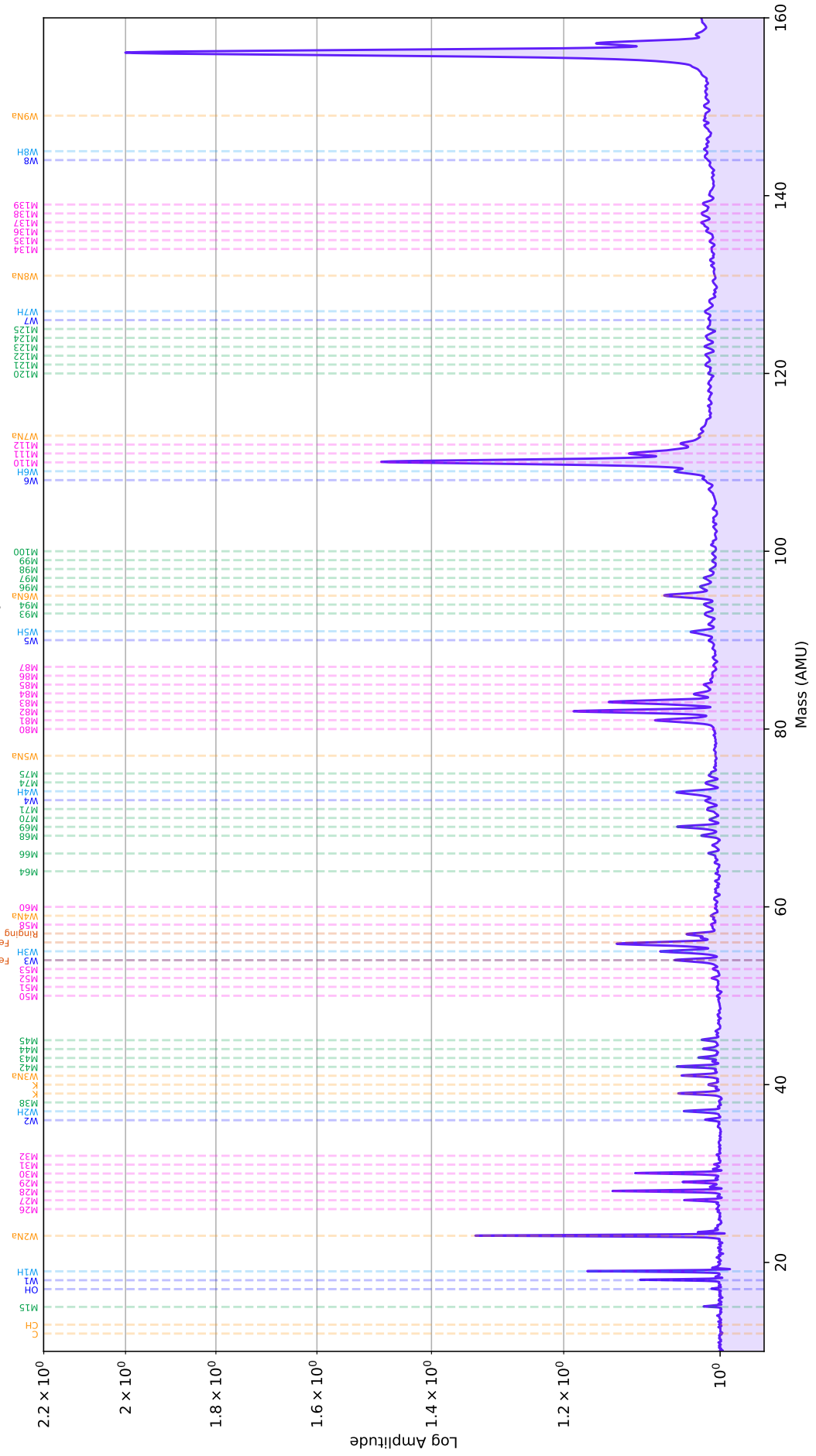


Figure 22: Summed spectra for impacts of velocities between 7 and 8 km/s in Experiment 1, which featured a bare histidine surface exposed to the dust beam. A detail without the dominating histidine line is shown in the supplemental Fig. 58.

Experiment 1  
 Histidine Without Ice Cover  
 14-15 km/s Summed Spectra

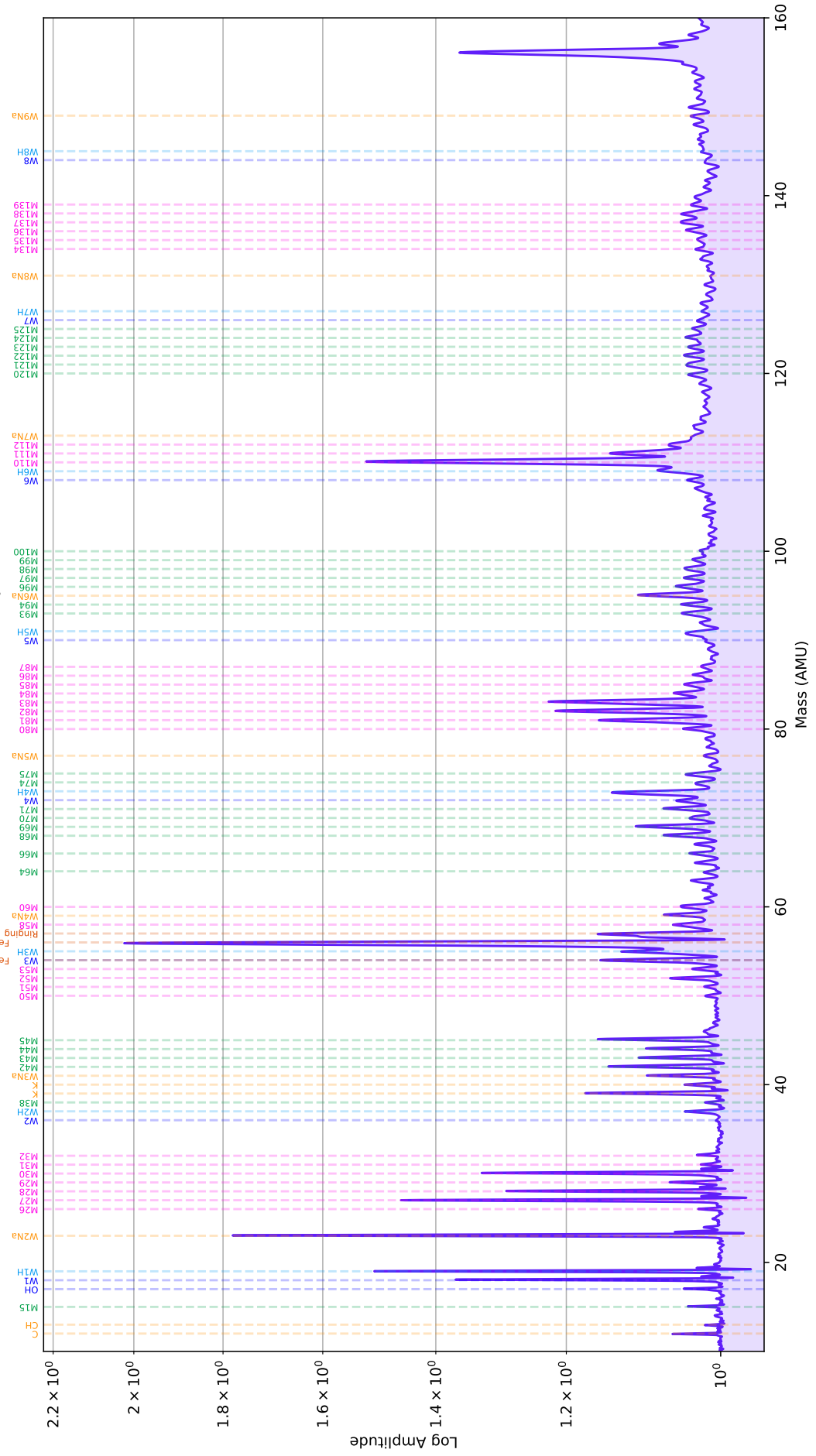


Figure 23: Summed spectra for impacts of velocities between 14 and 15 km/s in Experiment 1, which featured a bare histidine surface exposed to the dust beam. A detail without the histidine region is shown in the supplemental Fig. 65.

Experiment 2  
 Histidine With Ice Cover  
 3-4 km/s Summed Spectra

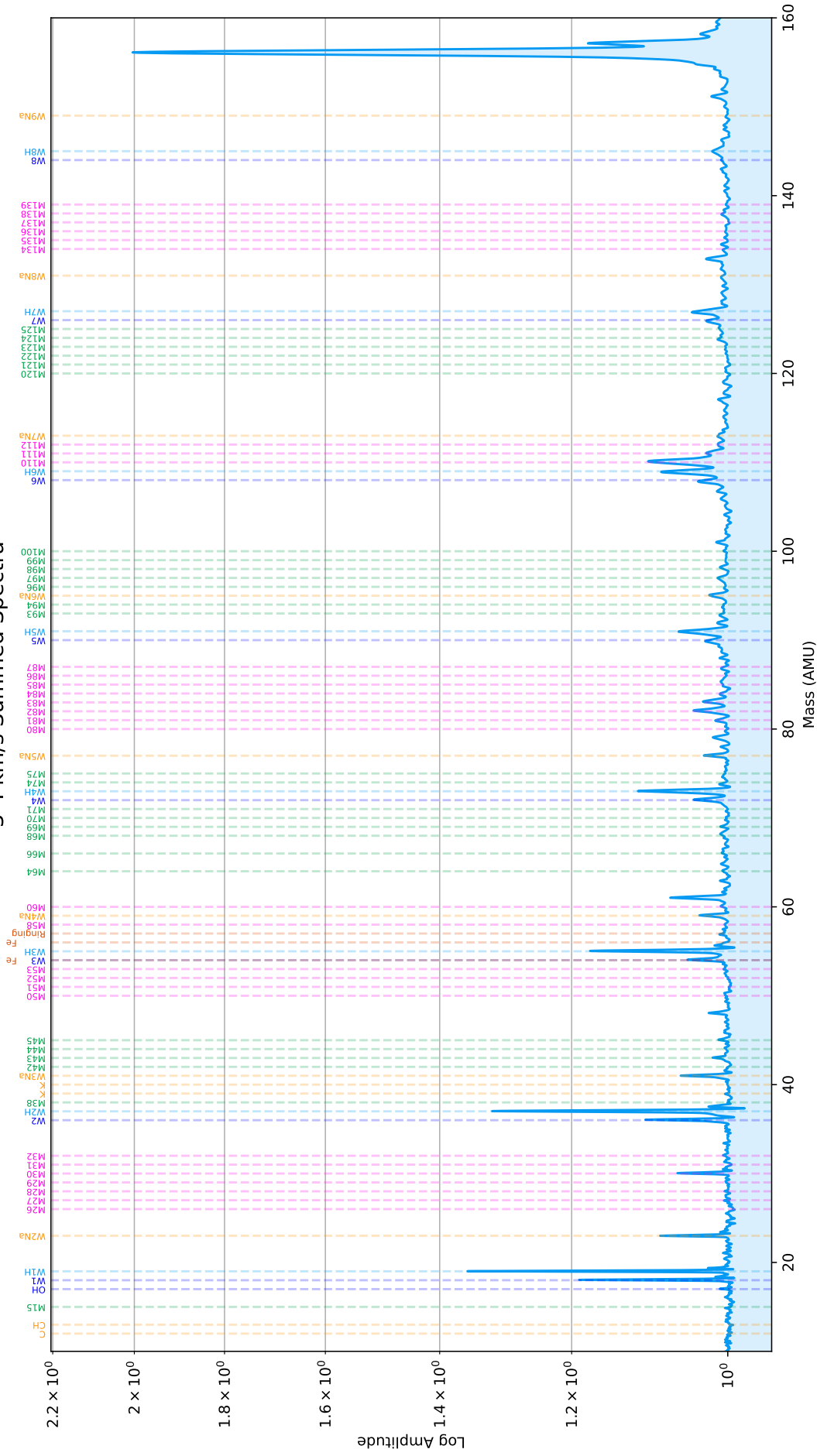


Figure 24: Summed spectra for impacts of velocities between 3 and 4 km/s in Experiment 2, which featured a 60 nm water ice layer covering the histidine surface. Pink and green lines denote mass groups of breakup products. Blue lines show water lines. Yellow lines denote contaminants or other mass aliases. The histidine molecule dominates the spectrum, and a detail without this dominating line is shown in the supplemental Fig. 66.

Experiment 2  
 Histidine With Ice Cover  
 7-8 km/s Summed Spectra

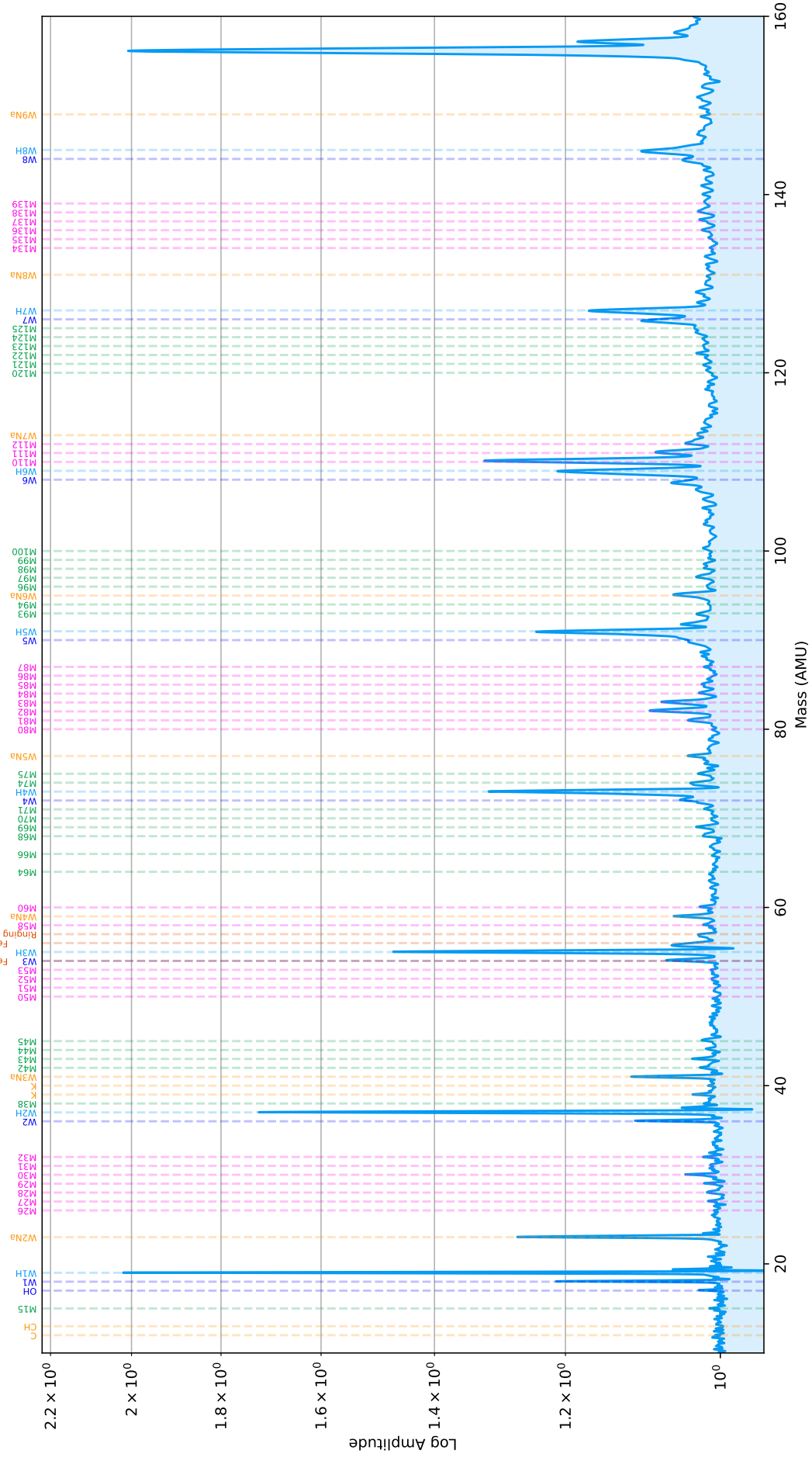


Figure 25: Summed spectra for impacts of velocities between 7 and 8 km/s in Experiment 2, which featured a 60 nm water ice layer covering the histidine surface. A detail without the dominating histidine line is shown in the supplemental Fig. 70.

Experiment 2  
 Histidine With Ice Cover  
 14-15 km/s Summed Spectra

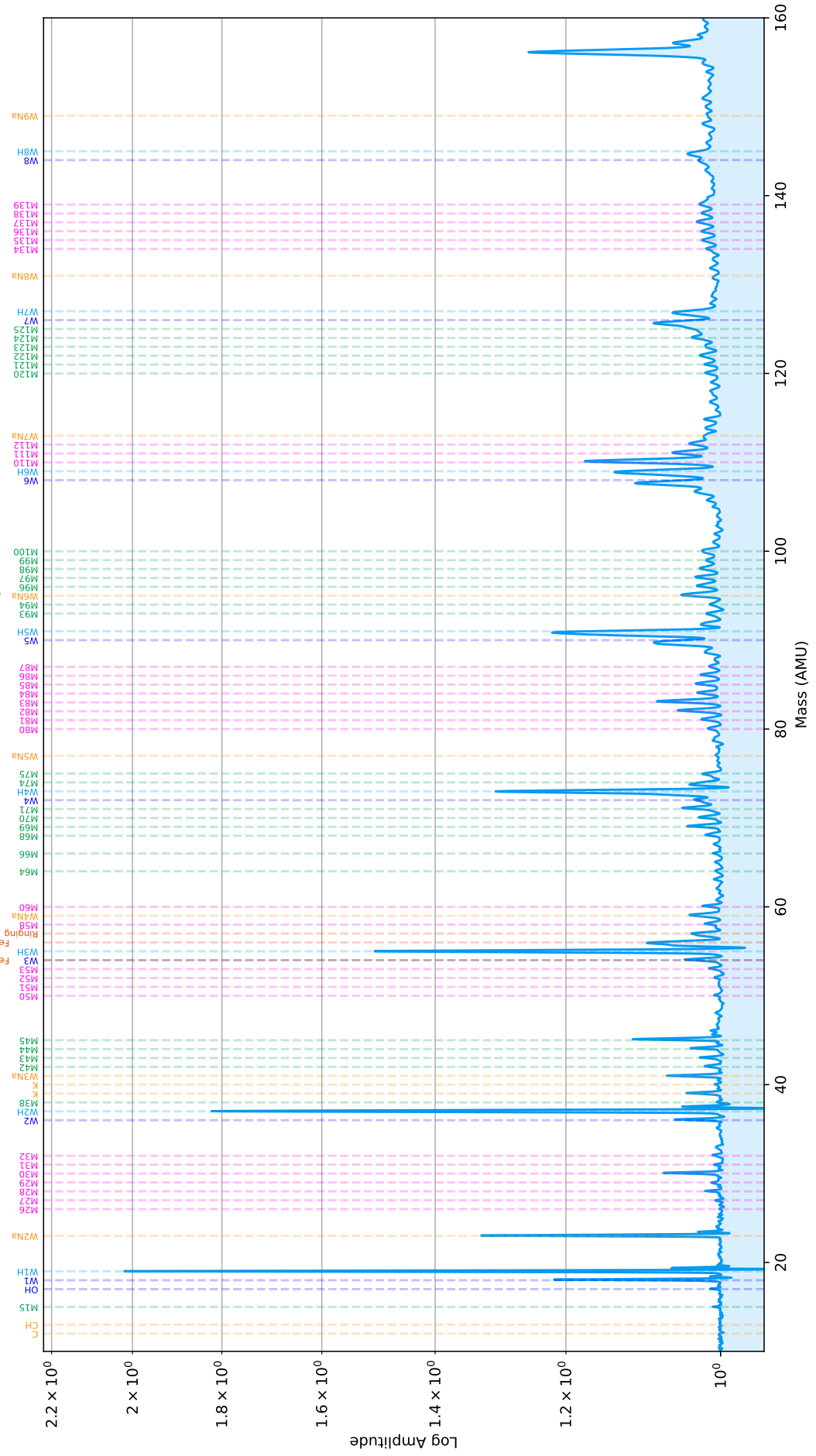


Figure 26: Summed spectra for impacts of velocities between 14 and 15 km/s in Experiment 2, which featured a 60 nm water ice layer covering the histidine surface. A detail without the histidine region is shown in the supplemental Fig. 77.

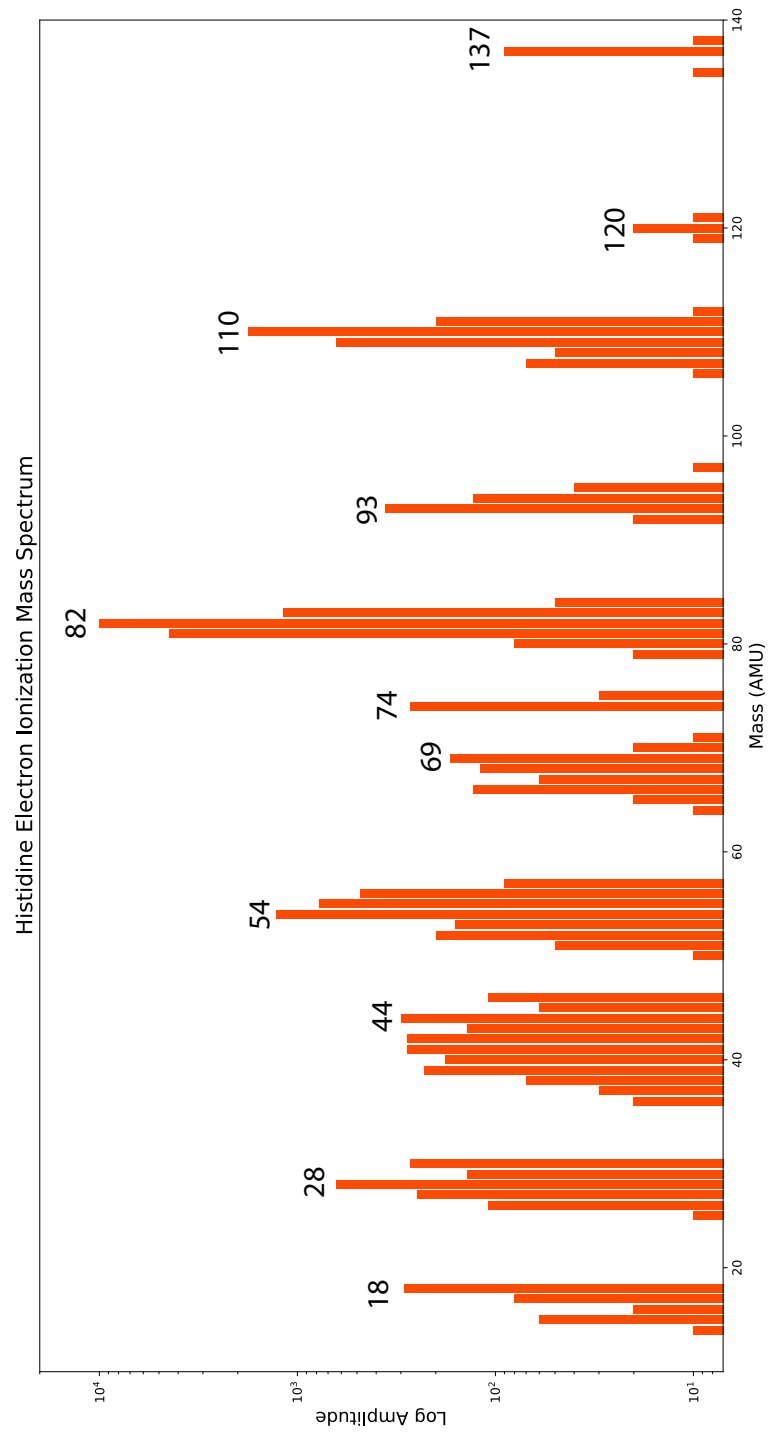


Figure 27: Electron ionization mass spectrum of histidine, modified from the NIST Webbook [143].

and  $(\text{H}_2\text{O})_3$ , 55 aliases to  $(\text{H}_2\text{O})_3\text{H}$ , 56 aliases to  $^{56}\text{Fe}$ , 57 is complicated by MCP ringing from the  $^{56}\text{Fe}$  line, and 59 aliases to  $(\text{H}_2\text{O})_2\text{Na}$ , and thus all these masses are removed from the mass group, leaving only masses 50-53, 58, and 60. The mass group dominated by mass 83, in contrast, has no ignored lines due to its distance from adjacent water cluster masses. Sodium and potassium are frequent contaminants found in ionization data due to their terrestrial abundance and low ionization potential. Mass lines 38 and 40, the two dominant isotopes of K have been removed as a precaution because they have sometimes been observed in our data in the past. However, it should be noted that including them does not significantly change our observed results, nor does including mass 57, discarded due to MCP ringing.

Ignoring aliased lines, the remaining breakup product masses are grouped according to the dominant ion species observed in each group. This grouping is detailed in Table 2. The lowest mass group, dominated in the NIST data by mass 18, is completely ignored because the only species observed in the TOF data that does not alias to a water- or carbon-related ion is mass 15, and this is present only in small amounts in the high velocity spectra.

Table 2 also gives the ion content for each mass group relative to observed histidine ion content. Purple rows denote Experiment 1 data, without the ice cover, while white rows denote Experiment 2 data with the 60 nm vapor deposited ice layer. It can be seen that there is a greater number of breakup product ions for Experiment 1 uniformly. The final row gives the ratios for all mass groups combined, yielding a measure of the total breakup product content to the parent molecule content. Taking each velocity bin as a separate measurement, the ratio of breakup products without the ice cover to those with the ice cover is measured to be  $2.2 \pm 0.2$ . In other words, the presence of the 60 nm ice layer appears to be suppressing the fragmentation rate by a factor of about two, but it should again be noted that several significant breakup products within multiple mass groups have been excluded from this analysis due to aliasing mass lines.

The dominant breakup products are masses 110 and 83, with masses 82 and 81 becoming more important for higher velocities. These species are observed in significant quantities for all velocity bins across both experiments. Fig. 28 shows the ion content of mass groups 110 and 83 relative to the histidine parent molecule as a function of impactor velocity. In the mass group 110 data, it can be seen that the breakup products from the bare histidine in Experiment 1 (purple circles) begin to diverge from the covered products from Experiment 2 (blue triangles) beyond 7 km/s. This effect is

Table of Mass Groups														
Mass Group	Observed Masses	Ignored Masses [Mass Aliases]	Ion Content Relative to Histidine											
			(Purple rows have no ice cover, white rows have 60 nm ice cover)											
			3-4	4-5	5-6	6-7	7-8	8-9	9-10	10-11	11-12	12-13	13-14	14-15
			km/s	km/s	km/s	km/s	km/s	km/s	km/s	km/s	km/s	km/s	km/s	km/s
18	13-18	All												
27	26-32	None	0.04	0.06	0.07	0.11	0.19	0.39	0.39	0.85	0.81	0.80	0.99	1.7
			0.04	0.08	0.07	0.05	0.06	0.05	0.14	0.08	0.08	0.15	0.22	0.31
42	37-46	37 [(H <sub>2</sub> O) <sub>2</sub> H] 39 [ <sup>39</sup> K] 40 [ <sup>40</sup> K] 41 [(H <sub>2</sub> O)Na]	0.03	0.02	0.03	0.05	0.08	0.17	0.2	0.36	0.4	0.39	0.54	0.73
52	50-60	54 [(H <sub>2</sub> O) <sub>3</sub> , <sup>54</sup> Fe] 55 [(H <sub>2</sub> O) <sub>3</sub> H] 56 [ <sup>56</sup> Fe] 57 [MCP Ringing] 59 [(H <sub>2</sub> O) <sub>2</sub> Na]	0	0	0	0.01	0.03	0.05	0.06	0.19	0.32	0.21	0.33	0.52
			0	0	0	0	0.02	0.02	0	0.02	0.05	0.07	0.13	0.16
69	64-75	72 [(H <sub>2</sub> O) <sub>4</sub> ] 73 [(H <sub>2</sub> O) <sub>4</sub> H]	0.02	0.02	0.03	0.06	0.12	0.19	0.19	0.45	0.51	0.48	0.58	0.78
			0.01	0.02	0.06	0.06	0.09	0.04	0.16	0.24	0.26	0.33	0.39	0.54
83	80-87	None	0.16	0.19	0.19	0.29	0.36	0.55	0.63	1.0	1.1	1.1	1.3	1.5
			0.09	0.08	0.09	0.06	0.21	0.12	0.19	0.25	0.36	0.43	0.51	0.68
93	91-100	91 [(H <sub>2</sub> O) <sub>5</sub> H] 95 [(H <sub>2</sub> O) <sub>4</sub> Na]	0.03	0.04	0.04	0.06	0.10	0.14	0.15	0.33	0.47	0.44	0.50	0.65
			0.02	0.01	0	0	0.17	0.09	0.16	0.13	0.29	0.30	0.31	0.46
110	107-112	108 [(H <sub>2</sub> O) <sub>6</sub> ] 109 [(H <sub>2</sub> O) <sub>6</sub> H]	0.35	0.39	0.37	0.50	0.53	0.74	0.85	1.1	1.0	1.1	1.2	1.3
			0.13	0.14	0.23	0.16	0.34	0.31	0.36	0.47	0.60	0.54	0.56	0.78
122	120-128	126 [(H <sub>2</sub> O) <sub>7</sub> ] 127 [(H <sub>2</sub> O) <sub>7</sub> H]	0	0	0.02	0.04	0.08	0.11	0.13	0.20	0.29	0.29	0.35	0.45
			0.02	0	0.04	0.01	0.06	0.06	0.13	0.17	0.29	0.27	0.32	0.39
137	134-139	None	0.01	0.02	0.02	0.06	0.10	0.13	0.14	0.31	0.36	0.34	0.43	0.46
			0.01	0	0	0	0.06	0.02	0.08	0.14	0.29	0.24	0.36	0.46
All	All of the Above	All of the Above	0.64	0.75	0.78	1.2	1.6	2.5	2.7	4.8	5.3	5.1	6.2	8.0
			0.33	0.36	0.49	0.39	1.18	0.77	1.3	1.6	2.4	2.6	3.1	4.2

Table 2: Explanation of mass groups and ignored lines. Species that alias to ignored mass lines are given in square brackets. Group names are taken from the dominant observed mass lines.

much more pronounced in the mass group 83 data. In Fig. 28, the dashed lines show fitted lines to the first three velocity bins, covering 3-6 km/s. The solid lines are fitted to the data from the 6-7 km/s bin and beyond. The ratio of the slopes of the solid lines is printed inside the figure, with the mass group 110 data showing a high velocity line fit ratio (Experiment 1 to Experiment 2) of 1.8, while the mass group 83 has a slope ratio of 2.4.

Regardless of the ratio between the bare and covered surfaces, it can also be seen, especially in the mass group 83 data, that the breakup product to parent molecule ratio increases dramatically beyond the 6-7 km/s bin. This trend can be seen in every single mass group, even those with relatively few studied mass lines. It is also apparent in both bare and covered datasets, excepting mass group 27, for which the effect for the covered histidine is muted. Fig. 29 shows the ion ratios for mass groups 27, 42, 52, and 69, while Fig. 30 shows the results for mass groups 93, 122, and 137. Fig. 31 shows the ion ratios for all mass groups combined, where the ratio of the line slopes fitted to the high velocity data is 1.9.

It is striking that all mass groups display significant divergence after the 6-7 km/s velocity bin. This would strongly suggest that fragmentation of the parent histidine molecule is largely uniform below these velocities, but beyond 6-7 km/s fragmentation increases dramatically. In other words, fragmentation is minimized below some velocity between 6 and 7 km/s.

#### 4.4.1 Discussion

Zhang et al., 2019 report amino acid breakup pathways and relative amplitudes over normalized collision energies for masses above 50 AMU [92, Supplementary Figs. S47 and S48], showing that the mass 110 line originates from the parent histidine molecule losing ( $\text{H}_2\text{O}^+\text{CO}$ ), and this mass 110 fragment further loses an HCN to become mass 83. In particular, they also show that in their collision-induced dissociation, mass line 110 is present at greater abundance than the parent molecule at all normalized energies. With the uncovered histidine surface in Experiment 1, the 110 mass line surpasses the 156 line in the 10-11 km/s bin and beyond, but it never surpasses the 156 line for the histidine with an ice layer, further illustrating the protective qualities of the water ice. Nonetheless, we similarly see that the 110 line is measured at significant quantities even at the smallest input energies, indicating that its cleavage site is particularly fragile.

In contrast, however, Zhang et al., also report that the three dominant

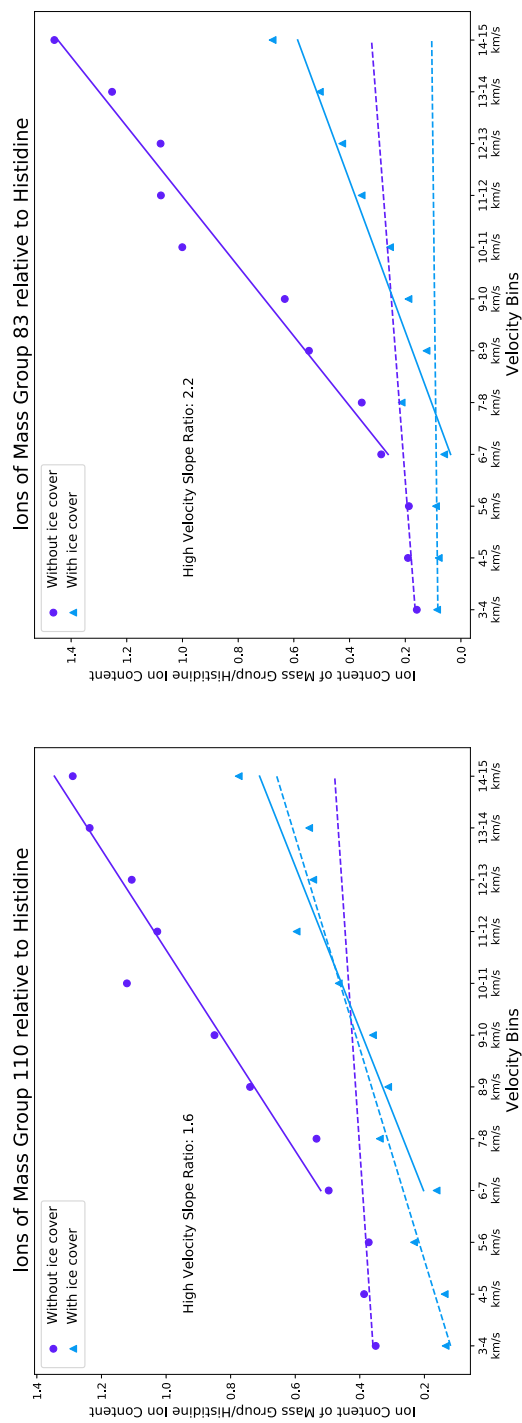


Figure 28: Ion content of mass groups 110 and 83 relative to the histidine parent molecule as functions of impact velocity. The dashed lines are fits to the first three velocity bins, and the solid lines are fits to the 6-7 km/s and higher velocity bins.

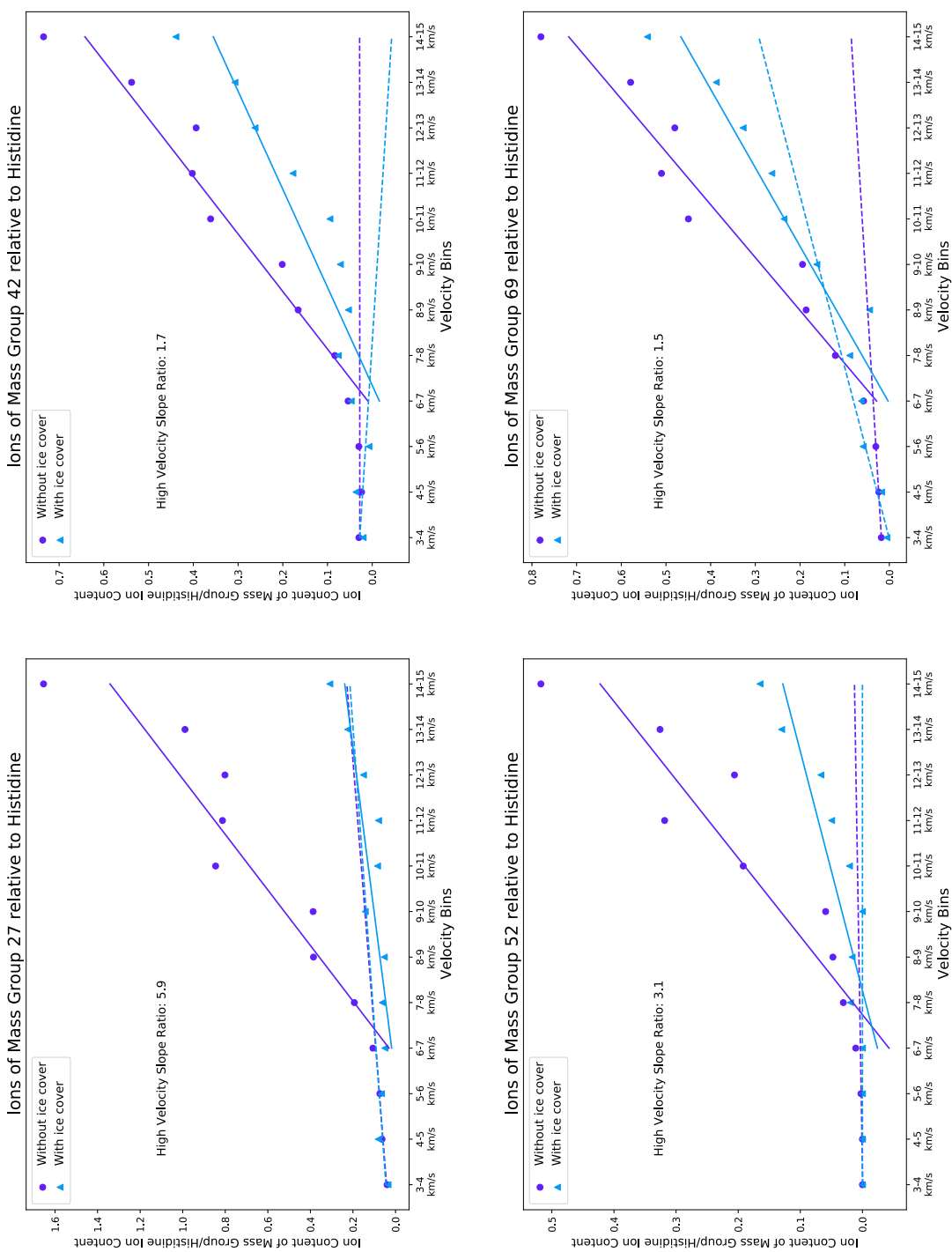


Figure 29: Ion content of mass groups 27, 42, 52, and 69 relative to the histidine parent molecule as functions of impact velocity. The dashed lines are fits to the first three velocity bins, and the solid lines are fits to the 6-7 km/s and higher velocity bins.

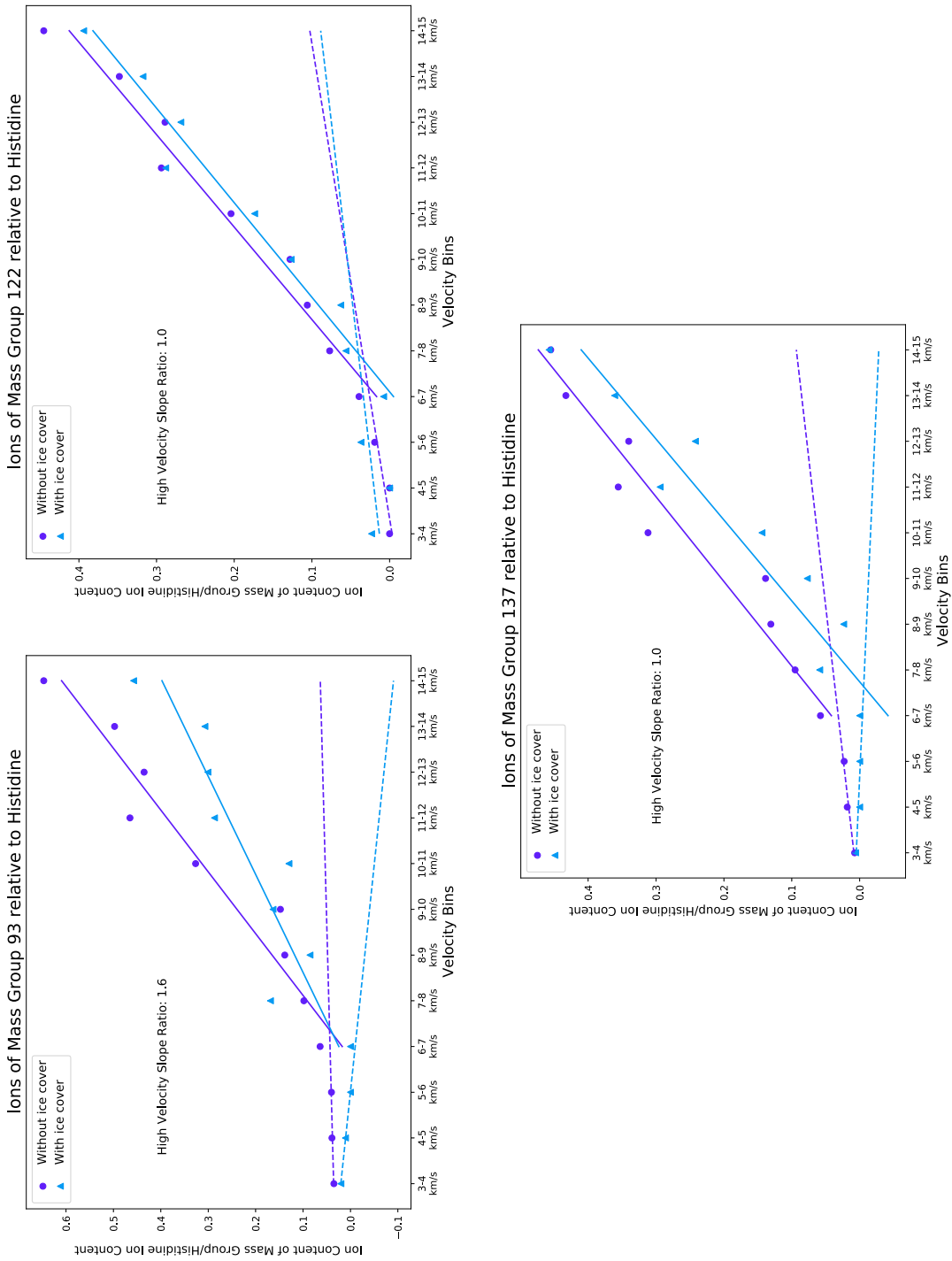


Figure 30: Ion content of mass groups 93, 122, and 137 relative to the histidine parent molecule as functions of impact velocity. The dashed lines are fits to the first three velocity bins, and the solid lines are fits to the 6-7 km/s and higher velocity bins.

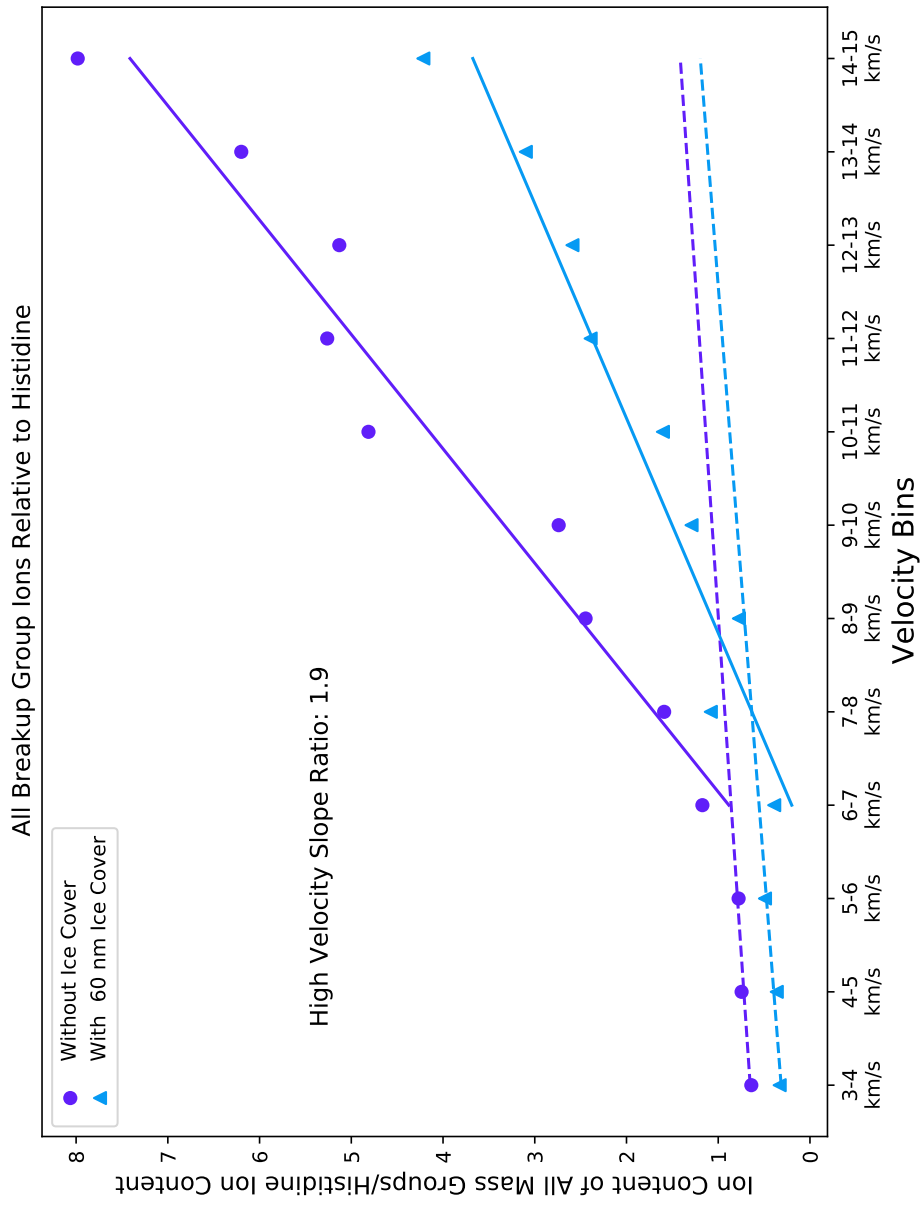


Figure 31: Ion content of all mass groups combined relative to the histidine parent molecule as functions of impact velocity. The dashed lines are fits to the first three velocity bins, and the solid lines are fits to the 6-7 km/s and higher velocity bins.

masses of mass group 83, masses 81, 82, and 83, are negligible until significant energy is supplied (half of their normalized collision energy), eventually becoming dominant over all other species at the top range of their studied collision energy [92]. We observe significant quantities of mass 83 at all velocities across both datasets. Because solutions were mixed on the morning of each experiment, typically about an hour before the system was cooled down to cryogenic temperatures, it is unlikely that significant preprocessing of the analytes occurred. Nonetheless, it is at least possible that some significant amount of these two dominant breakup products were already present in the surfaces before dust impact. It could also be that the freeze-drying process itself induces some amount of fragmentation. Regardless, even if that were the case, the primary results of water ice reducing fragmentation and fragmentation increasing beyond 7 km/s would not change.

Klenner et al., 2020 found that masses 18 and 30 were characteristic fragmentation products for all amino acids, and they noted that similar mass lines were observed in the CDA data [142]. While the mass 18 ( $\text{NH}_4$ ) line cannot be independently measured in the Experiment 2 data due to the mass aliasing of unprotonated water, it and mass 19 are clearly very strong features of the Experiment 1 data, indicating agreement with this water-beam result.

We also observe a strong line at mass 30. In the Experiment 1 data, this mass line is only sometimes the dominant mass line in mass group 27, which is alternately dominated by mass 27 (velocity bins 11-12 km/s and 14-15 km/s) and mass 28 (velocity bins 12-13 km/s, 7-8 km/s, 8-9 km/s, 9-10 km/s, and 10-11 km/s). Interestingly, however, mass 30, by a wide margin, is the dominant line for this mass group in all of the Experiment 2 data except 6-7 km/s, where it has only 10 % more ions than the mass 27 line.

Additional experiments could be performed with a higher resolution covering the 5-8 km/s range to determine if there is a sharp rise in fragmentation at a specific velocity. If there is such a well-defined critical velocity, it would also be interesting to determine if the ice-covered surface's critical velocity is slightly higher than the bare surface's. This could be done with the existing setup with more laboratory time dedicated to such an effort to collect more spectra over the relevant velocity ranges. In addition, a wider variety of species could be probed, in particular with other amino acids, fatty acids, or simple peptides, to investigate how consistent this result is across different organic molecules. Nonetheless, the result presented here that fragmentation is largely flat until some critical velocity between 6-7 km/s is both notable and consistent with the results from Klenner et al., 2020 [142]. Our results

for the bare histidine surface imply slightly stronger survival rates than the simulation results of Jaramillo-Botero et al., 2021, which predicted that bare amino acids would begin to fragment significantly beyond 5 km/s [139]. However, it is important to note that while this study looked at 10 different amino acids, histidine was not among them, and this study also defined the critical velocity as that which would produce even a single fragmentation product. In any case, we observe agreement between our laboratory results and that theoretical study's result that water ice encasement reduces fragmentation rates, and our observed critical velocity between 6 and 7 km/s is consistent with their optimal velocity range of 4-6 km/s for encased ice grains.

Drapatz and Michel analyzed iron micrometeoroid impacts into tungsten targets [148], determining that impactor surface ionization dominates low velocity impacts ( $< 10$  km/s) while bulk ionization dominates at high velocity ( $> 20$  km/s), and velocities in between exhibit a phase transition. In the low velocity regime, ionization occurs mainly at the surface, with little ionization occurring in the volume of the particle. They specifically report that for a typical iron dust particle, assuming a three percent alkali impurity, little or no iron content will be present in mass spectra below 7.3 km/s due to the limited energy available for ionization and the lower ionization potentials of the alkalis.

Mocker et. al. studied this phenomenon using TOF mass spectrometry of hypervelocity iron dust particle impacts into silver targets [149]. This study found good agreement with a phase transition between 10 and 20 km/s, and noted that iron detection occurs at velocities as low as 3.6 km/s, about half the value calculated by Drapatz and Michel [148, 149]. This discrepancy could be explained by a number of possibilities, most obviously that the assumption of three percent alkali impurity did not hold for the particles studied by Mocker et. al. Whatever the case, the value of 7.3 km/s calculated by Drapatz and Michel is rather striking in the context of the rise in fragmentation products beyond 7 km/s in our data for both the bare and covered histidine surfaces [148, 149].

Mocker et. al. describe target ionization as a complex mixture of both surface and bulk ionization [149]. Bulk ionization occurs at a small region immediately under the impact site, while acoustic shock waves may travel outward from the impact site in waves of ever-decreasing strength as the distance increases. It is important to note this second feature in the context of our results. When impact ionization TOF spectrometers on flyby spacecraft study icy ocean worlds, they do so by studying the impact plume of icy dust

grains impacting a large metallic target surface. In our data, the reciprocal process is studied, with metallic dust grains striking a large ice surface. Because acoustic waves may gently liberate target ions away from the impact site, but there is no corresponding process for impactor ions, there is a different avenue for ion production between the reciprocal processes. This presents an important distinction between our data and actual spaceflight data.

Because of the space limitations of the dust source in the dust accelerator's pelletron high voltage source, there is currently no way to generate and accelerate icy dust grains in the same manner as the iron dust particles described in this experiment. There are ongoing attempts to accelerate ice grains to flyby relevant velocities of several km/s using alternative acceleration methods, but these are not yet available. Such accelerators will be able to more accurately replicate actual flight data by accelerating actual icy dust grains into actual instruments, be they flight hardware or engineering models, thus eliminating the acoustic wave as a confounding factor.

This also highlights the importance of the true airbrush method as compared to the flash frozen method used here. Because the surface of a true airbrushed ice is composed of flash-frozen droplets with diameters on the order of  $10\ \mu\text{m}$ , the dynamics of the impact stress propagation will be different. Presumably, the surface topology of  $10\ \mu\text{m}$  droplets will dampen surface acoustic waves over shorter distance scales than the largely flat freeze-dried surfaces, perhaps limiting them to scale length not significantly higher than the droplet diameter itself. Future work should determine if and how true airbrush surfaces differ from the freeze-dried samples in fragmentation rates, as this may illuminate differences between metal dust impacts into freeze-dried surfaces and actual ice grain impact into flyby instruments.

However, even if acoustic waves or other confounding factors resulting from the reciprocal nature of our experiments compared to flight data are present, the striking increase in fragmentation rates beyond 7 km/s observed in both of our experiments indicates that some critical threshold occurs near this velocity. Thus, the major result of a suggested critical flyby velocity at 7 km/s remains unchanged. Additionally, our other conclusions, namely that breakup products are predictable and may be used to help identify the parent molecule even in the event of breakup and that water ice layers reduce fragmentation rates, likewise still stand.

## 5 Measurement of D-H Ratios

### 5.1 Importance

Isotopic ratios have long been used to provide indirect measurements of a wide variety of physical phenomena. The most famous is of course the use of carbon-14 to date carbon-bearing terrestrial biotic residue [150, 151]. Such dating makes use of the fact that carbon-14 is radioactive with a half-life of about 5700 years [152], but cosmic rays striking the earth upper atmosphere constantly produce new  $^{14}\text{C}$ , refreshing it in organic materials interacting with the atmosphere [153].

Deuterium (D), on the other hand, being an isotope of simple hydrogen (H) or protium, is highly stable. While it is produced in stars as a result of the proton-proton chain fusion reaction process, it is destroyed at a far faster rate through conversion to helium and heavier elements, meaning that stars present an active sink rather than source of deuterium in the cosmos. Thus virtually all extant deuterium was produced during big bang nucleosynthesis [154, 155, 156, 157]. It is believed that immediately following the big bang, the D/H ratio was approximately 25 parts per million (ppm), or  $2.5 \times 10^{-5}$ , but because of gradual losses due to star formation, the early sun had an abundance of about 21 ppm and the modern local interstellar medium has a current D/H abundance of about 16 ppm [157, 158, 159].

However, in cold systems, typically below 50 K, there is a preferential creation and preservation of HDO ice relative to  $\text{H}_2\text{O}$  water ice [160]. The reasons for this are complex, but they stem from the fact that in very cold ( $\sim 10\text{K}$ ) molecular gas, as might be found in stellar formation clouds, the reaction  $\text{H}_3^+ + \text{HD} \longrightarrow \text{H}_2\text{D}^+ + \text{H}_2$  dominates over its inverse reaction,  $\text{H}_2\text{D}^+ + \text{H}_2 \longrightarrow \text{H}_3^+ + \text{HD}$ . This is because the higher mass of  $\text{H}_2\text{D}^+$  relative to  $\text{H}_3^+$  creates a small but important activation barrier in the latter [161]. In other words, in very cold gasses, the ratio of  $\text{H}_2\text{D}^+/\text{H}_3^+$  is significantly higher than the base D/H ratio. This is important because the  $\text{H}_3^+$  ion and its isotopologues are among the most abundant molecular ions of stellar formation clouds, and ion interactions dominate over neutral-neutral interactions due to activation energy barriers [161].

Water, meanwhile, is typically formed in the early solar system when cosmic dust grains capture gaseous H, D, and O on their surfaces [161]. But again, as interactions in these clouds are dominated by ions rather than neutrals, and the most abundant source of H or D, the  $\text{H}_3^+$  ion, is en-

riched with D, water ice formed on grains is itself preferentially enriched with D. Thus, when early ice in a proto-solar system is formed, it forms with a significantly higher abundance of D than the local gas cloud D/H ratio [160, 161, 162, 163, 164]. In particular, these ices may develop D/H ratios ranging from .001 to .01 (or 1000 to 10,000 ppm) [146, 160], several orders of magnitude higher than the proto-solar cloud at  $2.1 \times 10^{-4}$  and the modern interstellar medium at  $1.6 \times 10^{-4}$  [157, 158, 159].

Such enriched ices will largely retain their enhanced D/H abundances at cold temperatures due to low isotopic exchanges in cold conditions [146, 160]. However, as the solar system forms and the parent star heats up, temperatures in the inner regions begin to rise dramatically. As this occurs, water ice may melt or sublimate, and the enriched ice will begin to equilibrate with background H, eventually returning it to the overall D/H ratio [146, 160].

The early proto-planetary disc may also have equilibrated due to viscous mixing of material from the inner and outer discs. Yang et al. modelled isotopic exchanges in the early solar system, producing the plot shown in Fig. 32, reprinted with permission [146]. This study found that within 0.1 Myr of the formation of the sun, the D/H ratio of water and ice out to 100 AU had largely equilibrated to the solar D/H abundance, but subsequent gravitational attraction of material from the far outer cloud restored higher D/H ratios in the middle proto-planetary disc by about 1 Myr. Interestingly, this infall of far outer ice does not affect the extremities of the outer planetary disc, meaning that maximum D/H ratios of ice in the early solar system (out to 1 Myr), were modelled to be between 2 and 50 AU [146].

Clark et al. studied the D/H ratios of the Saturnian B-Ring and moons Enceladus, Rhea, Hyperion, Iapetus, and Phoebe. This study used data from the Cassini spacecraft's Visual and Infrared Mapping Spectrometer (VIMS) [165] and combined it with other published work to produce Fig. 33, reprinted with permission from [159], which shows the measured D/H ratio of a wide variety of objects in the solar system. In particular, the measurement for Phoebe's D/H ratio is  $7.6 \pm 1.7$  times that the average of other objects in the Saturn system, strongly suggesting that it formed in a different environment than its modern neighbors [159].

Another item of note from Fig. 33 is that the Jovian system is almost entirely missing. Only a single high-error bar measurement of Callisto is present from the Near Infrared Mapping Spectrometer (NIMS) [166] instrument on the Galileo spacecraft [159]. While there have been some measurements of the atmospheres of Uranus and Neptune [167, 168], their moons are also

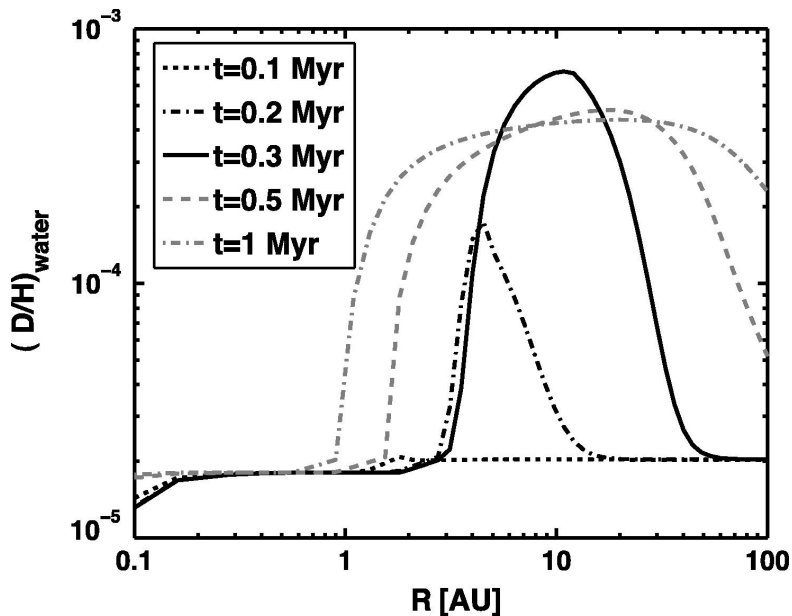


Figure 32: Plot of the modelled D/H ratio of water in the early planetary disc. Reprinted with permission from [146].

missing.

Lastly, while there have been a number of measurements of cometary D/H ratios, these have overwhelmingly relied on measurements of the vapor being ejected from the parent body [159, 169]. However, there is experimental and theoretical evidence that the D/H ratio of sublimating water differs from the bulk ratio in the nucleus. This has important implications for the ongoing debate about to what extent the Earth’s ocean water and other volatiles were accreted from impacting comets [158, 169, 170, 171, 172, 173, 174, 175].

All this is to say that the D/H ratio of water, particularly of ice in the outer solar system, has a rich astrophysical history, and with proper accounting for post-formation isotopic processing of H and D on planetary bodies, measurements of the D/H ratio can constrain the time and locations that planetary bodies formed in the solar system. This has made the D/H ratio an important metric for investigations into the formation and evolution of solar system bodies, including the origin of earth’s oceans [158, 159, 170, 176, 177], and measurements of the ratio at various solar system bodies can inform these models as well as constrain a variety of other geophysical phenomena [e.g.,



178]. As such, that there is great value in providing new measurements of the D/H ratio of celestial ices, especially in the outer solar system.

### 5.1.1 Impact Ionization Time of Flight Measurements

The majority of observations of outer solar system D/H ratios have come from infrared spectrometers [159], and only two have come from mass spectrometers. The ESA spacecraft Giotto's ion mass spectrometer measured the Oort Cloud Comet Halley's D/H ratio in 1986, although the results were not published until 1995 [179, 180]. The Rosetta spacecraft used its Rosetta Orbiter Spectrometer for Ion and Neutral Analysis (ROSINA) to measure the D/H ratio of outgassing vapor from 67P/Churyumov-Gerasimenko [169, 181]. This particular result was especially interesting, not only for being the sole use of mass spectrometry to measure the D/H of a JFC, but because it revealed a particularly high D/H ratio of about 530 ppm [169]. Whereas the rest of the JFCs have had D/H ratios at or slightly higher than the terrestrial ocean at 155 ppm [158, 159], 67P/Churyumov-Gerasimenko's D/H ratio was measured at  $530 \pm 7$  ppm, over three times the terrestrial value [169].

In particular, there is a complete lack of impact ionization TOF mass spectrometry data in these measurements. While the Cassini VIMS was able to measure D/H ratios with infrared spectrometry, the Cassini spacecraft's dust instrument, the CDA, was unable to provide an independent measurement [182]. While this instrument successfully studied the composition of dust grains from the surfaces of the Saturnian satellites and ring systems as well as the content of the Enceladus plumes [41, 61, 71, 75], it operated only in the positive ion detection mode. The mass resolution required to separate  $D^+$  and  $H_2^+$  cation lines (both at  $\sim 2amu$  far exceeded the capabilities of the instrument, and thus it was unable to resolve the D-H ratios for any of the planetary bodies it studied [182]. Similarly, the Giotto Particle Impact Analyzer and the PUMA 1 and 2 instruments aboard the Vega 1 and 2 spacecraft were unable to provide independent D/H measurements of comet Halley [72, 73].

However, because the  $H_2^-$  anion is meta-stable with a lifetime of only  $8.2 \pm 1.5 \mu s$  (meaning it is effectively non-existent outside of laboratory settings) [183, 184], even impact ionization TOF instruments with modest mass resolution could in principle be able to independently measure  $D^-$  and  $H^-$  in icy dust grains using a negative ion detection mode. This would mean that upcoming instruments such as SUDA [185] on the Europa Clipper

or proposed instruments such as the ENIJA on the ELF mission proposal [82, 84] could hypothetically measure the D-H ratio of icy dust grains from the surfaces of any planetary body they fly by. This would provide measurements independent from existing data, most notably from Saturnian satellites where measurements are provided from Cassini VIMS, but also measurements for bodies that do not yet have accurate D-H measurements, such as the Galilean moons [159]. The proposed FOSSIL instrument could potentially measure the bulk D/H ratios of bulk JFCs and OOCs [17], and dust analyzers sent through cometary tails or past moons of the ice giants could also potentially provide D/H ratios for those objects.

However, as no measurements have been made to date of D/H ratios using impact ionization TOF mass spectrometers, laboratory experiments must be performed to assess whether this approach is feasible. Here we present proof of concept measurements of the D/H ratio in water ice using impact ionization negative ion mass spectrometry.

## 5.2 Experimental Setup

To study the ability of impact ionization TOF instruments to measure the D/H ratio of water ice, a series of experiments were performed using the vapor deposition target. Mixtures of highly purified deuterium oxide ( $D_2O$ ) with high purity water were prepared in various concentrations and then deposited as ice onto the gold-coated copper mirror target system. Aluminum dust particles were impacted onto the surface at velocities below 50 km/s and anion TOF data was taken on each sample. Spectra were then summed, and the relative ion content of the deuterium and hydrogen mass lines were compared.

JT Baker 6906-02 18 MOhm water was sourced from Capitol Scientific and used to supply  $H_2O$  [145], and Sigma Aldrich 151882 ultra high purity deuterium oxide with D/H > 99.9% was used to supply  $D_2O$  [186].

Five experiments were performed, each on separate days, to study a total of three different mixtures of  $D_2O$  and  $H_2O$ . One experiment each was performed on a  $D_2O$ -dominated solution with a D/H ratio of approximately 4.2 and a mid-level solution with a D/H ratio of approximately 0.17. Finally, three experiments were performed on a single low-concentration mixture with a D/H ratio of approximately 0.034.

An SRS RGA 100 residual gas analyzer (RGA) was used to measure the partial pressures of each species as they were introduced into the chamber.

This device uses a quadrupole mass spectrometer to provide partial pressure measurements of individual ion species down to  $10^{-11}$  Torr [187]. By integrating the time-varying partial pressure of each species during the ice deposition period, the relative contributions of each ion mass can be measured, thus determining the deposited ice's composition. The RGA measurements from the D<sub>2</sub>O-dominated solution are shown in Fig. 34.

For the high concentration experiment, ice was grown over a period of 100 minutes at a vacuum pressure of  $1.11\text{-}1.30\cdot 10^{-5}$  Torr, producing a surface about  $9.5\ \mu$  thick. Subsequent experiments were all grown for 128 minutes or longer, producing surfaces  $> 12\mu$ . The partial pressure of each measured species is plotted with respect to time. In this first dataset, only masses 2, 3, 18, 20, 28, and 32 were recorded on the RGA during deposition, but following experiments additionally recorded masses 1, 3, 19, and 21. The mass line identifications are shown in Table 3. In the first  $\sim 1500$  seconds, various spikes are observed, likely from small virtual leaks escaping into the chamber. The target was being actively cooled by the LN2 at this time, resulting in gradual freeze out of the water and D2O. Once the leak valve blocking the D<sub>2</sub>O/H<sub>2</sub>O mixture was opened (at  $t \approx 1500\text{s}$ ), the pressures rise dramatically, plateauing and gradually decaying once the valve was left in a single position. Occasionally this decay would lower the pressure below the defined experimental range, and the valve would be gently turned open to allow more vapor into the chamber. This is the cause of the slight rise and fall in the various pressure lines, and why they correlate across species.

Each mass line in this RGA data was integrated to determine a relative abundance of the corresponding species during ice deposition. The bounds of integration are shown with the dashed vertical lines, although it should be noted that carrying out the integration over the whole field resulted only in minor variation of the species' relative concentrations in the 4<sup>th</sup> or 5<sup>th</sup> significant digit. While there are a number of contributing ions to several of the recorded mass lines, the dominant species within mass 20 and mass 18 are D<sub>2</sub>O and H<sub>2</sub>O, respectively. Thus, the number of D<sub>2</sub>O molecules is taken to be proportional to the integral of the mass 20 line, and the number of H<sub>2</sub>O molecules is taken to be proportional to the integral of the mass 18 line. As these two species are the fundamental sources of both H and D in the solution, these two mass lines are used as the measure the D/H ratio, ignoring other isotopologues. Because each D<sub>2</sub>O molecule supplies two deuterium atoms and each H<sub>2</sub>O molecule supplies two hydrogen atoms, the D/H ratio is then calculated simply as the integral of the mass 20 line divided

3-16-20 Experiment with D:H = 4.188

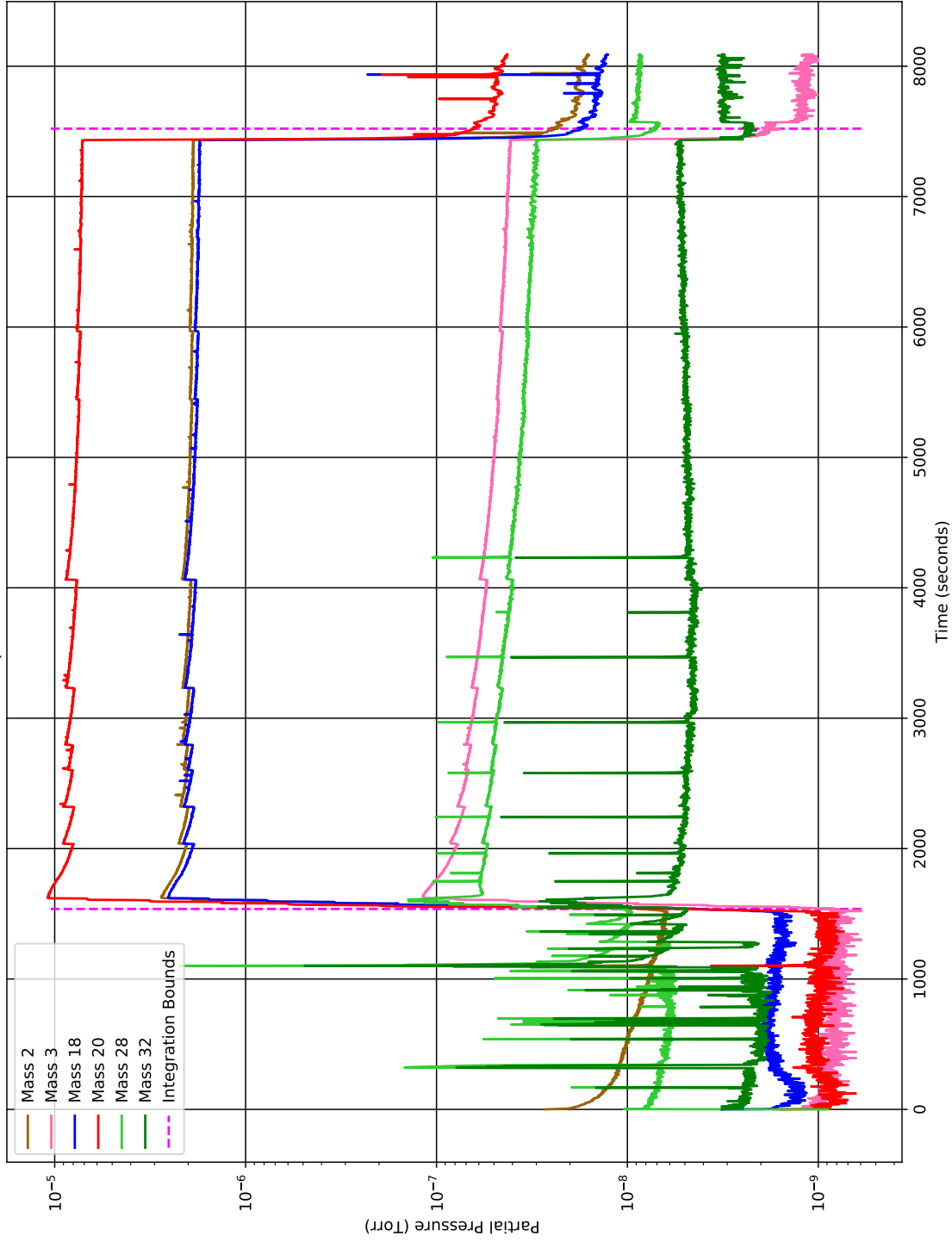


Figure 34: RGA partial pressure vs time plot for the  $D_2O$ -dominated solution with  $D/H = 4.2$ . The leak valve supplying the  $D_2O/H_2O$  mixture is opened at  $t \approx 1500s$  and closed at  $t \approx 7500s$ . Masses are described in Table 3.

Mass (AMU)	Identification	Mass (AMU)	Identification
<b>1</b>	H	<b>19</b>	(H <sub>2</sub> O)H, HDO
<b>2</b>	H <sub>2</sub> , D	<b>20</b>	D <sub>2</sub> O, (H <sub>2</sub> O)D, (HDO)H
<b>3</b>	HD	<b>21</b>	(D <sub>2</sub> O)H, (HDO)D
<b>4</b>	D <sub>2</sub>	<b>28</b>	N <sub>2</sub>
<b>18</b>	H <sub>2</sub> O, OD	<b>32</b>	O <sub>2</sub>

Table 3: A table of the ion masses recorded by the RGA during ice growth.

by the integral of the mass 18 line. Further discussion of this choice can be found in Sec. 5.3.

For the impact ionization TOF system, there is no well-defined time zero as may be found in laser ablation TOF systems [e.g., 141, 146]. Thus, pre-processing of the data was necessary to align the spectra with one another. The oscilloscope that records data was set to trigger off of the MCP signal, typically triggering on the electron peak in negative ion mode. However, while many spectra exhibit clean, crisp lines, most feature much broader line shapes, meaning that the scope doesn't consistently trigger at the same time in each spectrum.

To create a commonly defined time frame for each spectrum, exponentially modified Gaussians (EMGs) of the form

$$a_0 \frac{\lambda}{2} e^{\frac{\lambda}{2}(2\mu + \lambda\sigma^2 - 2t)} \cdot \operatorname{erfc}\left(\frac{\mu + \lambda\sigma^2 - t}{\sqrt{2}\sigma}\right) \quad (6)$$

were fitted to the electron mass lines. In this expression  $a_0$  is the amplitude,  $\lambda$  is an exponential decay term,  $\sigma^2$  is the variance,  $\mu$  is the mean, and  $\operatorname{erfc}$  is the complementary error function. The mean value  $\mu$  of the fitted EMG was then taken as a common start time for each spectrum.

The data is not highly uniform, exhibiting a wide variety of observed line widths and SNRs across the spectra. For this reason, during pre-processing the spectra were assigned to one of four qualitative groups based on data quality. Class 1 spectra exhibit clear, easily identifiable D and H lines without significant noise around them. Even as a class, there is significant variation among spectra, as some show crisp, thin mass lines, while others have much broader peaks, as shown in the four exemplar plots in Fig. 35. These plots show the region of the spectrum over which the D

and H are expected to appear, with pink dotted lines marking the hydrogen ion zone and the green dotted lines showing the deuterium ion zone. Because spectra were eventually added in the time domain, these plots are also given in the time domain. A wider ion region in the mass domain of a Class 1 spectra is shown in Fig. 36.

Class 2 spectra also have easily identifiable D and/or H lines, but are not of as high a quality as class 1 spectra. These spectra may have significant noise around the D and H lines, or the ions from these lines may be spread out and discrete, as opposed to clearly defined, continuous curves.

Class 3 spectra show what is clearly ion content in the expected D and H regions, but have very significant noise and/or stray ions around them, and they are often composed of very discretized peaks. The combination of these two features mean that it is often difficult to separate ion content and noise from one another. They also sometimes have very broad mass lines that extend beyond the typical zones found in class 1 and class 2 spectra. Exemplars of class 3 spectra are shown in Fig. 38.

In addition to class 1-3 spectra, there are a class of spectra that have been discarded for a variety of reasons. They most commonly were electron-dominated, and had very small SNR for other mass lines. However, as only class 1-3 spectra were used in the analysis, only they are discussed here. A few examples of discarded spectra are shown in the supplemental Fig. 50.

Once the spectra were assigned bins, they were co-added in the time domain with a common time ‘zero’ centered on the EMG  $\mu$ . Centering the spectra on either the D or H peaks would necessarily enhance that peak at the expense of the other. By centering on the electron peak, any small shot-to-shot variation in the x-axis stretch parameter would average out over the two lines equally, and would thus not favor one over the other. We also emphasize that time-domain spectrum alignment errors or effects from stretch-factor variations are minimized at low mass numbers (such as those for D and H) relative to heavier species.

After adding in the time domain, EMGs were fitted to the mass peaks at 1 and 2 AMU. The integral of these fitted lines then gives the calculated TOF relative ion yield of H and D respectively, and the D/H ratio is calculated as the deuterium yield divided by the hydrogen yield.

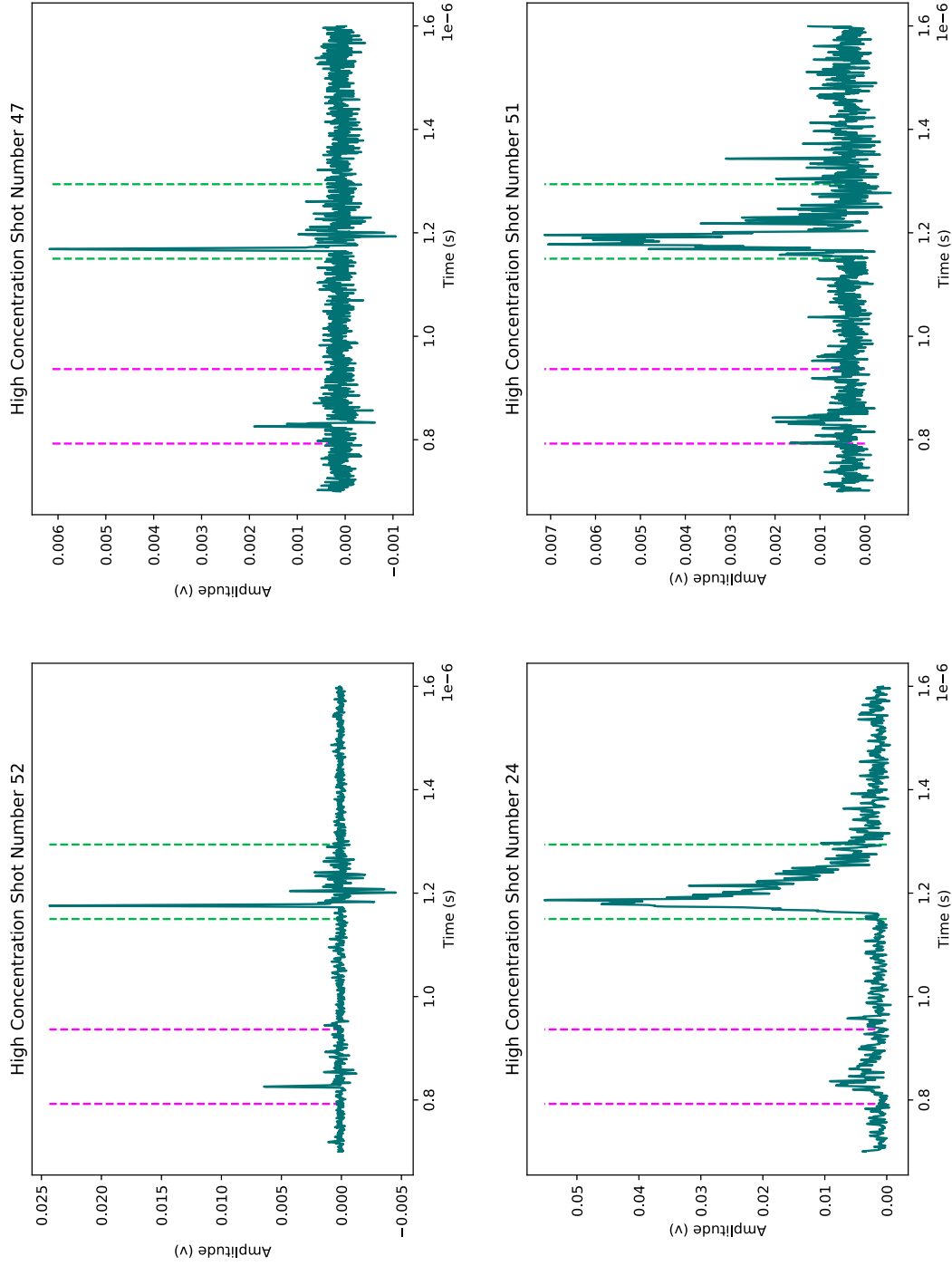


Figure 35: The D and H ion regions of individual class 1 spectra exemplars, which exhibit easy to identify hydrogen and deuterium mass lines without excessive noise around them. These spectra are all taken from the high concentration dataset, where the D/H ratio was measured by the RGA to be 4.2. The hydrogen ion region is bracketed by pink lines, and the deuterium region is bracketed by green lines.

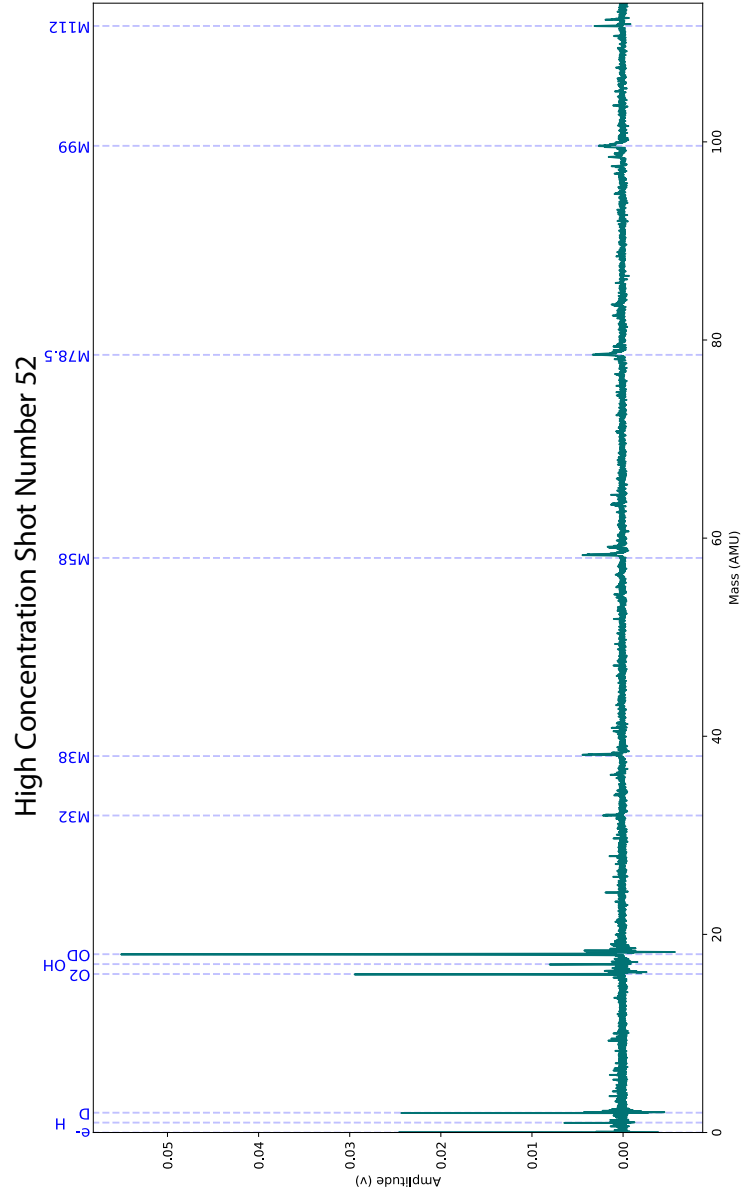


Figure 36: An expanded view of an individual class 1 exemplar spectrum.

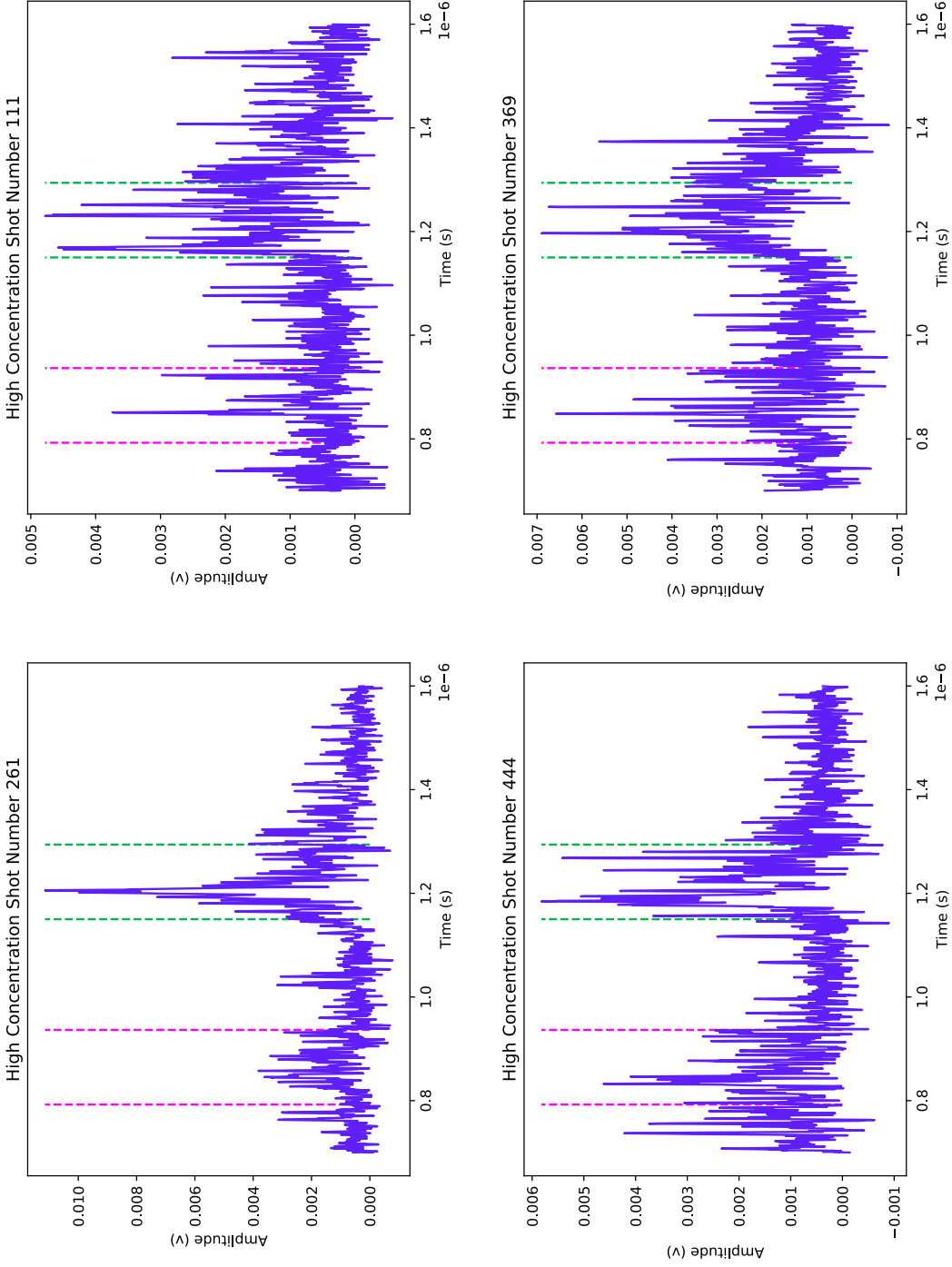


Figure 37: The D-H ion regions of individual class 2 spectra exemplars, which sometimes have significant noise around the D and H lines. Ions may also be spread out in discretized peaks rather than continuous curves. The hydrogen ion region is bracketed by pink lines, and the deuterium region is bracketed by green lines.

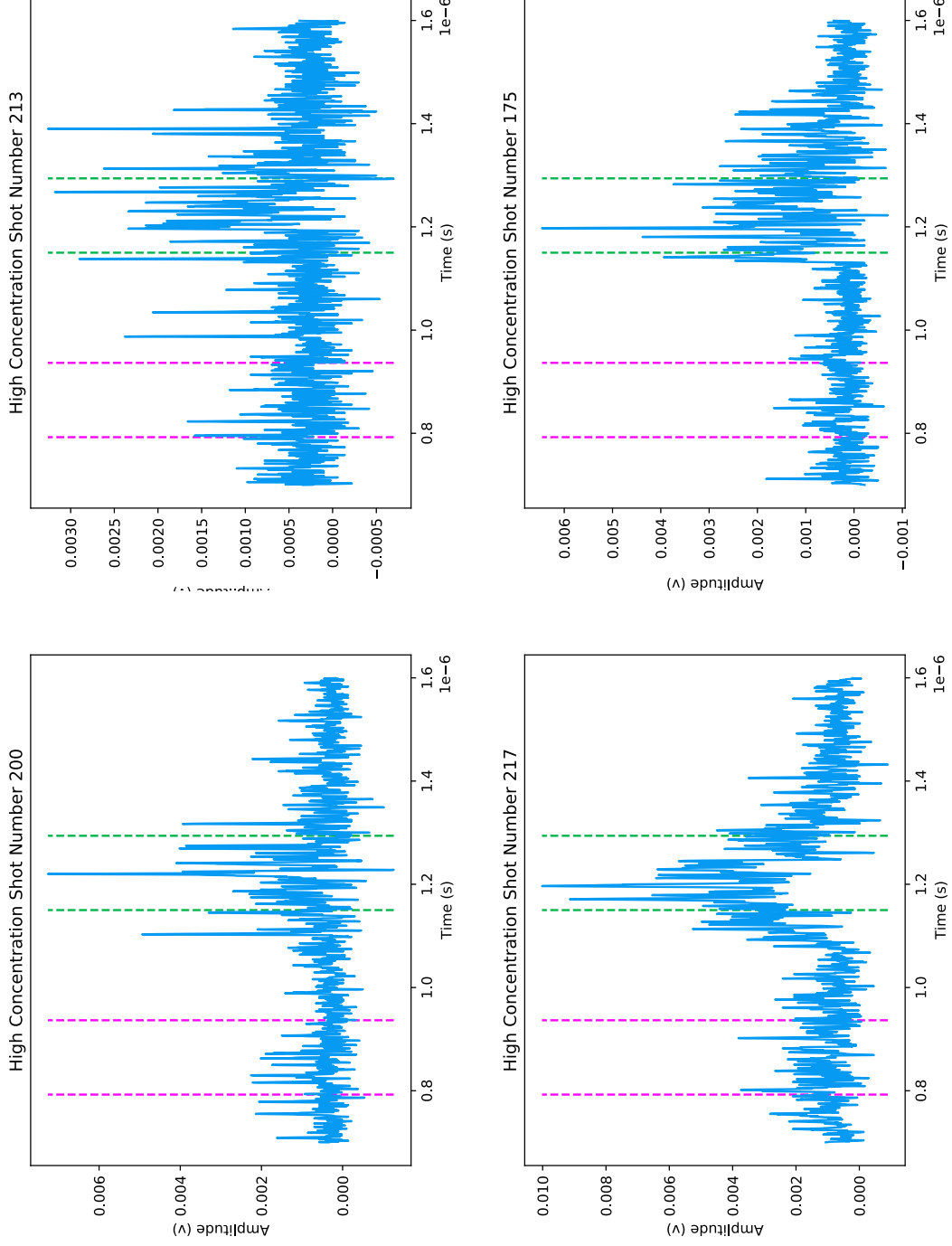


Figure 38: The D-H ion regions of class 3 spectra exemplars. The hydrogen ion region is bracketed by pink lines, and the deuterium region is bracketed by green lines.

Deposition Vapor Ion Content of Mass Lines Relative to Mass 18					
Mass Line (AMU)	High Concentration Experiment	Mid Concentration Experiment	Low Concentration Experiment 1	Low Concentration Experiment 2	Low Concentration Experiment 3
1		0.0024	0.1405	0.0037	0.0029
2	1.0610	0.1641	0.0717	0.1433	0.1022
3	0.0305	0.0082	0.0036	0.0181	0.0135
4		0.0012	0.0004	0.0014	0.0010
18	1	1	1	1	1
19		0.7312	0.3283	0.3324	0.3422
20	4.1876	0.1715	0.0331	0.0333	0.0351
21		0.0031	0.0012	0.0012	0.0010
28	0.0002	0.0039	0.0028	0.0020	0.0019
32	0.0028	0.0036	0.0025	0.0016	0.0019

Table 4: A table of the measured ion content relative to mass 18 ions for each mass line in the RGA scans. Since the RGA D/H ratio is calculated as the mass 20 line ion content relative to the mass 18 ion content, this row is highlighted in green.

### 5.3 Results

The RGA scan taken for the mid-level D/H ratio of 0.17 is shown in Fig. 39, and the third and final RGA scan from the low concentration datasets with D/H = 0.035 is shown in Fig. 40. The other two RGA scans for this sample (taken on different days) are shown in the supplemental Figs 48 and 49. A table of ion content for each line relative to the mass 18 H<sub>2</sub>O line is given in Table 4.

Because the spectra were binned into 3 different classes, each class can be summed independently or together. The D and H regions of the summed spectra for the high concentration data are shown in Fig. 41, with separate plots for the complete set of all summed spectra and the individual classes.

The D and H regions for the mid concentration data are shown in Fig. 42. The low concentration data spanned three experiments, and the total summed D and H regions are shown in Fig. 43. Results from individual days are shown in the Supplemental Figs. 51 through 53. For these experiments, class 2 and class 3 data were combined during the binning process, and so there is no additional plot showing separate class 3 data for this set.

The numerical results are summarized in Table 5. The high concentration water ice's D/H ratio as measured by all combined classes of spectra, D/H = 4.5, is within 7.1% of the value calculated by the RGA, D/H = 4.2. Similarly,

12-30-20 Experiment with D:H = 0.171

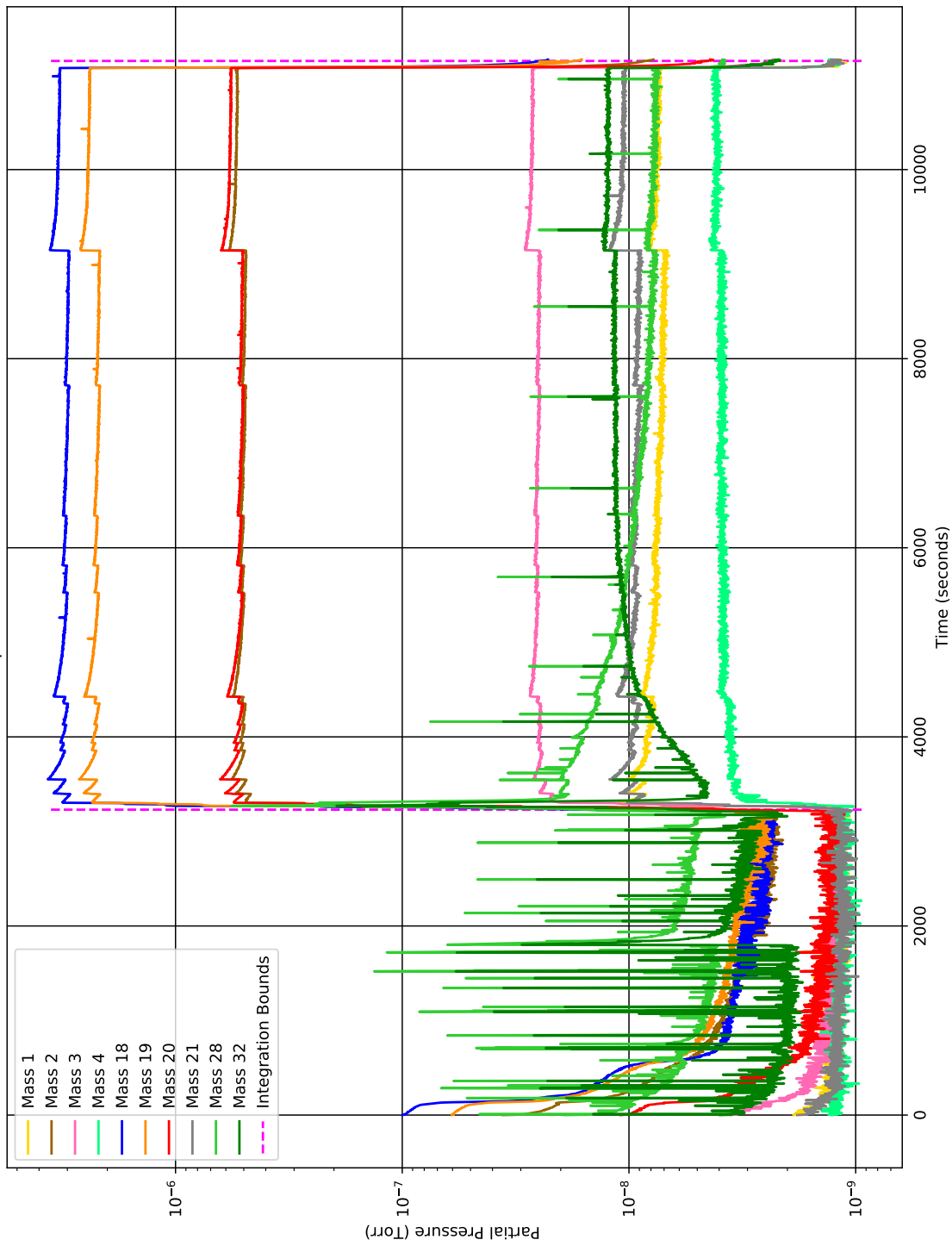


Figure 39: RGA partial pressure vs time plot for the mid level solution with D/H measured as 0.17. Masses are described in Table 3.

12-29-20 Experiment with D:H = 0.035

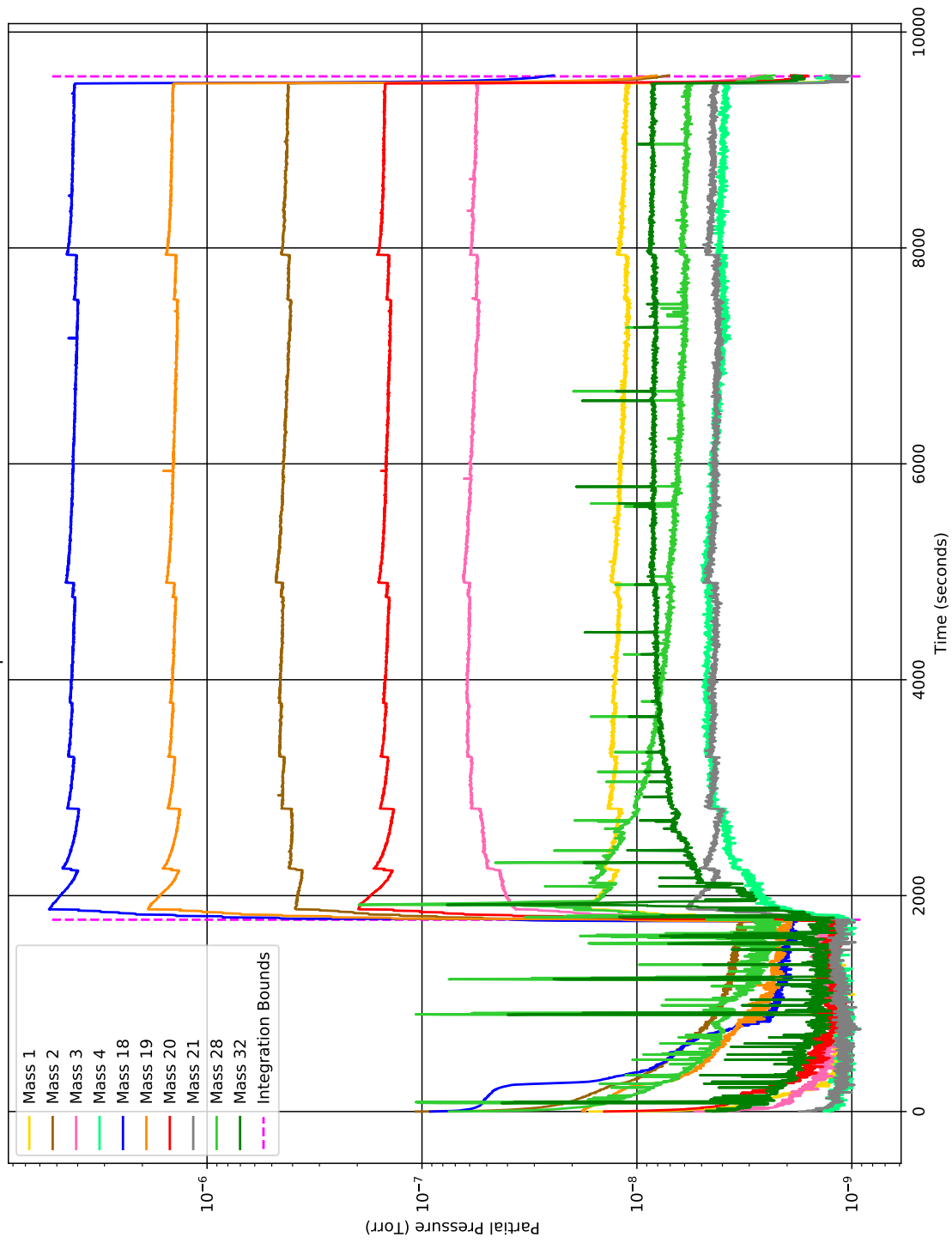


Figure 40: RGA partial pressure vs time plot for the third and final low level solution with D/H measured to be 0.035. Masses are described in Table 3.

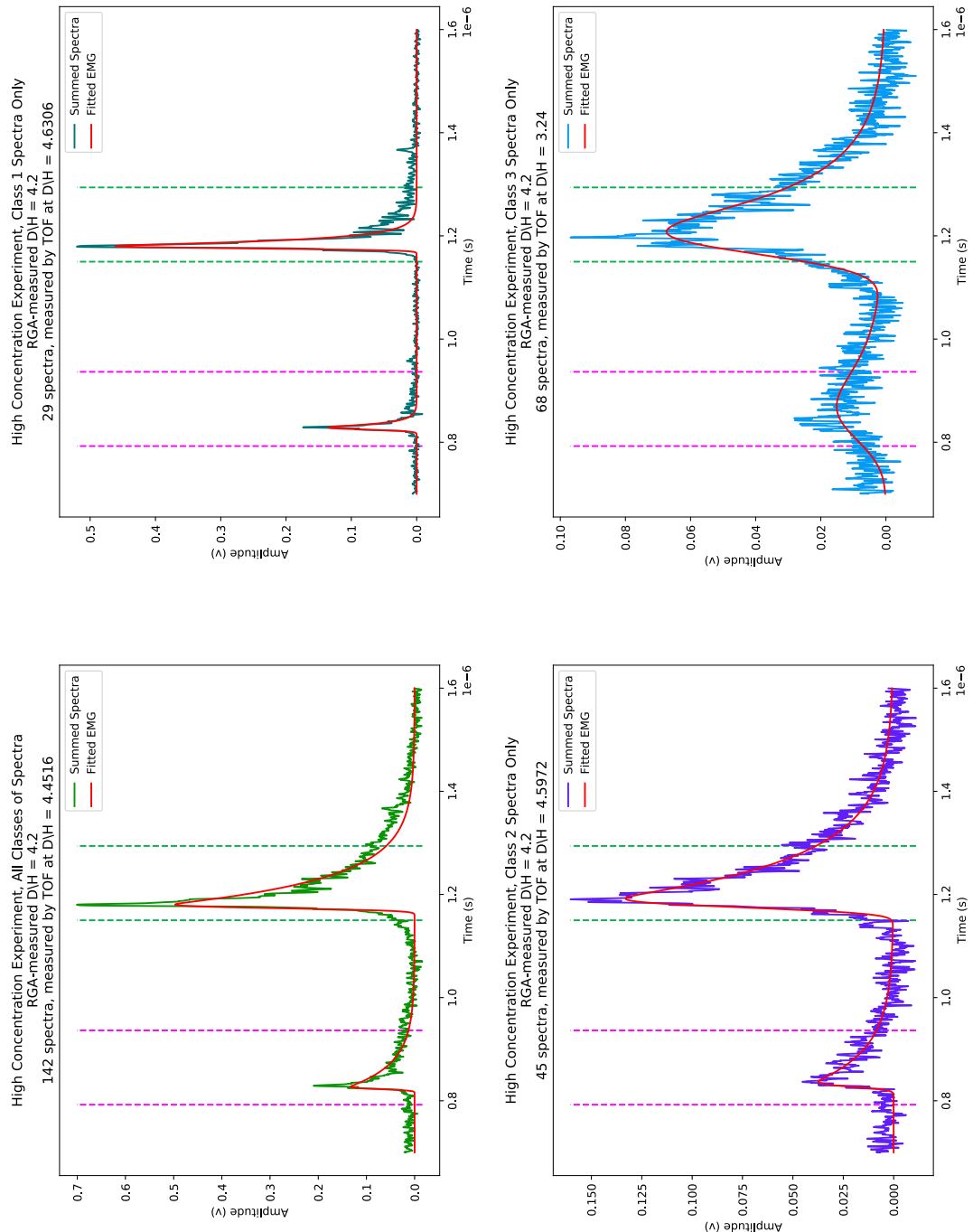


Figure 41: D and H regions of the summed spectra of the high concentration experiment with  $D/H = 4.2$ , separated by spectra class.

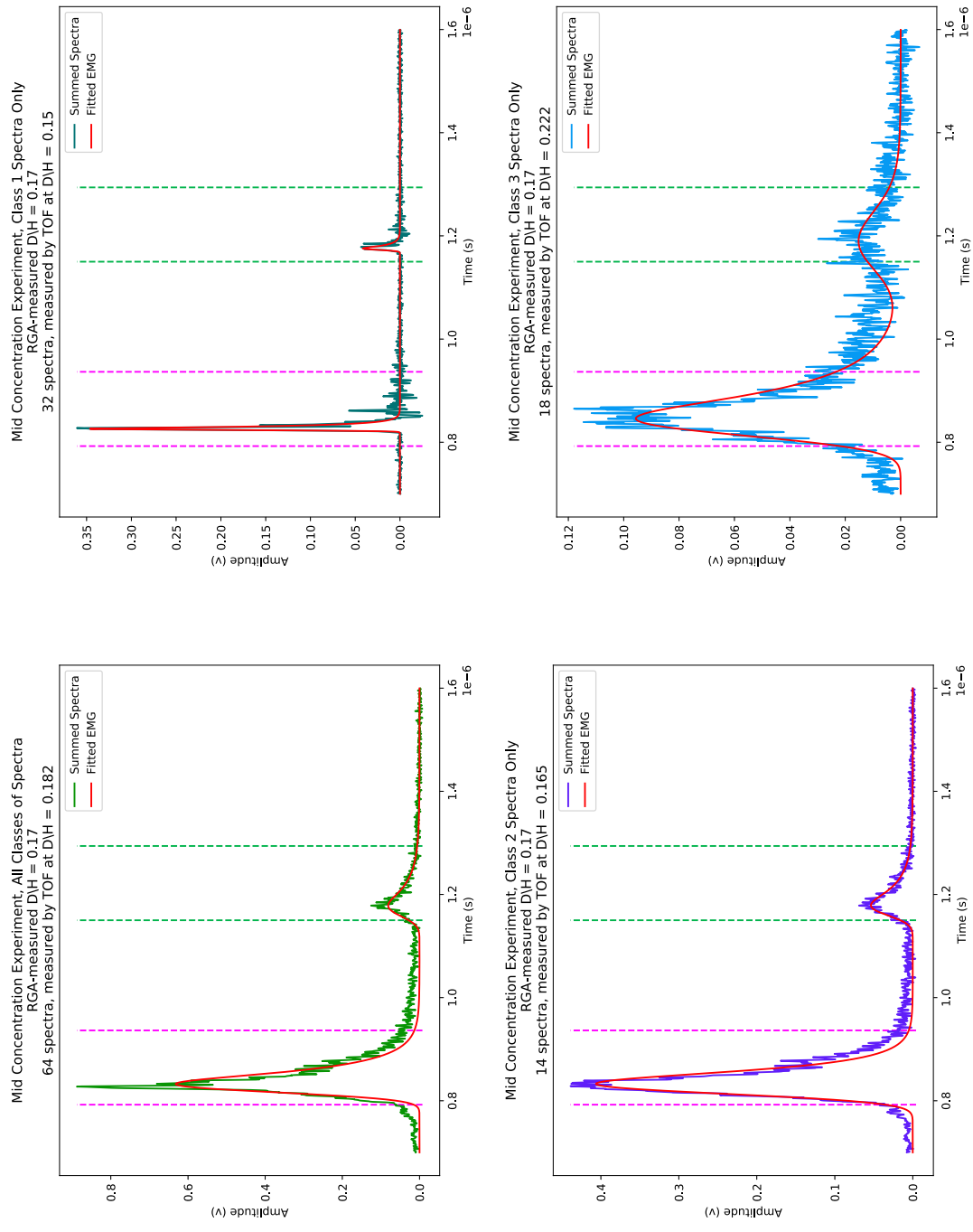


Figure 42: D and H regions of the summed spectra for the mid concentration experiment with  $D/H = 0.17$ , separated by spectra class.

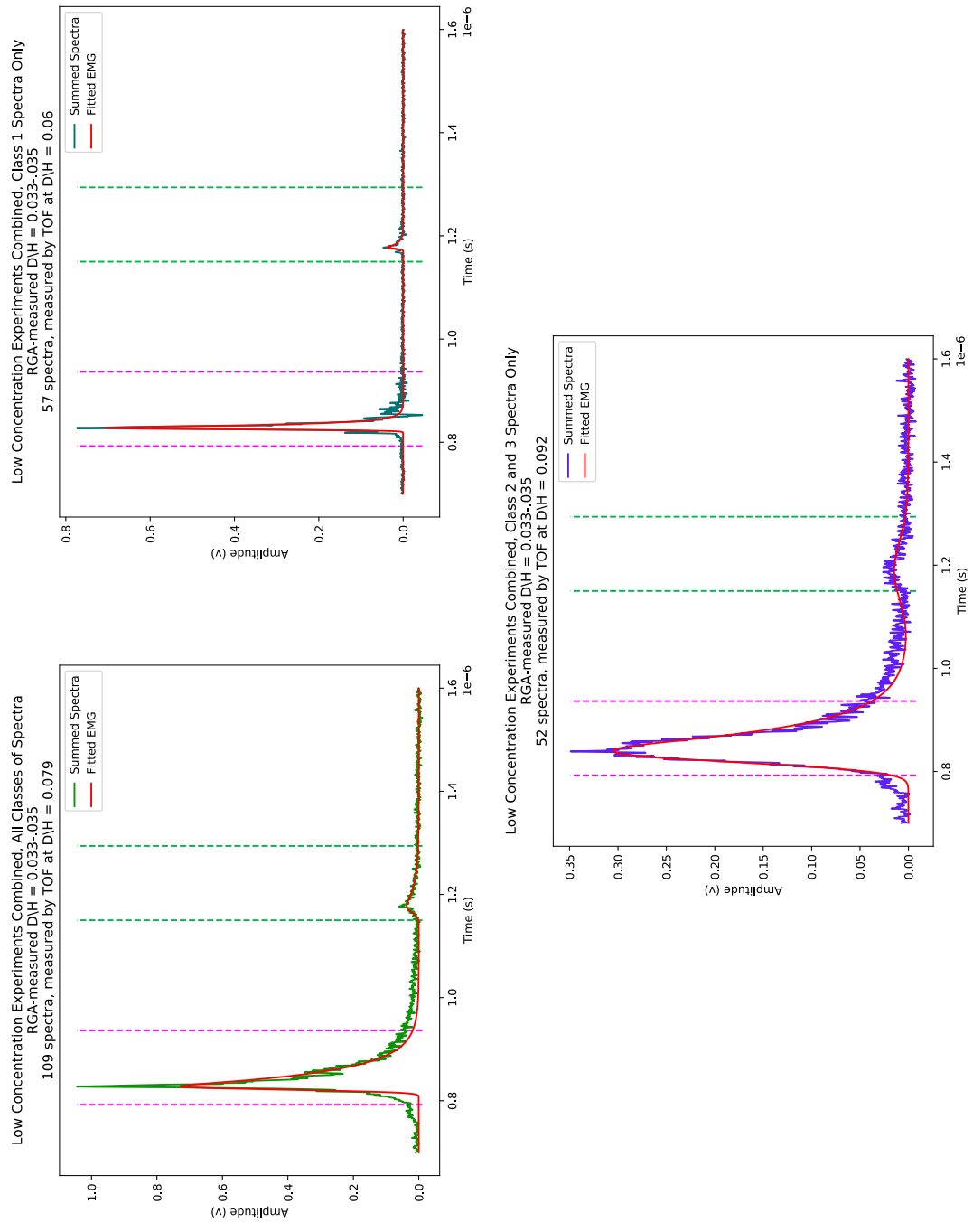


Figure 43: D and H regions of the summed spectra for the low concentration experiment with  $D/H = 0.033-0.035$ , separated by spectra class.

Experiment	Measurement	RGA Data	TOF Data- All Classes	TOF Data- Class 1	TOF Data- Class 2	TOF Data- Class 3
High Concentration	D/H Ratio	4.2	4.45	4.63	3.24	4.7
	Number of Spectra	n/a	142	29	45	68
Mid Concentration	D/H Ratio	0.17	0.182	0.15	0.165	0.222
	Number of Spectra	n/a	64	32	14	18
Low Concentration (Combined Data)	D/H Ratio	0.033-0.035	0.079	0.06	0.092	n/a
	Number of Spectra	n/a	109	57	52	n/a

Table 5: A table detailing the results of the D/H measurement experiments. The RGA data is provided by taking the integral of the mass 20 and mass 18 lines, while the TOF data is provided by fitting EMGs to the D and H mass lines of summed TOF mass spectra.

Low Concentration Experiment Number	Measurement	RGA Data	TOF Data- All Classes	TOF Data- Class 1	TOF Data- Class 2 and Class 3
Experiment 1	D/H Ratio	0.033	0.068	0.080	0.034
	Number of Spectra	n/a	45	24	21
Experiment 2	D/H Ratio	0.033	0.080	0.050	0.10
	Number of Spectra	n/a	44	25	19
Experiment 3	D/H Ratio	0.035	0.088	0.096	0.094
	Number of Spectra	n/a	20	8	12

Table 6: A table of the D/H results for the low concentration ice surface. The D/H ratio calculated by the TOF is over double that calculated by the RGA, but is consistent across the three experiments.

the mid concentration’s D/H by TOF data was within 5.9% of the RGA measurement, at  $D/H = 0.18$  and  $D/H = 0.17$  respectively.

The low concentration TOF-calculated D/H ratio is 0.079, over twice the RGA-measured value of 0.033-0.035. However, the three individual experiments that collectively make up this dataset are largely consistent with one another, having a TOF-calculated D/H ratio between 0.068 and 0.088, as shown in Table 6. Taking these three experiments as independent measurements with standard error, the TOF-calculated low concentration D/H ratio would be  $0.079 \pm 0.006$ . Thus, while the measured value is off by a factor of two, the self-consistency of this dataset is striking.

The RGA-measured D/H ratio in these tables is given simply by the integral of the mass 20 line divided by the integral of the mass 18 line. This

assumes that the protonated and deuterated water molecules (i.e.,  $(\text{H}_2\text{O})\text{D}$  and  $(\text{HDO})\text{H}$ ) are a negligible fraction of the mass 20 line. It also ignores the contribution of the mass 19 line entirely, despite the fact that some measure of it must be HDO, and thus must contribute to the measured D/H. However, the RGA lacks the mass resolution to break the ambiguity with  $\text{H}_2\text{OH}$ , and making the assumption that all of mass 19 is HDO yields D/H ratios far in excess of the TOF-calculated values. This mass 19 line is of particular note, since its integral is significantly higher than that of the mass 20 line which is used as a measure of the  $\text{D}_2\text{O}$  content.

Whatever the case may be, the TOF-measured D/H ratio of the high and mid concentration data is accurate to within 7%. The low concentration measurement's consistency across the three days of experimental runs suggests that while it is measuring some fundamental quantity, there is a confounding factor that only applies at this low concentration, and the most likely source of error is in discarding the entirety of the mass 19 RGA line.

Future experiments may be performed with higher performance mass spectrometers, preferably reflectron TOF systems, with greater ion collection efficiency and greater spectra count. Such experiments may be performed to probe down into the lower D/H ratios observed in outer solar system bodies. However, the results from this experiment provide proof of concept with high concentration ices, showing that impact ionization TOF instruments may be able to measure the D/H ratio of icy dust grains from the objects they study.

## 6 Suggestions for Future Work

### 6.1 Experiments

**Relative Abundances of Amino Acids** Because relative abundances of amino acids can be used as biosignatures, it would be useful to determine if impact ionization TOF instruments can measure the abundances of amino acids relative to others. Such measurements will not be straightforward, as differing ionization potentials and fragmentation rates mean that this will be velocity dependent and rarely if ever a simple ion comparison. Laboratory studies will have to be performed to find what signal levels any two amino acids present in the same solution. For example, a 50-50 mixture of glycine-histidine may yield an ion count of, say, 30-70. Can this be used to predict the ion ratio from a 90-10 solution? What about a 10-90 solution? If so, then relative abundances might be measureable by impact ionization instruments, effectively converting them into biosignature detection instruments.

Once a library has been established, complicated mixtures of amino acids can be prepared, say with an ‘abiotic’ 10:3:2:0 mixture of glycine:alanine:aspartic acid:histidine compared to a flat 1:1:1:1 ‘biotic’ mixture [97].

**Salinity Effects** Estimates for the salinity of Europa are not well constrained [188], but estimates for Enceladus suggest sodium levels of 0.5-1 mol  $kg^{-1}$  [189].

Klenner et al., 2020 used laser ablation of a stream of aqueous amino acids in vacuum to simulate impact ionization dust events [190]. This study found that fragmentation products were suppressed in high salt concentration, hypothesizing this to be the result of either salt neutralizing charged fragments or by reducing fragmentation itself due to increased robustness of sodiated amino acid molecules.

There should be a series of experiments to determine to what extent salt compounds affect the survivability of amino acids with physical dust impact.

**Half-Coated Dust** Self assembled monolayers can be used to graft complex organics, including amino acids to certain metallic substrates. A prime example would be the deposition of cysteamine and m-carborane onto gold substrates [191, 192]. Because of the difficulty in accelerating complex organic dust particles, one potential solution would be to half-coat a typical

dust particle, say iron or aluminum, with a thin layer of titanium-gold. Self-assembled organic monolayers could then be deposited onto the gold surface, but the remaining iron or aluminum surface would remain bare. If a pure gold dust particle were to be coated (or a completely coated Fe or Al particle was used), the organics may interfere with charging, resulting in either non-acceleration by the pelletron or dramatically reduced velocity. Thus, coating only half the particle would enable the dust particles to be charged as normal, as there is still a full conducting sphere to hold charge, but organics would cover roughly half the surface.

Half-coating particles is much easier than coating the entire surface area of a particle, and can be done with sputter or vapor deposition systems. Initial experiments were carried out using vapor deposition of titanium-gold onto typical dust particles, but do to time constraints, the experiment was never completed.

A particularly interesting element of such a study would be the ability to perform direct comparisons between reciprocal experiments. That is, after a half-coated iron dust particle with a particular organic was studied by impact onto a gold surface using the ice target TOF system, the same organic could be deposited onto a flat gold substrate and used as a target for uncoated iron dust. In this way, the differences between an organic impacting a metallic surface and a metallic dust particle hitting an organic surface could be directly compared using the same species.

Ice layers could also be deposited on the target surfaces using vapor deposition for both cases to again study how water ice layers change fragmentation rates.

**Ion Production Rates** Ion production rates for dust impact into water ice are not well-understood. A simple set of experiments would be to directly measure the ion production of a number of different ice surfaces. Amorphous ice as created by the vapor deposition system at cold temperatures, the flash freezing system, and the airbrush could all be compared. More importantly, different ice crystal structures could potentially be grown at different temperatures, although care should be taken to ensure that the desired crystal phases are indeed being created, perhaps by use of a spectrometer. If the vapor deposition does not reliably produce desired ice phases, the flash freezing modular target can be used to grow crystalline ice externally and then transferred to the vacuum chamber. In this way, the ion production rates for

a number of different ice phases may be measured. This can then be further extended to study how this changes with salinity.

To measure charge production, a CSA could be fitted to a grid with a well-characterized transmittance. A simpler method could use a solid target to collect all ion content, although this will block the MCP, preventing analysis of different species' contributions to the total charge. Such methods are briefly mentioned below.

### **Determination of Minimum Amino Acid Detection Concentrations**

The experiments described in Sec 4 were performed at extremely high concentration in order to make spectral features easy to see in individual spectra without having to resort to coadding. Klenner et al. 2020 report amino acid detection thresholds in their laser ablation data as tens of micro-molar or less, with histidine being detectable down to  $0.01 \mu\text{M}$  [142].

Experiments should be performed to determine the detection thresholds of several amino acids in airbrushed ice surfaces with actual hypervelocity dust impact. Initial experiments with the airbrush system have detected amino acids down to the tens of milli-molar, but nothing resembling an exhaustive program was made to determine the true minimum detection threshold. In particular, searches should utilize coadding of at least hundreds of spectra to increase SNR, as is routine in the laser ablation experiments. To facilitate this, a marker chemical may be employed with high mass to provide an easy to detect peak beyond the amino acid lines. This will make coadding significantly easier in the mass domain since the x-axis can be well constrained to masses in excess of the target amino acids.

**Pond Water** A simple experiment could be performed with the airbrush system to study a natural water source, such as pond water. Varying degrees of bioactivity could be studied, perhaps by taking samples from ponds or lakes which feature fish and from high-altitude lakes which feature only small amounts of bacterial life. This would not likely result in a publication, but it would be an interesting analysis of the ice target's ability to study biotic systems.

**Making Organics** It has long been suggested that impact shock physics is a mechanism for creating complex organic molecules [193, 194]. However, most studies focus on effects of large impactors such as meteors entering

atmospheres [193, 194, 195, 196, 197]. Nevertheless, IDP impacts may also play an important role in the synthesis of organic molecules necessary for life, as Chyba and Sagan hypothesized that on Earth such particles “may have been the dominant source of prebiotic organics” [194].

Various experimental studies have shown that laser-ablation of ice mixtures with relevant compounds at energies equivalent to dust impact will produce complex prebiotic hydrocarbon molecules [5, 195, 196]. Mvondo *et al.* created CO and methanol (CH<sub>3</sub>OH) from an H<sub>2</sub>O and CO<sub>2</sub> ice mixture. Similarly a water, methanol, and ammonium sulfate mixture produced ((NH<sub>4</sub>)<sub>2</sub>SO<sub>4</sub>), methane (CH<sub>4</sub>), ethane (C<sub>2</sub>H<sub>6</sub>), acetonitrile (CH<sub>3</sub>CN), and long carbon chains such as acetone (CH<sub>3</sub>COCH<sub>3</sub>), methyl formate (HCOOCH<sub>3</sub>), dimethyl formal (CH<sub>3</sub>OCH<sub>2</sub>OCH<sub>3</sub>). These experiments show that the energy levels associated with dust impacts are capable of producing prebiotic organic molecules, but are nonetheless *simulations* of actual IDP impact, and, as mentioned before, laser ablation occurs over a much shallower region and generates shock impacts of shorter duration than natural impacts [5].

Similarly, impacts with millimeter-sized steel impactors at velocities of less than 10 km/s have produced simple amino acids in ice with relevant compositions [198]. However, these studies often introduce contaminants from explosive powders, do not use impactors of appropriate mass or composition, and do not study speeds relevant to cometary impacts (>20 km/s) [5].

Because the IMPACT facility is capable of bombarding targets with micrometeoroids with a wide variety of compositions at rates of up to 1 particle cm<sup>-2</sup> s<sup>-1</sup> at velocities up to 100 km/s, this facility presents a unique opportunity to study realistic dust impacts into icy targets. Future experiments should probe the synthesis of organic chemistry in hypervelocity dust-ice impacts.

**Carbon Dioxide** Cruikshank *et al.* observed CO and CO<sub>2</sub> ices on the surface of Triton, finding that CO<sub>2</sub> ice covers as much as 10 percent of the surface [2, 199]. CO<sub>2</sub> has also been found on various other outer moons [200, 201, 202, 203, 204]. This CO<sub>2</sub> is typically thought to have been native to the body or to have arrived as C atoms from external sources and converted to CO<sub>2</sub> by UV or charged particle irradiation [205]. IDP impacts are not usually considered as there have not been experimental studies on the creation of CO<sub>2</sub> from IDP impacts. Hypervelocity impacts on water ice dissociates water

molecules to produce O and OH, and IDPs contain various carbon sources [205]. When these IDPs impact icy bodies, the liberated O and OH are expected to bond with the carbon in the IDP to create CO and CO<sub>2</sub>. It is not understood how efficient this process is, nor how this efficiency changes impactor parameters, such as mass and velocity, or ice characteristics, such as temperature. Since carbonaceous IDPs are ubiquitous in the solar system, an important source of CO<sub>2</sub> on icy bodies may be overlooked.

A number of experiments were performed studying the detectability of CO<sub>2</sub> in water ice. Gaseous CO<sub>2</sub> was bubbled through high purity water at room temperature to create carbonated water. This water was then flash frozen and impacted with dust. CO<sub>2</sub> could be observed at all velocities of dust impact, but at higher velocities, breakup products such as CO and CH could be observed as well. The minimum detection thresholds of CO<sub>2</sub> using the ice target have not been determined, however, and this simple set of experiments could potentially be useful to future spacecraft that wish to study CO<sub>2</sub> on a number of icy bodies. Again, the effects of salinity should be measured.

**Mass 32 and Methanol** In the above CO<sub>2</sub> experiments, high velocity spectra (typically > 15 km/s) showed strong, distinct lines at mass 32 as shown in Fig. 44. While this may simply be O<sub>2</sub> molecules, the O<sub>2</sub> molecule is not stable as a positive ion. What is most striking, however, is that this mass 32 line is such a strong feature only in this dataset. Other water ice datasets, which should be perfectly capable of producing O<sub>2</sub> molecules at high velocity, do not exhibit this mass 32 line, and certainly not at the signal strength measured in the CO<sub>2</sub> experiments.

Another possibility is that the mass is in fact methanol, CH<sub>3</sub>OH, created from constituent elements liberated in the high-energy impact plume. Such a detection would be most interesting, as it would show the conversion of simple inorganic chemistry (CO<sub>2</sub>) into simple organic chemistry (methanol).

Because of the ambiguity of the mass 32 line, a separate experiment could be performed using high purity isotopic carbon-13 CO<sub>2</sub>. This would shift the mass line from 32 to 33, although remnant C may mean that a small peak is still observed at 32. Because the existing datasets do not exhibit significant lines at mass 33, a strong mass 33 line would very heavily imply the creation of methanol from CO<sub>2</sub>-water ice, an easily publishable result.

Because of the expense of carbon-13 CO<sub>2</sub>, the same bubbling method

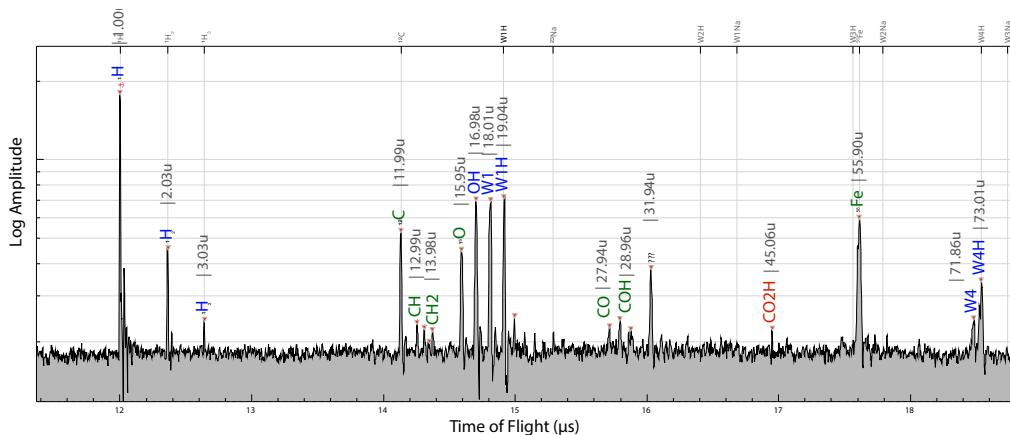


Figure 44: An example spectrum showing a strong mass 32 detection in water ice doped with  $\text{CO}_2$ . While mass 32 may simply be molecular oxygen, it may also be methanol,  $\text{CH}_3\text{OH}$ . Other features of the spectrum are protonated  $\text{CO}_2$ ,  $\text{COH}$ ,  $\text{CO}$ , and  $\text{C}$  and  $\text{CH}$  species. Note that elemental oxygen is also a strong feature of the spectrum. Even so, molecular  $\text{O}_2$  is expected to charge negatively, and thus should not typically be present in this positive ion spectrum.

used in the original  $\text{CO}_2$  experiments could not be used, as this process is wasteful of the impregnating gas. Instead, co-vapor-deposition of water and carbon-13  $\text{CO}_2$  gas was attempted. In the resulting mass spectra, however, only water was observed, with no significant  $\text{CO}_2$  content (at either isotopic mass) and no significant carbon content. This is likely the result of the inability of the vapor deposited water ice to entrap the  $\text{CO}_2$ , meaning that the grown ice was pure or largely pure water.

The experiment should be repeated, either using the original method of creating carbonated water (but this time with carbon-13  $\text{CO}_2$ , which will be expensive), or using some other method that more conservatively uses the expensive isotopic  $\text{CO}_2$  gas. If a different method is used, it should first be verified with standard  $\text{CO}_2$  that detection of the  $\text{CO}_2$  is possible in the resulting ice surfaces.

**Insoluble Organic Matter** Insoluble organic material (IOM) is an interesting type of organic content known to be present in meteorites [206, 207]. It would be interesting to see what such organics look like in TOF mass spec-

trometry systems to aid in future dust particle analysis. Solid IOM surfaces could be directly used as targets, but IOM could also be ground into particulates and, if ground finely enough, potentially even suspended in aqueous solution and used in the airbrush system.

## 6.2 System Improvements

**IR Spec** The ice target is currently only optimized to study the impact ejecta plumes from hypervelocity impact. However, there are a number of scientific questions that could be answered by studying the ice surfaces after a large volume of dust impacts. In particular, it would be interesting to use infrared spectrometry to study how the observed spectra change during dust bombardment. This would be interesting for different phases of crystalline ice, for ices containing differing salt contents [116], and for ices containing organics.

**Indium Conductivity Tests** The methods described in Section 2.5 have only been applied to studies using the older mirror system of titanium-gold coated sapphires. While the newer mirrors using copper substrates with gold mirror surfaces have been exceptionally useful in laboratory studies by reducing downtime between experiments and eliminating N-grease near the target surface, they have not been characterized with surface temperature tests. Similar tests should be performed to ensure that the surface temperature with these mirrors, which use indium foils as thermal conductant layers instead of N-grease, reach acceptably low temperatures.

**Silver Epoxied Mirror** In the event that the indium foil does not produce sufficiently low temperatures, the copper mirrors may be permanently fixed to the copper target modules by use of silver epoxy, which is vacuum-compatible and provides excellent thermal contact. Using such a method, the mirrors will become much more robust, and will not require a plastic cover to clamp them to the copper target module. This would increase the effective target cross-section due to the angle of dust-beam incidence and make installation easier. Since the mirrors would no longer be replaceable except by replacing the entire target module, a simple plastic cover could be bolted on that entirely encases the mirror surface to protect it during off-time when it is not installed.

**Aluminum Mirrors** A significant logistical problem with the ice target is the acquisition and protection of the gold-mirror surfaces. They are fragile to scratching, and they can only be cleaned with dry nitrogen, as abrasive cleaning with even just ethanol may remove the gold surface. Highly polished aluminum may present an acceptable mirror surface that is resistant to damage and can be gently cleaned with acetone, isopropyl, and ethanol. Further, the cost of each copper substrate mirror is on the order 200 USD, while strips of polished aluminum large enough for several mirrors cost < 100 USD. Initial experiments with polished aluminum from McMaster Carr have been unsuccessful, as the surface is not polished sufficiently and bounced laser light is not as coherent as is desired. However, higher grade polishes may be purchased from other sources that may drastically simplify this critical component of the vapor deposition system.

**A Note About Surface Morphology** It has long been suspected that ice surface morphology, or some other parameter in ice creation, leads to sometimes drastic differences in the measured MCP signal of each impact. This can be seen simply in the number of shots on target that produce a measurable ion signal.

In October of 2021, a series of five true airbrush experiments were carried out on the 11th, 14th, 19th, 20th, and 22nd, each studying different lysine-arginine admixtures (one experiment at 1:1, the other four at 9:1 or 1:9) and with an average of 5350 shots on target. As with all true airbrush experiments, these were carried out using the flash-freeze copper target at 80-85 K.

Importantly, the airbrushed target used on the 22nd was left in rough vacuum over the weekend to produce a freeze-dried surface. This surface was then used in a room temperature experiment on the 25th, meaning it had the same exact target and surface as on the 22nd, only with the water sublimated away.

In addition, a pair of experiments were performed on October 12th with a freeze-dried surface on the aluminum flatplate target, with one dataset collected at room temperature (with 890 shots on target) and one dataset collected with the typical seven minutes ice growth at 80-85 K (which had 3227 shots on target).

Figure 45 shows the spectra collection efficiency for these experiments. The x-axis shows the date of each experiment, while the color depends on

the type of airbrushing method. Red data denote experiments performed with the true airbrush, blue data denote experiments at room temperature, and cyan data denote experiments at 80-85 K with ice layers grown on top. A red horizontal line denotes the average true airbrush collection efficiency, which was found to be 10%.

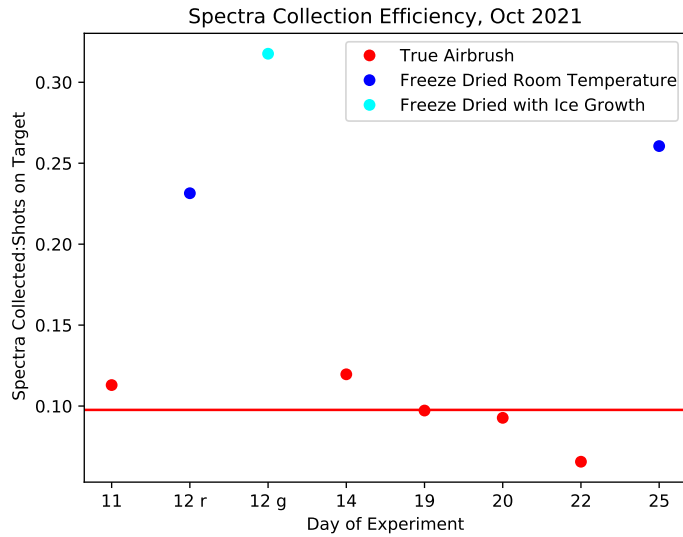


Figure 45: A plot of the spectrum collection efficiency for the month of October 2021. Experiments performed with the true airbrush method are colored in red, experiments performed with freeze-dried targets at room temperature are colored in blue, and experiments performed with freeze-dried targets with water layers grown on top are colored cyan. The red horizontal line denotes the average true airbrush collection efficiency.

It should be noted that even these statistics do not fully capture the effect, as there were several experimental runs using the true airbrush method in this time frame that were abandoned very soon after they began because little or no signals were measured in the first few hundred shots on target. It should also be noted that target-MCP alignment, while never confirmed to have a large effect so long as it was at least roughly aligned, would have been worse for the room temperature experiments performed on the 25th and 26th. This is because rough alignment had been performed on the 22nd when the system was at 85 K, but it was never realigned after that.

**Delay Line** A delay line detector can be used to determine the ion collection efficiency of the TOF system. Because the system must be cold when ice is present, it is difficult to determine if poor ion collection efficiency is a result of the ion production rates or poor ion beam alignment. Because of beam wandering as described in Section 2.4, when the system is cold, its alignment is not the same as when it is warm. Further, when ices are grown on the mirror system, the mirror cannot be used to align due to decoherence of the bounced laser beam.

Experiments were performed to apply up to 1 kV to the steering plates shown in Fig. 10. While it was possible to force all ions off the MCP at the highest potentials, the shot-to-shot variation in ion production rates made it difficult to determine if any particular set of voltages meaningfully improved ion collection rates. It is not known what the ideal step size in voltage should be, so experiments were carried out by moving the voltages by 50 volts in either axes, but even this step size may be too large. That is, it may be that the ideal step size should be 10 volts if precise beam alignment is particularly sensitive, so these experiments are highly inconclusive.

The delay line detector would allow more careful measurements of the ion beam position at the time it reaches the MCP, thus enabling use of the steering plates to increase ion collection. It may be that previous experiments have only collected a small percentage of the true yield. Future experiments should make use of the IMPACT delay line detector system that is currently being pursued.

**CSA Experiments** A much simpler method of measuring ion collection efficiency is to place CSA-connected grids in two parts of the TOF beamline, or one in the beamline and one attached to the ice target itself. In this way, the ion content at two points in the stream can be measured, and if the second CSA is placed near the MCP, it can be determined if significant quantities of the ion beam are being lost in the flight tube by comparing its signal to the first CSA signal. This could also be used to determine what the ideal steering plate potentials are.

This experiment was attempted at one point, and some basic hardware was created. A CSA was attached to the acceleration grid, and another was attached to a solid aluminum disc that was placed in the TOF tube instead of the MCP. This would enable measurement of the charge at the end of the TOF beamline as a ratio of the original impact charge. However,

CSA difficulties relating to background noise prevented the experiment from producing useful results in the allotted timeframe.

If the delay line detector does not work as anticipated, or if results are desired before it comes online, this simple experiment can be re-performed with greater time allotment to ensure that adequate data is collected and ion collection efficiency is accurately measured.

**Vertical and Horizontal Access** The system as-is can be very difficult to clean because there is no easy bottom access port. Dust that comes to rest on the bottom floor of the chamber cannot be simply cleared away since wiping with ethanol or other solvents usually just pushes dust particles around rather than pick them up. A bottom access port that is easily removed and replaced (say with a 2.75 inch CF flange) could be installed to make it easier to clean the bottom surface.

Even so, the absolute bottom internal surface of the chamber is the flange holding the ice target itself, and because this is in a recessed port, it is particularly difficult to clean without its complete removal. In the past, vacuums have been used to attempt to clear this surface, but inadequate suction typically leaves larger debris such as errant hair on the bottom surface. A jury-rigged solution was to use long tweezers to press Kapton tape to the bottom surface so that it removes whatever it touches when removed.

These problems are exacerbated by the fact that primary access to the chamber is through the top, meaning that gravity pulls in a greater amount of debris than side-access would.

If the ice target is ever completely re-designed, future iterations should take this into account, and perhaps the primary access port should be made on the side rather than the top of the chamber.

**Cold Getter Plate** A cold getter plate could be made from copper or perhaps even aluminum and inserted into the target chamber via one of the free 6-inch CF flanges. LN2 could then be run through the getter plate itself, in the same way that LN2 flows through the ice target assembly. This would allow the surface to act as a cheap cryopump, clearing out remnant water molecules from the chamber before the ice target itself is cooled. This would dramatically reduce contaminants to any ice target ices.

It could also be used to more rapidly clean the chamber during bakeout, as the getter plate could be removed when still cold, even as the rest of

the chamber is baking. It could then be cleaned by hand externally and then reinserted. Since the ice target assembly has many delicate pieces and cannot be baked to high temperatures, this will reduce the time necessary for bakeouts to clean the system.

## A Supplementary Images

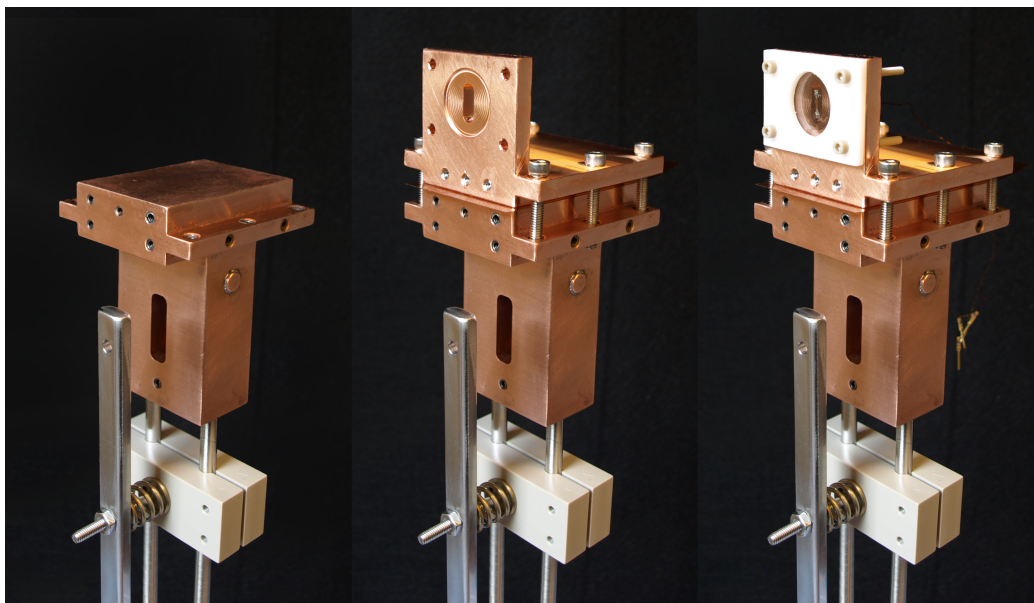


Figure 46: Three photographs showing the assembly process of the vapor deposition target.

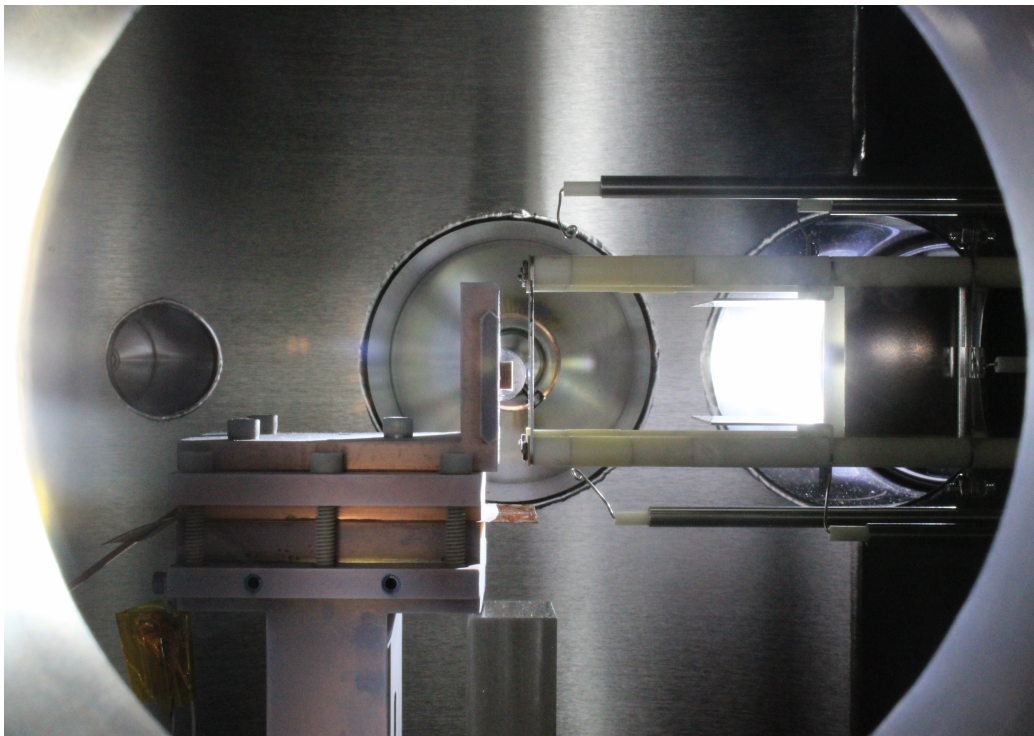


Figure 47: A photograph of the flash freezing target before the door has been removed in an actual experimental run.

12-27-20 Experiment with D:H = 0.033

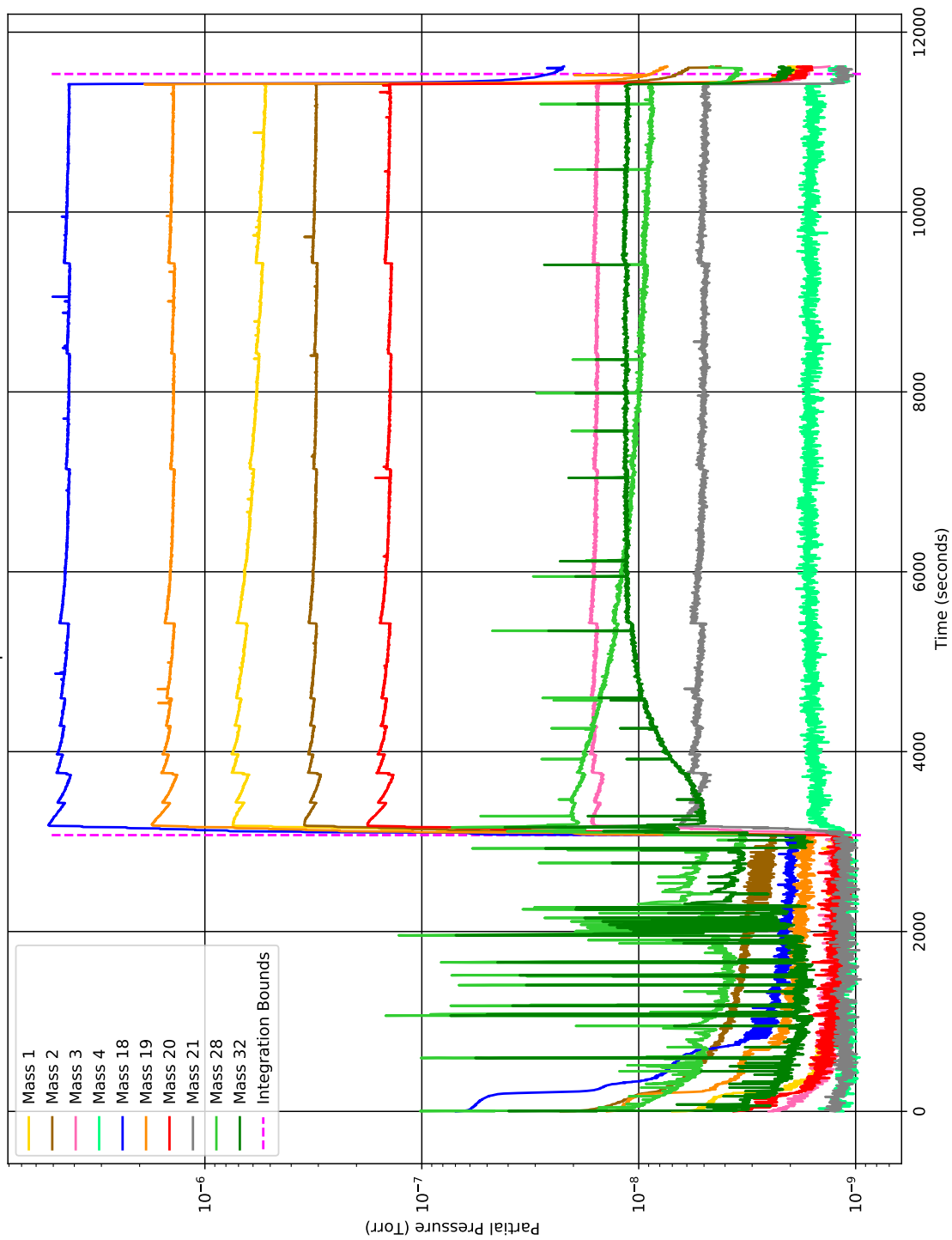


Figure 48: RGA partial pressure vs time plot for the first level solution with D/H measured as 0.033. Masses are described in Table 3.

12-28-20 Experiment with D:H = 0.033

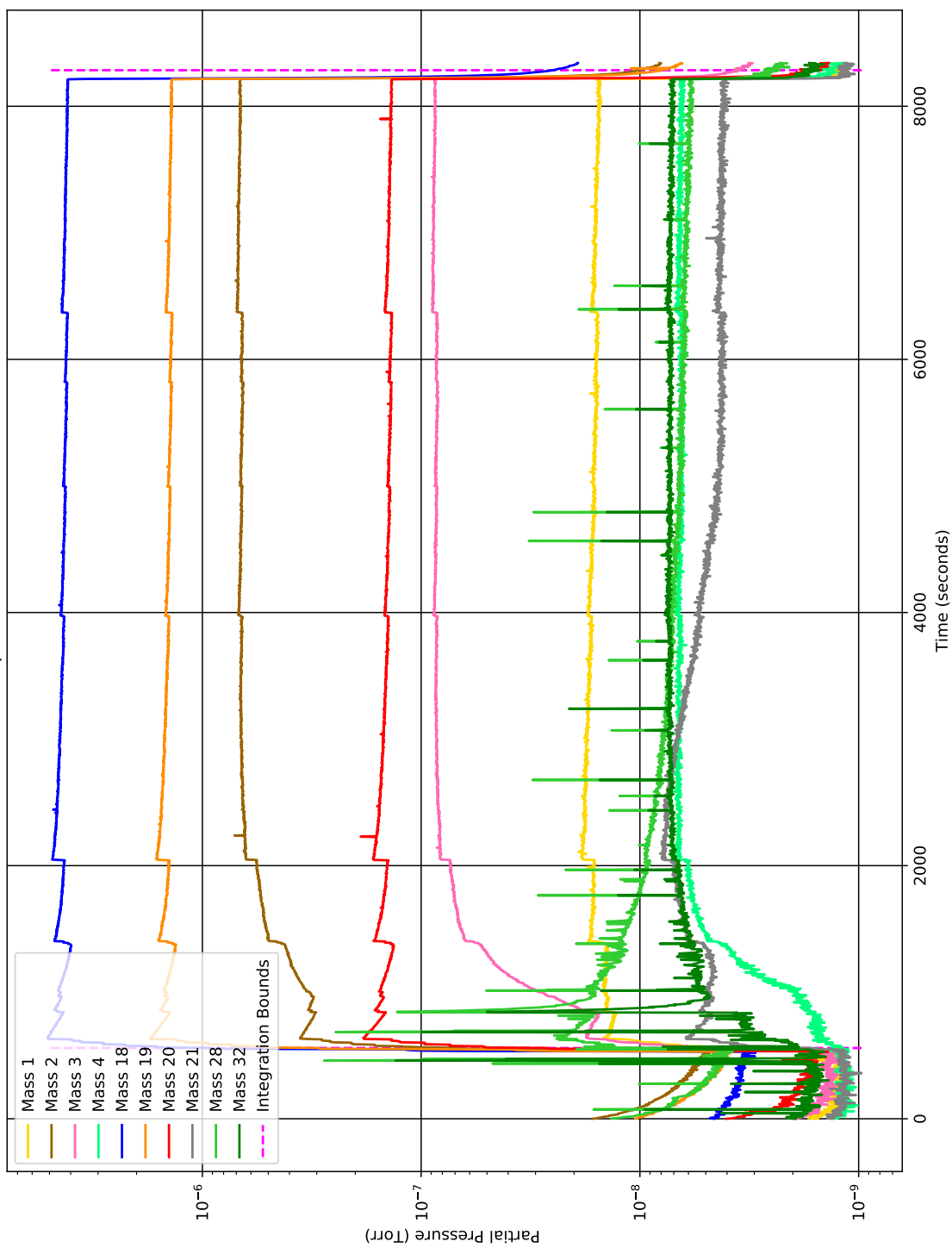


Figure 49: RGA partial pressure vs time plot for the second low level solution with D/H measured as 0.033. Masses are described in Table 3.

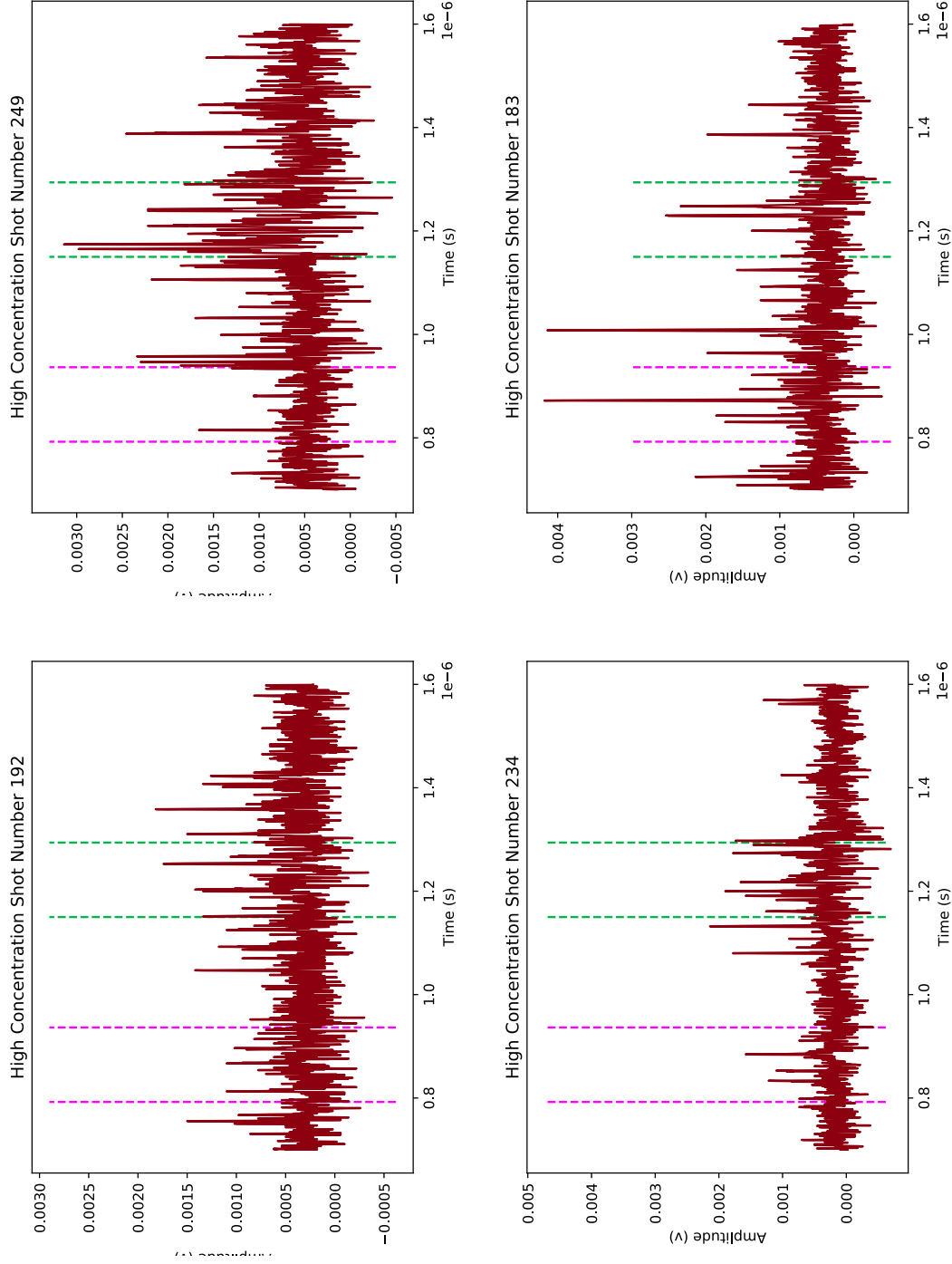


Figure 50: Examples of discarded spectra in the D-H experiments. Some of these spectra, e.g. Shot 249 in the upper right, very likely contain valid D and H ions, but the spectra are of such low quality that they were rejected. The expected hydrogen ion region is bracketed by pink lines, and the deuterium region is bracketed by green lines.

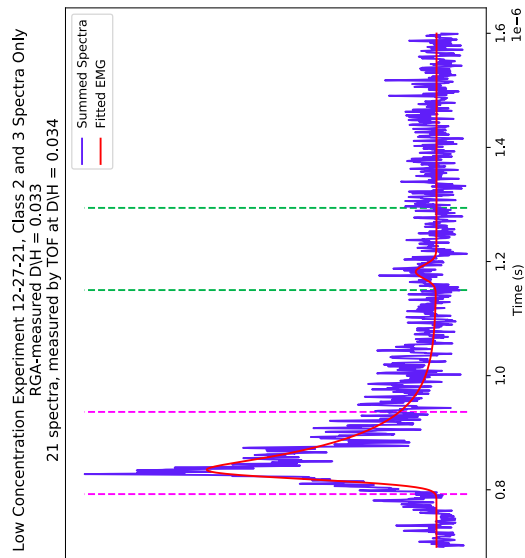
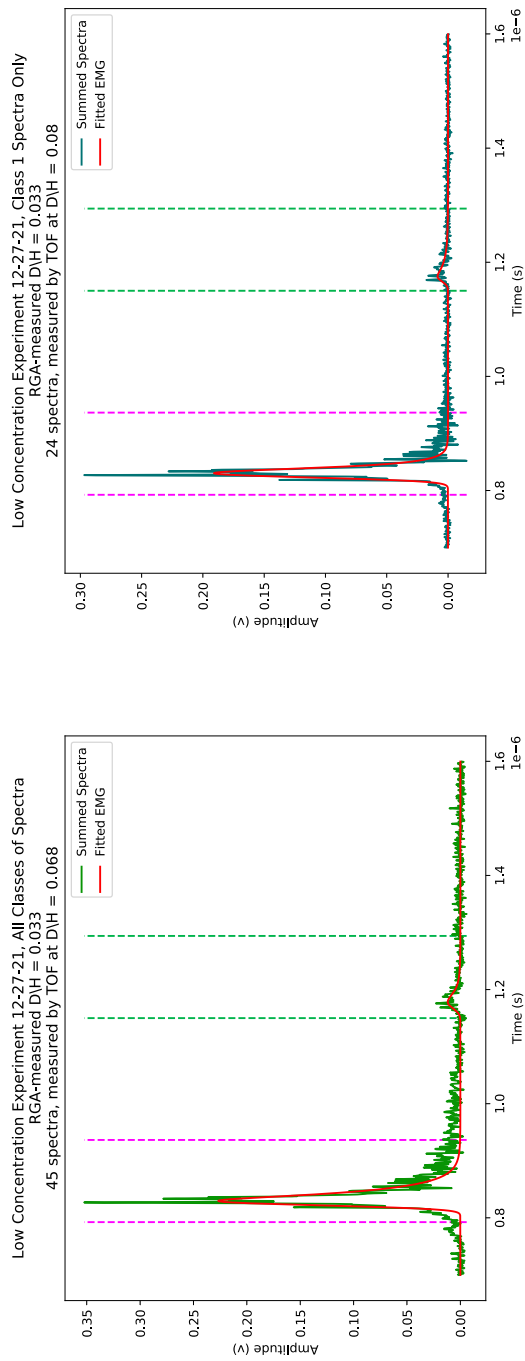


Figure 51: Plots of the D and H regions of the co-added spectra from the first low concentration experiment, where the RGA measured a D/H ratio of the water ice at 0.033.

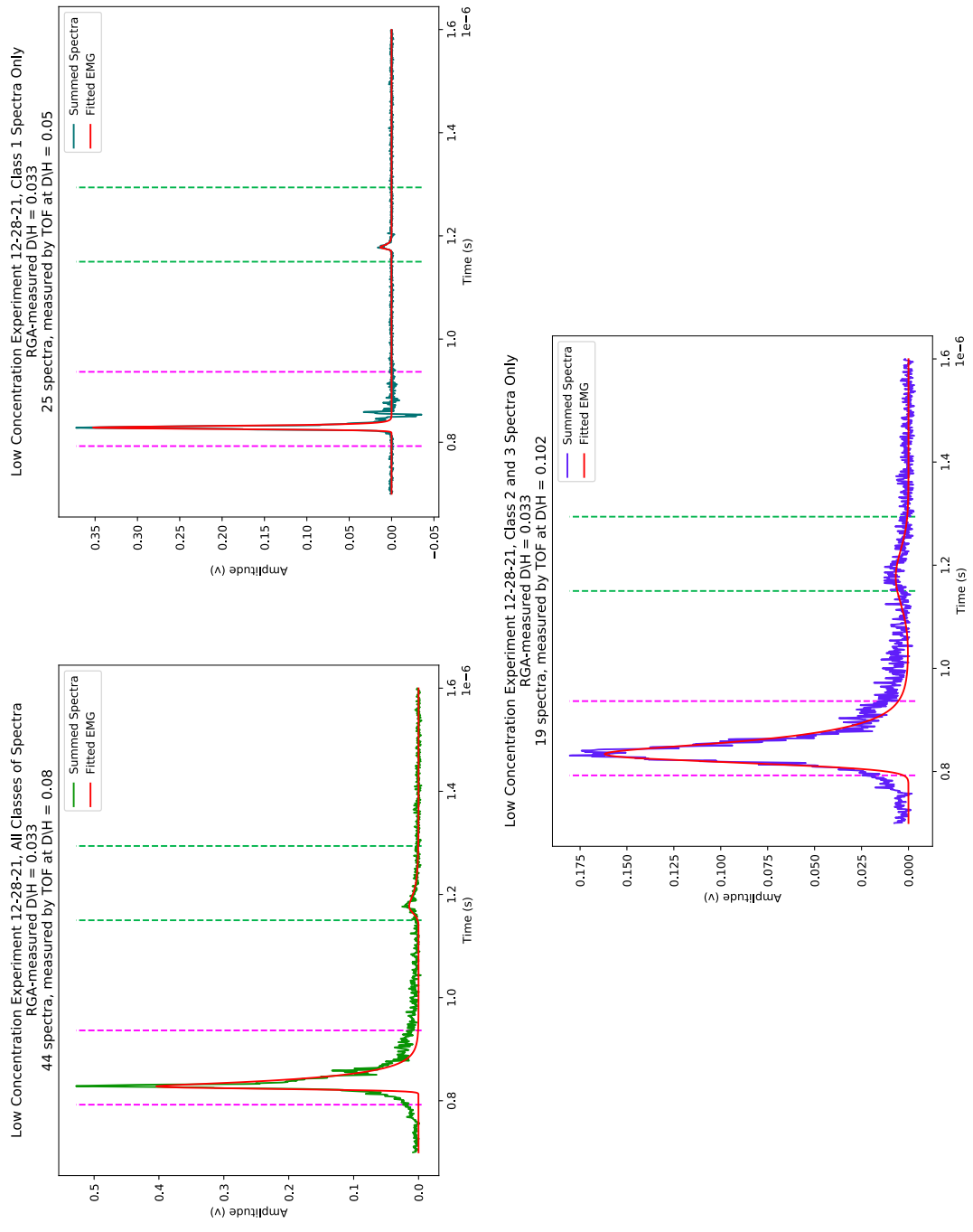


Figure 52: Plots of the D and H regions of the co-added spectra from the second low concentration experiment, where the RGA measured a D/H ratio of the water ice at 0.033.

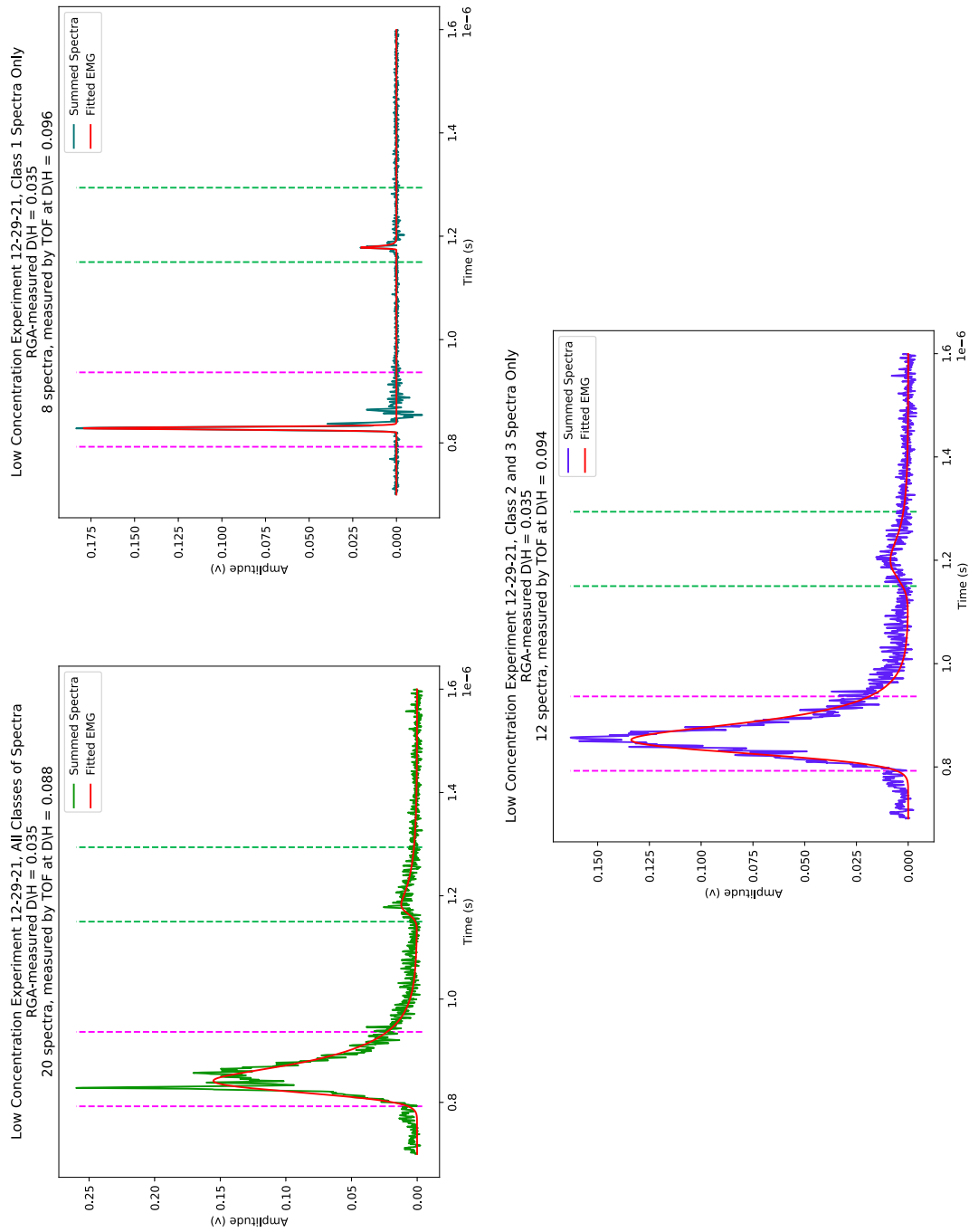


Figure 53: Plots of the D and H regions of the co-added spectra from the second low concentration experiment, where the RGA measured a D/H ratio of the water ice at 0.035.

Experiment 1  
Histidine Without Ice Cover  
3-4 km/s Summed Spectra Detail

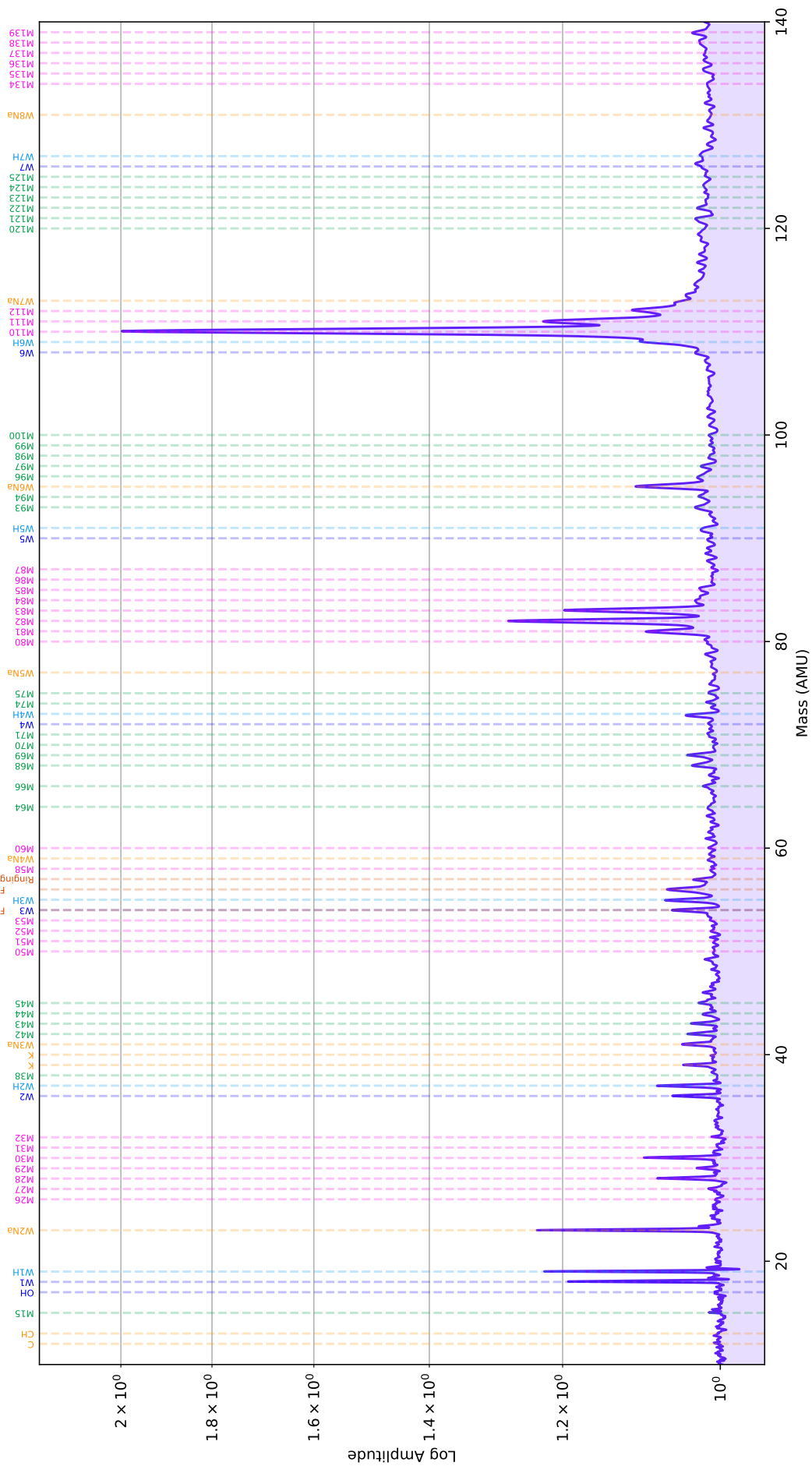


Figure 54: Detail of the summed spectra for impacts of velocities between 3 and 4 km/s in Experiment 1, which had no ice layer covering the histidine surface.



Experiment 1  
 Histidine Without Ice Cover  
 5-6 km/s Summed Spectra Detail

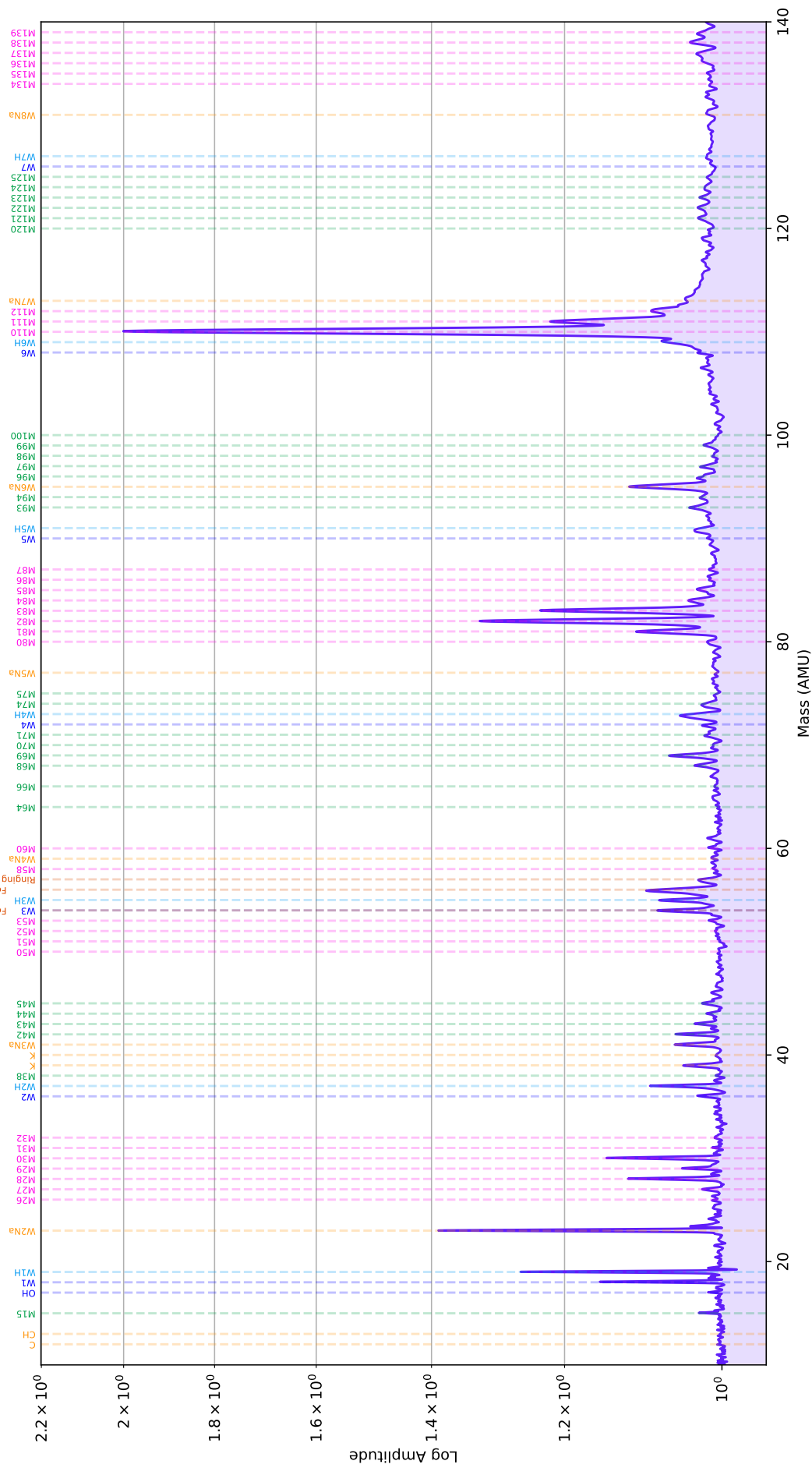


Figure 56: Detail of the summed spectra for impacts of velocities between 5 and 6 km/s in Experiment 1, which had no ice layer covering the histidine surface.

Experiment 1  
Histidine Without Ice Cover  
6-7 km/s Summed Spectra Detail

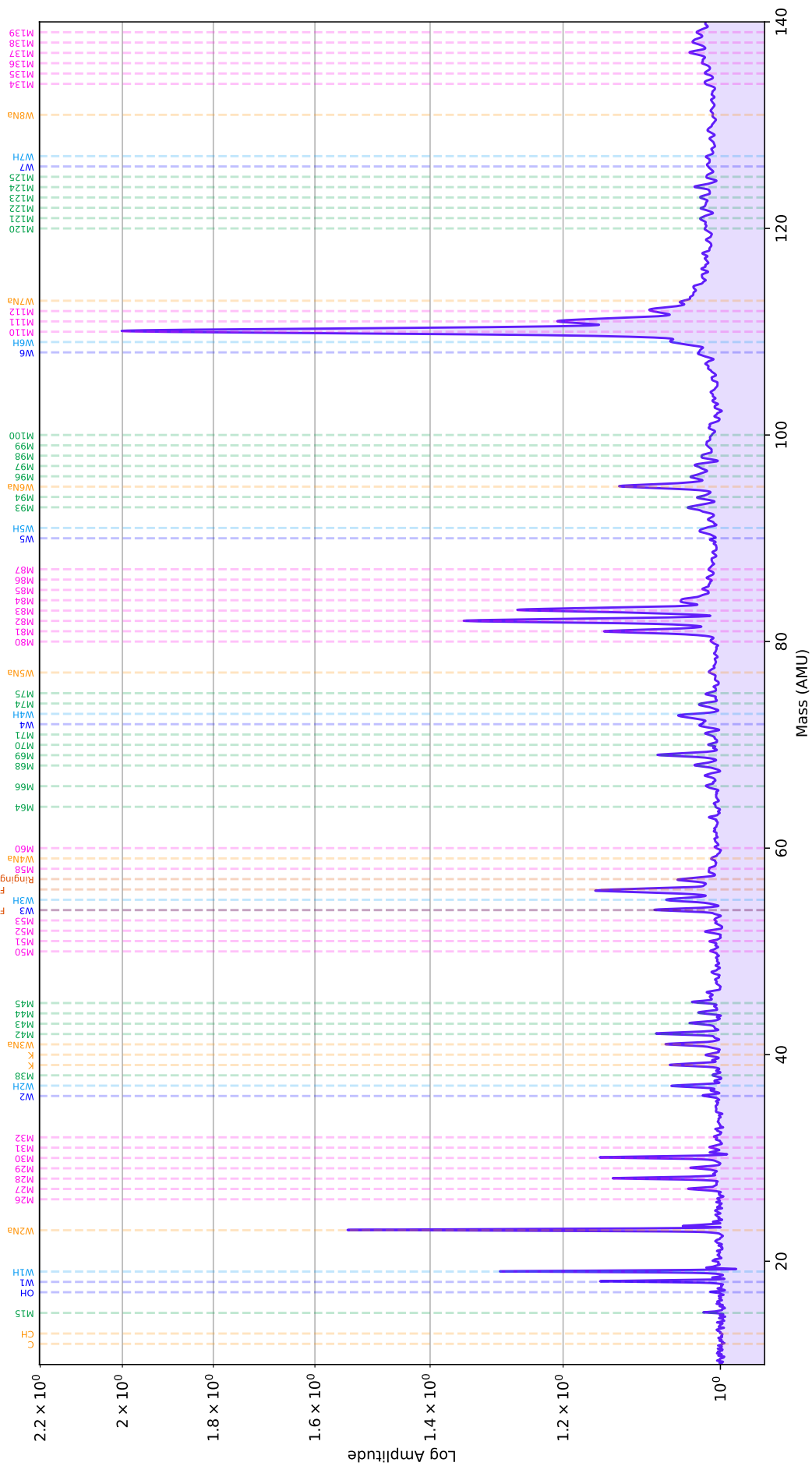


Figure 57: Detail of the summed spectra for impacts of velocities between 6 and 7 km/s in Experiment 1, which had no ice layer covering the histidine surface.

Experiment 1  
 Histidine Without Ice Cover  
 7-8 km/s Summed Spectra Detail

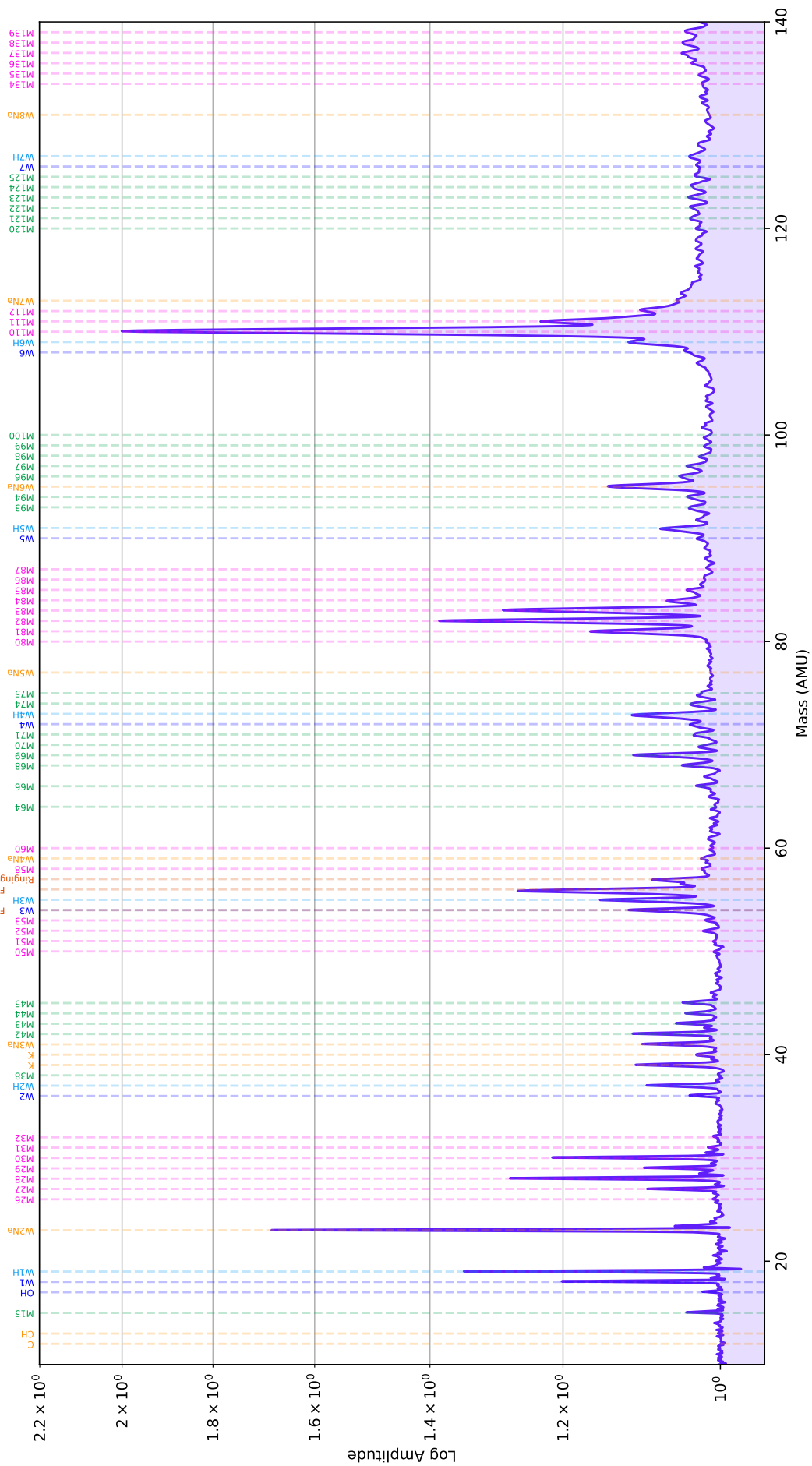


Figure 58: Detail of the summed spectra for impacts of velocities between 7 and 8 km/s in Experiment 1, which had no ice layer covering the histidine surface.

Experiment 1  
 Histidine Without Ice Cover  
 8-9 km/s Summed Spectra Detail

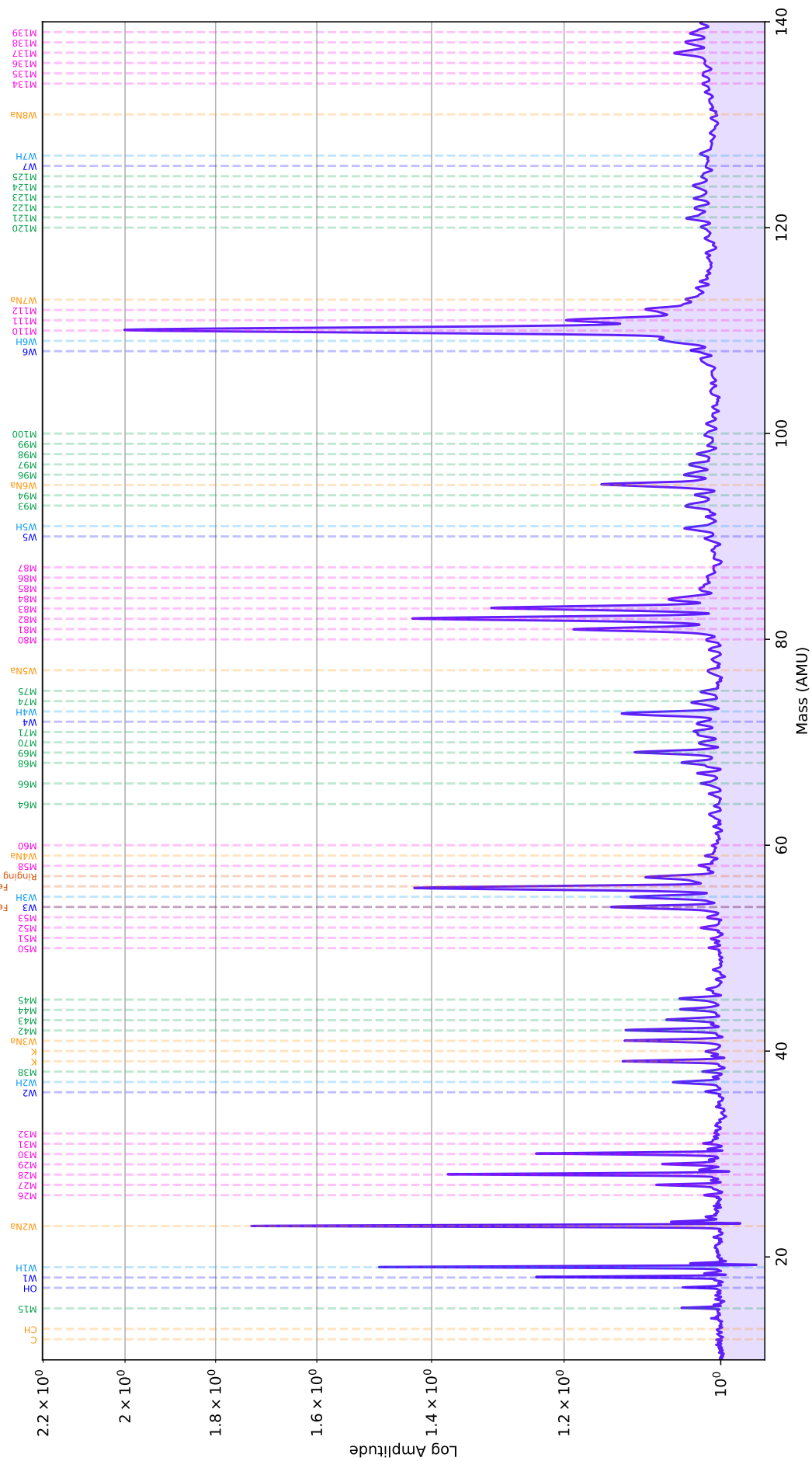


Figure 59: Detail of the summed spectra for impacts of velocities between 8 and 9 km/s in Experiment 1, which had no ice layer covering the histidine surface.

Experiment 1  
Histidine Without Ice Cover  
9-10 km/s Summed Spectra Detail

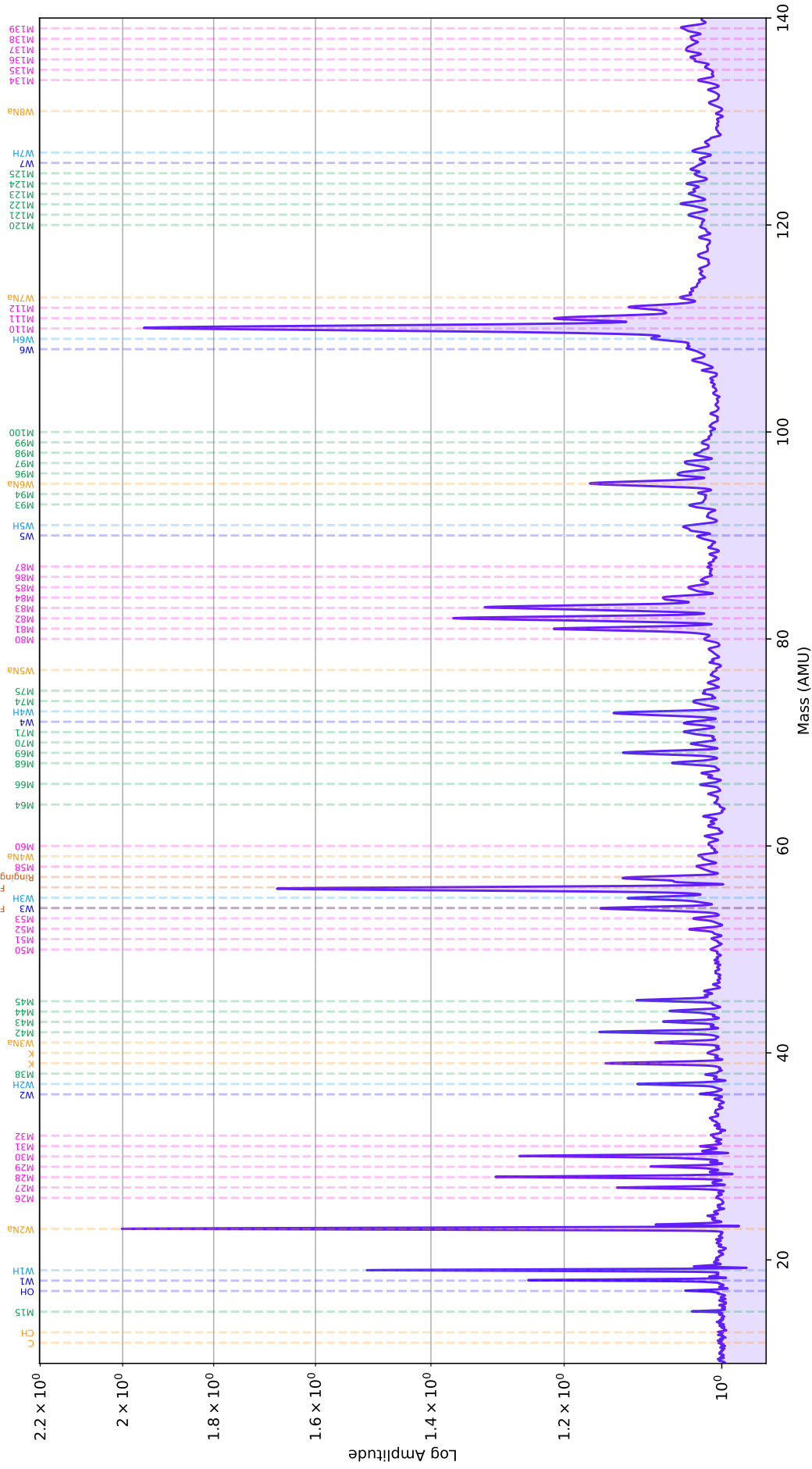


Figure 60: Detail of the summed spectra for impacts of velocities between 9 and 10 km/s in Experiment 1, which had no ice layer covering the histidine surface.

Experiment 1  
 Histidine Without Ice Cover  
 10-11 km/s Summed Spectra Detail

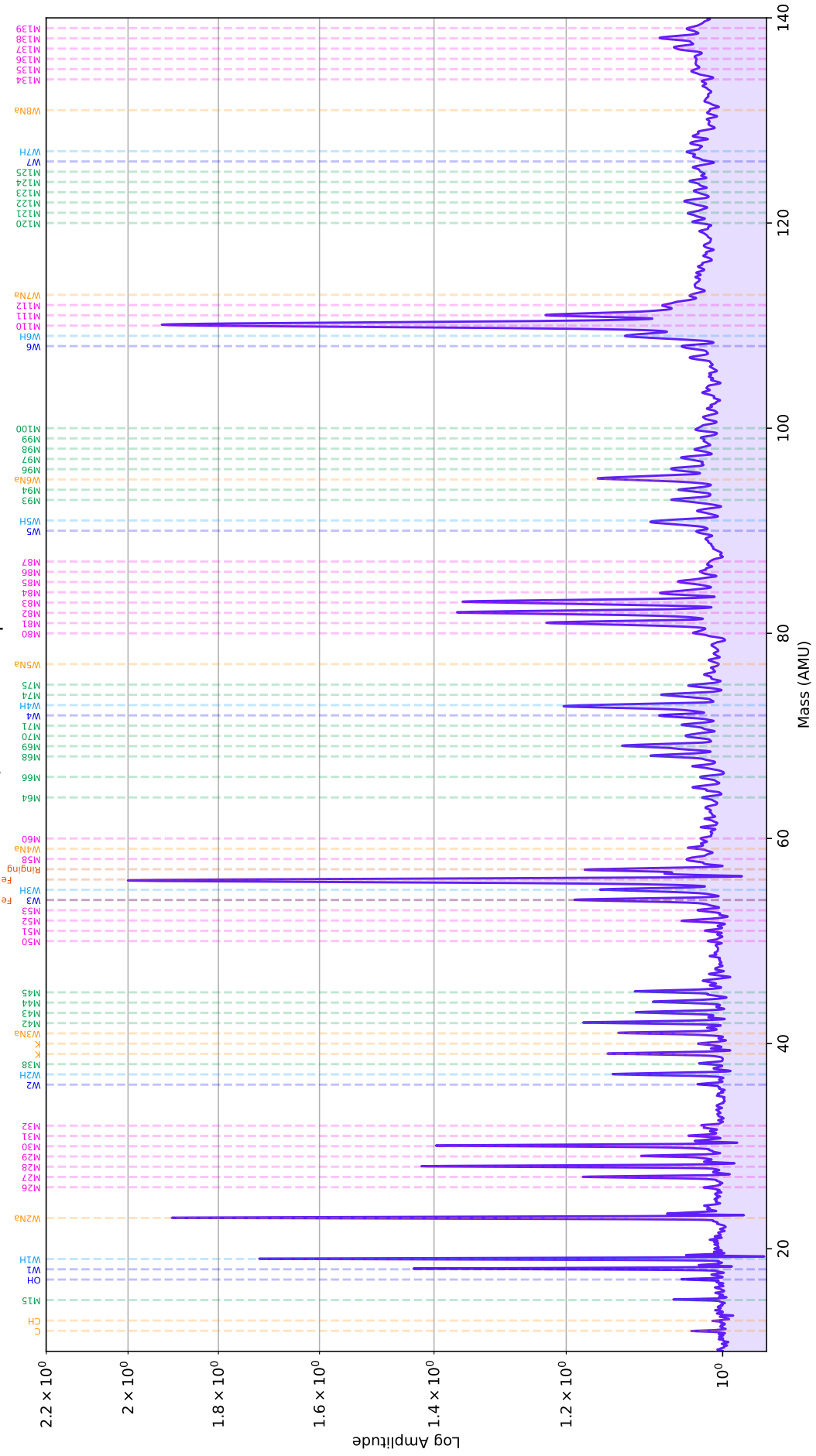


Figure 61: Detail of the summed spectra for impacts of velocities between 10 and 11 km/s in Experiment 1, which had no ice layer covering the histidine surface.

Experiment 1  
 Histidine Without Ice Cover  
 11-12 km/s Summed Spectra Detail

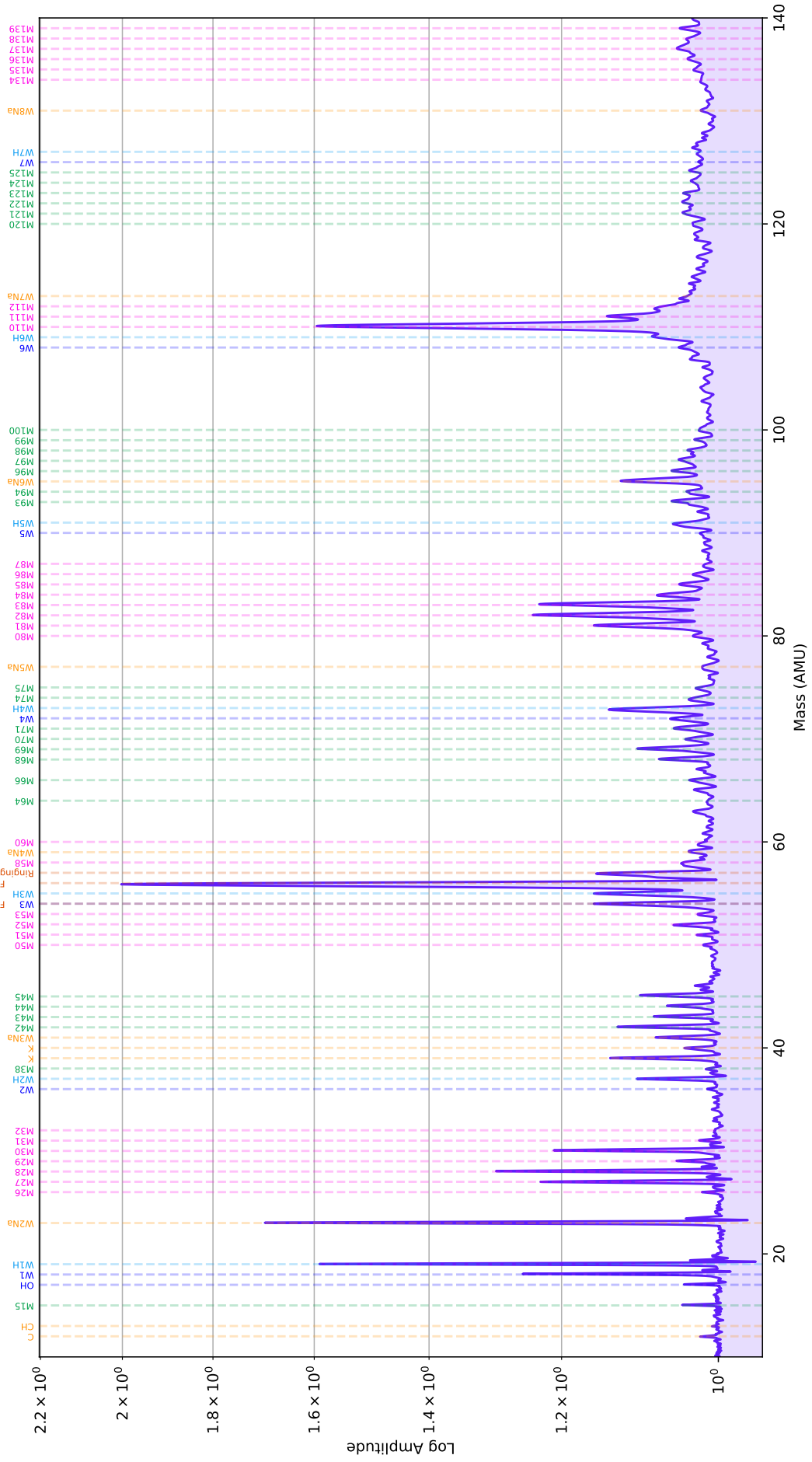


Figure 62: Detail of the summed spectra for impacts of velocities between 11 and 12 km/s in Experiment 1, which had no ice layer covering the histidine surface.

Experiment 1  
 Histidine Without Ice Cover  
 12-13 km/s Summed Spectra Detail

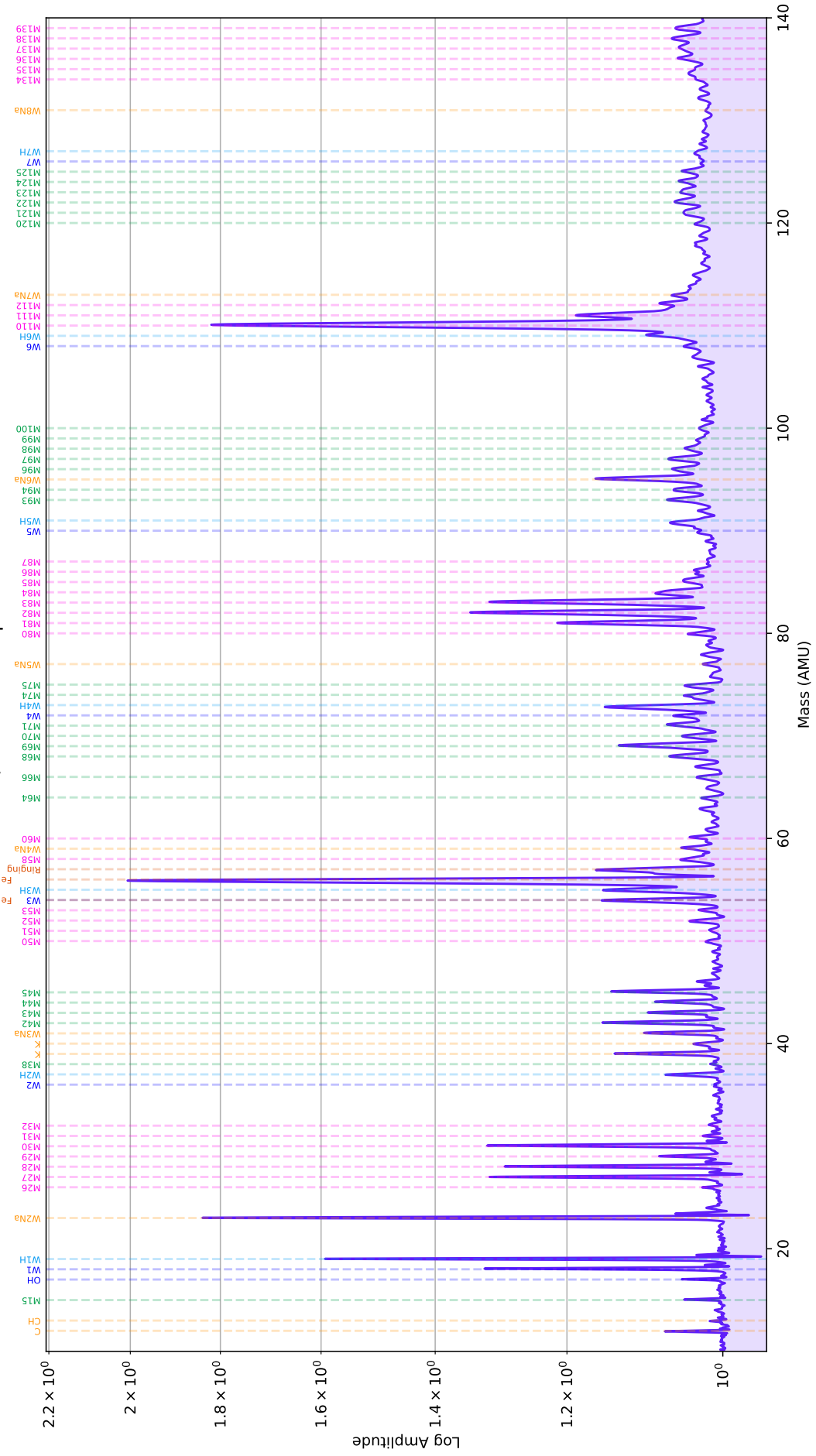


Figure 63: Detail of the summed spectra for impacts of velocities between 12 and 13 km/s in Experiment 1, which had no ice layer covering the histidine surface.

Experiment 1  
 Histidine Without Ice Cover  
 13-14 km/s Summed Spectra Detail

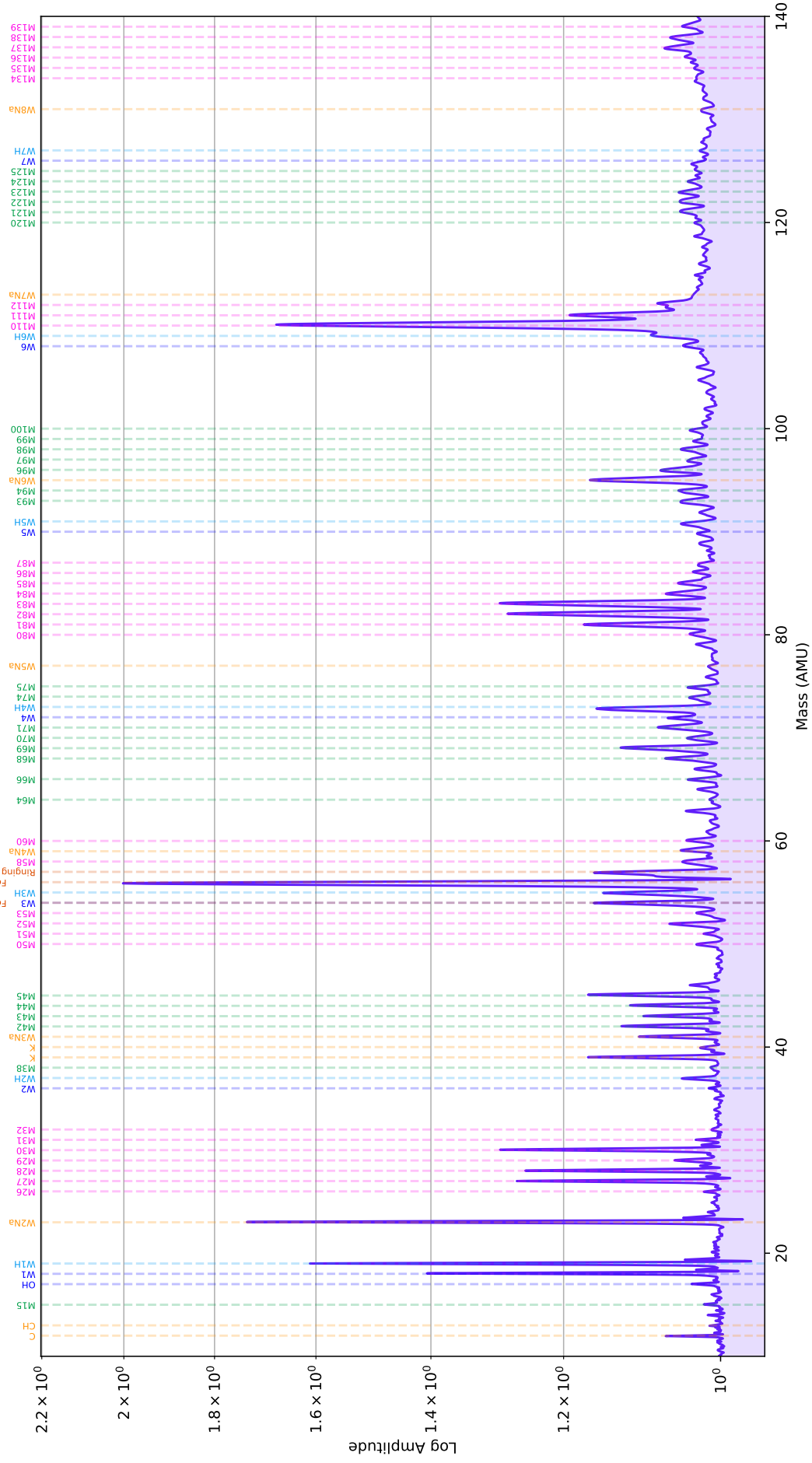


Figure 64: Detail of the summed spectra for impacts of velocities between 13 and 14 km/s in Experiment 1, which had no ice layer covering the histidine surface.

Experiment 1  
 Histidine Without Ice Cover  
 14-15 km/s Summed Spectra Detail

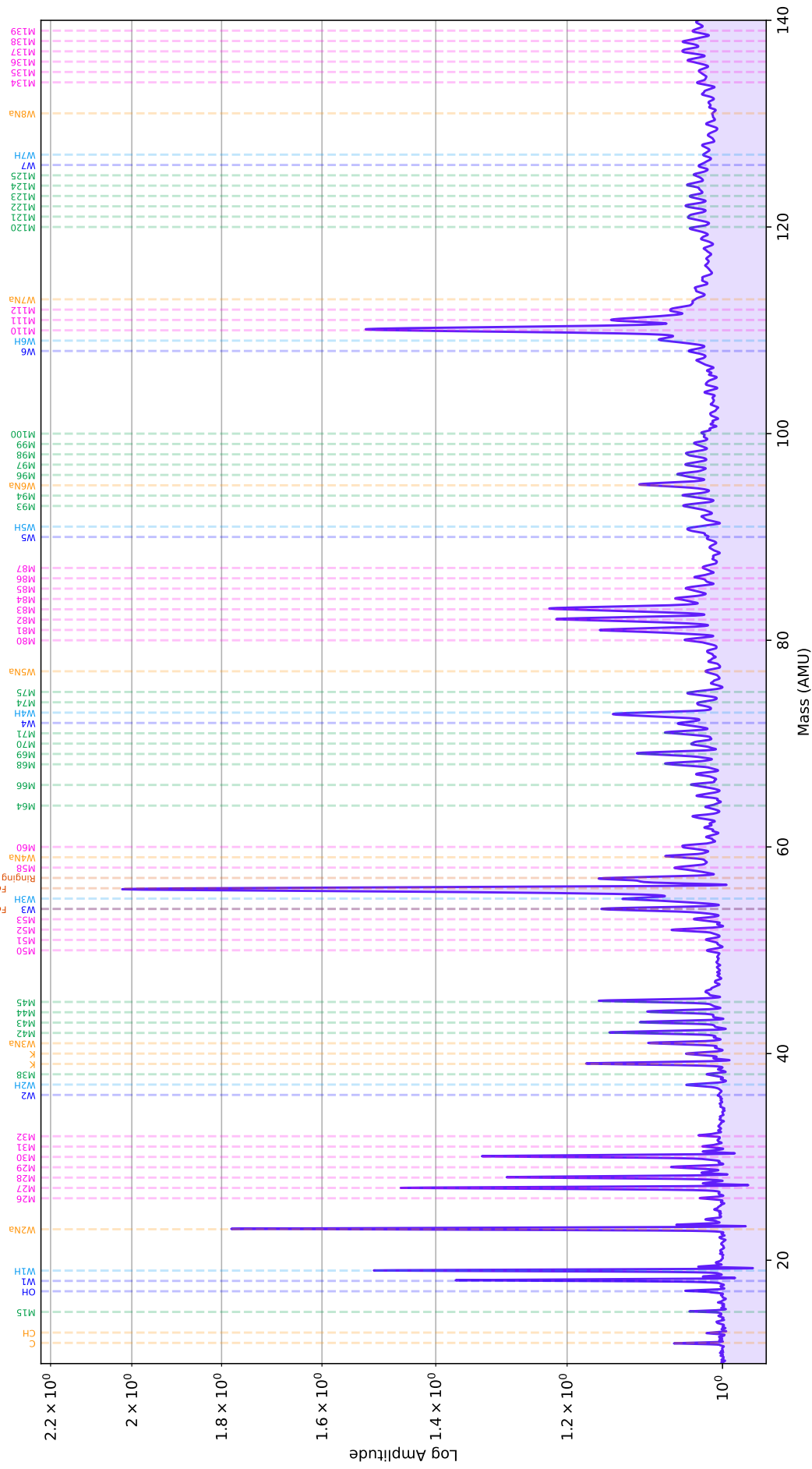


Figure 65: Detail of the summed spectra for impacts of velocities between 14 and 15 km/s in Experiment 1, which had no ice layer covering the histidine surface.

Experiment 2  
 Histidine With Ice Cover  
 3-4 km/s Summed Spectra Detail

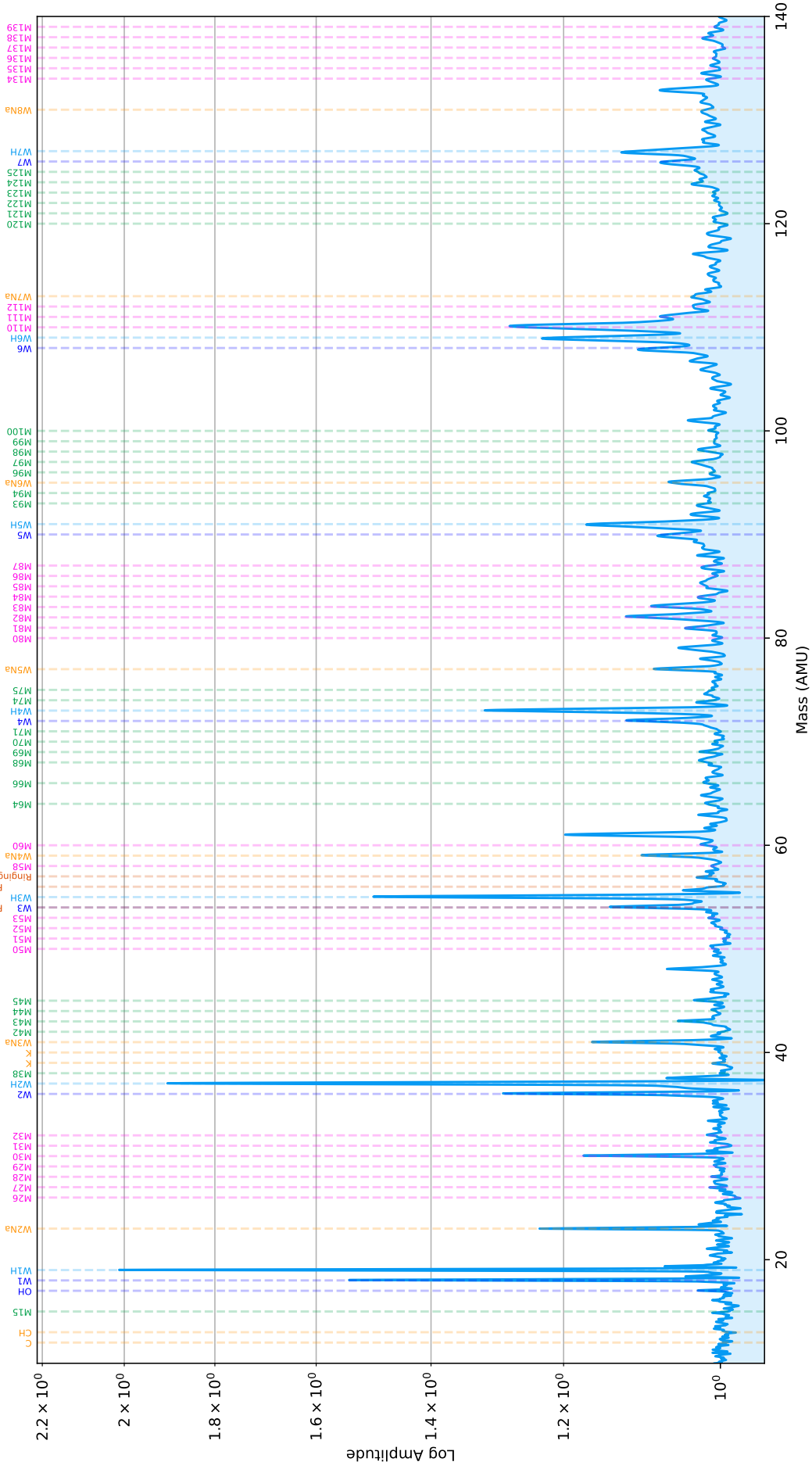


Figure 66: Detail of the summed spectra for impacts of velocities between 3 and 4 km/s in Experiment 2, which had a 60 nm water ice layer covering the histidine surface.

Experiment 2  
 Histidine With Ice Cover  
 4-5 km/s Summed Spectra Detail

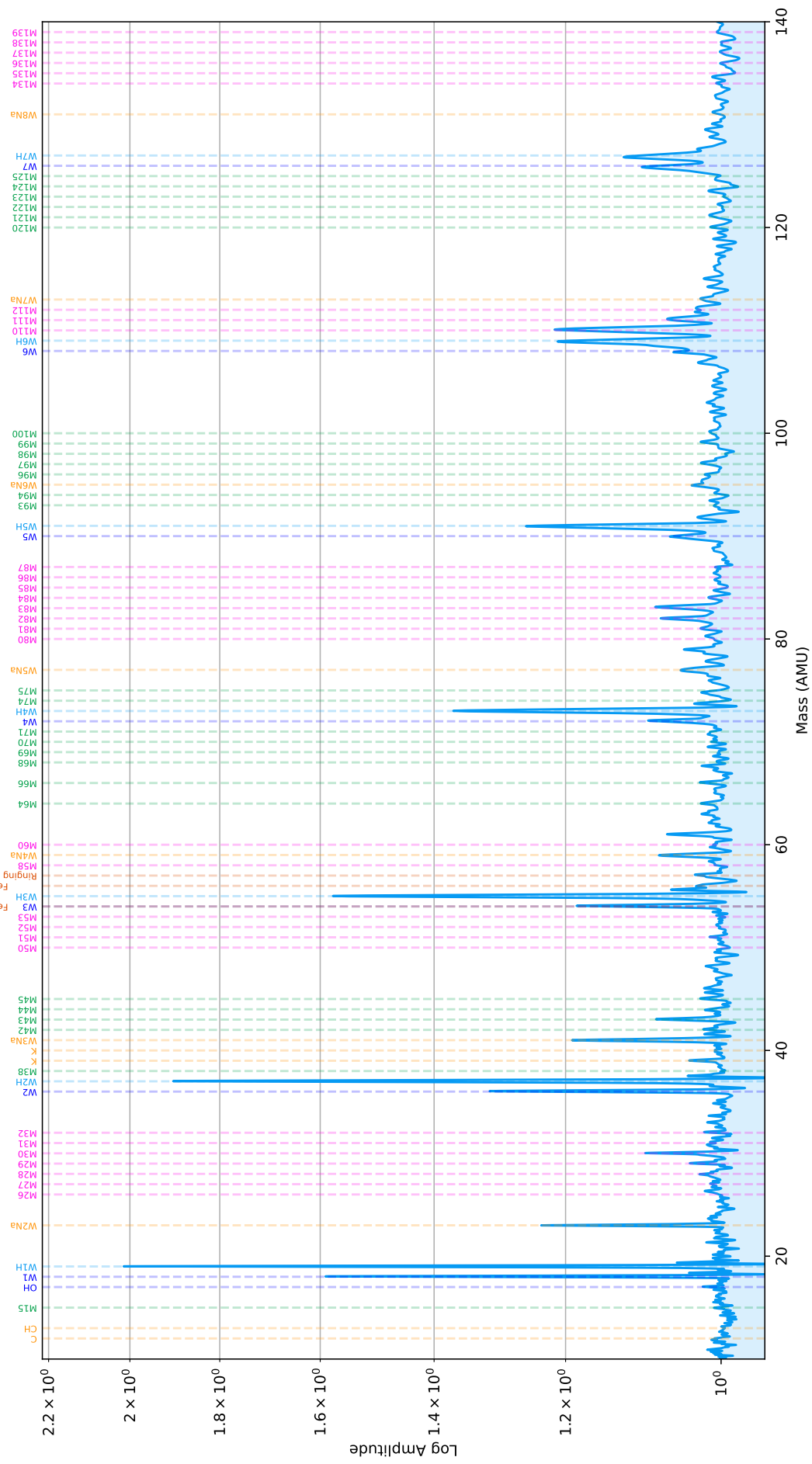


Figure 67: Detail of the summed spectra for impacts of velocities between 4 and 5 km/s in Experiment 2, which had a 60 nm water ice layer covering the histidine surface.

Experiment 2  
Histidine With Ice Cover  
5-6 km/s Summed Spectra Detail

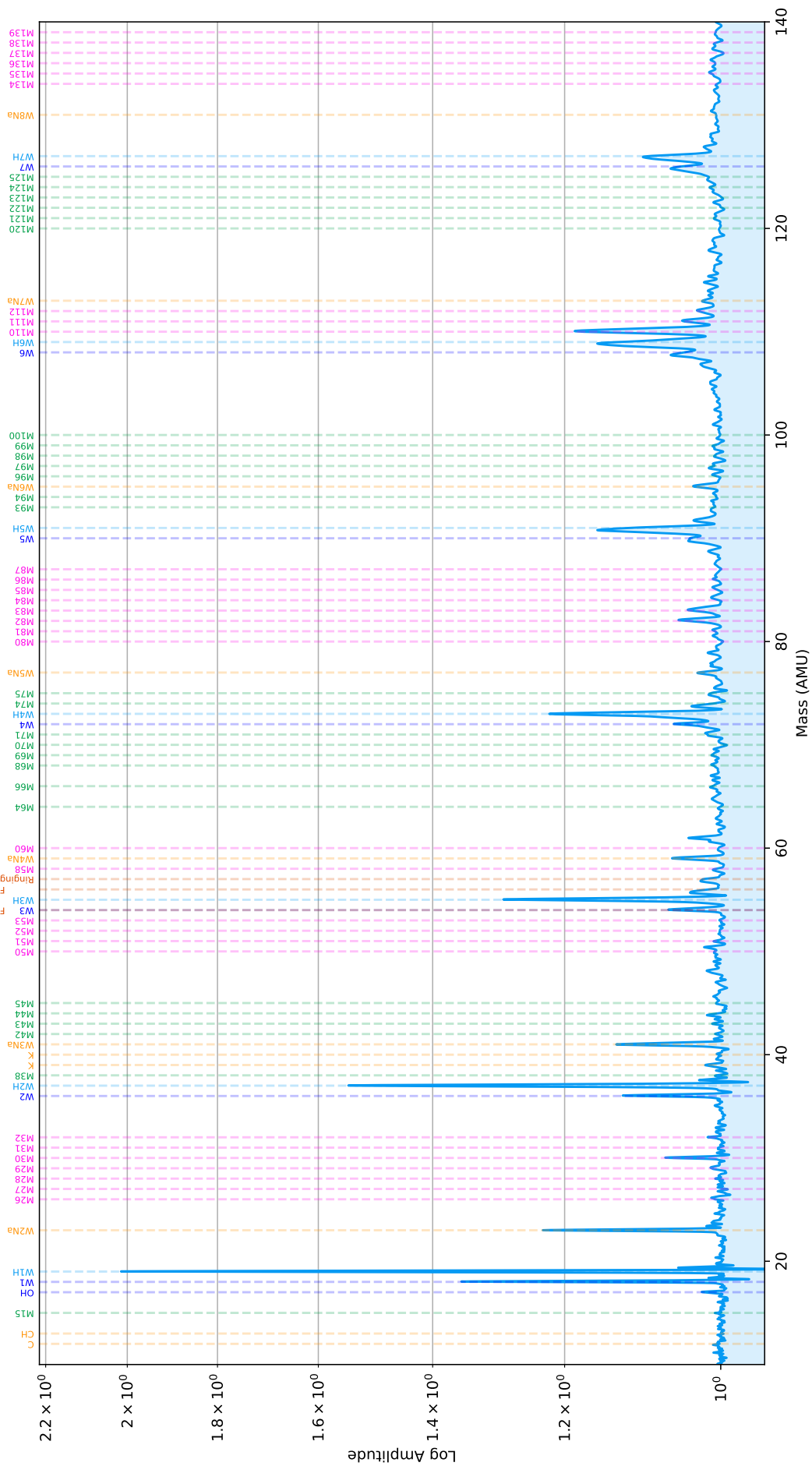


Figure 68: Detail of the summed spectra for impacts of velocities between 5 and 6 km/s in Experiment 2, which had a 60 nm water ice layer covering the histidine surface.

Experiment 2  
Histidine With Ice Cover  
6-7 km/s Summed Spectra Detail

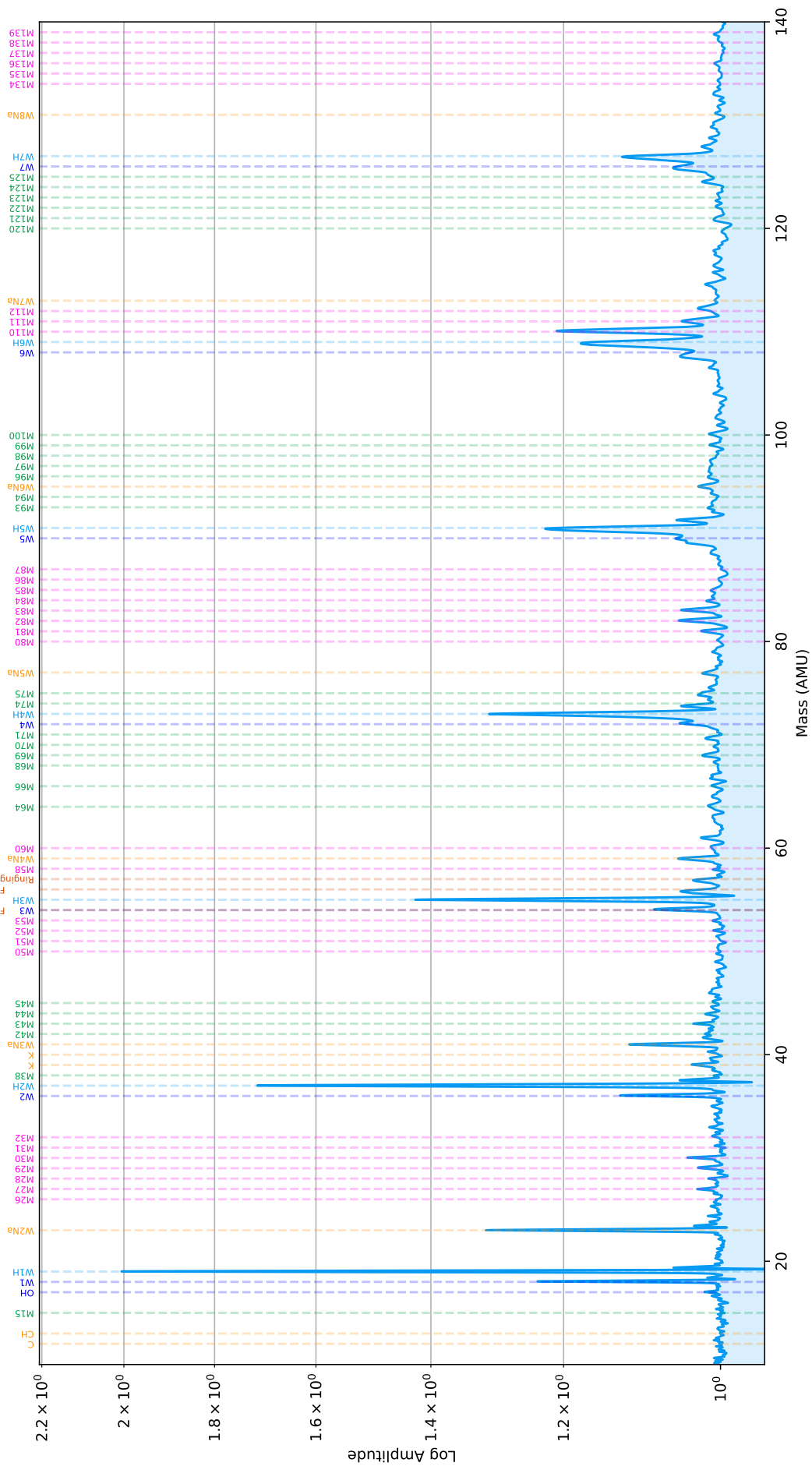


Figure 69: Detail of the summed spectra for impacts of velocities between 6 and 7 km/s in Experiment 2, which had a 60 nm water ice layer covering the histidine surface.



Experiment 2  
Histidine With Ice Cover  
8-9 km/s Summed Spectra Detail

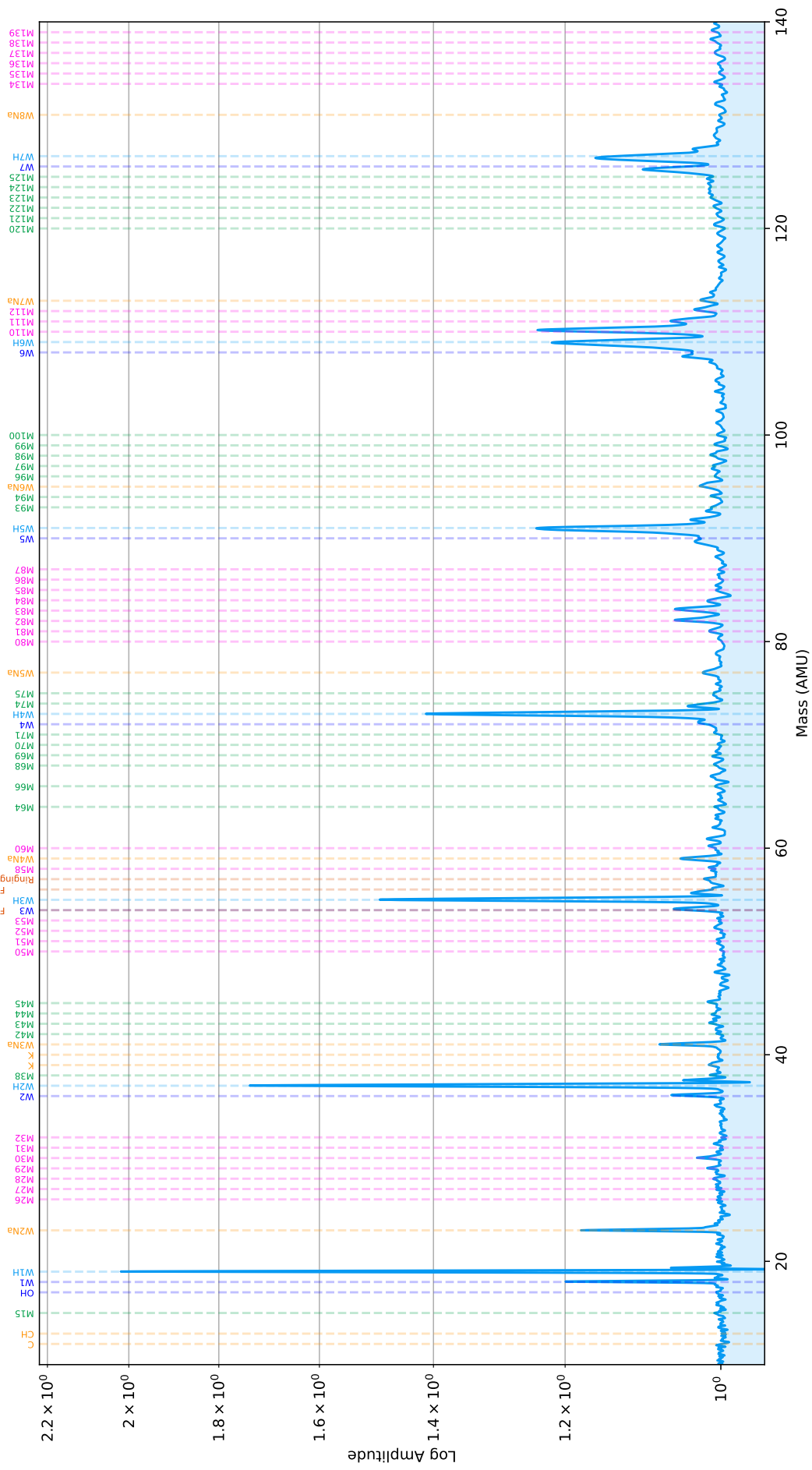


Figure 71: Detail of the summed spectra for impacts of velocities between 8 and 9 km/s in Experiment 2, which had a 60 nm water ice layer covering the histidine surface.



Experiment 2  
 Histidine With Ice Cover  
 10-11 km/s Summed Spectra Detail

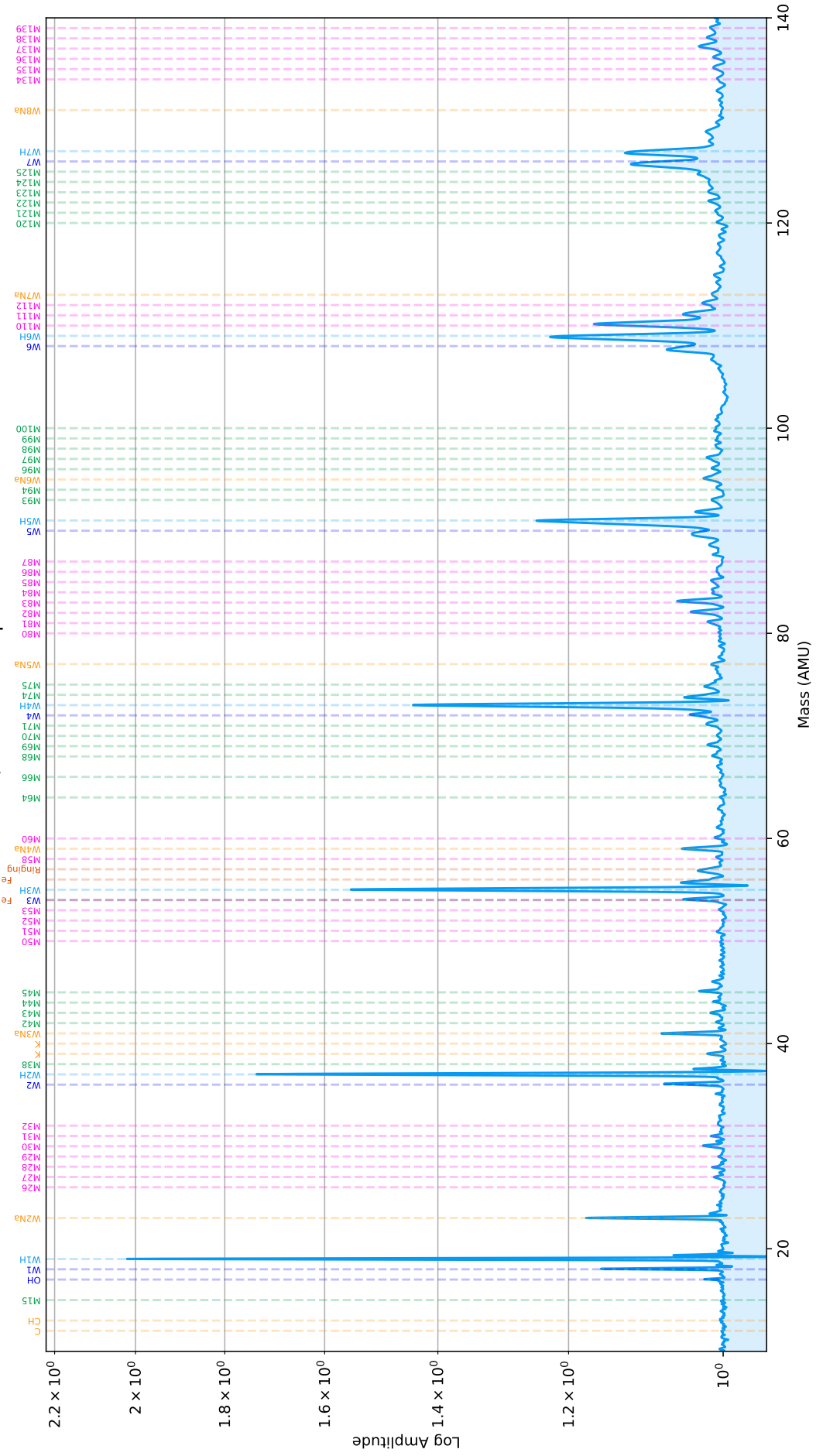


Figure 73: Detail of the summed spectra for impacts of velocities between 10 and 11 km/s in Experiment 2, which had a 60 nm water ice layer covering the histidine surface.



Experiment 2  
 Histidine With Ice Cover  
 12-13 km/s Summed Spectra Detail

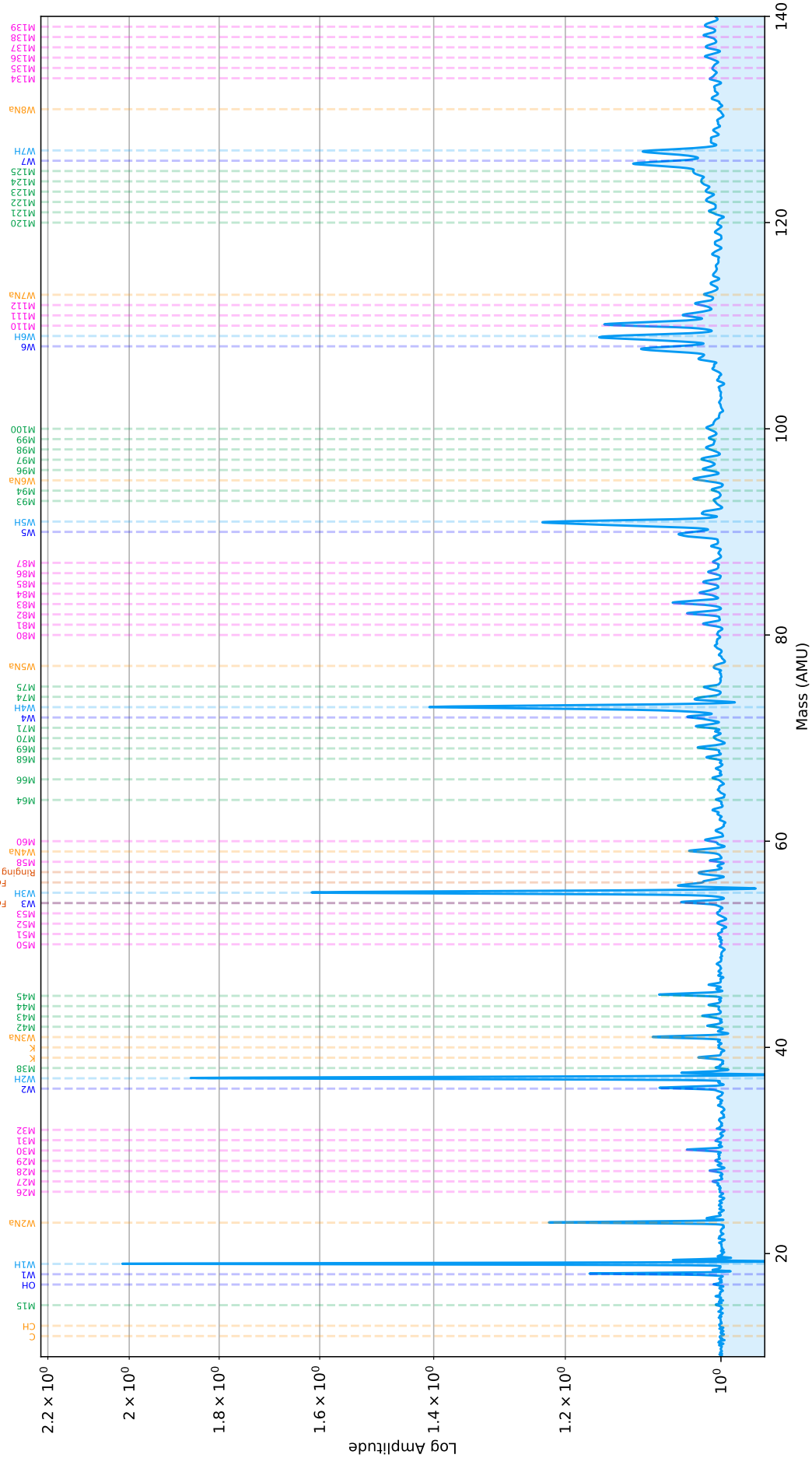


Figure 75: Detail of the summed spectra for impacts of velocities between 12 and 13 km/s in Experiment 2, which had a 60 nm water ice layer covering the histidine surface.

Experiment 2  
 Histidine With Ice Cover  
 13-14 km/s Summed Spectra Detail

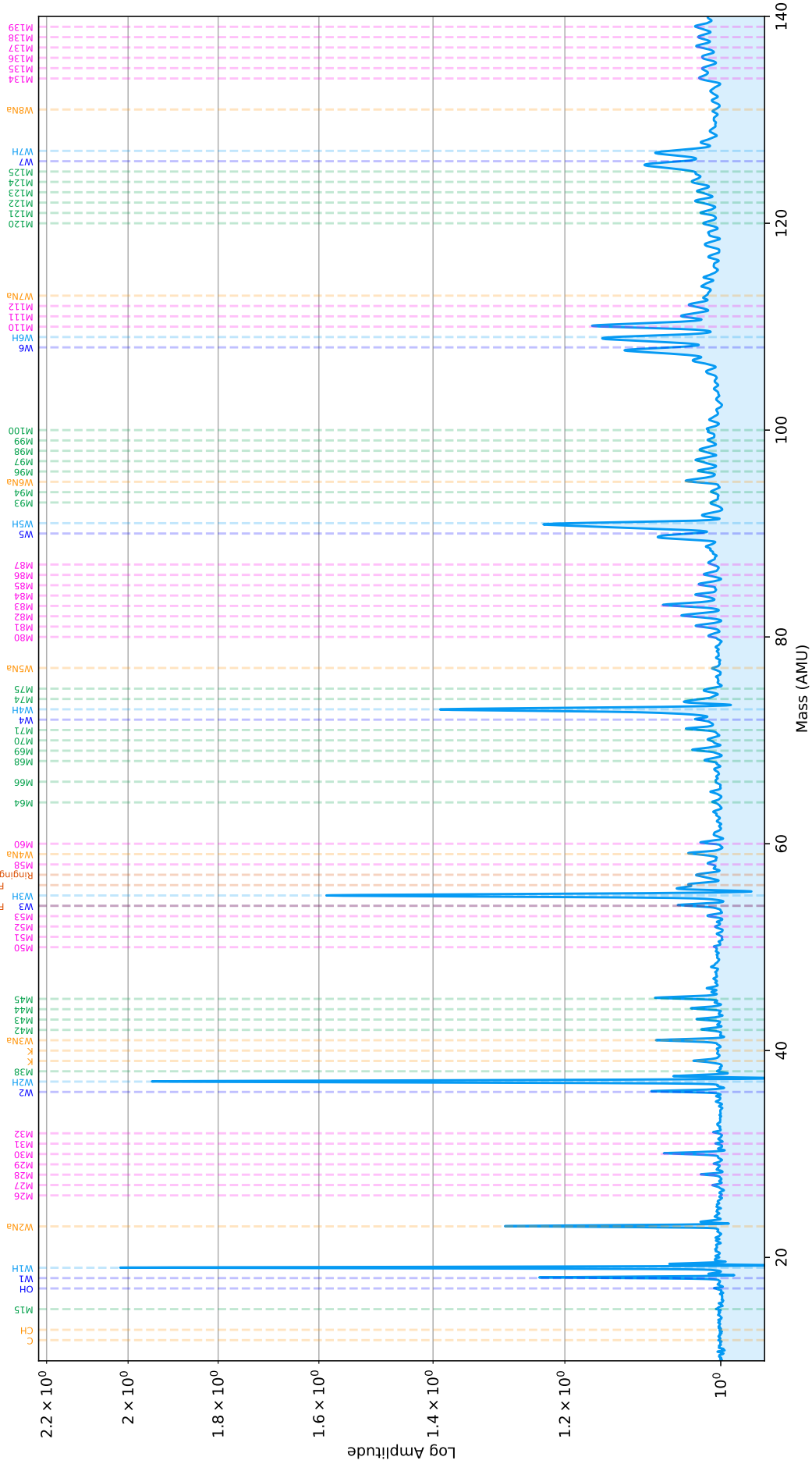


Figure 76: Detail of the summed spectra for impacts of velocities between 13 and 14 km/s in Experiment 2, which had a 60 mm water ice layer covering the histidine surface.

Experiment 2  
 Histidine With Ice Cover  
 14-15 km/s Summed Spectra Detail

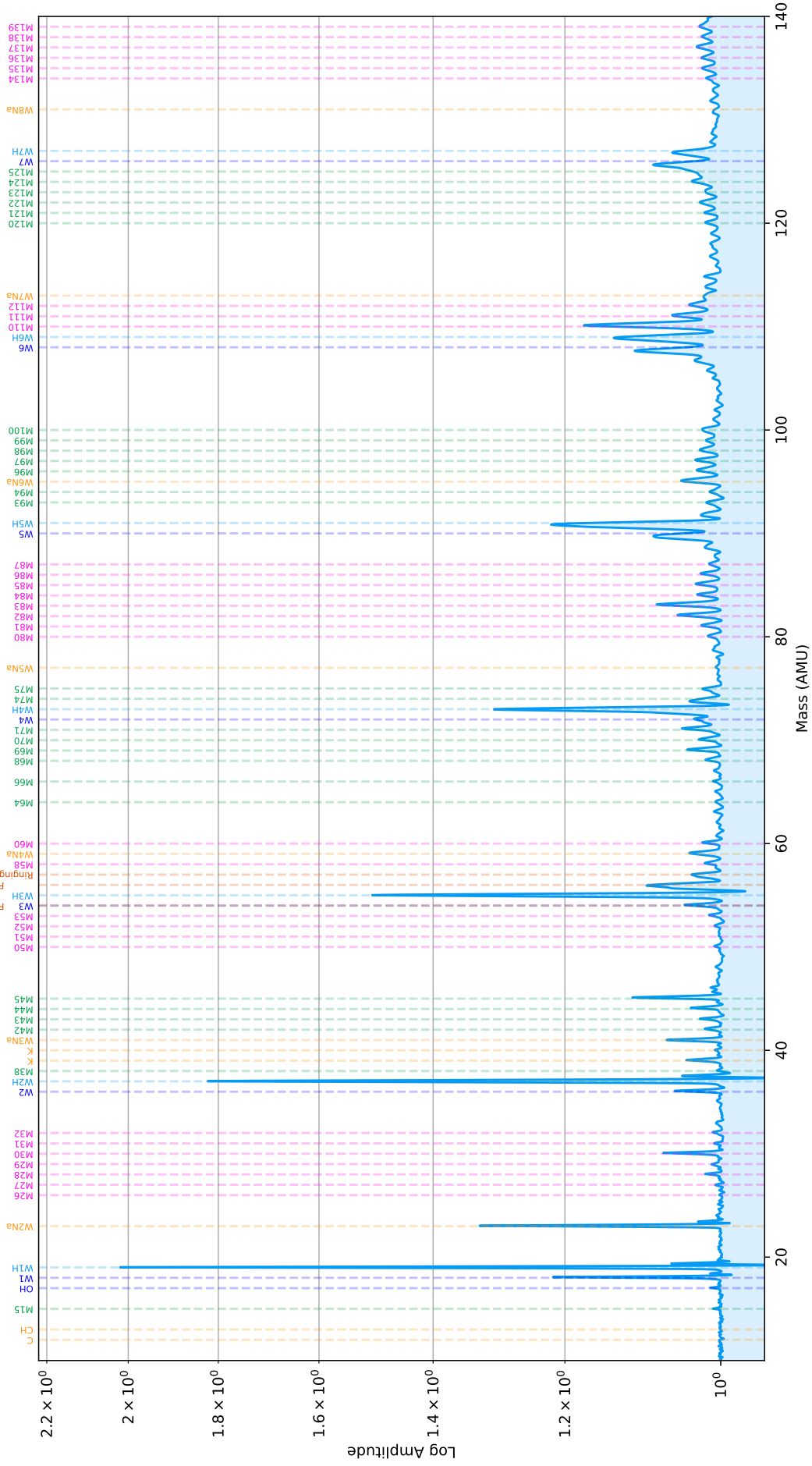


Figure 77: Detail of the summed spectra for impacts of velocities between 14 and 15 km/s in Experiment 2, which had a 60 nm water ice layer covering the histidine surface.

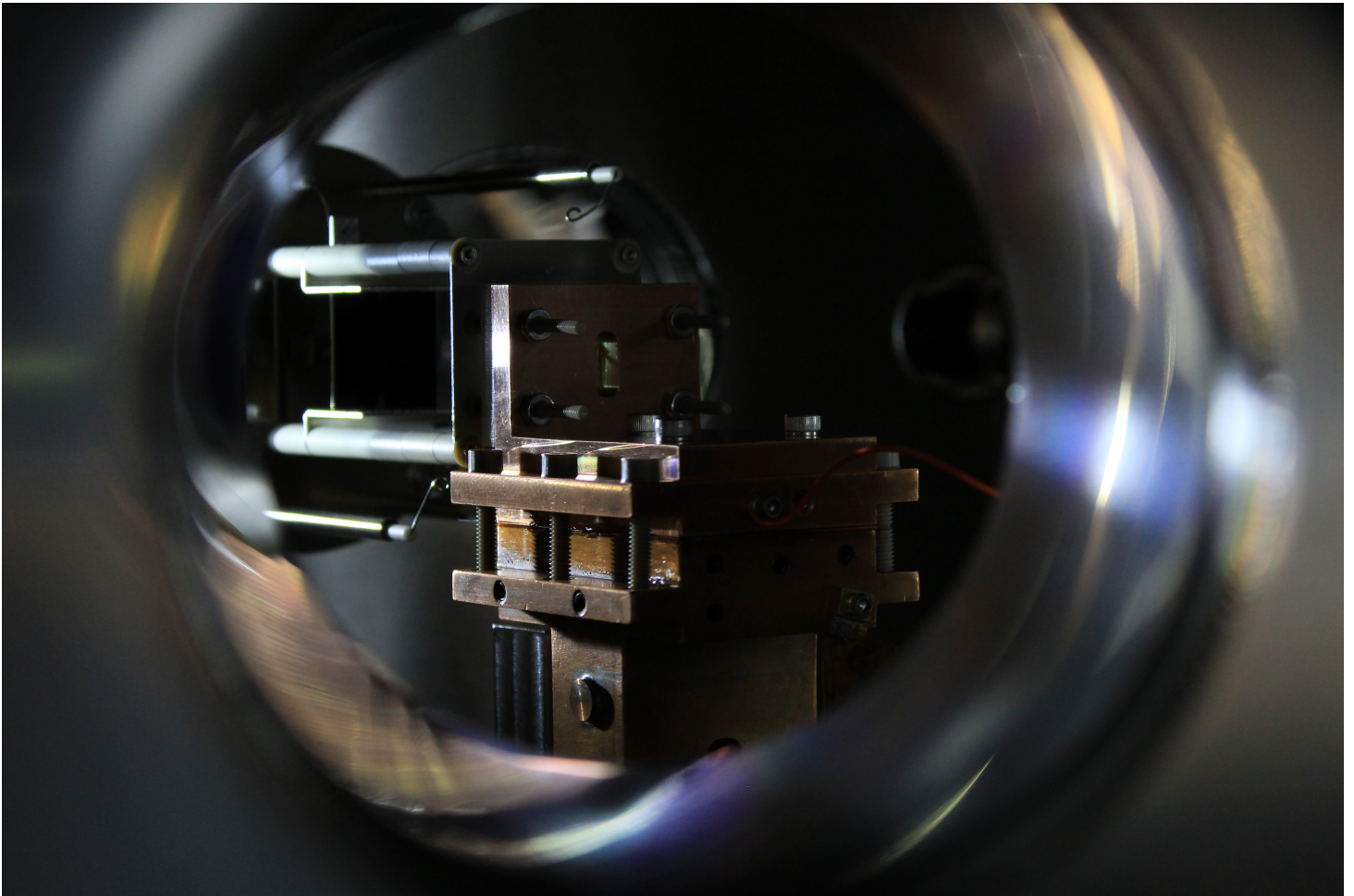


Figure 78: A beautiful photograph of the ice target from behind, looking upstream into the dust source.

## B The Colorado Solar Wind Experiment

Presented here is a paper that I wrote early in my graduate career about characterizing the solar wind

### B.1 Introduction

Airless planetary bodies, such as asteroids, dormant comets, and most moons, have no significant atmospheres or global magnetic fields and therefore have surfaces that are directly exposed to the solar wind plasma. Recent in situ observations on the lunar surface have shown that solar wind bombardment generates several physical processes on the upstream side. These processes include reflected and backscattered solar wind ions [208], neutral atoms backscattered by charge-exchange at the lunar surface [209, 210], and sputtering products.

On the downstream side, a distinct physical feature, plasma wakes (or voids), are formed. These wakes have much lower electron and ion densities than the bulk flow of the solar wind. Because thermal electrons have higher mobility than the supersonic ions, they move into the wakes first, resulting in charge separation near the wake boundaries. Ambipolar electric fields form and accelerate the ions into the wake regions. Complicated physical phenomena are created in the wake region [211], including ion acceleration, rarefaction waves that propagate into the ambient undisturbed plasmas, excitation of plasma oscillations and instabilities, and strong plasma discontinuities at the expansion front. The lunar plasma wake has been widely investigated by computer simulations and in-situ observations [212], and while there have been advances in our understanding of the refilling process [213], there is a lack of fully controlled laboratory experiments addressing wake formation in steady flowing plasmas which are necessary to corroborate these theoretical results. Few laboratory experiments have been performed to study wake formation behind planetary bodies in the solar wind, and even these were investigated using pulsed plasma sources [214, 215, 216, 217]. Further, the wake behind moons, asteroids, and even spacecraft is still being investigated, and laboratory experiments will further elucidate the results of these missions.

Recently, the plasma wakes created by smaller airless bodies such as asteroids and comets have attracted greater attention due to the increase in space missions investigating such bodies [218, 219]. We aim to investigate

the plasma wakes formed at obstacles of various sizes (relative to the Debye length) and shapes using laboratory experiments with more realistic solar wind plasma conditions than any attempted thus far.

Additionally, interactions between the solar wind plasma and localized features on the surface of airless bodies also generate interesting physical processes and phenomena. Studies have shown that the magnetic anomalies on the lunar surface (e.g., crustal magnetic fields) have a strong influence on the incoming solar wind plasma, and this results in deflection/reflection of the solar wind ions [220], the formation of mini-magnetospheres [221, 222, 223, 224, 225], and possibly large positive surface potentials [226, 227, 228, 229]. More interestingly, the high-albedo swirl-shaped markings observed on the lunar surface have been found to show a strong correlation with lunar magnetic anomalies and their interaction with the solar wind plasma [230]. Previously we have experimentally studied the dynamics of charged particles and electrostatic environments at a surface embedded in a magnetic dipole field with non-flowing plasmas [231, 232] and flowing plasmas with low ion energies [228]. The CSWE marks an upgrade to our laboratory studies that allows for realistic solar wind plasma conditions. When the solar wind flows over topographical features on the planetary surfaces (e.g., craters or large boulders), the process of plasma expansion into the craters or the downstream side boulders differs from the the global-scale plasma wakes due to the effects of the electric fields formed at the surface. Electric environments at the topographical surfaces have been mainly studied using computer simulations [233, 234] and have only been recently investigated with laboratory experiments [235].

Plasma-dust interaction has been an important topic for decades, as this determines the dynamics of cometary dust tails, dust exospheres and interplanetary dust [236, 237]. Electrostatic dust transport on the surfaces of airless planetary bodies has been suggested to explain a variety of unusual planetary phenomena [238, 239, 240, 241, 242]. Our recent experiments have shown that the emission and re-absorption of photo- and/or secondary electrons at rough dusty surfaces are responsible for the initial mobilization and launch of regolith dust particles [243]. However, while dust charging and dynamics in thermal plasma conditions have been investigated [244, 245, 246, 247, 248, 249, 250, 251, 252], these dynamics have not been studied under solar wind conditions in laboratory experiments [235].

In summary, many new physical processes have been observed in situ and through computer simulations, but these need to be combined with labora-

tory experiments to answer remaining questions. We have constructed the CSWE at IMPACT to advance our understanding of the solar wind interaction with airless planetary bodies and dust. This device is unique due to its steady state plasma flow with a large cross-section (greater than 12 cm in diameter) that allows for measurement using probes, high ion energy (up to 1 keV, a typical solar wind ion energy), and large ion flux (up to 0.1 mA/cm<sup>2</sup>). This is in contrast to pulsed plasmas or steady state flows with small cross sections mostly used in previous laboratory experiments. This paper describes the performance of the CSWE and the planned experiments.

## B.2 Ion Source and Vacuum Systems

The CSWE consists of a large aperture (12 cm in diameter) high-current Kaufman KDC 100 ion source attached to an experimental vacuum chamber 183 cm in length and 76 cm in diameter. A picture of the chamber is shown in Fig. 79, and a diagram of the ion source is shown in Fig. 80. Gas, such as nitrogen or argon, flows into the ion source where it is ionized by energetic electrons emitted from a heated cathode. Ions created in the source are extracted by a negatively biased accelerating grid through a screen grid into the chamber. The ion energy is selected by the anode potential with respect to ground (i.e. the ion energy is the value of the anode potential in eV). Curvature of the grids creates an ion optics system that diverges the ion flow by 7 degrees to increase the beam cross-section and uniformity in the experimental chamber. A neutralizing filament located at the exit of the source is used to maintain quasi-neutrality of the flowing plasma.

Since the gas flowing into the ion source will build up pressure in the experimental chamber and cause ion-neutral collisions (charge-exchange), a differential pressure chamber backed by a turbo-molecular pump isolates the ion source from the rest of the chamber, which is in turn backed by two diffusion pumps. The chamber itself has a base pressure of  $3 \times 10^{-7}$  Torr and an operating pressure of  $4 \times 10^{-5}$  Torr.

The CSWE has been tested using hydrogen, nitrogen, and argon. While hydrogen is the best analog for the solar wind, its low ionization cross-section requires higher gas flows in order to achieve desired currents. This results in a higher degree of charge-exchange, limiting the observed flux of high velocity ions in the experimental chamber. Nitrogen and Argon, however, can be ionized at a low pressure without significant charge-exchange collisions. For the characterization presented here, the CSWE used N<sub>2</sub><sup>+</sup> because it has a

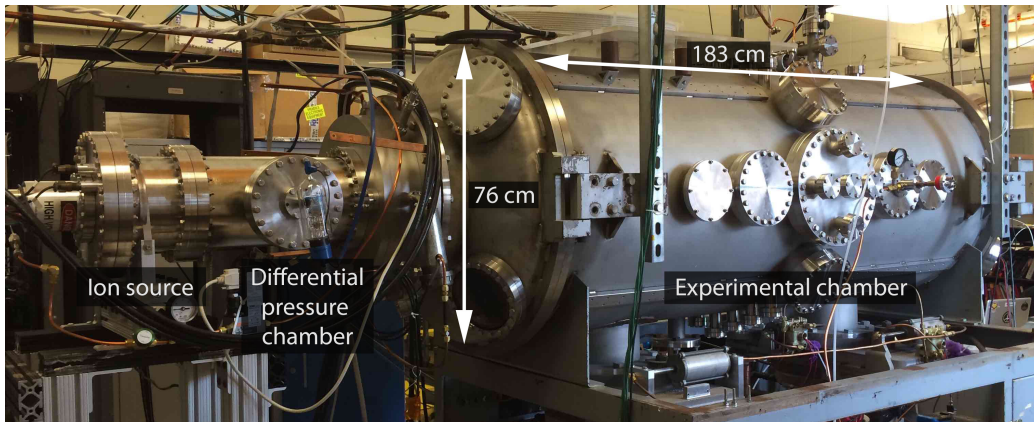


Figure 79: A photo of the CSWE chamber. Ionized gas is created in the ion source, and an accelerating potential pulls the ions into the experimental chamber. A differential pressure chamber prevents excess gas build up in the experimental chamber.

lower mass than Argon.

Depending on the purpose of investigations being performed when studying the solar wind interaction with airless surfaces, a variety of different types of ion sources may be used. For example, ion sources with small apertures (i.e., small cross-section plasma flow) are often used to study how surface processes such as sputtering and space weathering are sustained by solar wind bombardment. To study the physical processes of solar wind interaction with airless bodies, however, we require a large cross-sectional area of plasma flow (that is, a large aperture ion source) to allow access for probe measurements and to immerse the targets in the plasma flow. This large aperture necessarily reduces the effectiveness of differential pumping, resulting in a certain degree of ion-neutral charge-exchange collisions that create a population of thermal ions, a feature not present in the solar wind.

The KDC 100 ion source has a sophisticated set of ion optics which focus the flowing ions into a coherent beam. These optics are designed to operate within a specific parameter space as they become more or less efficient depending on the ion current and accelerating potential settings. For example, the source is not designed to supply large currents at low voltages (such as 80 mA of ion current with a beam energy of 200 eV). For this reason, when the ion current is doubled, the measured ion flux may not be doubled.

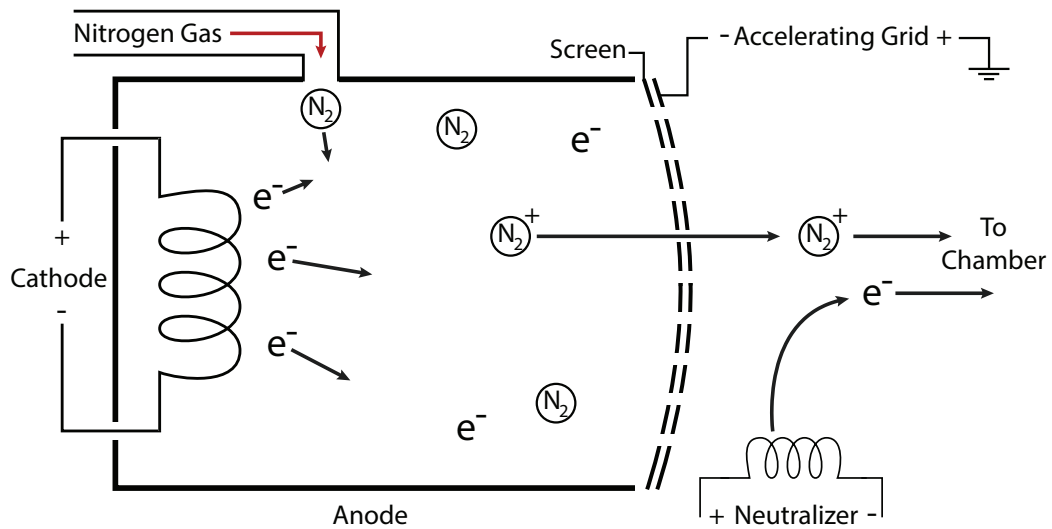


Figure 80: A diagram of the CSWE ion source. Nitrogen gas is ionized by energetic electrons emitted from a hot cathode. Ions are extracted through a screen grid by a negatively biased accelerating grid. Curvature of these grids diverges the beam to increase its cross-section and uniformity. A hot filament neutralizer supplies electrons to maintain quasi-neutrality of the flowing plasma.

## Normalized Energy Analyzer Sample Traces and Derivatives

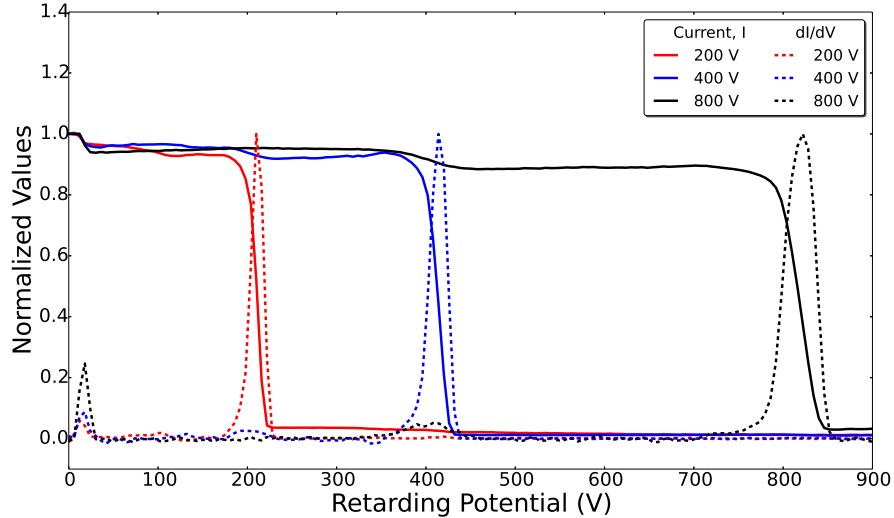


Figure 81: Sample traces from the Ion Energy Analyzer (IEA) showing measured ion current as a function of retarding potential for three different ion energies. Solid lines denote the measured current, while dotted lines denote the derivative. There is a sharp drop at each specified energy, indicating that the flow is highly uniform in its velocity distribution.

### B.3 Diagnostics

The parameters of the plasma produced in the CSWE are measured by a double planar Langmuir probe, which consists of two tantalum discs 6.35 mm in diameter with an insulating layer between them. With this probe, the plasma potential, the electron density, and electron temperature are measured.

An Ion Energy Analyzer (IEA) is used to measure the ion energy and flux [253]. This instrument uses retarding fields to measure the distribution of ion energies. Sample traces from the IEA are shown in Fig. 81. There is a sharp falloff at each selected energy, indicating that the beam energy is highly mono-energetic.

The double Langmuir probe and IEA are mounted on a 2-axis translation stage controllable from outside the vacuum chamber that allows them to be moved around the chamber to map out the plasma parameters in a 2D profile. Positions of the probe measurements are mapped according to the axes defined in Fig. 82.

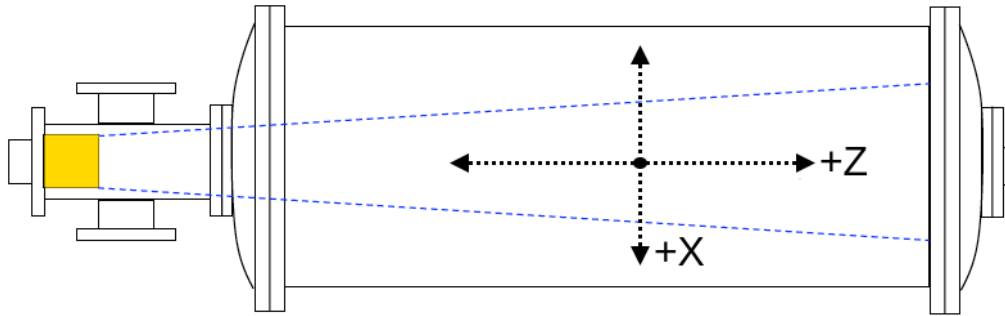


Figure 82: A top-down diagram of the coordinates used in the CSWE. The X-axis measures horizontal displacement from the beam's center axis, while the Z-axis measures the distance from the source itself.

## B.4 Performance

A comparison of plasma parameters between space and laboratory conditions is summarized in Table 7. While the CSWE is capable of achieving the typical solar wind ion energy of 1 keV, the mass of  $N_2^+$  is heavier than that of a proton, resulting in a slower ion velocity. The ion Mach number, however, which is the ratio of the ion flow speed to the ion sound speed, is the dominant term in the ion flow characterization. In both space and laboratory conditions, it is much larger than 1 (indicating supersonic flow). We note that the beam ion temperature has been used to calculate the ion sound speed since it is much larger than the dominant electron temperature. It is impossible and unnecessary to attain the same order of magnitude of either the density or the Debye length of the solar wind in laboratory settings. However, the dimensionless Debye ratio, which is the ratio of the Debye length to the size of an object, has more physical meaning when studying plasma interaction with objects. Planned experiments include inserting objects up to 10 cm in diameter into the plasma beam. Since the CSWE can be used to create Debye lengths of 0.2 cm, the CSWE Debye ratio has a lower limit of 0.02. The Debye ratio is therefore  $\ll 1$ , which is typical for many features of interest (for example, craters on the lunar surface, where the Debye length is on the order of 10 meters). Thus, the CSWE will provide accurate simulation of plasma processes in these regions.

Figure 83 shows results from the IEA as a function of position in both X and Z. The green shaded region denotes the designated experimental region,

	Solar Wind	Laboratory
Velocity, $v_i$	450 km/s	83 km/s
Ion Energy	1 keV	1 keV
Ion Species	H <sup>+</sup>	N <sub>2</sub> <sup>+</sup>
Electron Temperature, $T_e$	10 eV	0.5 eV (cold) 10 eV (hot)
Ion Temperature, $T_i$	10 eV	14 eV
<b>Ion Mach Number</b> , $\frac{v_i}{(T_i/m_i)^{1/2}}$	<b>9</b>	<b>11</b>
Density, $n$	10 cm <sup>-3</sup>	10 <sup>7</sup> – 10 <sup>8</sup> cm <sup>-3</sup>
Debye Length, $\lambda_d$	10 <sup>3</sup> cm	0.2 cm
<b>Debye Ratio</b> , $\lambda_d/L$ (L is the dimension of an object)	$\ll 1$	$\ll 1$ (minimum 0.02)

Table 7: Comparison of parameters between space and laboratory conditions.

while data points outside this space were investigated for completeness. Over the experimental region, the uniformity of the ion flux and electron density is around 30%. In general, the source behaves as expected except for the 200 eV 80 mA ion flow, in that the flux roughly doubles when the source current is doubled. The current density peaks in the center of the beam and drops as the distance from the source increases.

At 200 V anode potential, the flux from 80 mA is lower than that of 40 mA. This occurs because of the efficiency of the source’s ion optics, which is discussed in Section B.2. When operating with these parameters, the current through the accelerating grid in the source is an order of magnitude higher than at other settings, indicating that a significant fraction of the ions collide with the grid and are thus never flowed into the chamber. This provides a lower bound for the anode voltage when operating at high currents. Similarly, the 800 V, 80 mA ion flux is greater in magnitude than expected, and this is likely due to increased performance of the ion optics in this parameter region.

Fig. 84 shows the electron density as measured by the Langmuir probe. Two Maxwellian distributions of electrons are observed in the Langmuir probe current-voltage (I-V) characteristics, with the hot population having a temperature of around 10 eV and density that is approximately 1% of that of the cold population, which have temperatures near 0.5 eV. The plot shown in Fig. 84 includes both of these populations. Bi-Maxwellian electron populations often exist in hot-cathode generated plasmas. Hot electrons may be caused by primary electrons that carry the remaining energies after the ionization of neutral particles. Secondary electrons induced by the bombard-

## Ion Flux

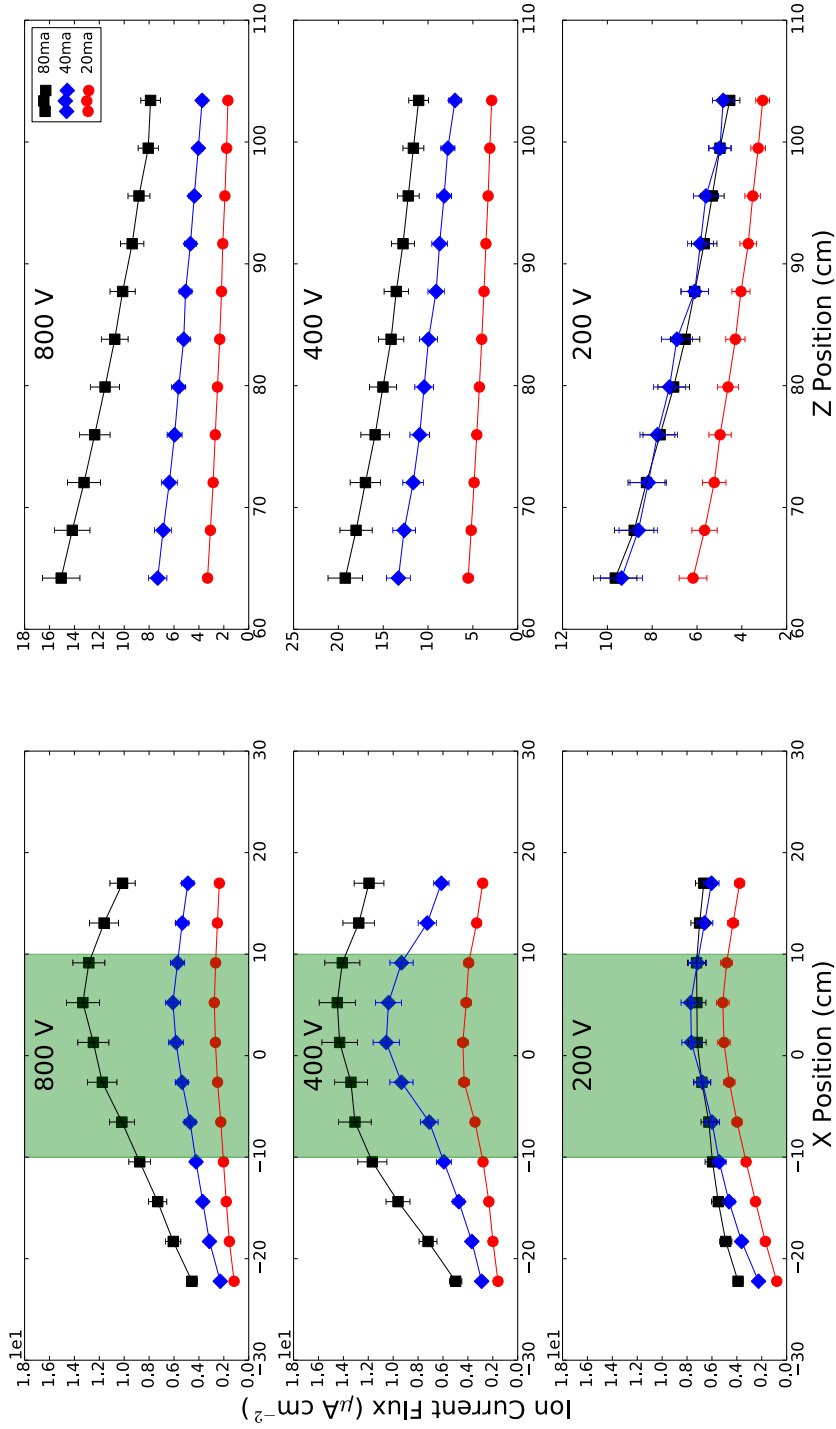


Figure 83: Plots of the particle flux for each position on the x and z axes. These values were calculated from the IEA measurements. The green shaded region denotes the designated experimental region. Note that the flux at 80 mA and 200 V is lower than the flux at 40 mA.

ment of primary electrons or beam ions on the chamber walls may also create such hot electrons [254]. The exact mechanisms remain unclear.

The solar wind ions have a supersonic flow speed with a thermal temperature of about 10 eV. I-V characteristics from the IEA were used to find the temperature of the beam ions. As described in Section B.2, the CSWE produces thermal ions in addition to supersonic ions due to charge-exchange collisions. Although the flux of flowing ions dominates the thermal ion flux, the density of thermal ions is not negligible. The ratio of the beam to thermal ion densities is shown in Fig. 85. Their densities were calculated by dividing the measured fluxes of ions at beam and thermal energies by the speeds at these energies. The ratio is close to one for 800 eV ions, and as high as two for lower ion energies. Thus, the effect of thermal ions on wake and surface topography experiments needs to be taken into account. For investigations of magnetic anomalies or dust charging and dynamics, the flux is a more important parameter than the density. The effect of thermal ions will therefore be less pronounced in these experiments.

## B.5 Planned Experiments

The planned experiments are schematically illustrated in Fig. 86 and detailed below.

### 1) Solar wind interaction with magnetic anomalies

This topic has been extensively studied recently as described in the introduction. However, most of the available in situ space observations addressed the dynamics of particles and fields at high altitudes. We will upgrade our previous laboratory studies [231, 232] from low-energy ( $< 50$  eV) to high-energy (1 keV) ion flow to investigate the electric environments at the surface in magnetic anomaly regions, which have important consequences for understanding various surface processes, such as space weathering and electrostatic dust transport. The ion inertial length,  $d_i$ , is an important parameter in the charge separation process associated with solar wind interaction with lunar magnetic anomalies. On the lunar surface,  $d_i$  is similar to or larger than the characteristic scale of magnetic anomalies [223]. However, the ion inertial length in the CSWE is on the order of a few hundred meters, much larger than CSWE experimental magnetic field length scales. The CSWE studies cases when ions penetrate the dipole field to impact the surface, as has been indicated from observations using the neutral atom energy spectrometer SARA/CENA on Chandrayaan-1 [226].

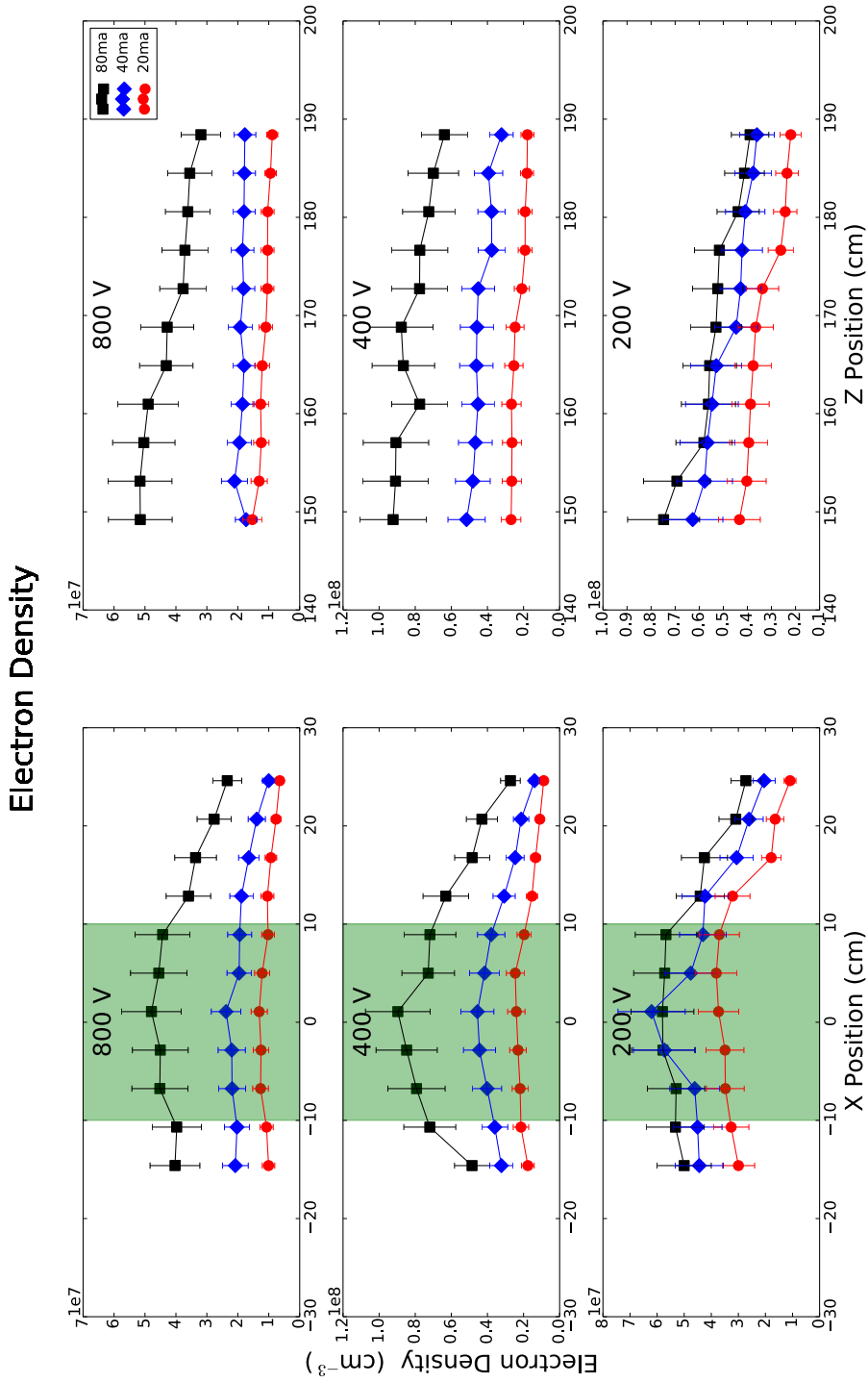


Figure 84: Plots of the electron density for each position on the x and z axes. These values were analyzed from the Langmuir probe measurements. The green shaded region denotes the designated experimental space.

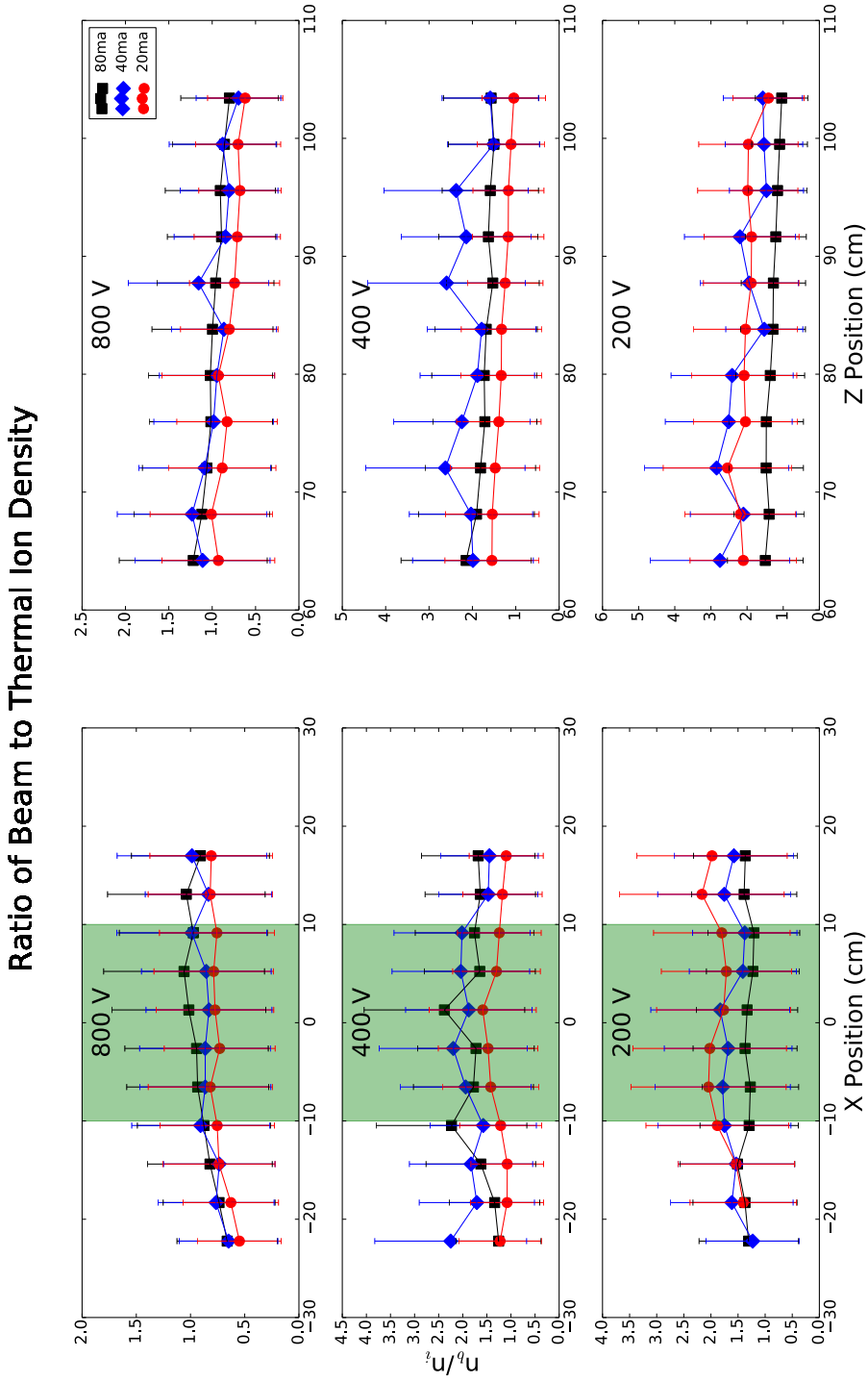


Figure 85: Plots of the ratio of beam to thermal ion density for each position on the x and z axes. These values were calculated from the IEA measurements.

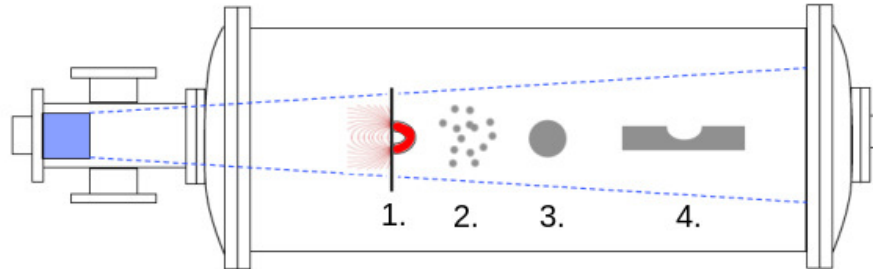


Figure 86: A diagram of the planned experiments. 1. Solar wind interaction with magnetic anomalies. 2. Dust charging and dynamics. 3. Plasma wakes. 4. topographical wakes.

## 2) Charging and dynamics of dust in the solar wind

Charging of dust particles exposed to non-flowing plasmas has been extensively studied, but the CSWE will allow us to study dust charging and dynamics in flowing plasmas with a variety of ion flow speeds. Additionally, interaction of solar wind with dust clouds (e.g., dust exospheres around planetary bodies) will be investigated.

## 3) Plasma wakes

Wake experiments will be performed by inserting objects as large as 10 cm in diameter in the simulated solar wind. The large cross-sectional plasma flow will allow probe diagnoses possible in the wake regions to unravel the dynamics of the electron and ion refilling of the wake. We will map the spatial profiles of plasma parameters and to measure waves and instabilities. In addition, the surface charging in the wake will be studied using a configuration of segmented surfaces with which floating potentials will be measured. We will also investigate the wake of irregular-shaped obstacles in the solar wind, such as asteroids and comets.

## 4) Wakes of topographic features

By inserting models of various surface features such as craters or boulders, we will measure the plasma wake effects of topographic entities. This study is particularly important for understanding the local electric environments in permanently shadowed regions, in which plasma may play a role in volatile

production/loss.

## **B.6 Summary and Conclusion**

A new, large cross-section, high-current, high-energy ion source at the SSERVI IMPACT has been constructed and tested. This source will provide laboratory solar wind simulations that more accurately model realistic conditions than previous experiments involving smaller cross-section sources or those involving low or non-flowing plasmas. The CSWE will provide laboratory investigations of a variety of outstanding questions about solar wind interaction with airless planetary bodies, such as surface electric environment in the presence of magnetic anomalies, dust charging and dynamics, and plasma wakes resulting from airless bodies and topographical features on their surfaces.

## C References

- [1] Dale P. Cruikshank, Robert H. Brown, Wendy M. Calvin, Ted L. Roush, and Mary Jane Bartholomew. *Ices on the Satellites of Jupiter, Saturn, and Uranus*, pages 579–606. Springer Netherlands, Dordrecht, 1998.
- [2] Dale P. Cruikshank, Tobias C. Owen, Cristina Dalle Ore, Thomas R. Geballe, Ted L. Roush, Catherine de Bergh, Scott A. Sandford, Francois Poulet, Gretchen K. Benedix, and Joshua P. Emery. A spectroscopic study of the surfaces of Saturn’s large satellites: H<sub>2</sub>O ice, tholins, and minor constituents. *Icarus*, 175(1):268 – 283, 2005.
- [3] Caitlin A. Griffith, Tobias Owen, Thomas R. Geballe, John Rayner, and Pascal Rannou. Evidence for the exposure of water ice on Titan’s surface. *Science*, 300(5619):628–630, 2003.
- [4] T.C. Owen, D.P. Cruikshank, C.M. Dalle Ore, T.R. Geballe, T.L. Roush, and C. de Bergh. Detection of water ice on Saturn’s satellite Phoebe. *Icarus*, 139(2):379 – 382, 1999.
- [5] Delphine Nna-Mvondo, Bishun Khare, Tomoko Ishihara, and Christopher P. McKay. Experimental impact shock chemistry on planetary icy satellites. *Icarus*, 194(2):822 – 835, 2008.
- [6] WM Grundy, RP Binzel, BJ Buratti, JC Cook, DP Cruikshank, CM Dalle Ore, AM Earle, K Ennico, CJA Howett, AW Lunsford, et al. Surface compositions across pluto and charon. *Science*, 351(6279):aad9189, 2016.
- [7] John F Cooper, Robert E Johnson, Barry H Mauk, Henry B Garrett, and Neil Gehrels. Energetic ion and electron irradiation of the icy galilean satellites. *Icarus*, 149(1):133–159, 2001.
- [8] T Cassidy, P Coll, F Raulin, RW Carlson, RE Johnson, MJ Loeffler, KP Hand, and RA Baragiola. Radiolysis and photolysis of icy satellite surfaces: experiments and theory. *Space science reviews*, 153(1-4):299–315, 2010.
- [9] M Famá, MJ Loeffler, U Raut, and RA Baragiola. Radiation-induced amorphization of crystalline ice. *Icarus*, 207(1):314–319, 2010.

- [10] MJ Loeffler, U Raut, and RA Baragiola. Radiation chemistry in ammonia-water ices. *The Journal of chemical physics*, 132(5):054508, 2010.
- [11] Raúl A Baragiola. Water ice on outer solar system surfaces: Basic properties and radiation effects. *Planetary and Space Science*, 51(14-15):953–961, 2003.
- [12] MJ Loeffler, U Raut, RA Vidal, RA Baragiola, and RW Carlson. Synthesis of hydrogen peroxide in water ice by ion irradiation. *Icarus*, 180(1):265–273, 2006.
- [13] RA Baragiola, M Fama, MJ Loeffler, U Raut, and J Shi. Radiation effects in ice: New results. *Nuclear Instruments and Methods in Physics Research Section B: Beam Interactions with Materials and Atoms*, 266(12-13):3057–3062, 2008.
- [14] John MC Plane. Cosmic dust in the earth’s atmosphere. *Chemical Society Reviews*, 41(19):6507–6518, 2012.
- [15] Eberhard Grün, Ralf Srama, Harald Krüger, Sascha Kempf, Valeri Dikarev, Stefan Helfert, and Georg Moragas-Klostermeyer. 2002 kuiper prize lecture: Dust astronomy. *Icarus*, 174(1):1–14, 2005.
- [16] Zoltan Sternovsky, Eberhard Grün, Keith Drake, Jianfeng Xie, Mihaly Horanyi, Ralf Srama, Sascha Kempf, Frank Postberg, Anna Mocker, Siegfried Auer, et al. Novel instrument for dust astronomy: Dust telescope. In *2011 Aerospace Conference*, pages 1–8. IEEE, 2011.
- [17] Mihály Horányi, Sascha Kempf, Zoltán Sternovsky, Scott Tucker, Petr Pokorný, Neal J Turner, Julie C Castillo-Rogez, Tibor Bálint, John L West, and Jamey R Szalay. Fragments from the origins of the solar system and our interstellar locale (fossil): A cometary, asteroidal, and interstellar dust mission concept. In *2019 IEEE Aerospace Conference*, pages 1–12. IEEE, 2019.
- [18] AH Delsemme. Pristine nature of comets as revealed by their uv spectrum. *Applied optics*, 19(23):4007–4014, 1980.
- [19] Paul R Weissman. How pristine are cometary nuclei? *Comet Nucleus Sample Return Mission*, 249:15–25, 1986.

- [20] Alexander V Krivov, Miodrag Sremčević, Frank Spahn, Valeri V Dikarev, and Konstantin V Kholshchikov. Impact-generated dust clouds around planetary satellites: spherically symmetric case. *Planetary and Space Science*, 51(3):251–269, 2003.
- [21] Harald Krüger, Alexander V Krivov, and Eberhard Grün. A dust cloud of ganymede maintained by hypervelocity impacts of interplanetary micrometeoroids. *Planetary and Space Science*, 48(15):1457–1471, 2000.
- [22] GJ Flynn, DD Durda, LE Sandel, JW Kreft, and MM Strait. Dust production from the hypervelocity impact disruption of the murchison hydrous cm2 meteorite: Implications for the disruption of hydrous asteroids and the production of interplanetary dust. *Planetary and Space Science*, 57(2):119–126, 2009.
- [23] K-U Thiessenhusen, AV Krivov, H Krüger, and E Grün. A dust cloud around pluto and charon. *Planetary and Space Science*, 50(1):79–87, 2002.
- [24] D Jewitt and J Luu. Kuiper belt: collisional production of dust around main-sequence stars. *Astrophysics and Space Science*, 223:164–165, 1995.
- [25] S Yamamoto and T Mukai. Dust production by impacts of interstellar dust on edgeworth-kuiper belt objects. *Astronomy and Astrophysics*, 329:785–791, 1998.
- [26] Andrew Poppe and Mihály Horányi. The effect of nix and hydra on the putative pluto–charon dust cloud. *Planetary and Space Science*, 59(13):1647–1653, 2011.
- [27] Joshua E Colwell and Mihály Horányi. Magnetospheric effects on micrometeoroid fluxes. *Journal of Geophysical Research: Planets*, 101(E1):2169–2175, 1996.
- [28] Detlef Koschny and Eberhard Grün. Impacts into ice–silicate mixtures: Crater morphologies, volumes, depth-to-diameter ratios, and yield. *Icarus*, 154(2):391–401, 2001.

- [29] Amanda R Hendrix, Terry A Hurford, Laura M Barge, Michael T Bland, Jeff S Bowman, William Brinckerhoff, Bonnie J Buratti, Morgan L Cable, Julie Castillo-Rogez, Geoffrey C Collins, et al. The nasa roadmap to ocean worlds. *Astrobiology*, 19(1):1–27, 2019.
- [30] Christopher F Chyba and Kevin P Hand. Astrobiology: the study of the living universe. *Annu. Rev. Astron. Astrophys.*, 43:31–74, 2005.
- [31] Norman Harold Horowitz and J Trefil. To utopia and back—the search for life in the solar system. *Nature*, 323:402, 1986.
- [32] B Schmidt. The astrobiology of europa and the jovian system. *Planetary Astrobiology*, 185, 2020.
- [33] Margaret G Kivelson, Krishan K Khurana, Christopher T Russell, Martin Volwerk, Raymond J Walker, and Christophe Zimmer. Galileo magnetometer measurements: A stronger case for a subsurface ocean at europa. *Science*, 289(5483):1340–1343, 2000.
- [34] Steve Vance, Mathieu Bouffard, Mathieu Choukroun, and Christophe Sotin. Ganymede’s internal structure including thermodynamics of magnesium sulfate oceans in contact with ice. *Planetary and Space Science*, 96:62–70, 2014.
- [35] Jeffrey M Moore and Michael C Malin. Dome craters on ganymede. *Geophysical Research Letters*, 15(3):225–228, 1988.
- [36] Veronica J Bray, Paul M Schenk, H Jay Melosh, Joanna V Morgan, and Gareth S Collins. Ganymede crater dimensions—implications for central peak and central pit formation and development. *Icarus*, 217(1):115–129, 2012.
- [37] Adam P Showman, Ignacio Mosqueira, and James W Head III. On the resurfacing of ganymede by liquid–water volcanism. *Icarus*, 172(2):625–640, 2004.
- [38] M. L. Cable, M. Neveu, H.-W. Hsu, T. M. Hoehler, and Renée Dotson. *Enceladus*, pages 217–246. University of Arizona Press, 2020.
- [39] Alice Le Gall, Cédric Leyrat, Michael A Janssen, Gael Choblet, Gabriel Tobie, Olivier Bourgeois, Antoine Lucas, Christophe Sotin, C Howett,

- Randolph Kirk, et al. Thermally anomalous features in the subsurface of enceladus's south polar terrain. *Nature Astronomy*, 1(4):1–5, 2017.
- [40] Ondřej Čadek, Ondřej Souček, Marie Běhounková, Gaël Choblet, Gabriel Tobie, and Jaroslav Hron. Long-term stability of enceladus' uneven ice shell. *Icarus*, 319:476–484, 2019.
- [41] Frank Postberg, J Schmidt, J Hillier, Sascha Kempf, and Ralf Srama. A salt-water reservoir as the source of a compositionally stratified plume on Enceladus. *Nature*, 474(7353):620–622, 2011.
- [42] F Postberg, S Kempf, JK Hillier, R Srama, SF Green, N McBride, and E Grün. The e-ring in the vicinity of enceladus: Ii. probing the moon's interior—the composition of e-ring particles. *Icarus*, 193(2):438–454, 2008.
- [43] Christophe Zimmer, Krishan K Khurana, and Margaret G Kivelson. Subsurface oceans on europa and callisto: Constraints from galileo magnetometer observations. *Icarus*, 147(2):329–347, 2000.
- [44] Robert T Pappalardo, Michael JS Belton, HH Breneman, MH Carr, Clark R Chapman, GC Collins, T Denk, S Fagents, Paul E Geissler, B Giese, et al. Does europa have a subsurface ocean? evaluation of the geological evidence. *Journal of Geophysical Research: Planets*, 104(E10):24015–24055, 1999.
- [45] Paul M Schenk. Thickness constraints on the icy shells of the galilean satellites from a comparison of crater shapes. *Nature*, 417(6887):419–421, 2002.
- [46] Richard Greenberg, Paul Geissler, Gregory Hoppa, B Randall Tufts, Daniel D Durda, Robert Pappalardo, James W Head, Ronald Greeley, Robert Sullivan, and Michael H Carr. Tectonic processes on europa: Tidal stresses, mechanical response, and visible features. *Icarus*, 135(1):64–78, 1998.
- [47] NASA JPL Planetary Photojournal, <https://photojournal.jpl.nasa.gov/index.html>.
- [48] Christopher F Chyba and Kevin P Hand. Life without photosynthesis. *Science*, 292(5524):2026–2027, 2001.

- [49] Christopher F Chyba and Cynthia B Phillips. Possible ecosystems and the search for life on europa. *Proceedings of the National Academy of Sciences*, 98(3):801–804, 2001.
- [50] Christopher D Parkinson, Mao-Chang Liang, Yuk L Yung, and Joseph L Kirschvink. Habitability of enceladus: planetary conditions for life. *Origins of Life and Evolution of Biospheres*, 38(4):355–369, 2008.
- [51] RT Pappalardo, D Senske, H Korth, R Klima, S Vance, K Craft, et al. The europa clipper mission: Exploring the habitability of a unique icy world. In *European Planetary Science Congress*, pages EPSC2017–304, 2017.
- [52] RT Pappalardo, S Vance, F Bagenal, BG Bills, DL Blaney, DD Blankenship, WB Brinckerhoff, JEP Connerney, KP Hand, Tori M Hoehler, et al. Science potential from a europa lander. *Astrobiology*, 13(8):740–773, 2013.
- [53] PC Thomas, R Tajeddine, MS Tiscareno, JA Burns, J Joseph, TJ Lored, P Helfenstein, and C Porco. Enceladus’s measured physical libration requires a global subsurface ocean. *Icarus*, 264:37–47, 2016.
- [54] Jonathan Lunine, Hunter Waite, Frank Postberg, Linda Spilker, and Karla Clark. Enceladus life finder: the search for life in a habitable moon. In *EGU General Assembly Conference Abstracts*, page 14923, 2015.
- [55] Olivier Grasset, MK Dougherty, A Coustenis, EJ Bunce, C Erd, D Titov, M Blanc, A Coates, P Drossart, LN Fletcher, et al. Jupiter icy moons explorer (juice): An esa mission to orbit ganymede and to characterise the jupiter system. *Planetary and Space Science*, 78:1–21, 2013.
- [56] Candice J Hansen, L Esposito, AIF Stewart, J Colwell, A Hendrix, W Pryor, D Shemansky, and R West. Enceladus’ water vapor plume. *Science*, 311(5766):1422–1425, 2006.
- [57] Frank Postberg, Roger N Clark, Candice J Hansen, Andrew J Coates, Cristina M Dalle Ore, Francesca Scipioni, M Hedman, and J Waite.

Plume and surface composition of enceladus. *Enceladus and the icy moons of Saturn*, pages 129–162, 2018.

- [58] Carolyn C Porco, Luke Dones, and Colin Mitchell. Could it be snowing microbes on enceladus? assessing conditions in its plume and implications for future missions. *Astrobiology*, 17(9):876–901, 2017.
- [59] Sascha Kempf, Uwe Beckmann, and Jürgen Schmidt. How the enceladus dust plume feeds saturn’s e ring. *Icarus*, 206(2):446–457, 2010.
- [60] J Hunter Waite, Michael R Combi, Wing-Huen Ip, Thomas E Cravens, Ralph L McNutt, Wayne Kasprzak, Roger Yelle, Janet Luhmann, Hasso Niemann, David Gell, et al. Cassini ion and neutral mass spectrometer: Enceladus plume composition and structure. *science*, 311(5766):1419–1422, 2006.
- [61] Frank Postberg, Nozair Khawaja, Bernd Abel, Gael Choblet, Christopher R Glein, Murthy S Gudipati, Bryana L Henderson, Hsiang-Wen Hsu, Sascha Kempf, Fabian Klenner, et al. Macromolecular organic compounds from the depths of enceladus. *Nature*, 558(7711):564–568, 2018.
- [62] Lorenz Roth, Joachim Saur, Kurt D Retherford, Darrell F Strobel, Paul D Feldman, Melissa A McGrath, and Francis Nimmo. Transient water vapor at europa’s south pole. *science*, 343(6167):171–174, 2014.
- [63] William B Sparks, KP Hand, MA McGrath, E Bergeron, M Cracraft, and SE Deustua. Probing for evidence of plumes on europa with hst/stis. *The Astrophysical Journal*, 829(2):121, 2016.
- [64] Xianzhe Jia, Margaret G Kivelson, Krishan K Khurana, and William S Kurth. Evidence of a plume on europa from galileo magnetic and plasma wave signatures. *Nature Astronomy*, 2(6):459–464, 2018.
- [65] HLF Huybrighs, Elias Roussos, Aljona Blöcker, Norbert Krupp, Y Futaana, S Barabash, LZ Hadid, MKG Holmberg, O Lomax, and O Witasse. An active plume eruption on europa during galileo flyby e26 as indicated by energetic proton depletions. *Geophysical Research Letters*, 47(10):e2020GL087806, 2020.

- [66] Randolph L Kirk, Laurence A Soderblom, RH Brown, SW Kieffer, and JS Kargel. Triton’s plumes: discovery, characteristics, and models. *Neptune and Triton*, pages 949–989, 1995.
- [67] Laurence A Soderblom, SW Kieffer, TL Becker, Robert H Brown, AF Cook, CJ Hansen, TV Johnson, Randolph L Kirk, and EM Shoemaker. Triton’s geyser-like plumes: Discovery and basic characterization. *Science*, 250(4979):410–415, 1990.
- [68] Paul M Schenk, Chloe B Beddingfield, Tanguy Bertrand, Carver Bier-son, Ross Beyer, Veronica J Bray, Dale Cruikshank, William M Grundy, Candice Hansen, Jason Hofgartner, et al. Triton: Topography and geology of a probable ocean world with comparison to pluto and charon. *Remote Sensing*, 13(17):3476, 2021.
- [69] Candice J Hansen, J Castillo-Rogez, W Grundy, JD Hofgartner, ES Martin, K Mitchell, F Nimmo, TA Nordheim, C Paty, Lynnae C Quick, et al. Triton: Fascinating moon, likely ocean world, compelling destination! *The Planetary Science Journal*, 2(4):137, 2021.
- [70] Petra Rettberg, Alexandre M Anesio, Victor R Baker, John A Baross, Sherry L Cady, Emmanouil Detsis, Christine M Foreman, Ernst Hauber, Gian Gabriele Ori, David A Pearce, et al. Planetary protection and mars special regions—a suggestion for updating the definition, 2016.
- [71] Ralf Srama, Sascha Kempf, Georg Moragas-Klostermeyer, Nicolas Al- tobelli, Siegfried Auer, Uwe Beckmann, Sebastian Bugiel, Marcia Bur- ton, T Economomou, Hugo Fechtig, et al. The cosmic dust analyser onboard cassini: ten years of discoveries. *CEAS Space Journal*, 2(1):3–16, 2011.
- [72] Manfred A Lange and Thomas J Ahrens. Impact experiments in low- temperature ice. *Icarus*, 69(3):506–518, 1987.
- [73] J Kissel, RZ Sagdeev, JL Bertaux, VN Angarov, J Audouze, JE Blam- ont, K Büchler, EN Evlanov, H Fechtig, MN Fomenkova, et al. Com- position of comet halley dust particles from vega observations. *Nature*, 321(6067):280–282, 1986.

- [74] J Kissel, A Glasmachers, Eberhard Grün, H Henkel, H Höfner, G Haerendel, H Von Hoerner, K Hornung, EK Jessberger, FR Krueger, et al. Cometary and interstellar dust analyzer for comet wild 2. *Journal of Geophysical Research: Planets*, 108(E10), 2003.
- [75] Frank Postberg, Sascha Kempf, Jürgen Schmidt, N Brilliantov, Alexander Beinsen, Bernd Abel, Udo Buck, and Ralf Srama. Sodium salts in e-ring ice grains from an ocean below the surface of enceladus. *Nature*, 459(7250):1098–1101, 2009.
- [76] N Khawaja, F Postberg, J Hillier, F Klenner, S Kempf, L Nölle, R Reviol, Z Zou, and R Srama. Low-mass nitrogen-, oxygen-bearing, and aromatic compounds in enceladean ice grains. *Monthly Notices of the Royal Astronomical Society*, 489(4):5231–5243, 2019.
- [77] Marc Neveu, Lindsay E Hays, Mary A Voytek, Michael H New, and Mitchell D Schulte. The ladder of life detection. *Astrobiology*, 18(11):1375–1402, 2018.
- [78] S Kempf, N Altobelli, C Briois, E Grün, M Horanyi, F Postberg, J Schmidt, R Srama, Z Sternovsky, G Tobie, et al. Suda: a dust mass spectrometer for compositional surface mapping for a mission to europa. In *International Workshop on Instrumentation for Planetary Missions*, volume 3, page 7, 2014.
- [79] William Goode, Sascha Kempf, and Jürgen Schmidt. Detecting the surface composition of geological features on europa and ganymede using a surface dust analyzer. *Planetary and Space Science*, 208:105343, 2021.
- [80] DJ McComas, ER Christian, Nathan A Schwadron, N Fox, J Westlake, F Allegrini, DN Baker, D Biesecker, M Bzowski, G Clark, et al. Interstellar mapping and acceleration probe (imap): A new nasa mission. *Space science reviews*, 214(8):1–54, 2018.
- [81] Zoltan Sternovsky, Rebecca Mikula, Mihaly Horanyi, Jon Hillier, Ralf Srama, and Frank Postberg. Laboratory calibration of the interstellar dust experiment (idex) instrument. In *AGU Fall Meeting 2021*. AGU, 2021.

- [82] Kim Reh, Linda Spilker, Jonathan I Lunine, J Hunter Waite, Morgan L Cable, Frank Postberg, and Karla Clark. Enceladus life finder: the search for life in a habitable moon. In *2016 IEEE Aerospace Conference*, pages 1–8. IEEE, 2016.
- [83] Giuseppe Mitri, Frank Postberg, Jason M Soderblom, Peter Wurz, Paolo Tortora, Bernd Abel, Jason W Barnes, Marco Berga, Nathalie Carrasco, Athena Coustenis, et al. Explorer of enceladus and titan (e2t): Investigating ocean worlds’ evolution and habitability in the solar system. *Planetary and space science*, 155:73–90, 2018.
- [84] R Srama, F Postberg, H Henkel, T Klopfer, Y Li, J Simolka, S Bugiel, S Kempf, J Hillier, N Khawaja, et al. Enceladus icy jet analyzer (enija): Search for life with a high resolution tof-ms for in situ characterization of high dust density regions. *Eur. Planet. Sci. Congr*, 10, 2015.
- [85] Anthony Shu, Andrew Collette, Keith Drake, Eberhard Grün, Mihaly Horanyi, Sascha Kempf, Anna Mocker, Tobin Munsat, Paige Northway, Ralf Srama, Zoltan Sternovsky, and Evan Thomas. 3 MV hypervelocity dust accelerator at the Colorado center for lunar dust and atmospheric studies. *Review of Scientific Instruments*, 83(7):075108, 2012.
- [86] MM Kreitman and JT Callahan. Thermal conductivity of apiezon n grease at liquid helium temperatures. *Cryogenics*, 10(2):155–159, 1970.
- [87] DuPont Kapton HN, <https://www.dupont.com/products/kapton-hn.html>.
- [88] Polyether ether ketone, acquired from Solidspot, [https://www.solidspot.com/peek\\_screws.html](https://www.solidspot.com/peek_screws.html).
- [89] Jordan Time of Flight Products, <http://www.rmjordan.com/linear-tof.html>.
- [90] Andrew Oakleigh Nelson, Richard Dee, Murthy S. Gudipati, Mihaly Horanyi, David James, Sascha Kempf, Tobin Munsat, Zoltan Sternovsky, and Zach Ulibarri. New experimental capability to investigate the hypervelocity micrometeoroid bombardment of cryogenic surfaces. *Review of Scientific Instruments*, 87(2):024502, 2016.

- [91] Perry A Gerakines, Reggie L Hudson, Marla H Moore, and Jan-Luca Bell. In situ measurements of the radiation stability of amino acids at 15–140 k. *Icarus*, 220(2):647–659, 2012.
- [92] Pengwei Zhang, Wan Chan, Irene L Ang, Rui Wei, Melody MT Lam, Kate MK Lei, and Terence CW Poon. Revisiting fragmentation reactions of protonated  $\alpha$ -amino acids by high-resolution electrospray ionization tandem mass spectrometry with collision-induced dissociation. *Scientific reports*, 9(1):1–10, 2019.
- [93] RA Jacobs-Fedore and DE Stroe. Thermophysical properties of vespel sp-1. *Thermal conductivity*, 27:231–238, 2005.
- [94] Paasche Airbrush Company, <https://www.paascheairbrush.com/TG-3AS>.
- [95] Millipore Sigma AtmosBag, <https://www.sigmaaldrich.com/US/en/product/aldrich/z530212>.
- [96] DFRobot SHT35 Relative Humidity Sensor, <https://www.dfrobot.com/product-2016.html>.
- [97] Paul G Higgs and Ralph E Pudritz. A thermodynamic basis for prebiotic amino acid synthesis and the nature of the first genetic code. *Astrobiology*, 9(5):483–490, 2009.
- [98] E Pierazzo and CF Chyba. Amino acid survival in large cometary impacts. *Meteoritics & Planetary Science*, 34(6):909–918, 1999.
- [99] Alyssa K Cobb and Ralph E Pudritz. Nature’s starships. i. observed abundances and relative frequencies of amino acids in meteorites. *The Astrophysical Journal*, 783(2):140, 2014.
- [100] Alyssa K Cobb, Ralph E Pudritz, and Ben KD Pearce. Nature’s starships. ii. simulating the synthesis of amino acids in meteorite parent bodies. *The Astrophysical Journal*, 809(1):6, 2015.
- [101] Kevin Zahnle and David Grinspoon. Comet dust as a source of amino acids at the cretaceous/tertiary boundary. *Nature*, 348(6297):157–160, 1990.

- [102] Michael H Engel and Bartholomew Nagy. Distribution and enantiomeric composition of amino acids in the murchison meteorite. *Nature*, 296(5860):837–840, 1982.
- [103] Toshiki Koga and Hiroshi Naraoka. A new family of extraterrestrial amino acids in the murchison meteorite. *Scientific reports*, 7(1):1–8, 2017.
- [104] John R Cronin and Carleton B Moore. Amino acid analyses of the murchison, murray, and allende carbonaceous chondrites. *Science*, 172(3990):1327–1329, 1971.
- [105] Akira Shimoyama, Cyril Ponnampereuma, and Keizo Yanai. Amino acids in the yamato carbonaceous chondrite from antarctica. *Nature*, 282(5737):394–396, 1979.
- [106] Jamie E Elsila, Daniel P Glavin, and Jason P Dworkin. Cometary glycine detected in samples returned by stardust. *Meteoritics & planetary science*, 44(9):1323–1330, 2009.
- [107] Kathrin Altwegg, Hans Balsiger, Akiva Bar-Nun, Jean-Jacques Berthelier, Andre Bieler, Peter Bochsler, Christelle Briois, Ursina Calmonte, Michael R Combi, Hervé Cottin, et al. Prebiotic chemicals—amino acid and phosphorus—in the coma of comet 67p/churyumov-gerasimenko. *Science advances*, 2(5):e1600285, 2016.
- [108] J Kissel, FR Krueger, J Silén, and BC Clark. The cometary and interstellar dust analyzer at comet 81p/wild 2. *Science*, 304(5678):1774–1776, 2004.
- [109] Chris Paranicas, JF Cooper, HB Garrett, RE Johnson, and SJ Sturmer. Europa’s radiation environment and its effects on the surface. In *Europa*, pages 529–544. University of Arizona Press Tucson, 2009.
- [110] TA Nordheim, KP Hand, and C Paranicas. Preservation of potential biosignatures in the shallow subsurface of europa. *Nature Astronomy*, 2(8):673–679, 2018.
- [111] Grazyna E Orzechowska, Jay D Goguen, Paul V Johnson, Alexandre Tsapin, and Isik Kanik. Ultraviolet photolysis of amino acids in a 100 k

- water ice matrix: Application to the outer solar system bodies. *Icarus*, 187(2):584–591, 2007.
- [112] Jeffrey M Moore, Greg Black, Bonnie Buratti, Cynthia B Phillips, John Spencer, and Robert Sullivan. Surface properties, regolith, and landscape degradation. In *Europa*, pages 329–349. University of Arizona Press Tucson, 2009.
- [113] Edward B Bierhaus, Kevin Zahnle, Clark R Chapman, RT Pappalardo, WR McKinnon, and KK Khurana. Europa’s crater distributions and surface ages. In *Europa*, page 161. University of Arizona Press Tucson, 2009.
- [114] Richard Greenberg, Gregory V Hoppa, BR Tufts, Paul Geissler, Jean-nemarie Riley, and Steven Kadel. Chaos on europa. *Icarus*, 141(2):263–286, 1999.
- [115] Geoffrey Collins and Francis Nimmo. Chaotic terrain on europa. *Europa*, pages 259–281, 2009.
- [116] Samantha K Trumbo, Michael E Brown, and Kevin P Hand. Sodium chloride on the surface of europa. *Science advances*, 5(6):eaaw7123, 2019.
- [117] C. P. McKay, A. Davila, C. R. Glein, K. P. Hand, and A. Stockton. *Enceladus Astrobiology, Habitability, and the Origin of Life*, pages 437–452. University of Arizona Press, 2018.
- [118] Stanley L Miller. A production of amino acids under possible primitive earth conditions. *Science*, 117(3046):528–529, 1953.
- [119] Stanley L Miller, Harold C Urey, and J Oro. Origin of organic compounds on the primitive earth and in meteorites. *Journal of Molecular Evolution*, 9(1):59–72, 1976.
- [120] Stanley L Miller. Which organic compounds could have occurred on the prebiotic earth? In *Cold Spring Harbor symposia on quantitative biology*, volume 52, pages 17–27. Cold Spring Harbor Laboratory Press, 1987.

- [121] Martin Ferus, Fabio Pietrucci, Antonino Marco Saitta, Antonín Knížek, Petr Kubelík, Ondřej Ivanek, Violetta Shestivska, and Svato-pluk Civiš. Formation of nucleobases in a miller–urey reducing atmosphere. *Proceedings of the National Academy of Sciences*, 114(17):4306–4311, 2017.
- [122] Shin Miyakawa, Hiroto Yamanashi, Kensei Kobayashi, H James Cleaves, and Stanley L Miller. Prebiotic synthesis from co atmospheres: implications for the origins of life. *Proceedings of the National Academy of Sciences*, 99(23):14628–14631, 2002.
- [123] H James Cleaves, John H Chalmers, Antonio Lazcano, Stanley L Miller, and Jeffrey L Bada. A reassessment of prebiotic organic synthesis in neutral planetary atmospheres. *Origins of Life and Evolution of Biospheres*, 38(2):105–115, 2008.
- [124] GM Muñoz Caro, Uwe J Meierhenrich, Willem A Schutte, Bernard Barbier, A Arcones Segovia, Helmut Rosenbauer, WH-P Thiemann, Andre Brack, and J Mayo Greenberg. Amino acids from ultraviolet irradiation of interstellar ice analogues. *Nature*, 416(6879):403–406, 2002.
- [125] Stanley L Miller. The atmosphere of the primitive earth and the prebiotic synthesis of amino acids. In *Cosmochemical Evolution and the Origins of Life*, pages 139–151. Springer, 1974.
- [126] R.J-C Hennes, NG Holm, and MH Engel. Abiotic synthesis of amino acids under hydrothermal conditions and the origin of life: a perpetual phenomenon? *Naturwissenschaften*, 79(8):361–365, 1992.
- [127] William L Marshall. Hydrothermal synthesis of amino acids. *Geochimica et Cosmochimica Acta*, 58(9):2099–2106, 1994.
- [128] Akiva Bar-Nun, N Bar-Nun, SH Bauer, and Carl Sagan. Shock synthesis of amino acids in simulated primitive environments. *Science*, 168(3930):470–472, 1970.
- [129] CU Lowe, MW Rees, and RFRS Markham. Synthesis of complex organic compounds from simple precursors: formation of amino-acids, amino-acid polymers, fatty acids and purines from ammonium cyanide. *Nature*, 199(4890):219–222, 1963.

- [130] Daisuke Yoshino, Kyoichi Hayatsu, and Edward Anders. Origin of organic matter in early solar system—iii. amino acids: Catalytic synthesis. *Geochimica et cosmochimica acta*, 35(9):927–938, 1971.
- [131] JM Berg, JL Tymoczko, and L Stryer. Biochemistry, international 7th edition, england.
- [132] Roger E Summons, Pierre Albrecht, Gene McDonald, and J Michael Moldowan. Molecular biosignatures. *Strategies of Life Detection*, pages 133–159, 2008.
- [133] Sandra Pizzarello, Michael Zolensky, and Kendra A Turk. Nonracemic isovaline in the murchison meteorite: Chiral distribution and mineral association. *Geochimica et Cosmochimica Acta*, 67(8):1589–1595, 2003.
- [134] André Brack. Chemical biosignatures at the origins. In *Biosignatures for Astrobiology*, pages 3–21. Springer, 2019.
- [135] K Hornung and J Kissel. On shock wave impact ionization of dust particles. *Astronomy and Astrophysics*, 291:324–336, 1994.
- [136] Morgan Cable, Sarah E Waller, Rob Hodyss, Amy E Hofmann, Michael J Malaska, Robert E Continetti, Andres Jaramillo-Botero, Bernd Abel, Frank Postberg, Morgan EC Miller, et al. Plume grain sampling at hypervelocity: Implications for astrobiology investigations. *Bulletin of the American Astronomical Society*, 53(4):054, 2021.
- [137] Béla Paizs and Sándor Suhai. Fragmentation pathways of protonated peptides. *Mass spectrometry reviews*, 24(4):508–548, 2005.
- [138] Ruth-Sophie Taubner, Karen Olsson-Francis, Steven D Vance, Nisha K Ramkissoon, Frank Postberg, Jean-Pierre de Vera, André Antunes, Eloi Camprubi Casas, Yasuhito Sekine, Lena Noack, et al. Experimental and simulation efforts in the astrobiological exploration of ex-oceans. *Space science reviews*, 216(1):1–41, 2020.
- [139] Andres Jaramillo-Botero, Morgan L Cable, Amy E Hofmann, Michael Malaska, Robert Hodyss, and Jonathan Lunine. Understanding hypervelocity sampling of biosignatures in space missions. *Astrobiology*, 21(4):421–442, 2021.

- [140] Ales Charvat and Bernd Abel. How to make big molecules fly out of liquid water: applications, features and physics of laser assisted liquid phase dispersion mass spectrometry. *Physical Chemistry Chemical Physics*, 9(26):3335–3360, 2007.
- [141] Fabian Klenner, Frank Postberg, Jon Hillier, Nozair Khawaja, René Reviol, Ralf Srama, Bernd Abel, Ferdinand Stolz, and Sascha Kempf. Analogue spectra for impact ionization mass spectra of water ice grains obtained at different impact speeds in space. *Rapid Communications in Mass Spectrometry*, 33(22):1751–1760, 2019.
- [142] Fabian Klenner, Frank Postberg, Jon Hillier, Nozair Khawaja, René Reviol, Ferdinand Stolz, Morgan L Cable, Bernd Abel, and Lenz Nölle. Analog experiments for the identification of trace biosignatures in ice grains from extraterrestrial ocean worlds. *Astrobiology*, 20(2):179–189, 2020.
- [143] National Institute of Standards and Technology. Histidine mass spectrum (electron ionization). Technical report, U.S. Department of Commerce, Washington, D.C., 2014.
- [144] Millipore Sigma Histidine Monohydrochloride 53370, <https://www.sigmaaldrich.com/US/en/product/sigma/53370>.
- [145] JT Baker 6906-02 UltrexII Ultra Pure Water, <https://www.capitolscientific.com/JT-Baker-6906-02-1L-Water-ULTREX-II-UltraPure-Reagent>.
- [146] Le Yang, Fred J Ciesla, and Conel MO'D Alexander. The d/h ratio of water in the solar nebula during its formation and evolution. *Icarus*, 226(1):256–267, 2013.
- [147] Pauli Virtanen, Ralf Gommers, Travis E. Oliphant, Matt Haberland, Tyler Reddy, David Cournapeau, Evgeni Burovski, Pearu Peterson, Warren Weckesser, Jonathan Bright, Stéfan J. van der Walt, Matthew Brett, Joshua Wilson, K. Jarrod Millman, Nikolay Mayorov, Andrew R. J. Nelson, Eric Jones, Robert Kern, Eric Larson, C J Carey, İlhan Polat, Yu Feng, Eric W. Moore, Jake VanderPlas, Denis Laxalde, Josef Perktold, Robert Cimrman, Ian Henriksen, E. A. Quintero, Charles R. Harris, Anne M. Archibald, Antônio H. Ribeiro, Fabian Pedregosa,

- Paul van Mulbregt, and SciPy 1.0 Contributors. SciPy 1.0: Fundamental Algorithms for Scientific Computing in Python. *Nature Methods*, 17:261–272, 2020.
- [148] S Drapatz and KW Michel. Theory of shock-wave ionization upon high-velocity impact of micrometeorites. *Zeitschrift für Naturforschung A*, 29(6):870–879, 1974.
- [149] Anna Mocker, Klaus Hornung, Eberhard Grün, Sascha Kempf, Andrew Collette, Keith Drake, Mihály Horányi, Tobin Munsat, Leela O’Brien, Zoltán Sternovsky, et al. On the application of a linear time-of-flight mass spectrometer for the investigation of hypervelocity impacts of micron and sub-micron sized dust particles. *Planetary and Space Science*, 89:47–57, 2013.
- [150] James R Arnold and Willard F Libby. Age determinations by radiocarbon content: checks with samples of known age. *Science*, 110(2869):678–680, 1949.
- [151] James R Arnold and Willard F Libby. Radiocarbon dates. *Science*, 113(2927):111–120, 1951.
- [152] Harry Godwin. Half-life of radiocarbon. *Nature*, 195(4845):984–984, 1962.
- [153] Christopher Bronk Ramsey. Radiocarbon dating: revolutions in understanding. *Archaeometry*, 50(2):249–275, 2008.
- [154] Richard I Epstein, James M Lattimer, and David N Schramm. The origin of deuterium. *Nature*, 263(5574):198–202, 1976.
- [155] Johannes Geiss and Hubert Reeves. Cosmic and solar system abundances of deuterium and helium-3. *Astronomy and Astrophysics*, 18:126, 1972.
- [156] Francesco Palla, Daniele Galli, and Joseph Silk. Deuterium in the universe. *The Astrophysical Journal*, 451:44, 1995.
- [157] Jeffrey L Linsky, Bruce T Draine, HW Moos, Edward B Jenkins, Brian E Wood, Cristina Oliveira, William P Blair, Scott D Friedman, Cecile Gry, David Knauth, et al. What is the total deuterium

- abundance in the local galactic disk? *The Astrophysical Journal*, 647(2):1106, 2006.
- [158] Paul Hartogh, Dariusz C Lis, Dominique Bockelée-Morvan, Miguel de Val-Borro, Nicolas Biver, Michael Küppers, Martin Emprechtinger, Edwin A Bergin, Jacques Crovisier, Miriam Rengel, et al. Ocean-like water in the jupiter-family comet 103p/hartley 2. *Nature*, 478(7368):218–220, 2011.
- [159] Roger N Clark, Robert H Brown, Dale P Cruikshank, and Gregg A Swayze. Isotopic ratios of saturn’s rings and satellites: Implications for the origin of water and phoebe. *Icarus*, 321:791–802, 2019.
- [160] LJ Hallis. D/h ratios of the inner solar system. *Philosophical Transactions of the Royal Society A: Mathematical, Physical and Engineering Sciences*, 375(2094):20150390, 2017.
- [161] Cecilia Ceccarelli, Paola Caselli, Dominique Bockelée-Morvan, Olivier Mousis, Sandra Pizzarello, Francois Robert, and Dmitry Semenov. Deuterium fractionation: the ariadne’s thread from the pre-collapse phase to meteorites and comets today. *arXiv preprint arXiv:1403.7143*, 2014.
- [162] William D Watson. Ion-molecule reactions, molecule formation, and hydrogen-isotope exchange in dense interstellar clouds. *The Astrophysical Journal*, 188:35–42, 1974.
- [163] François Robert. Solar system deuterium/hydrogen ratio. *Meteorites and the early solar system II*, 1:341–351, 2006.
- [164] Yuri Aikawa, Kenji Furuya, Ugo Hincelin, and Eric Herbst. Multiple paths of deuterium fractionation in protoplanetary disks. *The Astrophysical Journal*, 855(2):119, 2018.
- [165] Robert H Brown, Kevin H Baines, G Bellucci, J-P Bibring, Bonnie J Buratti, F Capaccioni, P Cerroni, Roger N Clark, Angioletta Coradini, Dale P Cruikshank, et al. The cassini visual and infrared mapping spectrometer (vims) investigation. *Space Science Reviews*, 115(1):111–168, 2004.

- [166] RW Carlson, PR Weissman, WD Smythe, JC Mahoney, et al. Near-infrared mapping spectrometer experiment on galileo. *Space Science Reviews*, 60(1-4):457–502, 1992.
- [167] H Feuchtgruber, E Lellouch, B Bézard, Th Encrenaz, Th de Graauw, and GR Davis. Detection of hd in the atmospheres of uranus and neptune: a new determination of the d/h ratio. *Astronomy and Astrophysics*, 341:L17–L21, 1999.
- [168] H Feuchtgruber, E Lellouch, G Orton, T De Graauw, Bart Vandebussche, B Swinyard, R Moreno, C Jarchow, F Billebaud, T Cavalié, et al. The d/h ratio in the atmospheres of uranus and neptune from herschel-pacs observations. *Astronomy & Astrophysics*, 551:A126, 2013.
- [169] Kathrin Altwegg, Hans Balsiger, A Bar-Nun, Jean-Jacques Berthelier, Andre Bieler, Peter Bochslers, Christelle Briois, Ursina Calmonte, Michael Combi, Johan De Keyser, et al. 67p/churyumov-gerasimenko, a jupiter family comet with a high d/h ratio. *Science*, 347(6220), 2015.
- [170] Michael J Drake. Origin of water in the terrestrial planets. *Meteoritics & Planetary Science*, 40(4):519–527, 2005.
- [171] Alessandro Morbidelli, J Chambers, JI Lunine, Jean-Marc Petit, F Robert, GB Valsecchi, and KE Cyr. Source regions and timescales for the delivery of water to the earth. *Meteoritics & Planetary Science*, 35(6):1309–1320, 2000.
- [172] Bernard Marty. The origins and concentrations of water, carbon, nitrogen and noble gases on earth. *Earth and Planetary Science Letters*, 313:56–66, 2012.
- [173] CM O’D Alexander, R Bowden, ML Fogel, KT Howard, CDK Herd, and LR Nittler. The provenances of asteroids, and their contributions to the volatile inventories of the terrestrial planets. *Science*, 337(6095):721–723, 2012.
- [174] Nicolas Dauphas. The dual origin of the terrestrial atmosphere. *Icarus*, 165(2):326–339, 2003.

- [175] Tobias Owen, Akiva Bar-Nun, and Idit Kleinfeld. Possible cometary origin of heavy noble gases in the atmospheres of venus, earth and mars. *Nature*, 358(6381):43–46, 1992.
- [176] Laurie Leshin Watson, Ian D Hutcheon, Samuel Epstein, and Edward M Stolper. Water on mars: Clues from deuterium/hydrogen and water contents of hydrous phases in snc meteorites. *Science*, 265(5168):86–90, 1994.
- [177] David H Weinberg. On the deuterium-to-hydrogen ratio of the interstellar medium. *The Astrophysical Journal*, 851(1):25, 2017.
- [178] Carver J Bierson and Francis Nimmo. Explaining the galilean satellites’ density gradient by hydrodynamic escape. *The Astrophysical Journal Letters*, 897(2):L43, 2020.
- [179] Hans Balsiger, Kathrin Altwegg, and J Geiss. D/h and  $^{18}\text{O}/^{16}\text{O}$  ratio in the hydronium ion and in neutral water from in situ ion measurements in comet halley. *Journal of Geophysical Research: Space Physics*, 100(A4):5827–5834, 1995.
- [180] P Eberhardt, M Reber, D Krankowsky, and R Rhttp Hodges. The d/h and  $^{18}\text{O}/^{16}\text{O}$  ratios in water from comet p/halley. *Astronomy and Astrophysics*, 302:301, 1995.
- [181] Hans Balsiger, Kathrin Altwegg, Peter Bochsler, Peter Eberhardt, Josef Fischer, Stephan Graf, Annette Jäckel, Ernest Kopp, U Langer, M Mildner, et al. Rosina–rosetta orbiter spectrometer for ion and neutral analysis. *Space Science Reviews*, 128(1):745–801, 2007.
- [182] Ralf Srama, Thomas J Ahrens, Nicolas Altobelli, S Auer, JG Bradley, M Burton, VV Dikarev, T Economou, Hugo Fechtig, M Görlich, et al. The cassini cosmic dust analyzer. pages 465–518, 2004.
- [183] O. Heber, R. Golser, H. Gnaser, D. Berkovits, Y. Toker, M. Eritt, M. L. Rappaport, and D. Zajfman. Lifetimes of the negative molecular hydrogen ions:  $\text{H}_2^-$ ,  $\text{D}_2^-$ , and  $\text{Hd}^-$ . *Phys. Rev. A*, 73:060501, Jun 2006.
- [184] B. Jordon-Thaden, H. Kreckel, R. Golser, D. Schwalm, M. H. Berg, H. Buhr, H. Gnaser, M. Grieser, O. Heber, M. Lange, O. Novotný,

- S. Novotny, H. B. Pedersen, A. Petrignani, R. Repnow, H. Rubinstein, D. Shafir, A. Wolf, and D. Zajfman. Structure and stability of the negative hydrogen molecular ion. *Phys. Rev. Lett.*, 107:193003, Nov 2011.
- [185] Sascha Kempf. The surface dust analyzer (suda) on europa clipper. In *European Planetary Science Congress*, pages EPSC2018–462, 2018.
- [186] Millipore Sigma Deuterium Oxide 151882, [www.sigmaaldrich.com/US/en/product/aldrich/151882](http://www.sigmaaldrich.com/US/en/product/aldrich/151882).
- [187] Stanford Research System RGA 100, <https://www.thinksrs.com/products/rga.html>.
- [188] Kevin P Hand and Christopher F Chyba. Empirical constraints on the salinity of the europa ocean and implications for a thin ice shell. *Icarus*, 189(2):424–438, 2007.
- [189] Mikhail Y Zolotov. An oceanic composition on early and today’s encedaladus. *Geophysical Research Letters*, 34(23), 2007.
- [190] Fabian Klenner, Frank Postberg, Jon Hillier, Nozair Khawaja, Morgan L Cable, Bernd Abel, Sascha Kempf, Christopher R Glein, Jonathan I Lunine, Robert Hodyss, et al. Discriminating abiotic and biotic fingerprints of amino acids and fatty acids in ice grains relevant to ocean worlds. *Astrobiology*, 20(10):1168–1184, 2020.
- [191] Mikael Wirde, Ulrik Gelius, and Leif Nyholm. Self-assembled monolayers of cystamine and cysteamine on gold studied by xps and voltammetry. *Langmuir*, 15(19):6370–6378, 1999.
- [192] J Nathan Hohman, Pengpeng Zhang, Elizabeth I Morin, Patrick Han, Moonhee Kim, Adam R Kurland, Patrick D McClanahan, Viktor P Balema, and Paul S Weiss. Self-assembly of carboranethiol isomers on au {111}: intermolecular interactions determined by molecular dipole orientations. *ACS nano*, 3(3):527–536, 2009.
- [193] A. Bar-Nun, N. Bar-Nun, S. H. Bauer, and Carl Sagan. Shock synthesis of amino acids in simulated primitive environments. *Science*, 168(3930):470–472, 1970.

- [194] C. Chyba and C. Sagan. Endogenous production, exogenous delivery and impact-shock synthesis of organic molecules: an inventory for the origins of life. *Nature*, 355:125–132, January 1992.
- [195] George G. Managadze, William B. Brinckerhoff, and Alexander E. Chumikov. Possible synthesis of organic molecular ions in plasmas similar to those generated in hypervelocity impacts. *International Journal of Impact Engineering*, 29(1-10):449 – 458, 2003. Hypervelocity Impact.
- [196] George G. Managadze, William B. Brinckerhoff, and Alexander E. Chumikov. Molecular synthesis in hypervelocity impact plasmas on the primitive Earth and in interstellar clouds. *Geophysical Research Letters*, 30(5):n/a–n/a, 2003. 1247.
- [197] Jennifer G. Blank, Gregory H. Miller, Michael J. Ahrens, and Randall E. Winans. Experimental shock chemistry of aqueous amino acid solutions and the cometary delivery of prebiotic compounds. *Origins of life and evolution of the biosphere*, 31(1):15–51, 2001.
- [198] Zita Martins, Mark C. Price, Nir Goldman, Mark A. Sephton, and Mark J. Burchell. Shock synthesis of amino acids from impacting cometary and icy planet surface analogues. *Nature Geosci*, 6(12):1045–1049, Dec 2013. Article.
- [199] Dale P. Cruikshank, Ted L. Roush, Tobias C. Owen, Thomas R. Geballe, Catherine de Bergh, Bernard Schmitt, Robert H. Brown, and Mary Jane Bartholomew. Ices on the surface of triton. *Science*, 261(5122):742–745, 1993.
- [200] T. B. McCord, R. W. Carlson, W. D. Smythe, G. B. Hansen, R. N. Clark, C. A. Hibbitts, F. P. Fanale, J. C. Granahan, M. Segura, D. L. Matson, T. V. Johnson, and P. D. Martin. Organics and other molecules in the surfaces of Callisto and Ganymede. *Science*, 278(5336):271–275, 1997.
- [201] T. B. McCord, G. B. Hansen, R. N. Clark, P. D. Martin, C. A. Hibbitts, F. P. Fanale, J. C. Granahan, M. Segura, D. L. Matson, T. V. Johnson, R. W. Carlson, W. D. Smythe, and G. E. Danielson. Non-water-ice constituents in the surface material of the icy Galilean satellites from

the Galileo near-infrared mapping spectrometer investigation. *Journal of Geophysical Research: Planets*, 103(E4):8603–8626, 1998.

- [202] B. J. Buratti, D. P. Cruikshank, R. H. Brown, R. N. Clark, J. M. Bauer, R. Jaumann, T. B. McCord, D. P. Simonelli, C. A. Hibbitts, G. B. Hansen, T. C. Owen, K. H. Baines, G. Bellucci, J.-P. Bibring, F. Capaccioni, P. Cerroni, A. Coradini, P. Drossart, V. Formisano, Y. Langevin, D. L. Matson, V. Mennella, R. M. Nelson, P. D. Nicholson, B. Sicardy, C. Sotin, T. L. Roush, K. Soderlund, and A. Muradyan. Cassini visual and infrared mapping spectrometer observations of Iapetus: Detection of CO<sub>2</sub>. *The Astrophysical Journal Letters*, 622(2):L149, 2005.
- [203] Roger N Clark, Robert H Brown, Ralf Jaumann, Dale P Cruikshank, Robert M Nelson, Bonnie J Buratti, Thomas B McCord, J Lunine, KH Baines, G Bellucci, et al. Compositional maps of saturn’s moon phoebe from imaging spectroscopy. *Nature*, 435(7038):66–69, 2005.
- [204] W. M. Grundy, L. A. Young, J. R. Spencer, R. E. Johnson, E. F. Young, and M. W. Buie. Distributions of H<sub>2</sub>O and CO<sub>2</sub> ices on Ariel, Umbriel, Titania, and Oberon from IRTF/SpeX observations. 2007.
- [205] Dale P. Cruikshank, Allan W. Meyer, Robert H. Brown, Roger N. Clark, Ralf Jaumann, Katrin Stephan, Charles A. Hibbitts, Scott A. Sandford, Rachel M.E. Mastrapa, Gianrico Filacchione, Cristina M. Dalle Ore, Philip D. Nicholson, Bonnie J. Buratti, Thomas B. McCord, Robert M. Nelson, J. Brad Dalton, Kevin H. Baines, and Dennis L. Matson. Carbon dioxide on the satellites of saturn: Results from the Cassini VIMS investigation and revisions to the VIMS wavelength scale. *Icarus*, 206(2):561 – 572, 2010. Cassini at Saturn.
- [206] Sylvie Derenne and François Robert. Model of molecular structure of the insoluble organic matter isolated from murchison meteorite. *Meteoritics & Planetary Science*, 45(9):1461–1475, 2010.
- [207] Laurent Remusat, Fabien Palhol, François Robert, Sylvie Derenne, and Christian France-Lanord. Enrichment of deuterium in insoluble organic matter from primitive meteorites: A solar system origin? *Earth and Planetary Science Letters*, 243(1-2):15–25, 2006.

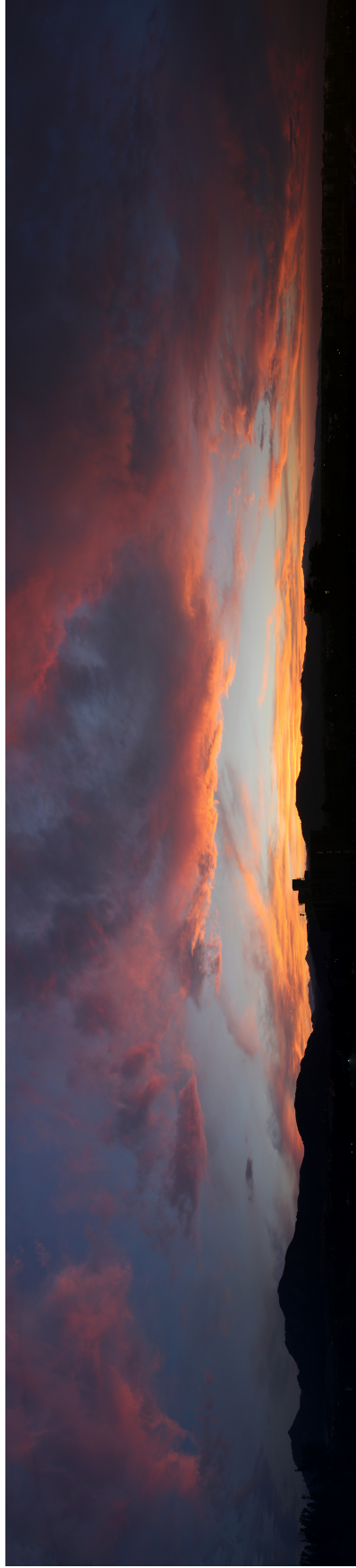
- [208] Y. Saito, S. Yokota, T. Tanaka, K. Asamura, M. N. Nishino, M. Fujimoto, H. Tsunakawa, H. Shibuya, M. Matsushima, H. Shimizu, F. Takahashi, T. Mukai, and T. Tersawa. Solar wind proton reflection at the lunar surface: Low energy ion measurement by map-pace onboard selene (kaguya). *Geophys. Res. Lett.*, 35:L24205, 2008.
- [209] D. J. McComas. Lunar backscatter and neutralization of the solar wind: First observations of neutral atoms from the moon. *Geophys. Res. Lett.*, 36:L12104, 2009.
- [210] A. Schaufelberger, P. Wurz, S. Barabash, M. Wieser, Y. Futaana, M. Holmström, A. Bhardwaj, M. B. Dhanya, R. Sridharan, and K. Asamura. Scattering function for energetic neutral hydrogen atoms off the lunar surface. *Geophys. Res. Lett.*, 38:L22202, 2011.
- [211] U. Samir, K. H. Wright, and N. H. Stone. The expansion of a plasma into a vacuum: Basic phenomena and processes and applications to space plasma physics. *Rev. Geophys.*, 21:1631–1646, 1983.
- [212] J. S. Halekas, Y. Saito, G. T. Delory, and W. M. Farrell. New views of the lunar plasma environment. *Plan. Space Sci.*, 59:1681–1694, 2011.
- [213] Jiong Wang and DE Hastings. Ionospheric plasma flow over large high-voltage space platforms. i: Ion-plasma-time scale interactions of a plate at zero angle of attack. *Physics of Fluids B: Plasma Physics*, 4(6):1597–1614, 1992.
- [214] Lars Kristoferson. Laboratory simulation experiment on solar wind interaction with the moon. *Journal of Geophysical Research*, 74(3):906–908, 1969.
- [215] IM Podgorny and Yu V Andriyanov. Simulation of the solar wind interaction with non-magnetic celestial bodies. *Planetary and Space Science*, 26(2):99–109, 1978.
- [216] DS Intriligator and GR Steele. Observations of structuring in the downstream region of a large spherical model in a laboratory simulated solar wind plasma. *Journal of Geophysical Research: Space Physics*, 87(A8):6053–6059, 1982.

- [217] DS Intriligator and GR Steele. Analyses of experimental observations of electron temperatures in the near wake of a model in a laboratory-simulated solar wind plasma. *Journal of Geophysical Research: Space Physics*, 90(A5):4027–4034, 1985.
- [218] M. I. Zimmerman, W. M. Farrell, and A. R. Poppe. Grid-free 2d plasma simulations of the complex interaction between the solar wind and small, near-earth asteroids. *Icarus*, 238:77–85, 2014.
- [219] T. A. Nordheim, G. H. Jones, J. S. Halekas, E. Roussos, and A. J. Coates. Surface charging and electrostatic dust acceleration at the nucleus of comet 67p during periods of low activity. *Planet. Space Sci.*, 119:24–35, 2015.
- [220] C. Lue, Y. Futaana, S. Barabash, M. Wieser, M. Holmstrom, A. Bhardwaj, M. Dhanya, and P. Wurz. Strong influence of lunar crustal fields on the solar wind flow. *Geophys. Res. Lett.*, 38:L03202, 2011.
- [221] J. S. Halekas, G. T. Delory, D. A. Brain, R. P. Lin, and D. L. Mitchell. Density cavity observed over a strong lunar crustal magnetic anomaly in the solar wind: a mini-magnetosphere? *Planet. Space Sci.*, 56:941–946, 2008.
- [222] M. Wieser, S. Barabash, Y. Futaana, M. Holmstrom, A. Bhardwaj, R. Sridharan, M. B. Dhanya, P. Wurz, A. Schaufelberger, and K. Asamura. First observation of a mini-magnetosphere above a lunar magnetic anomaly using energetic neutral atoms. *Geophys. Res. Lett.*, 37:L015103, 2010.
- [223] R. A. Bamford, B. Kellett, W. J. Bradford, C. Norberg, A. Thornton, K. J. Gibson, I. A. Crawford, L. Silva, L. Gargatã, and R. Bingham. Minimagetospheres above the lunar surface and the formation of lunar swirls. *Phys. Rev. Lett.*, 109:081101, 2012.
- [224] J. Deca, A. Divin, G. Lapenta, B. Lembège, S. Markidis, and M. Horányi. Electromagnetic particle-in-cell simulations of the solar wind interaction with lunar magnetic anomalies. *Phys. Rev. Lett.*, 112:151102, 2014.

- [225] J. Deca, A. Divin, B. Lembège, M. Horányi, S. Markidis, and G. Lapenta. General mechanism and dynamics of the solar wind interaction with lunar magnetic anomalies from 3-d particle-in-cell simulations. *J. Geophys. Res. Space Physics*, 120:6443–6463, 2015.
- [226] Y. Futaana, S. Barabash, M. Wieser, C. Lue, P. Wurz, A. Vorburger, A. Bhardwaj, and K. Asamura. Remote energetic neutral atom imaging of electric potential over a lunar magnetic anomaly. *Geophys. Res.*, 40:262–266, 2013.
- [227] R. Jarvinen, M. Alho, E. Kallio, P. Wurz, S. Barabash, and Y. Futaana. On vertical electric fields at lunar magnetic anomalies. *Geophys. Res. Lett.*, 41, 2014.
- [228] C. T. Howes, X. Wang, J. Deca, and M. Horányi. Laboratory investigation of lunar surface electric potentials in magnetic anomaly regions. *Geophys. Res. Lett.*, 42:4280–4287, 2015.
- [229] M. I. Zimmerman, W. M. Farrell, and A. R. Poppe. Kinetic simulations of kilometer-scale mini-magnetosphere formation on the moon. *J. Geophys. Res. Planets*, 120:1893–1903, 2015.
- [230] D. T. Blewett, E. I. Coman, B. R. Hawke, J. J. Gillis-Davis, M. E. Purucker, and C. G. Hughes. Lunar swirls: Examining crustal magnetic anomalies and space weathering trends. *J. Geophys. Res.*, 116:E02002, 2011.
- [231] X. Wang, M. Horányi, and S. Robertson. Characteristics of a plasma sheath in a magnetic dipole field: Implications to the solar wind interaction with the lunar magnetic anomalies. *J. Geophys. Res.*, 117:A06226, 2012.
- [232] X. Wang, C. T. Howes, M. Horányi, and S. Robertson. Electric potentials in magnetic dipole fields normal and oblique to a surface in plasma: Understanding the solar wind interaction with lunar magnetic anomalies. *Geophys. Res. Lett.*, 40:1686–1690, 2013.
- [233] WM Farrell, TJ Stubbs, JS Halekas, RM Killen, GT Delory, MR Collier, and RR Vondrak. Anticipated electrical environment within permanently shadowed lunar craters. *Journal of Geophysical Research: Planets*, 115(E3), 2010.

- [234] MI Zimmerman, WM Farrell, TJ Stubbs, JS Halekas, and TL Jackson. Solar wind access to lunar polar craters: Feedback between surface charging and plasma expansion. *Geophysical Research Letters*, 38(19), 2011.
- [235] W. Yu, J. Wang, and K. Chou. Laboratory measurement of lunar regolith simulat surface charging in a localized plasma wake. *IEEE Tran. Plasma Sci.*, 43:4175–4181, 2015.
- [236] D. A. Mendis and M. Rosenberg. Cosmic dusty plasma. *Annual Rev. Astron. Astrophys.*, 32:419–463, 1994.
- [237] M. Horányi. Charged dust dynamics in the solar system. *Annual Rev. Astron. Astrophys.*, 34:383–418, 1996.
- [238] J. J. Rennilson and D. R. Criswell. Surveyor observations of lunar horizon-glow. *The Moon*, 10(2):121–142, 1974.
- [239] C. K. Goertz and G. Morfill. A model for the formation of spokes in saturn’s ring. *Icarus*, 53:219–229, 1983.
- [240] P. Vernazza, M. Delbo, P.L. King, M.R.M. Izawa, J. Olofsson, P. Lamy, F. Cipriani, R.P. Binzel, F. Marchis, B. Merín, and A. Tamanai. High surface porosity as the origin of emissivity features in asteroid spectra. *Icarus*, 221(2):1162 – 1172, 2012.
- [241] Nicholas Thomas, Björn Davidsson, Mohamed Ramy El-Maarry, Sonia Fornasier, Lorenza Giacomini, AG Gracia-Berná, SF Hviid, W-H Ip, Laurent Jorda, HU Keller, et al. Redistribution of particles across the nucleus of comet 67p/churyumov-gerasimenko. *Astronomy & Astrophysics*, 583:A17, 2015.
- [242] M. S. Robinson, P. C. Thomas, J. Veverka, S. Murchie, and B. Carcich. The nature of ponded deposits on eros. *Nature*, 413(6854):396–400, Sep 2001.
- [243] X. Wang, J. Schwan, H. w. Hsu, E. Grün, and M. Horányi. Dust charging and transport on airless planetary bodies. *Geophys. Res. Lett.*, 43:6103–6110, 2016.

- [244] T. E. Sheridan, J. Goree, Y. T. Chiu, R. L. Rairden, and J. A. Kiessling. Observation of dust shedding from material bodies in a plasma. *J. Geophys. Res.*, 97:2935, 1992.
- [245] B. Walch, M. Horányi, and S. Robertson. Measurement of the charge on individual dust grains in a plasma. *IEEE Tran. Plasma Sci.*, 22(2):97–102, 1994.
- [246] A. A. Sickafoose, J. E. Colwell, M. Horányi, and S. Robertson. Experimental levitation of dust grains in a plasma sheath. *J. Geophys. Res.*, 107(A11):1408, 2002.
- [247] T. M. Flanagan and J. Goree. Dust release from surfaces exposed to plasma. *Phys. Plasmas*, 13:123504, 2006.
- [248] X. Wang, J. E. Colwell, M. Horányi, and S. Robertson. Charge of dust on surfaces in plasma. *IEEE Tran. Plasma Sci.*, 35(2):271–279, 2007.
- [249] X. Wang, M. Horányi, and S. Robertson. Experiments on dust transport in plasma to investigate the origin of the lunar horizon glow. *J. Geophys. Res.*, 114:A05103, 2009.
- [250] X. Wang, M. Horányi, and S. Robertson. Investigation of dust transport on the lunar surface in a laboratory plasma with an electron beam. *J. Geophys. Res.*, 115:A11102, 2010.
- [251] X. Wang, M. Horányi, and S. Robertson. Dust transport near electron beam impact and shadow boundaries. *Planet. Space Sci.*, 59:1791–1794, 2011.
- [252] N. Ding, J. Wang, and J. Polansky. Measurement of dust charging on a lunar regolith simulant surface. *IEEE Tran. Plasma Sci.*, 41:3498–3504, 2013.
- [253] C. Böhm and J. Perrin. Retarding field analyzer for measurements of ion energy distributions and secondary electron emission coefficients in low pressure radio frequency discharges. *Rev. Sci. Instr.*, 64:31–44, 1993.
- [254] Z. Sternovsky and S. Robertson. Langmuir probe interpretation for plasmas with secondary electrons from the wall. *Physics of Plasmas*, 11(7):3610–3615, 2004.



Mosaic photo taken by the author from the top of the IMPACT laboratory on July 15th, 2020.



The view from the top of Matterhorn Peak as photographed by the author on August 27th, 2017.

Uncompahgre Peak is on the left, and Wetterhorn Peak is on the right.



## IMPACT

Impact ionization time of flight mass spectrometers (TOF-MS) are a class of spaceflight instrument designed to study the molecular composition of dust grains ejected from airless solar system objects by impacting them at speeds of several km/s. The kinetic energy of the impact ionizes molecules from the dust grain, allowing them to be studied using TOF-MS. Such instruments have been used in the past to study a number of different solar system objects, most notably when the Cassini Cosmic Dust Analyzer (CDA) measured the chemistry of icy dust grains from the subsurface ocean of Enceladus. While some laboratory work has been performed to match CDA flight spectra, previous studies have not used actual hypervelocity dust impacts into ice. Here we describe a series of experiments based on a cryogenic target system at the University of Colorado dust accelerator at the Institute for Modeling Plasma, Atmospheres, and Cosmic Dust (IMPACT), which enables impact experiments into ice under highly realistic conditions.

Using a novel airbrush ice system, surfaces of histidine both with and without a water ice cover were bombarded by hypervelocity dust grains. TOF chemical analysis of the impact plume suggests that the amino acid fragmentation rate is largely constant below 6 km/s, but begins to rise significantly beyond 7 km/s. It also suggests that the presence of a water ice matrix mitigates impact stress and reduces the fragmentation rates at all velocities by a factor of about two. Further, the spectra show that fragmentation products are fundamentally related to those found in the NIST database of electron impact ionization mass spectra of histidine. This indicates that even in the event of breakup during detection, it may be possible to use the breakup products as a means to identify the parent molecule with impact ionization TOF instruments, thus enabling this type of instrument to detect and characterize complex organics.

Similar experiments were performed with ice created with a known D-H ratio. Co-added TOF spectra from the impact plume indicates that the D-H ratio can be accurately recovered with this method. This means that impact ionization mass spectrometers on a variety of future spacecraft may be able to measure the D-H ratio of icy ocean worlds, comets, and other airless icy bodies.